Dottorato di ricerca

In

INGEGNERIA STRUTTURALE, GEOTECNICA E RISCHIO SISMICO

XXXIV CICLO

Tsunami scenarios for hazard forecasting based on complex earthquake slip models

Hafize Başak Bayraktar

Relatore
Prof. Gaetano Festa
Dr. Stefano Lorito (*Istituto Nazionale di Geofisica e Vulcanologia*)

Coordinatore
Prof. Iunio Iervolino

ACKNOWLEDGEMENTS

I would like to thank the following people, without whom I would not have been able to complete this thesis. I would like to express my gratitude to my supervisors, Prof. Gaetano Festa and Dr. Stefano Lorito for their consistent support, guidance, encouragement, and patience. Their immense knowledge and plentiful experience have encouraged me in all the stages of my research. I would like to especially thank Dr. Antonio Scala, Dr. Fabrizio Romano, and Dr. Manuela Volpe for their assistance at every stage of my study and for spending limitless hours to develop and completion of this study. I also would like to express gratitude to Dr. Gareth Davies for his treasured support.

I would like to thank Dr. Deniz Ertuncay, Selen Caner Ertuncay, Dr. Stefania Tarantino, Esra Kalkan, Figen Eskiköy, Gamze Ateşoğlu, Ebru Kalkan, Dr. Elham Mousavian, and Stefano Piemontese and numerous friends who endured this long process with me, always offering support and love.

I also would like to thank Dr. Öcal Necmioğlu, Prof. Semih Ergintav, for their guidance and for sharing their valuable knowledge and skills throughout my study.

I would like to thank Prof. Alberto Armigliato and Prof. Jorge Macías Sánchez for their detailed revive and valuable comments on the thesis.

Last but not least, my warm and heartfelt thanks go to my husband Oğuz Bayraktar, my mother Sevgi Fırat, my father Gürsel Fırat whom I dedicate this thesis, and all other members of my family. I am grateful for their unconditional, unequivocal, and loving support.

TABLE OF CONTENTS

LIST OF FIGURES

LIST OF TABLES

INTRODUCTION

Tsunamis are natural phenomena that occur more rarely than many others. Moreover, they can be generated by different sources. Then, it is a challenging task to assess their frequency, characteristics, and consequences in coastal zones.

Tsunami hazard studies have been performed in various areas with different spatial scales: local, regional and global. Both deterministic and probabilistic approaches have been used for tsunami hazard estimation. The deterministic approach focuses on the maximum credible or worst-case scenarios to calculate associated tsunami impact in a target area (Tinti and Armigliato 2003; Tinti et al. 2005; Løvholt et al. 2006; Okal and Synolakis, 2008; Lorito et al, 2008; Harbitz et al. 2012; Omira et al. 2013). Although deterministic analysis requires less computational efforts, there is not any unique way to determine the worst-case scenarios, introducing a further contribution to the uncertainty, complementing the simplifications caused by first-order effect on the modelled tsunami wave heights (Geist and Bilek 2001; Gica et al. 2007; Davies et al. 2015; Mueller et al. 2015; Li et al. 2016; Butler et al. 2017; Mori et al. 2017).

To deal with these problems, probabilistic tsunami hazard analysis (PTHA) has become a widely used procedure for hazard estimation. The steps of the PTHA can be defined in three stages: (1) definition of potential tsunami sources and associated mechanism along with their rate of occurrence, (2) numerical modelling of the generation and propagation of tsunami waves and (3) tsunami hazard estimation including the epistemic and aleatoric uncertainties (Geist and Parsons, 2006; Geist and Lynett, 2014; Grezio et al., 2017, Basili et al. 2021). This

approach provides as output the probability of exceedance of a threshold for a given tsunami metric, such as the maximum runup or the maximum wave height, in a specific location within a given time (for example hundreds to thousands of years). The outputs of PTHA can be combined with the estimation of the local vulnerability and exposure for the estimation of the tsunami risk (Gonzalez et al., 2009; Geist and Lynett, 2014; Wood et al., 2015; Grezio et al., 2017). The outputs of PTHA are then used as input for loss models that estimate damage to the built environment, the economic impact, and the fatalities; these models help to set priorities on risk mitigation strategies (Chock, 2015; Løvholt et al., 2015, Suppasri et al., 2016; Thio et al., 2017; Wei et al., 2017; Yeh, 2010). PTHA results can be also naturally combined with similar results for other phenomena in multi-hazard assessments.

PTHA requires a large number of high-resolution numerical simulations to be able to explore the natural variability of the sources (González et al., 2009; Geist and Lynett, 2014). Since there are not sufficient catalogues of historical tsunamis due to their infrequent nature, the procedure relies on massive numerical simulations of tsunami generation and propagation, producing as many as possible, from thousands to millions of synthetic scenarios, usually considering non-linear models in the shallow water approximation (Geist and Lynett, 2014; Behrens and Dias, 2015; Grezio et al., 2017; Behrens et al., 2021). Therefore, PTHA is a challenging procedure in terms of both modelling and computational points of view. Lorito et al. (2015) developed a method to identify a subset of sources able to preserve the accuracy of results for Seismic PTHA (SPTHA) significantly reducing the computational cost of the assessment. Moreover, Selva et al. (2016) suggest an operation for the joint and unbiased quantification of epistemic and aleatory uncertainty of earthquake source in SPTHA, including the filtering procedure of Lorito et al. (2015). Volpe et al. (2019) combine these two

procedures and develop a computationally efficient approach to achieve robust assessment of site-specific SPTHA. Modifying the approach proposed by Lorito et al. (2015) to enhance its computational efficiency and improve the accuracy, they applied a separate treatment for remote and local sources, selecting near-field scenarios on the basis of the similarity of the coseismic tsunami initial conditions. It is possible to perform simulations rapidly (faster than real time) with the implementation of tsunami numerical codes using Graphical Processing Units (GPUs). HPC accelerates the tsunami forecasting in real-time (Løvholt et al. 2019) and supports the performance of high resolution local PTHA studies. Gibbons et al. (2021) is a pioneering study which applies a site-specific PTHA workflow using Tsunami-HySEA model (Macías et al., 2016) which can run in multi-GPU architectures. This kind of flexibility and scalability would help to bridge gaps between long-term tsunami hazard analysis and early warning since it allows to make tsunami hazard analysis at a local scale with high resolution inundation calculations.

The probabilistic approach can also be an effective method for tsunami forecasting. Arrival time of tsunami waves to the coast can vary from minutes to days and it has a crucial importance to forecast tsunamis and make a warning in a very short time after a potentially tsunamigenic earthquake. Since we need time after the earthquake occurrence to define a reasonably well constrained tsunami initial condition, it is crucial to explore methods that deal with a correct representation of the uncertainty due to many different possible source mechanisms, especially for local tsunamis. The recent study of Selva et al. (2021) mainly aims to propagate this uncertainty from the source to the alert level using probabilistic methods. Current practices use a deterministic approach, such as Decision Matrices, Envelopes or Best Matching scenarios, for tsunami forecasts and some specific strategies are accepted to replace

uncertainty assessment. Probabilistic Tsunami Forecasting (PTF), on the other hand, can generate probability distributions of a selected tsunami intensity measure at all forecast points. An ensemble of tsunami scenarios from a set of sources weighted by the probability of being consistent with available real-time observations (seismic, geodetic, tsunami) and pre-computed local long-term tsunami hazard information are used for uncertainty quantification. Since PTF can be updated continuously with new and more accurate information, it is in principle possible to reduce the uncertainty in real-time.

For both long-term hazard assessment and tsunami forecasting in real time, tsunami source modeling is a first-order uncertainty driver (Geist and Parsons, 2006; Tselentis et al., 2006; Løvholt et al., 2012c; Mueller et al., 2014; Fukutani et al., 2014; Davies et al., 2015). For example, the heterogeneous slip distribution plays an important part in assessing the impact of local tsunamis (Geist & Dmowska, 1999). Mueller et al. (2015) have demonstrated that uniform slip models underestimate the inundation extent and heterogenous slip models increased the inundation extent by the equivalent of 0.3–0.4 Mw units with respect to uniform slip models. It is also observed that the location of the maximum slip affects the distribution of the maximum tsunami heights on the coast, even though the moment magnitude and the rupture area are the same (Geist, 2002; McCloskey et al., 2008; Goda et al., 2014). Li et al. (2016) also indicated that heterogeneous models generate 20-60% larger wave amplitudes than the uniform slip models for a 500-year return period on the South China Sea region, also at a certain distance from the source.

Several studies deal with incorporating shallow slip amplification with tsunami hazard analysis, and the effect of depth dependence of slip on tsunami waves. Murphy et al. (2016) introduced a concept to generate depth-dependent slip distributions with dynamic

simulations and indicated these slip distributions enhance tsunami hazard. Shallow slip amplification can merge to updip rupture facilitated by along-depth bi-material effects (Rubin and Ampuero, 2007; Ma and Beroza, 2008; Scala et al., 2017) and free-surface reflected waves within the accretionary wedge (Nielsen, 1998; Lotto et al., 2017a; van Zelst et al., 2019) using dynamic rupture earthquake models. Such physics-based models can be directly linked to tsunami models and they complement PTHA by improving the complexity of tsunami source.

In the context of PTHA, Scala et al. (2020) proposes an approach to generate k^{-2} stochastic slip distributions, considering shallow slip amplification, which is imposed depending on the variation of the rigidity and coupling with depth. The study showed that the sensitivity of mean hazard curves is different for the depth-dependent and depth-independent slip distributions at the same point of interest. A depth-dependent probability of occurrence is also defined for each single event slip distribution to make scenarios compatible with the expected long-term uniform cumulative slip distribution. This probability of occurrence is forced to increase with increasing average rigidity of the rupture area. This change has been done to balance the shallow slip amplification for higher magnitude events which rupture everywhere over the subduction interface. Therefore, the probability of occurrence of relatively small events is decreased in the shallow part of the fault interface while deeper ones are more likely to occur. The comparison of depth-dependent SPTHA approach with depth-independent model showed that the depth dependent model shows lower probability for smaller hazard intensities and larger probability for higher intensities.

Overall, different approaches have been proposed to generate heterogeneous slip distributions for tsunami hazard assessment purposes (LeVeque et al., 2016; Murphy et al., 2016; Sepulveda et al., 2017; Davies 2019; Scala et al. 2020). The inter-comparison of these

models and the calibration of their parameterization against real observations is a challenging task.

Davies et al. (2015) tested the performance among eight k^{-2} type models by comparison with 66 finite-fault inversions. The subsequent study of Davies (2019) was probably the first one of his kind; it tested different source modeling strategies against tsunami observations from multiple events. Stochastic scenarios are generated assuming with earthquake location and magnitude similar to the observation. For each event, the agreement between the observed tsunami data and scenario is measured using a weighted least-squares goodness-of-fit statistic. Further assessment of model biases is done using the good fitting scenarios. It has been observed that variable area-uniform-slip models scenarios generally have higher slip than the expected according to scaling relation, which demonstrate bias in that model. It showed that models with fixed area-uniform slip have a poor agreement with the tsunami observations while tsunamis generated by heterogenous slip and variable area-uniform-slip models fit better to observed tsunamis for both constant and depth-varying rigidity cases. Davies & Griffin (2020) further analyzed the sensitivity of far-field PTHA to slip modelling including constant and depth-varying rigidity models combined with three slip models, which are fixed area-uniform slip, variable area-uniform slip and heterogenous slip models. Slip model biases are examined by comparing earthquake-tsunami scenarios with DART-buoy tsunami observations. Uncertainties in seismic coupling, maximum-magnitudes and Gutenberg-Richter b-values are accounted using Bayesian techniques to model scenario occurrence rates. They showed that the tsunami hazard is weakly sensitive to the choice of rigidity model. However, tsunami hazard is significantly affected by the choice of the slip model. They showed that fixed area-uniform slip model produces lower slip than the other

models and this approach should not be used, even in the far-field. However, heterogeneous-slip and variable area-uniform-slip models produce similar tsunami hazard in the far-field and they argue that both models can usefully represent earthquake-generated tsunamis for PTHA.

It nevertheless remains difficult to test the PTHA results as a whole, because one should in principle wait a non-realistically long time for different tsunamis to occur at a given location. This study is then on the same lines of the ones just mentioned, in particular Davies et al. (2019), as it deals with testing one fundamental PTHA component which is the earthquake modelling one. This thesis mainly aims to test synthetic tsunamis produced with different slip generation techniques, against tsunami observations from open ocean DART buoys and models are also tested against each other to understand how different slip and rigidity treatments affect the random simulated tsunamis. Here, we compare synthetic tsunamis produced by recent stochastic slip generation techniques (Scala et al., 2020) against tsunami observations at open ocean DART buoys, for 15 earthquakes and ensuing tsunamis analyzed also by Davies (2019). We also expand the Scala et al. (2020) model, which considered only sources of circular shape, by introducing sources of rectangular shape. In addition to stochastic slip models, kinematic slip models from teleseismic inversions of Ye et al. (2016) for 10 of the same 15 earthquakes are also considered as tsunami sources. Tsunami simulations are performed for 79.620 scenarios in total, using the Tsunami-HySEA code (Macías et al., 2016). The simulated results are validated and compared to the DART observations in the same framework proposed by Davies (2019). This also allows to compare the performance of all these models with respect to observations with the source models tested by Davies (2019).

This thesis is organized as follows. In the first chapter, Shallow Water Equations are derived from Navier-Stokes equations. After that, tsunami sources and their characteristics

are briefly presented. Then, tsunami propagation is defined using the derived shallow water equations. Subsequently, tsunami shoaling and inundation are defined and finally commonly used tsunami models and numerical methods for tsunami propagation are explained. In the second chapter, first of all earthquake occurrence is explained defining the fault types and earthquake occurrence mechanism. After that, the characteristics of subduction zones are defined. Then, earthquake source is described using the point source approximation. Later on, some scaling relations among the size of an earthquake, rupture dimensions, average slip and the stress drop are explained. Then, the stochastic source modelling is defined based on the fractal composite model. In the last section, sea floor deformation from simplified rectangular and complex fault planed earthquake sources are defined. In the third chapter, first of all, the ingredients of the study and the data is explained. Then, the methodology of generation of synthetic earthquake scenarios and extraction of finite-fault models are defined. Later on, the details of the tsunami modelling and simulations setup are described. Then, details of the methods to test tsunami waveforms is explained and the comparison of each slip generation methods with observations and against each other is done. At the end of Chapter 3, the comparison results are summarized and concluded. In Chapter 4, some of the articles in which I was involved during my doctoral education are presented.

In this work, my contribution starts from the generation of stochastic slip models for each scenario event using the ANTI-FASc tool; here I have also contributed to its development and testing. After that, I have converted the finite-fault inversion results of Ye et al. (2016) to be used as inputs for the tsunami numerical model. The catalog provides slip maps of each event on a regular grid with cells along strike, dip and depth and hypocenter of each event. Using the latitude and longitude information of hypocenter and the distance between the central points of the cells, geographical coordinates have been calculated for each grid center. Using any earthquake

scenario, either from the ensemble of stochastic models or kinematic models of the Ye et al. (2016) teleseismic inversion catalog, I have prepared inputs for tsunami numerical modelling. Before lunching massive number of simulations, I have calibrated and validated the tsunami model (Tsunami-HySEA). Afterwards, I have tested tsunami modelling results against observations. To do that, I have extracted de-tided tsunami observations from DART records and tsunami time series of each model scenario from tsunami simulation results. Subsequently, observed and modelled time series have been cut within the time limits of the high-frequency part of the de-tided DART signal. I have developed an algorithm and benchmarked it using the data considered by Davies (2019) to test tsunami modelling results with respect to observations. I have tested and compared the modelling results with the observations in the same framework as proposed by Davies (2019). Besides that, I have also tested stochastic models against other models to understand how slip and rigidity affect the random simulated tsunamis and thus which factors are important to reflect the natural variability of real tsunamis in the context of tsunami hazard assessment.

I also would like to state that this thesis has benefitted from the contribution and support of many researchers. Initially, stochastic slip models are generated with the support of Dr. Antonio Scala using the ANTI-FACSc tool. I have used the slab geometries which are discretized by triangular meshes by Dr. Fabrizio Romano from Slab 2.0 model (Hayes et al., 2018) or from the modelling proposed by Geoscience Australia. All the tsunami simulations have been run in Marconi100 by Dr. Manuela Volpe and Dr. Carlos Sánchez Linares under the Project TSU-CAST (TSUnami-ForeCASTing) using Tsunami-HySEA numerical model (Macías et al., 2016).

CHAPTER 1- TSUNAMIS AND TSUNAMI MODELLING

Although tsunamis are rare events, they may have severe consequences, and because of their rarity there is a lack of availability of tsunami data from historical events. Therefore, it is crucial to understand their physical mechanisms, and to perform numerical simulations to support coastal planning and risk assessment.

1.1. Physics of tsunamis

Shallow water equations (SWE) can accurately describe the offshore tsunami propagation. SWE are a set of partial differential equations that describe a thin layer of fluid in hydrostatic balance with constant density. The layer of fluid is bounded by the bottom topography from below and the free surface from above. Navier-Stokes equations describe the conservation of mass and linear momentum under specific conditions (Vreugdenhil, 1994). SWE are derived from the general equations of hydrodynamics, the Navier-Stokes equations, by assuming that the wavelength of the tsunami is much longer than the sea depth (long wave approximation). Therefore, the vertical motion of fluid can be considered negligible compared with the horizontal motion. The SWE are suitable for offshore tsunamis, particularly for those generated by earthquakes, since under a relatively broad range of conditions, the earthquake rupture size is much bigger than the sea depth (Synolakis & Bernard, 2006; Behrens & Dias, 2015; Marras & Mandli, 2020).

1.1.1 Derivation of Navier-Stokes Equations

1.1.1.1. Conservation of mass (continuity equation)

The conservation of mass requires that the rate of change of total mass in a control volume V is equal to the net mass flux across the boundary of V. This is given by

$$\frac{d}{dt}\int_V \rho dV = -\int_{\partial V} (\rho \boldsymbol{v}) \cdot \boldsymbol{n} dA \qquad \text{(Eq.1.1.1)}$$

where ρ is the density of the fluid (kg/m^3), $\boldsymbol{v}$ is the velocity of the fluid (m/s) and **n** is the outward unit normal vector on ∂V. To obtain the differential form of the Eq. 1.1.1, we need to apply Gauss Theorem

$$\frac{d}{dt}\int_V \rho dV = -\int_V \nabla \cdot (\rho \boldsymbol{v})\ dV \qquad \text{(Eq.1.1.2)}$$

If ρ is assumed smooth, applying the Leibniz integral rule to the Eq. 1.1.2 we obtain

$$\int_V \left[\frac{\partial \rho}{\partial t} + \nabla \cdot (\rho \boldsymbol{v})\right]\ dV = 0$$

Since the control volume V is arbitrary

$$\frac{\partial \rho}{\partial t} + \nabla \cdot (\rho \boldsymbol{v}) = 0 \qquad \text{(Eq.1.1.3)}$$

Eq. 1.1.3 is the differential form of the mass conservation, or continuity equation. If there is not any significant change in the absolute pressure or temperature, it can be assumed that the flow is incompressible, the density is constant and Eq. 1.1.3 becomes

$$\nabla \cdot \boldsymbol{v} = 0 \qquad \text{(Eq.1.1.4)}$$

1.1.1.2. Conservation of Linear Momentum

Newton's second law of motion, law of conservation of (linear, as opposed to angular) momentum, states that the time rate of change of total momentum in the control volume V is equal to the summation of all external forces acting on that volume V:

$$\frac{d}{dt}\int_V \rho \boldsymbol{v}\, dV = -\int_{\partial V} (\rho \boldsymbol{v})\boldsymbol{v} \cdot \boldsymbol{n}\, dA + \int_V \rho \boldsymbol{b}\, dV + \int_{\partial V} \boldsymbol{\varepsilon n}\, dA \qquad \text{(Eq.1.1.5)}$$

where the first term on the right-hand side of the equation is the net momentum flux across the boundary of V, the second term describes the body force density per unit mass b (N/kg) acting on the volume V of the fluid, the last term describes the external contact forces acting on ∂V where $\boldsymbol{\varepsilon}$ is the viscous stress tensor (N/m^2) (Panton, 2005; Oden, 2006). If we apply Gauss's Theorem to Eq. 1.1.5, we obtain

$$\frac{d}{dt}\int_V \rho \boldsymbol{v}\, dV + \int_V \nabla \cdot (\rho \boldsymbol{vv})\, dV - \int_V \rho \boldsymbol{b}\, dV - \int_V \nabla \cdot \boldsymbol{\varepsilon}\, dV = 0 \qquad \text{(Eq.1.1.6)}$$

If $\rho \boldsymbol{v}$ is assumed smooth, Leibniz integral rule can be applied to Eq. 1.1.6

$$\int_V \left[\frac{\partial}{\partial t}(\rho \boldsymbol{v}) + \nabla \cdot (\rho \boldsymbol{vv}) - \rho \boldsymbol{b} - \nabla \cdot \boldsymbol{\varepsilon}\right] dV = 0$$

Since the control volume V is arbitrary

$$\frac{\partial}{\partial t}(\rho \boldsymbol{v}) + \nabla \cdot (\rho \boldsymbol{v}\boldsymbol{v}) = \rho \boldsymbol{b} + \nabla \cdot \boldsymbol{\varepsilon} \qquad \text{(Eq.1.1.7)}$$

If we neglect other body forces such as Coriolis force or centrifugal force due to the rotation of the Earth

$$\rho \boldsymbol{b} = \rho \boldsymbol{g}$$

where g is the gravitational acceleration (m/sn^2). Since the ocean water is a Newtonian fluid, which means the viscosity of the fluid is independent of the flow speed or shear rates, the stress tensor can be given as

$$\boldsymbol{\varepsilon} = -\mathrm{p}\mathbf{I} + \boldsymbol{\tau}$$

where p is the pressure, $\boldsymbol{\varepsilon}$ is the total stress and $\boldsymbol{\tau}$ is the viscous stress or deviatoric stress. The material derivative can be given using the chain rule, and indicating the components of the velocity in the x, y, z directions respectively as u, v, w by

$$\frac{D\boldsymbol{v}}{Dt} = \frac{\partial \boldsymbol{v}}{\partial t}\frac{dt}{dt} + \frac{\partial \boldsymbol{v}}{\partial x}\frac{dx}{dt} + \frac{\partial \boldsymbol{v}}{\partial y}\frac{dy}{dt} + \frac{\partial \boldsymbol{v}}{\partial z}\frac{dy}{dt} = \frac{\partial \boldsymbol{v}}{\partial t} + \frac{\partial \boldsymbol{v}}{\partial x}u + \frac{\partial \boldsymbol{v}}{\partial y}v + \frac{\partial \boldsymbol{v}}{\partial z}w\frac{\partial \boldsymbol{v}}{\partial t}$$

$$\frac{D\boldsymbol{v}}{Dt} = \frac{\partial \boldsymbol{v}}{\partial t} + \boldsymbol{v} \cdot \nabla \boldsymbol{v}$$

If we add body force and stress parameters and include the material derivative to the Eq. 1.1.7, the equation becomes

$$\rho \frac{D\boldsymbol{v}}{Dt} = -\nabla \mathrm{p} + \rho g + \nabla \cdot \boldsymbol{\tau} \qquad \text{(Eq.1.1.8)}$$

Eq. 1.1.4 and Eq. 1.1.8 are called Navies Stokes Equations that can written out for an incompressible and isotropic Newtonian fluid (Dawson and Mirabito, 2008)

$$\frac{\partial u}{\partial x}+\frac{\partial v}{\partial y}+\frac{\partial w}{\partial z}=0$$

$$\rho\left(\frac{\partial(u)}{\partial t}+\frac{\partial(u^2)}{\partial x}+\frac{\partial(uv)}{\partial y}+\frac{\partial(uw)}{\partial z}\right)=-\nabla p+\rho g+\frac{\partial \tau_{xx}}{\partial x}+\frac{\partial \tau_{xy}}{\partial y}+\frac{\partial \tau_{xz}}{\partial z}$$

$$\rho\left(\frac{\partial(v)}{\partial t}+\frac{\partial(uv)}{\partial x}+\frac{\partial(uv^2)}{\partial y}+\frac{\partial(vw)}{\partial z}\right)=-\nabla p+\rho g+\frac{\partial \tau_{xy}}{\partial x}+\frac{\partial \tau_{yy}}{\partial y}+\frac{\partial \tau_{yz}}{\partial z} \quad \text{(Eq.1.1.9)}$$

$$\rho\left(\frac{\partial(w)}{\partial t}+\frac{\partial(uw)}{\partial x}+\frac{\partial(vw)}{\partial y}+\frac{\partial(vw^2)}{\partial z}\right)=-\nabla p+\rho g+\frac{\partial \tau_{xz}}{\partial x}+\frac{\partial \tau_{yz}}{\partial y}+\frac{\partial \tau_{zz}}{\partial z}$$

1.1.2 Shallow Water Equations

Shallow water equations can be described as a layer of fluid that is bounded by the bottom topography from below and free surface from above (Figure 1.2.1), in a simplified way. This definition let us to focus only the sea surface anomaly and depth-averaged horizontal velocities, since the change of vertical momentum and the vertical velocity component w is neglectable.

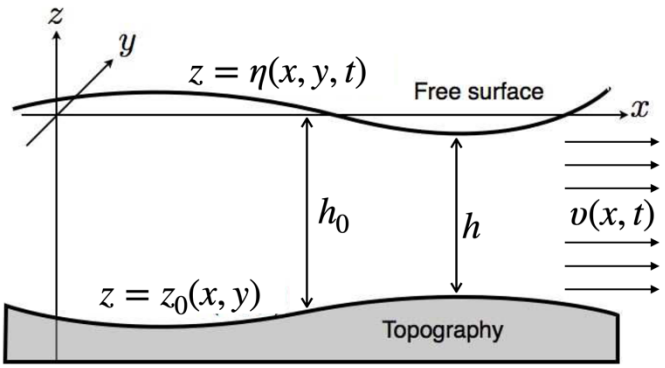

Figure 1.1.1: *Sketch of the quantities that describe the free-surface evolution with time.* $\boldsymbol{\eta(x, y, t)}$ *is the vertical displacement, z is the sea-bottom topography,* $\boldsymbol{h_0}$ *is the undisturbed water depth and h is the total depth (Modified from Segur and Yamamato 2009).*

Using this configuration, we may write the following boundary conditions

Free surface conditions on $z = \eta(x, y, t) = z_0(x, y) + h(x, y, t)$*;*

1) Pressure is zero ($p = 0$)

2) No relative normal flow ($\frac{\partial \eta}{\partial t} + u\frac{\partial \eta}{\partial x} + v\frac{\partial \eta}{\partial y} - w = 0$)

3)Surface shear stress is; $\tau_{sx} = -\tau_{xx}\frac{\partial \eta}{\partial x} - \tau_{xy}\frac{\partial \eta}{\partial y} + \tau_{xz}$

Bottom Boundary conditions on $z = z_0(x, y)$*;*

1)No normal flow ($w = u\frac{\partial z_0}{\partial x} + v\frac{\partial z_0}{\partial y} + w$)

2)Bottom shear stress is; $-\tau_{bx} = \tau_{xx}\frac{\partial z_0}{\partial x} + \tau_{xy}\frac{\partial z_0}{\partial y} - \tau_{xz}$

The first step of the derivation of the SWEs is the integration of continuity equation (Eq. 1.1.4) from z = z_0 to z = η (Figure 1.1.1), since the general characteristics of shallow flow is that the wavelength is much greater than the water depth and we can average continuity equation over depth as follows

$$\int_{z_0}^{\eta} (\nabla \cdot \boldsymbol{v})\, dz = 0$$

$$\int_{z_0}^{\eta} \left(\frac{\partial v}{\partial x} + \frac{\partial v}{\partial y} + \frac{\partial v}{\partial z}\right) dz = 0$$

$$\int_{z_0}^{\eta} \left(\frac{\partial u}{\partial x} + \frac{\partial v}{\partial y}\right) dz + w|_{\eta} - w|_{z_0} = 0$$

$$\frac{\partial}{\partial x}\int_{z_0}^{\eta} u\, dz + \frac{\partial}{\partial y}\int_{z_0}^{\eta} v\, dz - \left(u|_{\eta}\frac{\partial \eta}{\partial x} + u|_{z_0}\frac{\partial z_0}{\partial x}\right) - \left(v|_{\eta}\frac{\partial \eta}{\partial y} + v|_{z_0}\frac{\partial z_0}{\partial y}\right) + w|_{\eta} - w|_{z_0} = 0$$

Depth-averaged velocities can be defined as

$$\bar{u} = \frac{1}{h}\int_{z_0}^{\eta} u\, dz\,, \bar{v} = \frac{1}{h}\int_{z_0}^{\eta} v\, dz$$

After the application of boundary conditions, we can obtain the depth-averaged continuity equation

$$\frac{\partial h}{\partial t} + \frac{\partial}{\partial x}(h\bar{u}) + \frac{\partial}{\partial y}(h\bar{v}) = 0$$

For the next step, we can assume that the wave length is much greater than the depth of fluid, which is called a long-wave approximation. Through this approximation, all of the terms

except the pressure derivative and the gravity term are neglected in the vertical component of the momentum equation (Eq. 1.1.9) and it collapses to simple hydrostatic pressure,

$$\frac{\partial \mathrm{p}}{\partial z} = \rho g$$

If we integrate this equation we obtain hydrostatic pressure distribution (assuming density does not change with depth)

$$\mathrm{p} = g\int_{z_0}^{\eta} \rho dz = \rho g(\eta - z)$$

For the next step, we need to integrate the x and y momentum equations (Eq. 1.1.9) over depth. We start with the left-hand side of the x-momentum equation

$$\int_{z_0}^{\eta}\left[\frac{\partial u}{\partial t} + \frac{\partial u^2}{\partial x} + \frac{\partial uv}{\partial y} + \frac{\partial u}{\partial z}w\right] dz$$

$$= \frac{\partial}{\partial t}\int_{z_0}^{\eta} u\, dz + \frac{\partial}{\partial x}\int_{z_0}^{\eta} u^2\, dz + \frac{\partial}{\partial y}\int_{z_0}^{\eta} uv\, dz - u|_{\eta}\frac{\partial \eta}{\partial t} - u^2|_{\eta}\frac{\partial \eta}{\partial x} - (uv)|_{\eta}\frac{\partial \eta}{\partial y} + (uw)|_{\eta}$$

$$- u|_{z_0}\frac{\partial z_0}{\partial t} + u^2|_{z_0}\frac{\partial z_0}{\partial x} + (uv)|_{z_0}\frac{\partial \eta}{\partial y} - (uw)|_{z_0}$$

This equation can be rearranged to be able to define the boundary conditions

$$\int_{z_0}^{\eta}\left[\frac{\partial u}{\partial t} + \frac{\partial u^2}{\partial x} + \frac{\partial uv}{\partial y} + \frac{\partial u}{\partial z}w\right] dz$$

$$= \frac{\partial}{\partial t}\int_{z_0}^{\eta} u\, dz + \frac{\partial}{\partial x}\int_{z_0}^{\eta} u^2\, dz + \frac{\partial}{\partial y}\int_{z_0}^{\eta} uv\, dz - u|_{\eta}\left(\frac{\partial h}{\partial t} + u|_{\eta}\frac{\partial \eta}{\partial x} + v|_{\eta}\frac{\partial \eta}{\partial y} - w|_{\eta}\right)$$

$$+ u|_{z_0}\left(\frac{\partial z_0}{\partial t} + u|_{z_0}\frac{\partial z_0}{\partial x} + v|_{z_0}\frac{\partial z_0}{\partial y} - w|_{z_0}\right)$$

If we apply the boundary conditions and depth averaged velocity eq. last 2 terms can be eliminated

$$\int_{z_0}^{\eta}\left[\frac{\partial u}{\partial t}+\frac{\partial u^2}{\partial x}+\frac{\partial uv}{\partial y}+\frac{\partial u}{\partial z}w\right]dz$$

$$=\frac{\partial}{\partial t}\int_{z_0}^{\eta}u\,dz+\frac{\partial}{\partial x}\int_{z_0}^{\eta}u^2\,dz+\frac{\partial}{\partial y}\int_{z_0}^{\eta}uv\,dz$$

$$=\frac{\partial(h\bar{u})}{\partial t}\frac{\partial}{\partial x}\int_{z_0}^{\eta}u^2\,dz+\frac{\partial}{\partial y}\int_{z_0}^{\eta}uv\,dz$$

The integration of the pressure term on the right-hand side of the Eq. 1.1.9

$$-\int_{z_0}^{\eta}\frac{1}{\rho}\frac{\partial \mathrm{p}}{\partial x}\,dz=\;-\frac{1}{\rho}\int_{z_0}^{\eta}\frac{\partial}{\partial x}(P_a-\mathrm{p}gz+\mathrm{p}g\eta)\,dz$$

$$=-\frac{1}{\rho}\int_{z_0}^{\eta}\rho\frac{\partial}{\partial x}g\eta\,dz=-g\frac{\partial}{\partial x}\eta\int_{z_0}^{\eta}dz=-gh\frac{\partial\eta}{\partial x}$$

The integration of the stress term on the right-hand side of the Eq. 1.1.9 one by one

$$\int_{z_0}^{\eta}\frac{\partial\tau_{xx}}{\partial_x}dz=\frac{\partial}{\partial_x}\int_{z_0}^{\eta}\tau_{xx}\,dz-\tau_{xx}|_{\eta}\frac{\partial\eta}{\partial x}+\tau_{xx}|_{z_0}\frac{\partial z_0}{\partial x}$$

$$=\frac{\partial(\bar{\tau}_{xx}h)}{\partial_x}-\tau_{xx}|_{\eta}\frac{\partial\eta}{\partial x}+\tau_{xx}|_{z_0}\frac{\partial z_0}{\partial x}$$

$$\int_{z_0}^{\eta}\frac{\partial\tau_{xy}}{\partial_y}dz=\frac{\partial}{\partial_y}\int_{z_0}^{\eta}\tau_{xy}\,dz-\tau_{xy}|_{\eta}\frac{\partial\eta}{\partial y}+\tau_{xy}|_{z_0}\frac{\partial z_0}{\partial y}$$

$$=\frac{\partial(\bar{\tau}_{xy}h)}{\partial_y}-\tau_{xy}|_{\eta}\frac{\partial\eta}{\partial x}+\tau_{xy}|_{z_0}\frac{\partial z_0}{\partial y}$$

$$\int_{z_0}^{\eta} \frac{\partial \tau_{xz}}{\partial_z} dz = \tau_{xz}|_{\eta} - \tau_{xz}|_{z_0}$$

If we apply the bottom and surface shear stress conditions and combine all terms we obtain the preliminary depth-integrated momentum equation in direction of the x-axis, which can be done in the same way for the y and z-axis

$$\frac{\partial(h\bar{u})}{\partial_t} + \frac{\partial}{\partial_x}\int_{z_0}^{\eta} u^2\, dz + \frac{\partial}{\partial_y}\int_{z_0}^{\eta} uv\, dz = -gh\frac{\partial \eta}{\partial x} + \frac{1}{\rho}\frac{\partial(\bar{\tau}_{xx}h)}{\partial_x} + \frac{1}{\rho}\frac{\partial(\bar{\tau}_{xy}h)}{\partial_y} + \frac{\tau_{sx}}{\rho} - \frac{\tau_{bx}}{\rho} \qquad \text{(Eq.1.1.10)}$$

In the next step, the vertical field of momentum is divided into a depth-integrated mean value and a fluctuation part. For the velocity component in direction of the x-axis this division is given by,

$$u(z) = \bar{u} - \tilde{u} \text{ with } \int_{z_0}^{\eta} \tilde{u}\ dz = 0 \qquad \text{(Eq.1.1.11)}$$

where $\bar{u}$ is the mean velocity over the vertical axis and $\tilde{u}$ is the fluctuation part. The following rule of integration also holds

$$\int_{z_0}^{\eta} (\bar{u} + \tilde{u})\,(\bar{u} + \tilde{u})\, dz = \int_{z_0}^{\eta} \bar{u}^2 dz + \int_{z_0}^{\eta} \tilde{u}\tilde{u}\, dz \qquad \text{(Eq.1.1.12)}$$

Substituting Eq. 1.1.11 and 1.1.12 into Eq. 1.1.10 yields the following depth-averaged momentum equation in the direction of the x-axis

$$\frac{\partial(h\bar{u})}{\partial_t}+\frac{\partial(h\bar{u}^2)}{\partial_x}+\frac{\partial(h\bar{u}\bar{v})}{\partial_y}+\frac{\partial}{\partial_x}\int_{z_0}^{\eta}\tilde{u}\tilde{u}\,dz+\frac{\partial}{\partial_y}\int_{-h}^{\eta}\tilde{u}\tilde{v}\,dz = -gh\frac{\partial\eta}{\partial x}+\frac{1}{\rho}\frac{\partial(\bar{\tau}_{xx}h)}{\partial_x}+\frac{1}{\rho}\frac{\partial(\bar{\tau}_{xy}h)}{\partial_y}+\frac{(\tau_{sx}-\tau_{bx})}{\rho} \quad \text{(Eq.1.1.13)}$$

As one of the last steps, we can isolate the depth-integrated continuity equation from the left-hand side of the Eq. 1.1.13 using partial differentiation,

$$\frac{\partial(h\bar{u})}{\partial_t}+\frac{\partial(h\bar{u}^2)}{\partial_x}+\frac{\partial(h\bar{u}\bar{v})}{\partial_y}$$

$$= h\frac{\partial\bar{u}}{\partial_t}+h\bar{u}\frac{\partial\bar{u}}{\partial_x}+h\bar{v}\frac{\partial\bar{u}}{\partial_y}+\bar{u}\left(\frac{\partial h}{\partial t}+\frac{\partial(h\bar{u})}{\partial_x}+\frac{\partial(h\bar{v})}{\partial_y}\right)$$

$$= h\left(\frac{\partial\bar{u}}{\partial_t}+\bar{u}\frac{\partial\bar{u}}{\partial_x}+\bar{v}\frac{\partial\bar{u}}{\partial_y}\right)$$

If we arrange the Eq. 1.1.13, the general form of the depth-averaged momentum equation can be given as

$$\frac{\partial\bar{u}}{\partial_t}+\bar{u}\frac{\partial\bar{u}}{\partial_x}+\bar{v}\frac{\partial\bar{u}}{\partial_y}$$

$$= -g\frac{\partial\eta}{\partial x}+\frac{1}{h}\left[\frac{\partial}{\partial x}h\left(\frac{\tau_{xx}}{\rho}-\overline{\tilde{u}\tilde{u}}\right)\right]+\frac{1}{h}\left[\frac{\partial}{\partial y}h\left(\frac{\tau_{xy}}{\rho}-\overline{\tilde{u}\tilde{v}}\right)\right]+\frac{1}{h}\left[\frac{\partial}{\partial x}h\left(\frac{\tau_{sx}}{\rho}-\frac{\tau_{bx}}{\rho}\right)\right]$$

In tensor form

$$\frac{\partial\bar{u}_i}{\partial_t}+\bar{u}_j\frac{\partial\bar{u}_i}{\partial_{x_j}} = -g\frac{\partial\eta}{\partial x_i}+\frac{1}{h}\left[\frac{\partial}{\partial x_j}h\left(\frac{\tau_{ij}}{\rho}-\overline{\tilde{u}_i\tilde{u}_j}\right)\right]\frac{1}{h}\frac{\tau_{sx,i}}{\rho}-\frac{\tau_{bx,i}}{\rho}$$

If we simplify and summarize the part with stress and fluctuation part of the velocity

$$\tau_{ij} - \rho\,\overline{\tilde{u}_i \tilde{u}_j} = \tau_{ij,g} = \tau_{ij}$$

We can obtain simplified shallow water equations as follows

$$\frac{\partial u}{\partial_t} + u\frac{\partial u}{\partial_x} + v\frac{\partial u}{\partial_y} = -g\frac{\partial \eta}{\partial x} + \frac{1}{h\rho}\frac{\partial}{\partial x}h\tau_{xx} + \frac{1}{h\rho}\frac{\partial}{\partial y}h\tau_{xy} - \frac{1}{h}\frac{\tau_{sx}}{\rho} + \frac{1}{h}\frac{\tau_{bx}}{\rho}$$

$$\frac{\partial v}{\partial_t} + u\frac{\partial v}{\partial_x} + v\frac{\partial v}{\partial_y} = -g\frac{\partial \eta}{\partial y} + \frac{1}{h\rho}\frac{\partial}{\partial x}h\tau_{xy} + \frac{1}{h\rho}\frac{\partial}{\partial y}h\tau_{yy} - \frac{1}{h}\frac{\tau_{sy}}{\rho} + \frac{1}{h}\frac{\tau_{by}}{\rho}$$

$$\frac{\partial h}{\partial t} + \frac{\partial}{\partial x}(h\bar{u}) + \frac{\partial}{\partial y}(h\bar{v}) = 0$$

1.2. Sources of tsunamis

Around 80% of all tsunamis worldwide occurred after an earthquake. Nonetheless, there exist some other sources, which are landslides, volcanic activity, atmospheric disturbances, and meteorite impacts.

Plate motions produce regional stress accumulation that may cause compression, extension or lateral offset in parts of the lithosphere and consequently earthquakes will feature reverse (thrust), normal, and strike-slip focal mechanisms, respectively.

When there is an earthquake offshore or near the coast, it may cause a sudden seafloor deformation that induces the displacement of the entire water column above it. Tsunamis are mainly due to the vertical displacement of the sea bottom. However, the horizontal co-seismic deformation of the seafloor characterized by significant slopes can also contribute to give rise to a tsunami (Tanioka & Satake, 1996; Song et al.,2017). Earthquakes with larger magnitude generally cause larger co-seismic deformation and that generates larger tsunamis. Earthquake rupture is a dynamic process and the rupture nucleates at the hypocenter and moves across the rupture interface. The rupture speed and the amount of slip vary during the rupture evolution. Temporal evolution of the seafloor deformation can be another factor that controls the efficiency of tsunami generation by large earthquakes (Le Gal et al., 2017). Tsunami earthquakes, for example, generate tsunamis with higher amplitude than would be typically expected from their seismic moment magnitude (Polet an Kanamori, 2016). These events are characterized by having a slow rupture process and this can influence tsunami generation. Nonetheless, their slowness can be related to the location of these events in the shallow part of the subduction zone. Tsunami earthquakes in that zone may generate greater slip due to

the existence of low-rigidity and/or low-friction sediments which can contribute to cause unexpectedly high slip hence tsunami wave amplitudes.

Dynamic modeling of earthquake rupture in 3D can provide mechanically feasible tsunami source description on complex faults (Galvez et al., 2014; Murphy et al., 2016; Uphoff et al., 2017; Murphy et al., 2018; Ma and Nie, 2019; Saito et al., 2019; Ulrich et al., 2020) and such simulations can be used together with modern tsunami numerical methods and high-performance computing (HPC) to explain dynamics and severity of earthquake behavior (Wirp et al., 2021).

Hovewer, in many situations it is an acceptable approximation to neglect the complexity of the seismic rupture and sea floor deformation process, and to describe seafloor deformation by analytical solutions (Okada, 1985). as uniform rectangular dislocations within a homogeneous elastic half space. Due to the relative slowness of the tsunami propagation with respect to the evolution of the rupture process, the displacement of the seafloor is assumed instantaneous, and the deformation is transferred exactly into a sea level vertical perturbation (Grezio et al, 2017).

Direct transfer of the sea bottom deformations to the water surface cause unrealistically short waves on tsunami spectrum. These short waves may cause artificial resonances in bays and finally inaccurate estimation of runup heights or instability in numerical calculations (Nosov and Kolesov, 2011). The initial water surface elevation can be obtained by applying a low-pass filter (Kajiura, 1963), especially in the cases where the oceanic depth is comparable to the horizontal extension of the source (Nosov and Kolesov, 2011).

The characteristics of landslide tsunamis, on the other hand, greatly depend on their sizes and origins. Landslides with immense volumes, which could be several thousand cubic kilometers, may trigger severe tsunamis with localized impact (Masson et al., 2006). The occurrence of these giant submarine landslides is likely controlled by geology and their return periods are very low (Solheim et al., 2005). Nevertheless, the return period of these events can be shorter in the areas where large-scale debris flows surround active volcanoes or for submarine landslides initiated by sediment supply in river deltas. The submarine landslides are mainly controlled by the initial landslide acceleration, speed, volume and shape (Løvholt et al., 2015). The temporal evolution of the landslides plays an important role on the magnitude of the tsunamis (Hammack, 1973; Løvholt et al., 2015; Watts, 2000). If tsunami generation time is short, that makes rapidly accelerating landslides more tsunamigenic due to the limitation of damaging interference of wave crests and troughs produced by the frontal and rear parts of the slide, respectively. However, if tsunami generation, retrogression, and acceleration time is slower, landslides generate weak tsunamis even with giant volumes. Froude number, which is the ratio between the speed of landslide and the linear hydrostatic wave celerity, is a critical factor to define the tsunamigenic potential of the landslide. Landslides in the shallower waters have higher Froude numbers since the speed of wave increases with water depth and that makes these landslides more effective tsunami generators (Harbitz et al., 2014). Subaerial landslides produce tsunamis with a different generation mechanism (Figure 1.2.1 (b2)) than submerged landslides since subaerial landslides commonly reach to the water body at high speed. The initial height of the subaerial landslides tsunamis mainly depends on the Froude number together with the frontal area of the landslide volume (Fritz et al., 2004; Mohammed & Fritz, 2012).

Volcanic eruptions are another source of the tsunamis. Underwater explosions, lava and lahars entering the water, pyroclastic flows, slope failures, volcanic earthquakes, caldera subsidence are included in the specific source mechanisms of volcanic tsunamis (Begét, 2000; Day, 2015; Latter, 1981; Kienle et al., 1987; Paris, 2015). Although the variety of source mechanisms cause different types of waves, they are commonly defined as short period waves with greater dispersion and restricted far-field effect with respect to the seismically generated tsunamis (Choi et al., 2003; Le M.haut. & Wang, 1996; Nomanbhoy & Satake, 1995; Maeno & Imamura, 2011; Ulvrova, Paris, et al., 2016; Watts & Waythomas, 2003; Yokoyama, 1987).

Meteotsunamis or meteorological tsunamis are related to remarkably strong and sudden atmospheric pressure fluctuations. Atmospheric pressure variation may cause small oscillations on the sea level. The resonance between the atmospheric forcing and the ocean, effects these small oscillations and causes significant long ocean waves, closely associated with the behavior of tsunamis, with periods varying between 2 minutes to 2 hours (Pattiaratchi & Wijeratne, 2015). The atmospheric disturbances keep giving energy into the sea during the resonance process and ocean waves become destructive when they arrive to the coastal zones as a result of the combination of other amplification mechanisms such as local resonance and shoaling effects.

The fall of meteorites or asteroids in the earth's oceans may, very rarely, generate large waves. These tsunamis may proceed similarly to subaerial landslide tsunamis during generation and initial propagation. However, they remain strongly nonlinear over hundreds or thousands of kilometers away from the source (Wünnemann & Weiss, 2015).

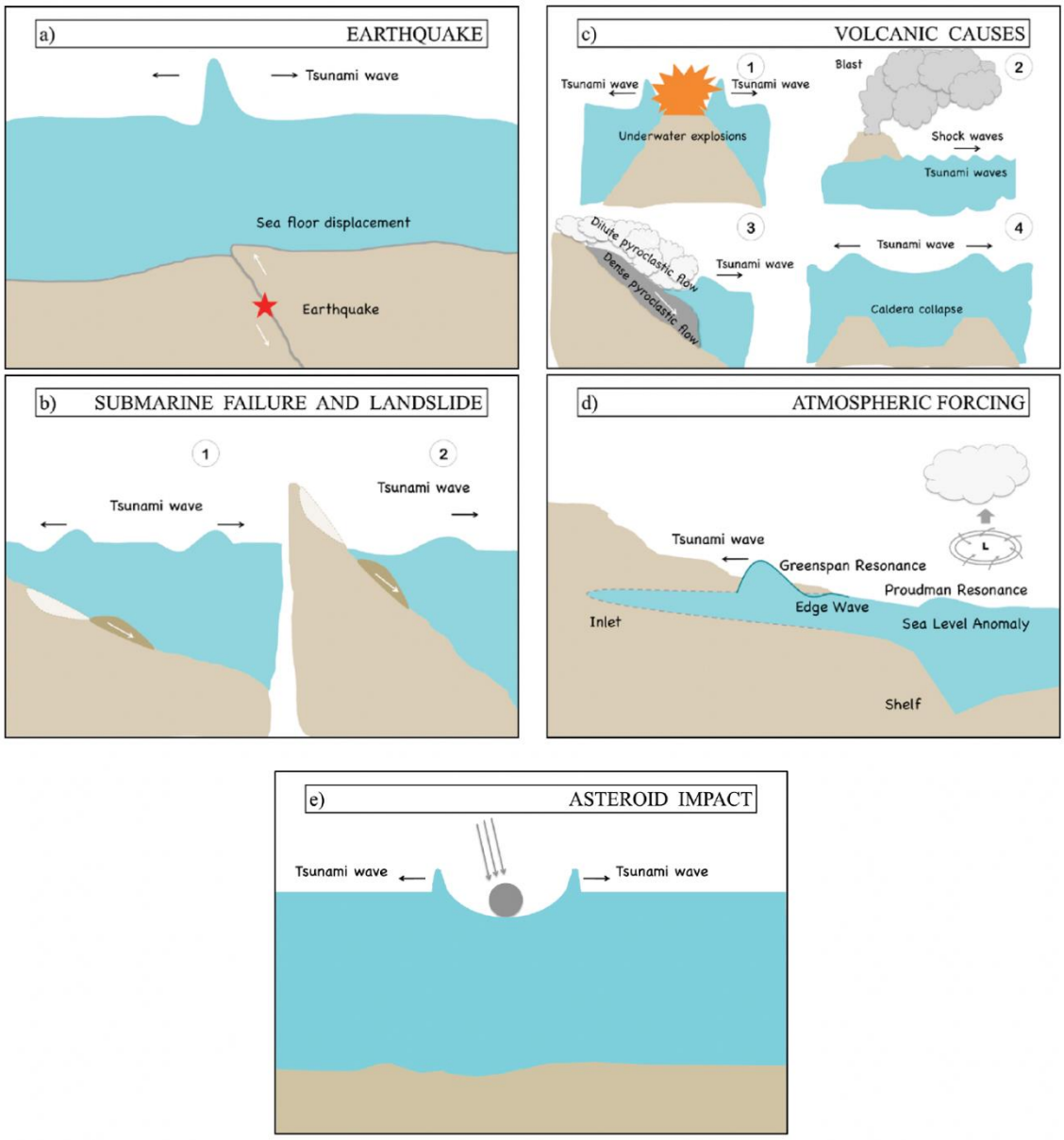

Figure 1.2.1: *Sources of tsunami waves (a)earthquake sources, (b1) submarine and (b2) and subaerial mass failures, (c) volcanic causes (c1) underwater explosion, (c2) blast exciting free waves in the atmosphere which transfer energy to water, (c3) pyroclastic flows, and (c4) rapid ground deformations or caldera collapses, (d) Proudman resonance occurring after atmospheric disturbances, (e) oceanic impacts of asteroids and comets. (Taken from Grezio et al., 2017)*

1. 3. Tsunami propagation

The propagation of the tsunami waves in the open ocean can be described by the shallow water equations (Section 1.2). We consider a vertical displacement of the sea surface $\eta(x, y, t)$ (Figure 1.1.1) that propagates along the x-axis as a monochromatic plane wave with the angular frequency ω and the wavenumber k which can be given as

$$\eta(x, y, t) = \eta_0 e^{i(kx-\omega t)} \quad \text{(Eq.1.3.1)}$$

The velocity potential, $\nabla\phi(\boldsymbol{x}, t) = \boldsymbol{v}(\boldsymbol{x}, t)$, can also be represented with $e^{i(kx-\omega t)}$ as

$$\phi(\boldsymbol{x}, t) = f(z)e^{i(kx-\omega t)} \quad \text{(Eq.1.3.2)}$$

The Laplace equation of velocity potential can be given by using continuity equation (Eq. 1.1.4) as

$$\Delta\phi(\boldsymbol{x}, t) = 0$$

Using the Eq. 1.3.2 into the Laplace equation of velocity potential gives an ordinary differential equation with respect to z as

$$\frac{d^2 f(z)}{dz^2} = k^2 f(z)$$

The general solution to this equation can be given by

$$f(z) = A\cosh(kz) + B\sinh(kz)$$

where A and B are the coefficients that should be determined so to satisfy the boundary conditions (as defined in section 1.1.2). The velocity potential is then represented as

$$\phi(\boldsymbol{x},t) = [Acosh(kz) + Bsinh(kz)]e^{i(kx-\omega t)} \quad \text{(Eq.1.3.3)}$$

The boundary condition with respect to the velocity potential can be written as (Saito, 2019)

$$\frac{\partial \phi(\boldsymbol{x},t)}{\partial t}\Big|_{z=0} + g\eta(x,y,t) = 0 \quad \text{(Eq.1.3.4)}$$

This is a dynamic boundary condition since it defines the relation between the force and sea-surface motion where sea-surface is assumed to be continuous. At the surface $z = \eta(x,y,t)$ we can write (Saito, 2019)

$$v_z = \frac{\partial \eta(x,y,t)}{\partial t} + v_x \frac{\partial \eta(x,y,t)}{\partial x} + v_y \frac{\partial \eta(x,y,t)}{\partial y}$$

This relation is given by using the velocity potential as

$$\frac{\partial \eta(x,y,t)}{\partial t}\Big|_{z=0} = \frac{\partial \phi(\boldsymbol{x},t)}{\partial z}\Big|_{z=0} \quad \text{(Eq.1.3.5)}$$

This is cited as a kinematic boundary condition. Using Eq.1.3.4 and Eq.1.3.5, the boundary condition with respect to the velocity potential at z=0 can be written as

$$\frac{\partial^2 \phi(\boldsymbol{x},t)}{\partial t^2}\Big|_{z=0} + g\frac{\partial \phi(\boldsymbol{x},t)}{\partial z}\Big|_{z=0} = 0 \quad \text{(Eq.1.3.6)}$$

The sea bottom is accepted as a rigid boundary condition where vertical flow is not allowed, only horizontal flow exists at the boundary. Then, the boundary condition at the sea bottom ($z=z_0$) is given by

$$\frac{\partial \phi(\boldsymbol{x},t)}{\partial z}\Big|_{z=z_0} = 0 \quad \text{(Eq.1.3.7)}$$

Using the boundary condition (Eq.1.3.7) such that the vertical velocity is zero at the sea bottom Eq. 1.3.3 can be written as

$$\frac{\partial \phi(\boldsymbol{x},t)}{\partial z}\Big|_{z_0} = [Acosh(kz) + Bsinh(kz)]\Big|_{z_0} e^{i(kx-\omega t)} = [-Aksinh(kz_o) + Bkcosh(kz_0)]\, e^{i(kx-\omega t)} = 0 \quad \text{(Eq.1.3.8)}$$

Since this always needs to be satisfied for each x and t

$$B = \frac{sinh(kz_o)}{cosh(kz_o)} A$$

The velocity potential given at Eq. 1.3.3 is then written as

$$\phi(\boldsymbol{x},t) = A\left[cosh(kz) + \frac{sinh(kz_o)}{cosh(kz_o)} sinh(kz)\right] e^{i(kx-\omega t)}$$

By substituting this into the sea surface boundary condition (Eq. 1.3.6), we obtain

$$-\omega^2 A\left[cosh(kz) + \frac{sinh(kz_o)}{cosh(kz_o)} sinh(kz)\right]\Big|_{z=0} e^{i(kx-\omega t)} + gA\left[ksinh(kz) + k\frac{sinh(kz_o)}{cosh(kz_o)} cosh(kz)\right]\Big|_{z=0} e^{i(kx-\omega t)} = 0$$

That gives

$$\left[-\omega^2 + gk\frac{sinh(kz_o)}{cosh(kz_o)}\right] A e^{i(kx-\omega t)} = 0 \quad \text{(Eq.1.3.9)}$$

We can obtain the relation between the angular frequency ω and wave number k, which is the dispersion relation, satisfying Eq. 1.3.9 as

$$\omega = \sqrt{gktanh(kh)} \quad \text{(Eq.1.3.10)}$$

Furthermore, sea surface height $\eta(x,y,t)$, can be obtained by using dynamic boundary condition (Eq. 1.3.4) at sea surface as

$$\eta(x,y,t) = -\frac{1}{g}\frac{\partial\phi(\boldsymbol{x},t)}{\partial z}\Big|_{z=0}$$
$$= \frac{i\omega A}{g}\left[cosh(kz) + \frac{sinh(kz_o)}{cosh(kz_o)}sinh(kz)\right]\Big|_{z=0} e^{i(kx-\omega t)} \quad \text{(Eq.1.3.11)}$$
$$= \frac{i\omega A}{g}e^{i(kx-\omega t)}$$

Coefficient A can be obtained by the comparing Eq 1.3.1 and 1.3.11, we can finally obtain the velocity field as

$$\phi(\boldsymbol{x},t) = \frac{g\eta_0}{i\omega}\left[cosh(kz) + \frac{sinh(kz_o)}{cosh(kz_o)}sinh(kz)\right]e^{i(kx-\omega t)}$$

$$= \frac{g\eta_0}{i\omega}\frac{\cosh\left[k(z+z_0)\right]}{\cosh\left(kz_0\right)}e^{i(kx-\omega t)}$$

The change of velocity and pressure from the hydrostatic pressure are given by using the velocity potential as (Saito, 2019)

$$\boldsymbol{v}(\boldsymbol{x},t) = \nabla\phi(\boldsymbol{x},t)$$

$$p(\boldsymbol{x},t) = -\rho\frac{\partial\phi(\boldsymbol{x},t)}{\partial t}$$

When the sea surface propagates along the x-axis as represented in Eq.1.3.1, $v_x(\boldsymbol{x},t)$ is given by the gradient of the velocity potential

$$v_x(\boldsymbol{x},t) = \frac{\partial\phi(\boldsymbol{x},t)}{\partial x} = \frac{g\eta_0 k}{w}\frac{\cosh\left[k(z+z_0)\right]}{\cosh\left(kz_0\right)}e^{i(kx-\omega t)} = \omega\eta_0\frac{gk}{\omega^2}\frac{\cosh\left[k(z+z_0)\right]}{\cosh\left(kz_0\right)}e^{i(kx-\omega t)}$$

Using the Eq.1.3.10

$$v_x(\boldsymbol{x},t) = \omega\eta_0\frac{\cosh[k(z+z_0)]}{\sinh(kz_0)}e^{i(kx-\omega t)} \quad \text{(Eq.1.3.12)}$$

Similarly, we can obtain $v_y(\boldsymbol{x},t)$ and $v_z(\boldsymbol{x},t)$ as

$$v_y(\boldsymbol{x}, t) = 0 \quad \text{(Eq.1.3.13)}$$

$$v_z(\boldsymbol{x}, t) = -i\omega\eta_0 \frac{\sinh[k(z+z_0)]}{\sinh(kz_0)} e^{i(kx-\omega t)} \quad \text{(Eq.1.3.14)}$$

We can obtain the displacement, by integrating velocity with respect to time, as

$$u_x(\boldsymbol{x}, t) = i\eta_0 \frac{\cosh[k(z+z_0)]}{\sinh(kz_0)} e^{i(kx-\omega t)} \quad \text{(Eq.1.3.15)}$$

$$u_y(\boldsymbol{x}, t) = 0$$

$$u_z(\boldsymbol{x}, t) = \eta_0 \frac{\sinh[k(z+z_0)]}{\sinh(kz_0)} e^{i(kx-\omega t)} \quad \text{(Eq.1.3.16)}$$

Eq. 1.3.15 and 1.3.16 indicate that the wave propagates in the positive x direction according to $e^{i(kx-\omega t)}$. The phase velocity is given by

$$c = \frac{\omega}{k}$$

Using the Eq. 1.3.10, the phase velocity c is calculated as

$$c = \frac{\omega}{k} = \sqrt{gh}\sqrt{\frac{\tanh(kh)}{kh}}$$

$$c = \begin{cases} \sqrt{\dfrac{g}{k}} & kh \gg 1 \\ \sqrt{gh} & kh \ll 1 \end{cases} = \begin{cases} \sqrt{\dfrac{g\lambda}{2\pi}} & \lambda \ll h \\ \sqrt{gh} & \lambda \gg h \end{cases} \quad \text{(Eq.1.3.17)}$$

where

$$\tanh(kh) = \begin{cases} 1 & kh \gg 1 \\ kh & kh \ll 1 \end{cases}$$

Eq. 1.3.17 shows that the phase velocity of tsunami wave depends on the wavelength λ. If the tsunami wavelength is much larger than the sea depth, the phase velocity is an approximation given by $c = \sqrt{gh}$. However, if the tsunami wavelength is much shorter than

the sea depth the velocity is given by $c = \sqrt{g\lambda/2\pi}$ and it only depends on tsunami wavelength, independent of the sea depth h_0.

There are various kinds of tsunami equations depending on the different approximations (Madsen and Sørensen 1992; Imamura 1996), more approximations make equations simpler and decrease the computational cost of the simulations. One of the most general approximation for tsunami propagation is using 2-D depth-averaged equations, which are derived from 3-D equations of motion. In general, different types of 2-D tsunami equations are used based on the purpose and situation. A classification of tsunami equations can be done as shown in Table 3.1 according to the tsunami wave height, tsunami wave length and sea depth.

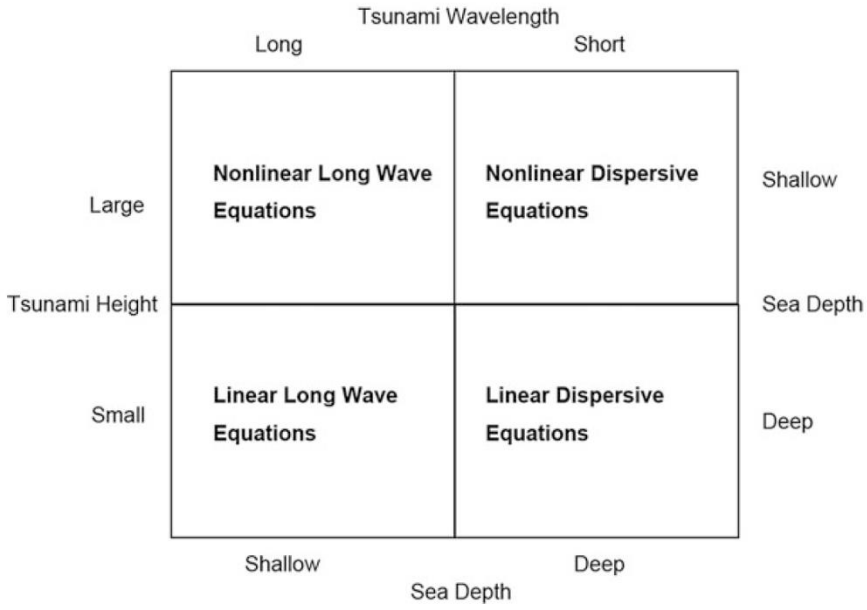

Table 3.1: *A classification of non-linear/linear long-wave and non-linear/linear dispersive tsunami equations (Taken from Saito, 2019)*

Let us consider the tsunami height first. When the tsunami height is much smaller than the sea depth in open ocean, the propagation can be simulated using linear long wave and

linear dispersive equations. Non-linear effects become important, when the tsunami height is not much smaller than the sea depth as tsunami approaches the coast. The simulation of this non-linear phenomena, the nonlinear long-wave and nonlinear dispersive equations are used.

The velocity of tsunami propagation generally depends on the wavelength as shown in Eq. 1.3.17. Therefore, simulation of frequency-dependent tsunami propagation should be done by non-linear/linear dispersive tsunami equations. However, if the wavelength is much greater than the sea depth, the propagation velocity does not change with the frequency and nonlinear/linear long-wave equations can be used.

In this study, synthetic tsunami time series are computed at the location of several open ocean pressure sensors using different sources around the Pacific. Since the tsunami waves move along the deep sea, the propagation is a linear problem and it might be simulated as linear non-dispersive wave using SWE. However, it should be noted that Tsunami-HySEA model, which solves non-linear SWE, is used in this study for the wave propagation.

1.4. Tsunami shoaling and inundation

Tsunami shoaling and inundation are the last phases of the tsunami progress, when the wave approaches, reaches, and floods the coast. A deep knowledge of tsunami inundation is crucial to predict the impact of possible future events on coastal zones.

In the previous section, it has been shown that tsunami propagation speed changes with sea depth. Besides the velocity, tsunami height also depends on the sea depth. The tsunami height becomes greater as the tsunami approaches the coast since the propagation transitions from deep sea to shallow waters. The tsunami height on the shore can be two times bigger than its offshore height (Saito, 2019).

The tsunami height η and the velocity c can be addressed relying on the tsunami energy flux conservation. The tsunami energy flux at the deep sea where tsunami wavelength is much larger than the sea depth can be represented as follows

$$J = \rho g |\eta|^2 c = \rho g |\eta|^2 \sqrt{gh}$$

The energy flux density J could be considered constant, independent from the location and the sea depth, if it is assumed that there are no reflected tsunami waves during the propagation. This can be given as

$$|\eta(x_1)|^2 \sqrt{gh(x_1)} = |\eta(x_2)|^2 \sqrt{gh(x_2)}$$

$$|\eta(x_2)| = |\frac{h(x_1)}{h(x_2)}|^{\frac{1}{4}} \ |\eta(x_1)| \qquad \text{(Eq.1.4.1)}$$

where $\eta(x)$ is tsunami height and $h(x)$ is the ocean depth at the location x. When the point x_2 is placed near the shore and the sea depth at this point ($h(x_2)$) is shallower than the point x_1 ($h(x_1)$), the tsunami height at point x_2 ($\eta(x_2)$) should be larger than the tsunami height at the offshore point x_1 ($\eta(x_1)$). This relation is known as Green's law. The basis of the derivation of this law is the assumption of an idealistic model where there is not reflected tsunami waves. However, this is not the real situation in nature (Hayashi 2010). Therefore, this equation (Eq. 1.4.1) only allows to make a good estimation about the mechanism of tsunami amplification, but is not always quantitatively correct.

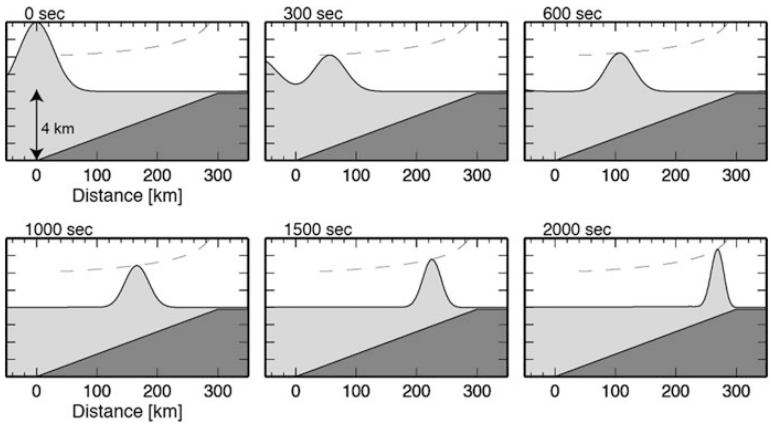

Figure 1.4.1: *Tsunami amplification near coast. (Taken from Saito, 2019)*

As described above, the tsunami wave amplitude increases as it approaches the coast due to the conservation of the wave energy. When the sea depth is decreased, the velocity of wave propagation decreases and that causes the compression of wave packet in space and the amplification of the wave amplitude.

The inundation is the result of the penetration of tsunami waves inland. The maximum vertical height on the land above the sea level that tsunami waves reach is named as run-up

(Figure 1.4.2). The run-up height can reach to 30-40 meters (Mori et al., 2011) for earthquake generated tsunamis and hundreds of meters, for other tsunami sources, as observed at 1958 Lituya Bay, Alaska event (Fritz et al., 2001) where the maximum runup is recorded as 524 m.

The transformation of tsunami waves in near shore regions highly depends on the characteristics of the beach profile and the wave itself. For instance, if the beach profile is steep and the tsunami wave height is small, then the runup process can be similar to a wave hitting a vertical wall and the runup height will be almost twice the offshore tsunami height. If the beach profile is not steep but the slope is mild and the tsunami wave is large, the process of the shallow water becomes highly nonlinear (Lynett, 2011). Shoaling and refraction due to the large-scale coastal features, such as small islands, large shoals, canyons, and shelves also play an important role in tsunami inundation (Briggs et al., 1994; Yeh et al., 1994; González et al., 1995; Liu et al., 1995; Carrier, 1996;).

The propagation of tsunami on land is also affected by the ground roughness and obstacles (Lynett, 2007; Synolakis, 1987; Tadepalli and Synolakis, 1994; Tomita, 2007). The ground roughness is controlled by the composition of the ground and cause damping of the bottom friction. The interaction of tsunami with obstacles, such as buildings, may also lead to a highly variable local flow pattern (Cross, 1967; Tomita, 2007). The velocity of strong flows can reach tens of meters per second and these flows are able to break up structures, trees etc. and displace them. Besides the power of the flow, the secondary effect of the inundation can be considered as the debris flow.

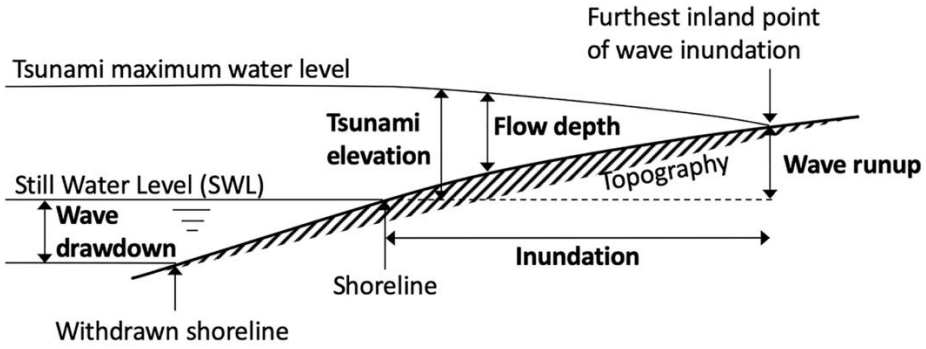

Figure 1.4.2: *The terms used for the quantitative measures of tsunami intensity (Taken from Kalligeris et al., 2021)*

1.5. Common tsunami models and approaches

Reproducing the behavior of tsunami waves has been attempted with different models using a number of approaches and assumptions. Tsunami numerical modelling requires to define physics of tsunami wave propagation and inundation with mathematical equations; then relevant numerical methods must be employed to solve these equations.

Navier-Stokes equations, for incompressible fluids, are the most complete definition of a tsunami as a free surface flow. These equations are able to capture the interaction of the flow with the coastal characteristics and estimate the hydrodynamic forces responsible for the damages during the inundation and run-up (Behrens and Dias, 2015; Lynett et al., 2017; Larsen and Fuhrman, 2019).

However, simpler equations have been successfully adopted for modelling tsunami propagation and inundation (Synolakis, 2006; Behrens and Dias, 2015). Linear and non-linear shallow water theory is one of the most common used approach for tsunami propagation and inundation modelling (Behrens and Dias, 2015). However, long wave assumption becomes questionable when the frequency dispersion, the velocity changes with the wavelength, affects the wave propagation. Boussinesq equations can be used when wavelengths decrease to roughly a few water depths. These equations can be obtained averaging over the water column and keeping only first-order effects of nonlinearity and frequency dispersion (Lynett, 2011; Behrens and Dias, 2015; Marras and Mandli, 2020).

1.5.1. Numerical Methods to solve equations

There are several methods to solve modelling equations mentioned above. Although, finite differences (FD) method is the most commonly used numerical method (Titov and Gonzalez, 1997; Imamura et al., 2006), other numerical methods, such as Galerkin-type finite element, finite volume, smoothed particle etc., have been implemented in tsunami simulations to solve hyperbolic or weakly parabolic equation (Behrens and Dias, 2015).

The discretization schemes of Galerkin-type methods replace the continuous function space by a discrete approximation to that space usually represented as a piecewise polynomial. This finite element method can be represented as continuous Galerkin (CG) and discontinuous Galerkin (DG) methods. DG methods are capable of simulating the inundation process and they are well scalable on parallel computing environments (Vater and Behrens, 2014).

Finite-volume (FV) is another method to solve hydrodynamic equations. FV methods are closely related to finite difference methods they can be interpreted as a finite difference approximation to the differential equation. However, FV methods are derived using the integral form of the conservation law with a finite partitioning set of volumes to discretize the equations (LeVeque, 2002; Behrens and Dias, 2015).

Each method has its advantages and disadvantages. The FD method, for instance, is least costly but it has insufficient geometrical flexibility to handle complex coastal areas with respect to the Galerkin and FV methods. Both FV and FD allow a more general approach to non-equispaced meshes, FV can deal with curvature more naturally in two and three

dimensions due to the integral nature of the equations. DG and FV methods are also optimal for the grid refinement (Behrens, 2006; Berger et al., 2011; Bonev et al., 2018).

As a result, all the numerical methods of solution and the mathematical models depend on the different cases and assumptions. It is significant to decide which metric lead to the decisions to choose one model over another and what can we sacrifice. Table 1.5.1.1 shows some most common tsunami simulators with the considered equations and numerical methods.

Model	Space Dimension	Equations	Spatial Discretization
GeoCLAW (Berger et al. 2011)	1D/2D/2D(multi-layer)	SW	FV
NUMA2D (Marras et al., 2015; Marras et al., 2018)	1D/2D	SW	SE/DG
MOST (Titov and González, 1997)	1D/2D	SW	FD
Cliffs (Titov and González, 1997; Tolkova, 2014)	1D/2D	SW	FD
Tsunami-HySEA (Macías et al., 2017; Macías et al., 2020a, 2020b)	1D/2D	SW/B	FV
Multilayer-HySEA (Macías et al., 2020c, 2020d)	1D/2D(multi-layer)	SW/B	FV
TUNAMI (Imamura, 1989; Imamura et al., 2006)	1D/2D	SW	FD
NAMI-DANCE (Yalciner et al., 2006)	1D/2D	SW	FD
COMCOT (Wang, 2009)	1D/2D	SW	FD

Table 1.5.1 1: *Some most common tsunami models. Acronyms used in this table: SW Shallow Water, B Boussinesq, FV Finite-volume, SE spectral element, FD finite-difference (Modified from Marras and Mandli, 2020).*

CHAPTER 2- EARTHQUAKE SOURCE MODELLING FOR TSUNAMI

A great number of destructive tsunamis (~80%), have been triggered by an earthquake. The sudden seafloor deformation, due to an earthquake rupturing beneath the sea, generates a motion of the water column above the earthquake source and produces tsunami waves (Grezio et al., 2017). Earthquake triggered tsunamis pose a risk to human lives (Løvholt et al., 2012), cause economic losses (Løvholt et al., 2015) and damages to coastal structures and critical infrastructures (Argyroudis et al., 2020) or even may generate secondary cascading events such as Fukushima nuclear accident (Synolakis & Kânoğlu, 2015). The Probabilistic Tsunami Hazard Assessment is highly sensitive to fault geometry and earthquake mechanism. Various studies proved that tsunami wave height and inundation height directly depend on the spatial variation of slip (Geist and Parsons, 2006; Tselentis et al., 2006; Løvholt et al., 2012c; Mueller et al., 2014; Fukutani et al., 2014; Davies et al., 2015) not only in the near field region (Geist 2002; Okal & Synolakis 2008; Lauterjung et al. 2010; McCloskey et al. 2007) but also in the far-field domain (Gica et al. 2007; González et al. 2009; Li et al. 2016; Butler et al. 2017). Therefore, it is crucial to understand the processes that yield earthquake occurrence and source mechanism, how the final slip distributes on the fault plane and how the seafloor deformation is connected to the earthquake source to use as an initial condition for tsunami analysis.

2.1. Earthquake occurrence

Tectonic earthquakes occur on pre-existing faults or plate interfaces with a rapid slippage. The characteristics of the tectonic earthquakes are different from the non-tectonic ones which may have volcanic origin or can be induced by water recharge processes in dams. Earthquake ruptures result from yielding the static friction level on faults, which are nearly planar interfaces within the Earth crust. Those interfaces have broken in the past and hosted dislocation, and therefore they are relatively weak to accumulate elastic energy in deformation with time.

Geometrically, the orientation of the fault plane is provided by its azimuth direction and the dip angle. The azimuth or the strike of the fault (φ) is the angle, measured clockwise, between the fault trace on the surface and the north, and it ranges from 0° to 360°. The dip angle (δ) is formed by the fault plane and the horizontal plane and ranges from 0° to 90°. There is a third angle that completes the description of the fault rupture mechanism, the rake (λ) angle, which individuates the direction of the motion on the fault, it is defined as the angle between the strike direction and the direction of slip and it ranges from -180° to 180°.

Faults can be classified according to the characteristic of their motion (Figure 2.1.1). Pure strike-slip faults, for which $\delta = 90°$ and $\lambda = 0°$, generate a horizontal motion parallel to the strike and are nearly vertical interfaces. These faults can be distinguished in right-lateral and left-lateral faults, based on the direction of movement of one side of the fault as seen from the other side. Dip-slip faults have the cross-section of the fault motion in a vertical plane. Dip-slip vertical faults have $\delta = 90°$ and $\lambda = \pm 90°$ while dip-slip faults on an inclined plane have $0° < \delta < 90°$ and $\lambda = 90°$. Dip-slip faults are also divided into normal and reverse faults. Normal

faults are produced when the block above the fault (hanging-wall) moves downward with respect to the block below (foot-wall). Reverse faults are generated when the motion of the block above is upward with respect to the block below. Reverse faults are also called thrust faults when the dip angle is small. Normal faults have a negative rake angle and reverse faults have a positive rake angle.

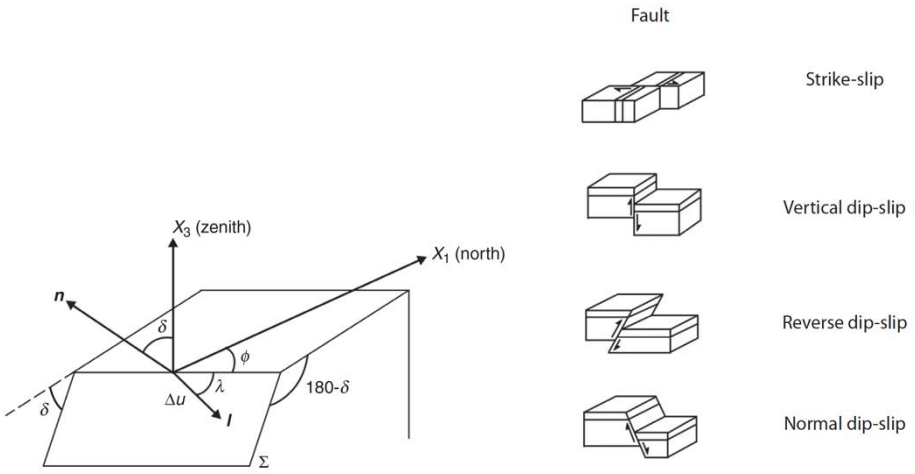

Figure 2.1.1: *(left) Geometry of a shear fault. The fault orientation is given either by the angles ϕ (azimuth or strike) and δ (dip) or by the unit vectors n (normal to the fault plane) and l (in the slip direction). λ is rake or slip angle, Δu is the amount of fault slip and the fault surface is Σ. (right) Types of faults. (Taken from Udías et al., 2014)*

Earthquake generation process can be simply illustrated by the mechanism of stick-slip motion (Brace and Byerlee, 1966). The model contains a single block of mass that is at rest, in contact with a fixed block through a frictional surface and this mass is connected to a spring that is loaded at a constant velocity. The tectonic process of the accumulation of the elastic deformation on the fault is represented by the initial process of the stick-slip model where the end of the spring is stretched but the block is still at rest. The loading velocity V that generates the stretching at the end of the spring represents the relative velocity of tectonic loading,

which is driven by the motion of the lithospheric plates. If the strain in a zone exceeds a specific threshold ($\sigma > \sigma_s$), an earthquake occurs (Figure 2.1.2). Correspondingly, in the model the block starts to suddenly move when the force exerted by the spring exceeds the static friction between the block and the surface. During the motion of the block, the friction dissipates energy as heat, while elastic energy can generate seismic waves radiated away from the source. The motion of the fault stops eventually when the friction increases over the dynamic value ($\sigma_f > \sigma_k$). The difference in stress between the shear stress just before and after the slip is called the static **stress drop** ($\Delta\sigma_s = \sigma_s - \sigma_f$). The drop of the stress during the motion, on the other hand, represents the dynamic stress drop ($\Delta\sigma_d = \sigma_s - \sigma_k$). After the motion of the block has stopped, the spring starts to be stretched again due to the constant loading velocity V. This represents the beginning of another loading phase, which is referred to as the earthquake cycle.

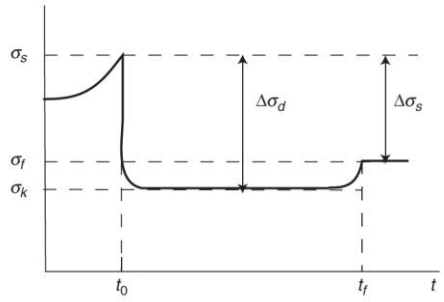

Figure 2.1.2: *The stress acting on a block subject to friction as a function of time, before ($t < t0$), during ($t_0 < t < t_f$) and after ($t > t_f$) sliding: $\Delta\sigma_d$, dynamic stress drop; $\Delta\sigma_s$, static stress drop. (Taken from Udías et al., 2014)*

2.2. Subduction zones

Subduction zones are convergent plate boundaries where one plate subdues below another one and sinks into the mantle due to the density difference between these two plates. These zones are the most seismically active regions on the globe and about 90% of historical events, including the largest ones with magnitude M>9, occurred along these regions (Hayes et al., 2018). Most of these events were followed by devastating tsunamis with, in some cases, unexpected wave height distributions. A great number of destructive tsunamis have been triggered after an earthquake, within or nearby the subduction zone, in the past.

Observation of events in the megathrust environment reveals that rupture characteristics of these events, such as slip and energy radiation distribution, indicate a depth-dependent frictional property of the slab interface. The shallow part of the subduction zone, in the upper 15 km of the seismogenic zone, is considered as frictionally stable and shows periodically unusual seismic energy release features (Lay and Bilek 2007; Yao et al., 2013). This portion of the slab interface is the source region for the tsunami earthquakes and events in this zone tend to have considerably longer source durations than the deeper ones, with the same seismic moment, and appear depleted in short-period energy (Kanamori and Kikuchi 1993; Bilek and Lay 2002; Bilek et al. 2004; Lay and Bilek 2007; Lay et al., 2012; Yao et al., 2013). The slab interface at the depth range 15-35 km is unstable and it is the place where megathrust earthquakes are nucleated with large slip. Moreover, intermediate short-period seismic energy radiation is observed from events occurred in that zone (Bilek and Lay 2002; Lay et al., 2012; Yao et al., 2013). The deeper part of the subduction, between the depths 35-45 km, is

seismically unstable and dominant in high-frequency radiation (Wang and Mori, 2011; Lay et al., 2012; Yao et al., 2013).

The common idea, before the 2011 Tohoku Earthquake, was that the shallow part of the subduction, the accretionary sediment wedge, could not produce large co-seismic slip (Hyndman et al. 1997; Moore and Saffer 2001). The 2011 Tohoku-Oki earthquake and related tsunami are one of the most studied events in different disciplines (Lay, 2018). It has been observed that this event generated a large amount of slip near the trench. The first finite-fault slip model has been addressed by Hayes (2011), using body and surface wave inversion, with about 34 m peak slip toward the trench. Saito et al. (2011), used the tsunami records as a first attempt at ocean bottom pressure and GPS wave gauge for the inversion and estimated 30 m of slip at 20 km depth and 20 m of slip near to trench. On the other hand, joint inversion results of Lee et al. (2011) proposed that the maximum slip is larger than 50 m; also, the slip has started slowly near the hypocenter and then has grown towards the shallow part of the interface. Most of the following studies (Suzuki et al., 2011; H Yue & Lay, 2011; Yokota et al. 2011; Romano et al., 2012; Satake et al., 2013; Han Yue & Lay, 2013; Romano et al., 2014) have featured large slip values in the shallow part of the subduction zone.

The 2004 Sumatra-Andaman is also one of the most destructive and deadly events in the last century. The maximum runup has been measured as about 50m in Banda Aceh by tsunami survey team (Wijayaratna et al., 2005). Lorito et al. (2010) revealed that the source of the event has a complex geometry and the rupture was slower in the shallow part of the subduction zone than in the deeper part since joint inversion results show that the source rigidity is smaller than the value suggested by the PREM model and increases with depth.

The cause of such devastating events can be associated with slip amplification in the shallow part of the fault, eventually due to the existence of a sediment layer below the subducting plate, and a slower rupture process. For events sharing the same magnitude, the tsunami can be enhanced by slip amplification in the shallow part of the fault, by the existence of a soft wedge, by the low rigidity and stress drop changes with depth (Bilek and Lay 1999; Geist and Bilek 2001). On the other hand, earthquake rupture may propagate from deeper part of the subduction up to the trench, causing a strong tsunami due to the frictional environment, yielding conditional stability of the shallow portion of the subduction interface (Scholz, 1998; Hu and Wang, 2008; Murphy et al., 2018).

2.3. Earthquake source

Tectonic earthquakes occur as a result of the relative sliding of two sides of the fault. During the faulting process, there is a complex energy balance between the dissipation occurring along the fault and in the surrounding volume and the radiated field. This radiated field is represented by seismic waves and includes the information about the source process. The recordings of seismic waves at or nearby the Earth's surface is used by the seismologists to infer the characteristics of the rupture referring to its space-time evolution.

Determination of the mechanism of an earthquake can be simplified by ignoring the finite size of the source and point source approximation can be used. This approximation is valid if the distance between the source and the observation point (d) is much larger when compared with the source dimensions (L is the length of the fault and W is the width of it) and if the wavelengths of the observed signal (λ) are larger than the source dimension ($L \ll \lambda \ll d$).

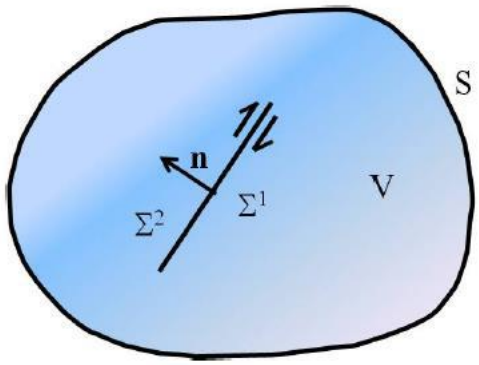

Figure 2.3.1: *A seismic fault is here represented as a surface inside a volume V along which slip occurs. The two lips of the fault are divided to interpret the displacement discontinuity across such a surface (Taken from Festa and Zollo,2012).*

Let us consider a volume V internal to the Earth that is bounded by the S=∂V. Inside this volume V the linear elastodynamics holds except for the fault surface Σ where slip occurs. Homogeneous boundary conditions are assumed on S which are, for instance, representative of the traction-free Earth surface. The two sides of the fault that move away from each other, are indicated as Σ_1 and Σ_2. The normal **n** is defined on the fault as the normal to Σ_1 entering Σ_2 (Figure 2.3.1). It can be assumed that the small-strain approximation holds and we refer all quantities on the fault to a reference configuration determined at time zero, since the amount of slip is small (centimeters to meters) with respect to the size of the process zone (tens to few hundreds of meters). The displacement and its time derivative across the surface Σ are discontinuous due to the slippage. The slip function is defined as the difference of the Lagrangian displacement **u** across the two sides of the fault surface $\delta\mathbf{u}=\mathbf{u}_1-\mathbf{u}_2$. The traction, on the other hand, must be continuous across Σ for spontaneous rupture. Using Betti's theorem, the displacement seismogram observed at a location **x** inside the Earth or at its surface can be computed as the convolution of the slip function with the elastic response of the medium:

$$u_m(\boldsymbol{x},t) = \int_{-\infty}^{+\infty} d\tau \int_{\Sigma} \delta u_i(\boldsymbol{\xi},t)\ c_{ijkl}\, n_j \frac{\partial G_{mk}}{\partial \xi_l}(\boldsymbol{x}, t-\tau, \boldsymbol{\xi}) d\boldsymbol{\xi} \qquad \text{(Eq.2.3.2)}$$

where c_{ijkl} is elastic coefficient tensor and it is symmetric with respect to the exchange of all the indices. Although it has 21 independent components for a general elastic solid, it reduces to 2 independent coefficients, which are Lamé constants λ and μ, for an isotropic medium, $c_{ijkl} = \lambda\delta_{ij}\delta_{kl} + \mu(\delta_{ik}\delta_{jl} + \delta_{il}\delta_{jk})$. **G** in the formula is the Green's function tensor that represents the impulse response of the medium. $G_{ij}(x,t,\xi)$ defines the i-th component of the displacement recorded at the position **x** and at time t, generated by a unidirectional impulse force acting in the j-th direction at $\boldsymbol{\xi}$ at time zero. Using the reciprocity feature of the Green's function,

the positions of the source and receiver can be exchanged yielding $G_{mk}(x, t-\tau, \xi) = G_{km}(\xi, t-\tau, x)$. The quantity

$$c_{ijkl}\frac{\partial G_{km}}{\partial \xi_l}(\boldsymbol{\xi}, t-\tau, \boldsymbol{x})n_j = T_{im}^{G}(\boldsymbol{\xi}, t-\tau, \boldsymbol{x})$$

is the stress on the fault plane generated by an impulse force at **x**, contracted by the normal, leading to the Green's traction T_m^G on the fault plane generated by an impulse force at **x** directed along the m-th direction. Eq. 2.3.1, the representation theorem, can be simplified as

$$u_m(\boldsymbol{x}, t) = \int_{\Sigma} \delta u_i(\boldsymbol{\xi}, t) * T_{im}^{G}(\boldsymbol{\xi}, t-\tau, \boldsymbol{x}) d\boldsymbol{\xi} \qquad \text{(Eq.2.3.2)}$$

where the time integral is replaced by the convolution operator (*) to suppress the time dependence. We assumed that the rupture may only occur in plane mode (slip parallel to the rupture direction) or anti-plane mode (on-fault slip orthogonal to the rupture direction), for a dominant shear faulting mechanism, which represents the seismic rupture. Therefore, the component of the slip normal to the fault is always zero, reducing to six the number of non-zero components of the traction needed for the computation of the displacement.

Eq. 2.3.2 can be changed to represent an extended seismic source as a superposition of double-couple point sources, as it is common in seismology. To do that, it should be noted that only the components of **c** with i≠j contribute to the Green's tractions since the slip vector lies on the fault plane and the normal is orthogonal to it. Therefore, the observed displacement is independent of λ for an isotropic medium, leading to

$$u_m(\boldsymbol{x}, t) = \int_{-\infty}^{+\infty} d\tau \int_{\Sigma} \delta u_i(\boldsymbol{\xi}, \tau)\, \mu \left(\frac{\partial G_{mi}}{\partial \xi_j}(\boldsymbol{\xi}, t-\tau, \boldsymbol{x}) + \frac{\partial G_{mj}}{\partial \xi_i}(\boldsymbol{\xi}, t-\tau, \boldsymbol{x}) \right) n_j d\boldsymbol{\xi} \qquad \text{(Eq.2.3.3)}$$

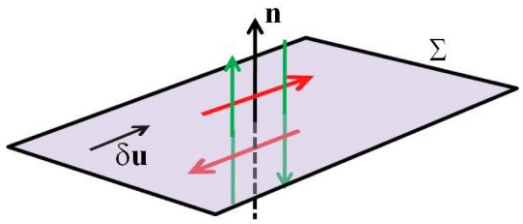

Figure 2.3. 2: *The double couple forces (Taken from Festa and Zollo,2012).*

Using the finite difference approximation, contribution in the Green's function can be written as

$$\frac{\partial G_{mi}}{\partial \xi_j}\, n_j = \frac{\partial G_{mi}}{\partial \xi_n} \approx \frac{G_{mi}^2 - G_{mi}^1}{\Delta \xi_n} \qquad \text{(Eq.2.3.4)}$$

Superscripts indices represent the quantities computed on the two sides of the fault, while $\Delta\xi_n$ is the distance along the normal direction. Eq. 2.3.4 represents the superposition of the displacement due to a couple source (couple of opposite forces acting on the two sides of the fault), in the direction of the slip (red couple in Figure 2.3.2). As $\Delta\xi_n \to 0$, the distance between the forces composing the couple approaches zero, with in-plane forces and arm along the normal direction. That moment may tend to rotate the fault locally. However, it is balanced with the second force couple acting on a plane perpendicular to the fault. The second term in the Green's function derivatives indicates that this force couple is formed by two forces directed along the fault normal with the arm along the slip direction (green couple in Figure 2.3.2). The representation theorem (Eq. 2.3.3) can be simplified by indicating with D_{mi} the m-th component of the displacement generated by such a double couple

$$u_m(\boldsymbol{x}, t) = \mu \int_{\Sigma} \delta u_i(\boldsymbol{\xi}) * D_{mi}(\boldsymbol{\xi}, \boldsymbol{x})\, d\boldsymbol{\xi}$$

Here, Green's function term is replaced by the displacement generated by a double couple force, whose orientation is defined by the slip and the fault normal vectors.

Eq. 2.3.3 can be also written as

$$u_m(\boldsymbol{x}, t) = \int_{-\infty}^{+\infty} d\tau \int_{\Sigma} \mu\left(\delta u_i n_j + \delta u_j n_i\right) \frac{G_{mi}}{\partial \xi_j}\, d\boldsymbol{\xi} \qquad \text{(Eq.2.3.5)}$$

The quantity $m_{ij} = \mu(\delta u_i n_j + \delta u_j n_i)$ is the moment density tensor, which is symmetric by definition, and it has the dimension of a moment per area unit. Green's function derivatives can be assumed constant in Eq. 2.3.5 for observer distance and wavelength of the signal much larger than the dimension of the fault. If we bring constant Green's function terms out of the integral in Eq. 2.3.5

$$\int_{\Sigma} m_{ij}\, d\boldsymbol{\xi} = M_o = \mu A \Delta\overline{u}$$

gives the moment tensor, which is a significant overall measure of the earthquake size, where μ is the shear modulus of the embedding medium, $\Delta\underline{\overline{u}}$ is the average displacement on the fault surface and A is the area of the fault.

2.4. Scaling laws for source geometry

Earthquakes occur in a wide variety of sizes, from very small ones to very large ones that produce many hundreds of kilometers of rupture. In section 2.1 the mechanism of the earthquake is explained in detail. We can sum up this mechanism when shear stress exceeds the static friction an earthquake occurs and two sides of the locked fault displace. After the earthquake friction forces lock the fault again. This simple model of the source can be used to explain essential concepts such as stress drop, fault slip, seismic moment and magnitude. The location in space and time and the orientation of the fault do not depend on the earthquake size. However, some scaling relations can be established among the size of an earthquake, rupture dimensions, average slip and the stress drop. Aki (1967) argued that some of the source parameters are dependent and can be expressed in terms of other parameters.

The size of an earthquake caused by a shear fracture can be measured by its seismic moment M_0 (Eq. 2.3.6). In the simplified earthquake occurrence model, the relative slip Δu of the two sides of the fault is generated when the acting shear stress, at a given moment, overcomes the friction and stress drop $\Delta\sigma$ is defined by the difference of the shear stresses before (σ_0) and after (σ_f) the occurrence of an earthquake (Figure 2.4.1).

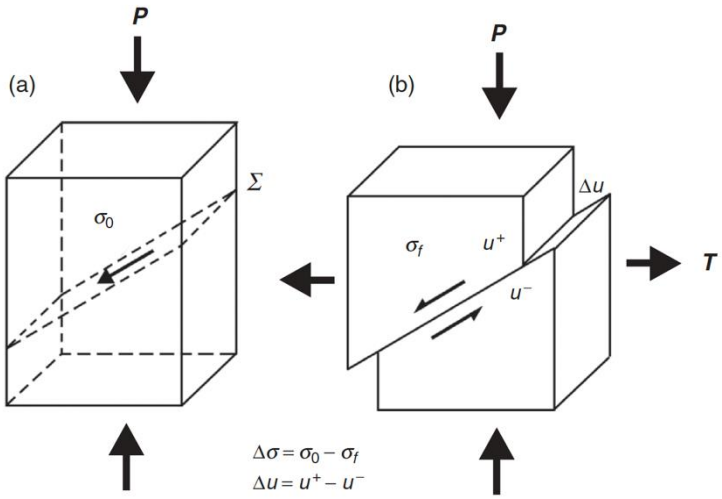

Figure 2.4. 1: *Schematic representation of acting stresses, (a) before and (b) after an occurrence on a shear normal fault with slip Δu and stress drop Δσ (Taken from the Udías et al., 2014).*

The relation between the average stress drop and the average displacement can be written as

$$\Delta\bar{\sigma} = C\mu\frac{\Delta\bar{u}}{L'}$$

where C is a non-dimensional factor that depends on the shape of the fracture and it is $\frac{7\pi}{16}$ for circular fault and L' is the length of the fault, this latter being equal to the radius a in the case of a circular rupture. The average stress drop can be written as

$$\Delta\bar{\sigma} = \frac{7\pi}{16}\frac{\Delta\bar{u}}{a}$$

The seismic moment in terms of stress drop and fault area ($A=\pi a^2$) is given by

$$M_0 = \frac{16\Delta\bar{\sigma}}{7\pi^{3/2}}A^{3/2}$$

If we take logarithms we get

$$M_w = \left(\frac{\log M_0}{1.5}\right) - 10.73$$

where M_0 is seismic moment and given in Nm. The moment magnitude Mw is widely used since it does not saturate at large values.

Figure 2.4.2 shows the relation between fault area and seismic moment M_0 with some constant stress drop lines for inter-plate and intra-plate earthquakes. The figure shows that most of the events have stress drops between 10 and 100bars although one order of magnitude variation is observed.

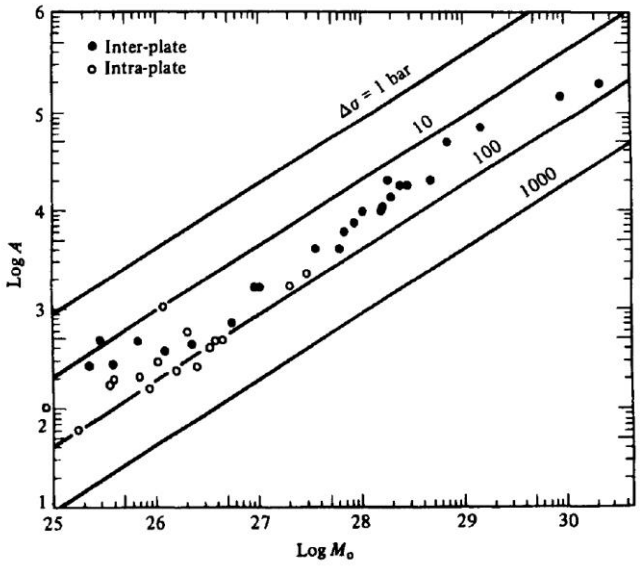

Figure 2.4. 2: *Relation between A (fault area) and Mo (seismic moment). The straight lines give the relations for circular cracks with constant Δσ (stress drop) (Taken from Lay and Wallace, 1995 which is modified from Kanamori and Anderson, 1975)*

Scaling relations are predominantly used to assume the possible dimensions of an earthquake fault for a given magnitude, estimated from instrumental recordings. Wells and Coppersmith relation (Wells and Coppersmith, 1994) is one of the most commonly used

relations which considers source parameters of 244 crustal earthquakes to develop empirical relationships among other source parameters.

The first scaling laws derived specifically for subduction-zone earthquakes have been proposed by Strasser et al. (2010). They have presented empirical relations between the rupture area (A), rupture length and width (L, W) and moment magnitude (M_w) of earthquakes that occur in subduction zones (Table 2.4.1). Their database, mainly based on SRCMOD database (Mai 2004; 2007)., includes 160 events, 95 interface and 20 intra-slab events, within the magnitude range M_w 5.9-9.4. Their study shows that there is an important difference in scaling with respect to the relations for crustal events, especially relating to rupture width and therefore rupture area and aspect ratio.

Equation	a	Standard error (a)	b	Standard error (b)
$\log(L)=a+b*M_w$	-2.477	0.222	0.585	0.029
$\log(W)=a+b*M_w$	-0.882	0.226	0.351	0.029
$\log(A)=a+b*M_w$	-3.476	0.397	0.952	0.051

Table2.4.1: *Equations of Strasser et al. (2010) scaling relations with coefficients and their standard error.*

Murotani et al. (2013) also derived empirical relations of seismic moment (M_0), rupture area (A), average slip (D) and asperity size (S_a) for subduction-zone earthquakes. In their database, the source parameters of seven M~9 earthquakes from the inversion results of the tsunami waveforms and geodetic data are used. The rupture area is defined for these seven events combined with 25 other events with M_w 6.7 – 8.4 to conduct regression analysis. They argued that these scaling relations are applicable to M~9 megathrust earthquakes. The equations of these relations are given by

$$A = 1.34 * 10^{-10} * M_0^{2/3}$$

$$D = 1.66 * 10^{-7} * M_0^{1/3}$$

$$S_a = 2.81 * 10^{-11} * M_0^{2/3}$$

2.5. Stochastic source modelling

For the simulation of earthquake scenarios, we assume a variability of the slip on the fault plane, as expected for large earthquake ruptures. For the aim we consider composite source models, that assume that an earthquake consists of many subevents, each subevent being defined by different source parameters such as size, stress drop, seismic moment and source-time function. In the literature, various composite source models have been proposed to consider the heterogeneities of the seismic rupture such as the fractal composite model (e.g. Andrews 1981; Boatwright 1982, 1988; Frankel 1991; Zeng et al. 1994), the specific barrier model (Papageorgiou & Aki 1983), and the empirical Green's functions (EGF) model (e.g. Hartzell 1978; Irikura & Kamae 1994; Frankel 1995). These models mainly differ from each other in terms of the hypothesis mode on the subevent size distribution. It can be assumed equal size distribution (e.g. Hartzell 1978; Papageorgiou & Aki 1983; Frankel 1995; Beresnev & Atkinson 1997) or a heterogeneous size distribution (e.g. Frankel 1991; Zeng et al. 1994). The overlapping or non-overlapping features of the subevents can be another reason for model differences.

Frankel (1991) suggests a general composite source model in which the size of the subevents is defined by a fractal distribution. This study also indicates that resulting high-frequency falloff of the displacement spectrum follows the spectral decay in ω^{-2} (Aki, 1967); in this case a constant stress drop is assumed and fractal dimension of the slip function of 2. However, this model is not able to predict the low frequency content, since the seismic moment related to the slip distribution is lower than the one of the target events.

Zeng et al. (1994), adjusted the composite model by Frankel (1991) by assuming that the total seismic moment of subevents must be equal to the seismic moment of the target event. Their composite model proposes that the stress drop is independent of the source size, the subevents are randomly distributed in a uniform manner on the fault plane, and allowed to be overlapped. This model differs from Frankel (1991) since the overlapped distribution of subevents implies that the total area of the subevents is larger than the surface of the target. Point source approximation is used for each subevent and each of them radiates with a Brune's (1970) source–time function when the rupture front reaches the center. Directivity at the subevent scale is ignored by Zeng et al. (1994) composite source model.

2.5.1. Generating a fractal distribution of earthquake sizes

Considering the composite fractal source model suggested by Frankel (1991), which assumes that the distribution of subevents follows a fractal distribution of subevent sizes and these sizes are self-similar, the number of circular subevents with radius R is given by

$$\frac{dN}{d\ ln(R)} = pR^{-D} \qquad \text{(Eq.2.5.1)}$$

where N is the number of subevents, p is a constant of proportionality and D is the fractal dimension. The concept is to generate a set of subevents following a fractal distribution of sizes, using the Zeng et al. (1994)'s method, satisfying Eq 2.5.1 between the smallest (R_{min}) and the largest radius (R_{max}). The distribution of subevents can be evaluated, constraining the total moment of the subevents to be equal to the seismic moment of the target event. The stress drop of each subevent should be assumed constant. The p value can be predicted analytically by accepting that subevents have a continuous distribution of sizes.

To model an earthquake on the fault, we should provide a discretization, characterized by a grid size Δx; this size is related to minimum modelled wavelength (according to the Nyquist theorem). Also, the smallest circular source should cover at least the size imposed by the grid mesh to be able to correctly model synthetic seismograms, imposing a minimum event magnitude that can be modelled with this discretization. These parameters allow defining p value by setting the fractal dimension to 2 (D=2). For instance, the fractal distribution of sizes can be generated for a magnitude Mw 6.0 event assuming Rmin= Δx/2, where Δx is the grid size of the fault plane, Rmin=0.35W, where W is the width of the fault plane. In this case, the number of subevents is calculated about N=25000. Figure 2.5.1 shows the spatial distribution of subevents on the fault plane for Mw 6.0 event with the cumulative number of subevents against the radius of each one of them.

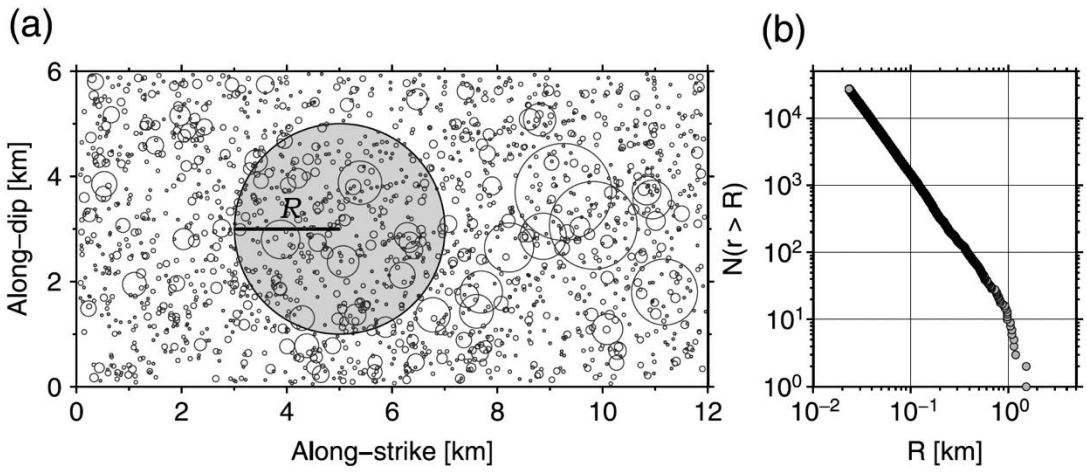

Figure 2.5. 1: *Example of a set of subevents generated for a magnitude Mw 6.0 earthquake with a fractal distribution of sizes using D= 2(a) Spatial distribution of the 10 percent of subevents and (b) cumulated number of subevents as a function of their radius R (Taken from Ruiz et al., 2011).*

The distribution fractal of sizes can be more complicated for complex non-planar faults. Herrero and Murphy (2018) propose a multi-lateration method to compute the distance

across complex non-planar surfaces, as the curvature of the surface is linked to the distance, based on a corollary of the Huygens' geodetic principle.

2.5.2. Spatial spectral property for a composite slip

The composite slip can be generated by a fractal distribution of sizes. To generate the final slip distribution on the fault plane, each subevent is defined as a circular crack (Anderson, 1997), with a slip function defined by (Eshelby, 1957)

$$\Delta u(r) = \begin{cases} \frac{24}{7\pi}\frac{\Delta\sigma_d}{\mu}\sqrt{R^2 - r^2} & r < R \\ 0 & r > 0 \end{cases}$$

where μ is rigidity, R is radius of the crack, r the radial distance from a point on the fault to its center, $\Delta\sigma_d$ is the stress drop of the subevent.

The slip spectrum for a single crack is analyzed in the spatial wavenumber domain to characterize the final composite slip spectrum. The location of a single crack is randomly distributed reflecting the subevent distribution. Therefore, the square of the final slip spectrum amplitude can be written as

$$|\Delta\tilde{u}^2(\boldsymbol{k})| = \int |\Delta\tilde{u}^2(\boldsymbol{k}, R)|\, dN$$

where $\Delta\tilde{u}^2(k, R)$ is the 2-D Fourier transform of the slip for a single crack. Simplified version of this expression can be given by

$$|\Delta\tilde{u}(\boldsymbol{k})| \propto k^{-3+\frac{D}{2}} \qquad \text{(Eq.2.5.2)}$$

where k is the wavenumber. Andrews (1980) argues that k^{-2} decay at high wavenumber must be taken to generate a far-field displacement radiation following ω^{-2} spectrum. Eq. 2.2 also confirms that the fractal dimension must be D = 2 to generate a final slip spectrum that decays as k^{-2}.

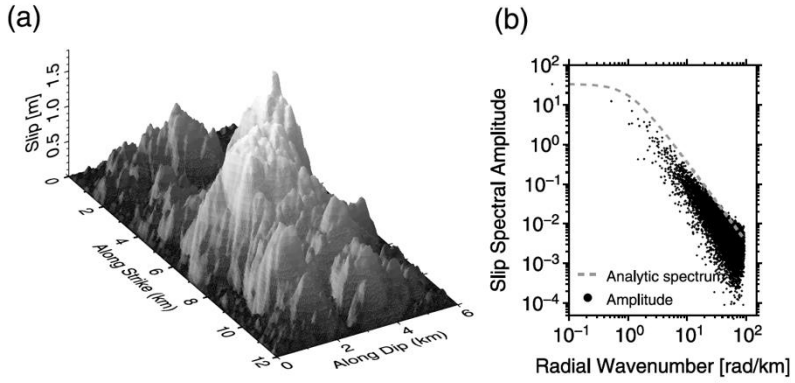

Figure 2.5. 2: *Example of a slip distribution for a Mw 6.0 earthquake generated with a fractal approach satisfying a k^{-2} asymptotic behavior at high wavenumbers. (a) Spatial and (b) spectral representations. Dashed line is a reference curve which is proportional to $1 / [1 + (k/k_c)^2]$, where $k_c = 2\pi/W$, is the corner wavenumber, and W is the fault width (Taken from Ruiz et al., 2011).*

2.6. Seafloor deformation from earthquake sources

The ground motion dynamics produced by an earthquake has complex characteristics. However, static deformation can make use of elastic dislocation theory to calculate the displacements, strains and stresses related to faulting from an earthquake rupture (e.g., Burgmann et al., 2002; McGuire & Segall, 2003; Savage & Burford, 1973). As a first approximation, fault surface can be parametrized as a collection of rectangular or point sources since there is a lack of analytical solutions for the deformation on a continuous fault (Okada, 1985, 1992). However, this parametrization cannot be adapted for complex fault surfaces, such as those at subduction zones, since it causes some geometrical gaps. Thus, complex fault surface geometry can be obtained using triangular meshes (Plesch et al., 2003).

Let us first focus on the rectangular parametrization. We adopt Okada model (Okada, 1985) to describe seafloor deformation. The model presents analytical expressions for the surface displacement, strain and tilt as a result of inclined shear and tensile faults in an isotropic half-space for both point and finite rectangular sources. Figure 2.6.1 shows the fault parameters considered in the Okada model.

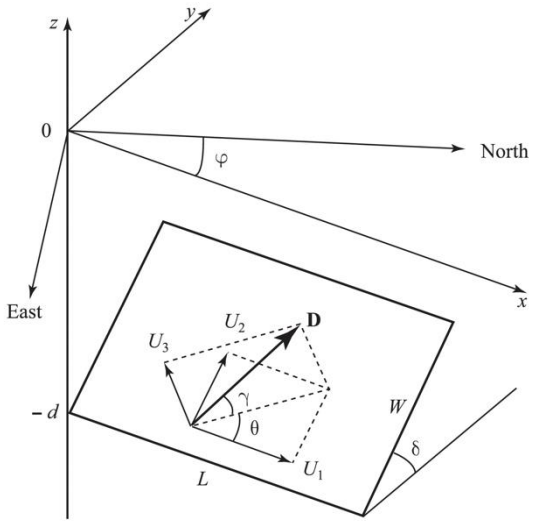

Figure 2.6. 1: *Geometry of the source model (length L, width W, Burger's vector D, dip angle δ, rake angle, angle between Burger's vector D and the fault plane) (Taken from Levin & Nosov, 2009).*

The Burger's vector D= (U_1,U_2,U_3) represents the movement of the hanging-wall with respect to the foot-wall. U_1,U_2 and U_3 correspond to strike-slip, dip-slip and tensile components of arbitrary dislocations with the tensile component is normal to the fault plane. Elementary dislocations are linked to the burger vector as U_1=|**D**|cosγ cosθ, U_2=|**D**|cosγ sinθ, U_3=|**D**|sinγ. The deformation field can be derived by taking x-ξ', y-η'cosδ and d-η'sinδ in place of x, y, and d, where ξ= x-ξ' and η= (y cosδ+d sinδ)-η' for a finite rectangular fault. Displacements for strike-slip dislocation is given by

$$u_x = \frac{-U_1}{2\pi}\left[\frac{\xi q}{R(R+\eta)} + arctan\left(\frac{\xi\eta}{qR}\right) + I_1\, sin\delta\right]\Big|\Big|$$

$$u_y = \frac{-U_1}{2\pi}\left[\frac{\tilde{y}q}{R(R+\eta)} + \frac{q\, cos\delta}{R+\eta} + I_2\, sin\delta\right]\Big|\Big|$$

$$u_z = \frac{-U_1}{2\pi}\left[\frac{\tilde{d}q}{R(R+\eta)} + \frac{q\, sin\delta}{R+\eta} + I_4\, sin\delta\right]\Big|\Big|$$

For dip-slip dislocation

$$u_x = \frac{-U_2}{2\pi}\left[\frac{q}{R} - I_3\, sin\delta\, cos\delta\right]\Big\|$$

$$u_y = \frac{-U_2}{2\pi}\left[\frac{\tilde{y}q}{R(R+\xi)} + cos\delta\, arctan\left(\frac{\xi\eta}{qR}\right) - I_1\, sin\delta\, cos\delta\right]\Big\|$$

$$u_z = \frac{-U_2}{2\pi}\left[\frac{\tilde{d}q}{R(R+\xi)} + sin\delta\, arctan\left(\frac{\xi\eta}{qR}\right) - I_5\, sin\delta\, cos\delta\right]\Big\|$$

For tensile dislocation

$$u_x = \frac{U_3}{2\pi}\left[\frac{q^2}{R(R+\eta)} - I_3 \sin^2\delta\right]\Big\|$$

$$u_y = \frac{U_3}{2\pi}\left[\frac{-\tilde{d}q}{R(R+\xi)} - sin\delta\left\{\frac{\xi q}{R(R+\eta)} - arctan\left(\frac{\xi\eta}{qR}\right)\right\} - I_1 \sin^2\delta\right]\Big\|$$

$$u_z = \frac{U_3}{2\pi}\left[\frac{\tilde{y}q}{R(R+\xi)} + cos\delta\left\{\frac{\xi q}{R(R+\eta)} - arctan\left(\frac{\xi\eta}{qR}\right)\right\} - I_5 \sin^2\delta\right]\Big\|$$

where

$$I_1 = \frac{\mu}{\lambda+\mu}\left(\frac{\xi}{(R+\tilde{d})cos\delta}\right) - I_5\, tan\delta$$

$$I_2 = \frac{\mu}{\lambda+\mu}\ln(R+\eta) - I_3$$

$$I_3 = \frac{\mu}{\lambda+\mu}\left(\frac{\tilde{y}}{(R+\tilde{d})cos\delta} - \ln(R+\eta)\right) + I_4\, tan\delta$$

$$I_4 = \frac{\mu}{\lambda+\mu}\frac{1}{cos\delta}\left[ln\left(R+\tilde{d}\right) - sin\delta\ln(R+\eta)\right]$$

$$I_5 = \frac{\mu}{\lambda+\mu}\frac{2}{cos\delta}\arctan\left(\frac{\eta(X-qcos\delta)+X(R+X)sin\delta}{\xi(R+X)cos\delta}\right)$$

If the dip angle (δ) is 90°, cosδ=0

$$I_1 = \frac{\mu}{2(\lambda+\mu)} \frac{\xi q}{\left(R+\tilde{d}\right)^2}$$

$$I_3 = \frac{\mu}{2(\lambda+\mu)} \left(\frac{\eta}{(R+\tilde{d})} + \frac{\tilde{y} q}{\left(R+\tilde{d}\right)^2} - \ln\left(R+\eta\right) \right)$$

$$I_4 = \frac{\mu}{\lambda+\mu} \frac{q}{R+\tilde{d}}$$

$$I_5 = \frac{\mu}{\lambda+\mu} \frac{\xi sin\delta}{R+\tilde{d}}$$

where λ and μ are Lame constants and

$$p = y\, cos\delta + d\, sin\delta$$

$$q = y\, sin\delta - d\, cos\delta$$

$$\tilde{y} = \eta cos\delta + q\, sin\delta$$

$$\tilde{d} = \eta sin\delta - q\, cos\delta$$

$$R^2 = \xi^2 + \eta^2 + q^2$$

$$X^2 = \xi^2 + q^2$$

In a more complex geometry, let us consider the fault surface as tessellated by a triangular mesh. Meade (2007) proposes an analytical algorithm for the calculation of the displacement, strain and stress associated with slip on a triangular dislocation element (TDE) in a homogeneous elastic half space. To compute the total deformation related with slip on a single TDE, the line integrals around the element edges (legs) should be calculated. Therefore,

total displacement can be given by the summation of displacements from each of three legs (Figure 2.6.2).

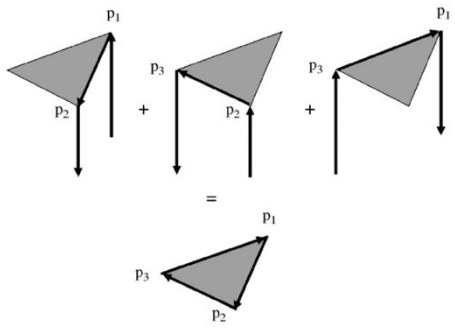

Figure 2.6. 2:*Triangular dislocation element and triangle leg geometry. Arrows indicate sense of orientation of the slip components (Taken from Meade, 2017).*

Each of the three legs can be produced by the superposition of two angular dislocations between each set of triangle vertices (Figure 2.6.3). The displacement from each leg ($\mathbf{u}_k$) can be calculated by taking the superposition of deformation fields from two angular dislocations ($\mathbf{u}_k = \mathbf{u}_k^1 + \mathbf{u}_k^2$)

$$\boldsymbol{u} = \sum_{j=1}^{N} \sum_{k=1}^{3} \boldsymbol{u}_{k_j}^1 - \boldsymbol{u}_{k_j}^2$$

where k is the index over the three legs of each triangle, j is the index for each TDE and N is the number of TDEs (Comninou, 1973; Jeyakumaran et al., 1992). To compute the deformation associated with slip in an arbitrary direction on a TDE, the TDE Burgers vector should be converted to strike-slip, dip-slip and tensile-slip components on each angular dislocation. The

solution is constructed by associating the geometry of the TDE to that of each angular dislocation using orthogonal unit vectors to define their respective orientations. Moreover, the slip vectors from the TDE are projected onto each angular dislocation patch.

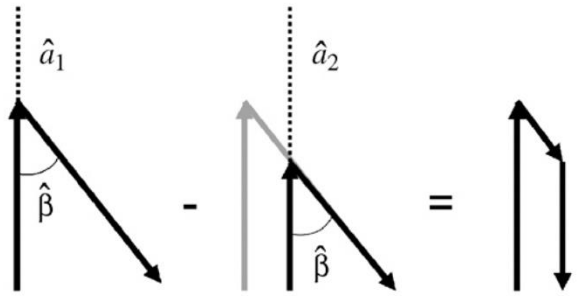

Figure 2.6. 3:*Construction of a single dislocation leg by means of summation of two angular dislocations. Inclination of each angular dislocation is given by a common inclination* $\widehat{\boldsymbol{\beta}}$ *while vertices are buried to depths* $\widehat{\boldsymbol{a}}_{\mathbf{1}}$ *and* $\widehat{\boldsymbol{a}}_{\mathbf{2}}$ *respectively. Common, dipping segment of each angular dislocation cancels after summation (Taken from Meade, 2017).*

Total slip is related with the given strike-slip, dip-slip and tensile-slip components (**s**) on a triangular fault patch ($\mathbf{v_s}$) which is given by,

$$\boldsymbol{v}_s = \begin{pmatrix} v_s^x \\ v_s^y \\ v_s^z \end{pmatrix} = \begin{pmatrix} n_t^x & n_s^x & n_d^x \\ n_t^y & n_s^y & n_d^y \\ n_t^z & n_s^z & n_d^z \end{pmatrix} \begin{pmatrix} s_t \\ s_s \\ s_d \end{pmatrix}$$

where $\mathbf{n}_t$ is the unit vector normal to the face of the triangle, $\boldsymbol{n}_t = \frac{\mathbf{p_1} \text{ x } \mathbf{p_2}}{||\mathbf{p_1} \text{ x } \mathbf{p_2}||}$, while one parallel to the strike of the patch, $\boldsymbol{n}_s = (-sin\gamma, cos\gamma, 0)$ where $\gamma = arctan\left(\frac{n_t^y}{n_t^x}\right)$ and a third direction vector can be defined parallel to the TDE dip as $\boldsymbol{n}_d = \boldsymbol{n}_t \text{ x } \boldsymbol{n}_s$.

Projection of slip vectors into the strike-slip, dip-slip and tensile-slip components should be done for each of the three different dislocation legs. The strike-slip and tensile-slip

components are parallel and they are perpendicular to the strike of the dislocation leg, $\widehat{\boldsymbol{n}}_s = (\cos(\alpha), \sin(\alpha), 0)$, $\widehat{\boldsymbol{n}}_t = (-\sin(\alpha), \cos(\alpha), 0)$ and dip-slip unit vector is orthogonal to the plane defined by $\widehat{\boldsymbol{n}}_s$ and $\widehat{\boldsymbol{n}}_t$ ($\widehat{\boldsymbol{n}}_d = \widehat{\boldsymbol{n}}_t \times \widehat{\boldsymbol{n}}_s$). Since $\widehat{\boldsymbol{n}}_s$ and $\widehat{\boldsymbol{n}}_t$ are always consist in $\hat{x}$-$\hat{y}$ plane, $\widehat{\boldsymbol{n}}_d = \boldsymbol{n}^z = (0,0,1)$. The slip vector into the corresponding strike-slip, dip-slip, and tensile-slip components can be given by,

$$\hat{\boldsymbol{s}} = \begin{pmatrix} \hat{\boldsymbol{s}}_t \\ \hat{\boldsymbol{s}}_s \\ \hat{\boldsymbol{s}}_d \end{pmatrix} = \begin{pmatrix} \hat{n}_t^x & \hat{n}_s^x & \hat{n}_d^x \\ \hat{n}_t^y & \hat{n}_s^y & \hat{n}_d^y \\ \hat{n}_t^z & \hat{n}_s^z & \hat{n}_d^z \end{pmatrix} \begin{pmatrix} v_s^x \\ v_s^y \\ v_s^z \end{pmatrix}$$

where subscripts t, s, d represents tensile-slip, strike-slip and dip-slip components, respectively.

The time-scale of an earthquake rupture is generally much shorter than the tsunami wave propagation due to the small compressibility of water and horizontal extent of the earthquake rupture is generally greater than water depth, the seafloor movement can be assumed as an impulsive motion. Instantaneous vertical deformation of seafloor disturbs the hydrostatic equilibrium in the entire water column above and generates tsunami waves.

CHAPTER 3 – TESTING SLIP MODELS FOR TSUNAMI GENERATION

The uncertainty quantification of PTHA generally contains empirical analysis and subjective judgement together (Grezio et al., 2017). Moreover, testing PTHA results can be very challenging. Gutenberg-Richter relation, for instance, can be used to characterize the recurrence of intermediate earthquakes from historical catalogs. However, recurrence time of large earthquakes requires a concept of judgment using the current understanding of earthquake processes, since the recurrence time of those events is very long with respect to historical records. On the other hand, it is feasible to test separately PTHA components, such as slip distribution variability.

Using homogenous slip distributions as an earthquake source for tsunami generation in tsunami hazard analysis is a widespread approach, despite the co-seismic slip distribution complexity has an important impact on hazard results. Additionally, numerous methods have been proposed to generate synthetic heterogenous slip distributions for tsunami hazard calculations (Davies et al., 2015; LeVeque et al., 2016; Murphy et al., 2016; Sepulveda et al., 2017; Davies 2019; Scala et al., 2020). Slip distributions informed by kinematic models from inversion of real events are also employed (Goda et al., 2014).

The main goal of this chapter is to test synthetic tsunamis produced by different slip generation techniques against tsunami observations from open ocean bottom pressure sensors and also testing these different methods one against the other. For this purpose, the approach proposed in Scala et al. (2020) have been used for the generation of depth-independent and depth-dependent stochastic slip models. Furthermore, kinematic slip

models obtained with teleseismic inversions from the earthquake catalog of Ye et al. (2016), have been also used as initial conditions for tsunami numerical models. Tsunami simulations have been performed for each scenario from a single kinematic rupture model and modelling results have been tested and compared within the framework of Davies (2019).

The following figure (Figure 3.1) shows the steps of the procedure with the brief explanation of each one of them. Details of each step are explained in the following sections of the chapter.

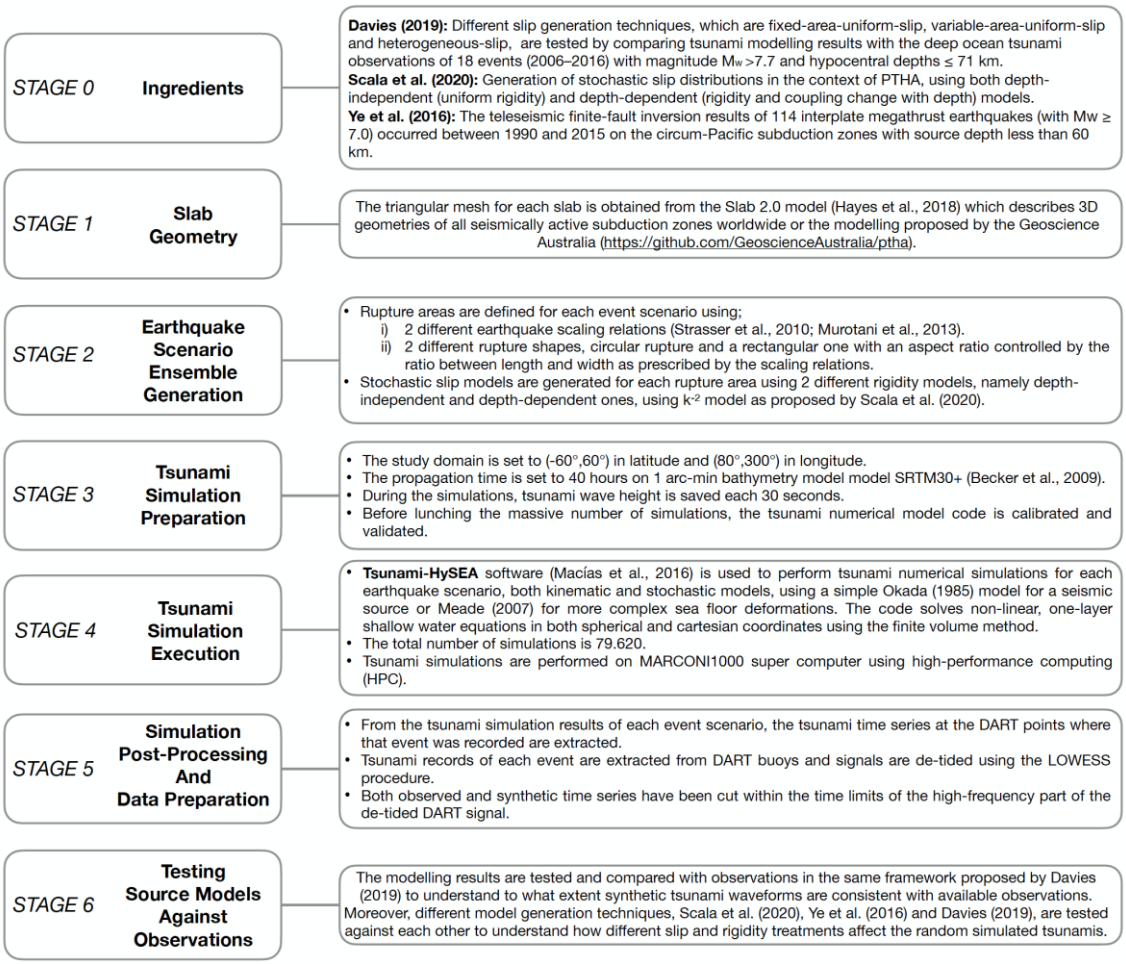

Figure 3. 1: *The work flow of the study.*

3.1. Ingredients of the study and data

The study of Scala et al. (2020), proposes an approach to generate k^{-2} stochastic slip distributions in the context of PTHA, using both depth-independent (uniform rigidity) and depth-dependent (rigidity and coupling change with depth) models. Scala et al. (2020) showed that mean hazard curves are different for depth-dependent and depth-independent slip distributions at the same point of interest. Stochastic slip models are generated for three subduction zones in the Mediterranean Sea by adopting a realistic 3D geometry, to model earthquakes with magnitude between M_w 6.0 and 9.0. In the depth-dependent models, shallow slip amplification results as an effect of the variation of the rigidity and coupling with depth. In this case, it is necessary to impose lower probability for smaller hazard intensities and larger probability for higher intensities, since the probability of occurrence of relatively smaller events is decreased in the shallow part of a subduction zone, while they are more likely to occur at depth. This is required to make, in the long-term, over multiple events, the cumulative slip uniform over the subduction plate. In this study, in addition to the performance of models generated using Scala et al. (2020) approach, the validity of diverse physical assumptions, such as different rupture geometries and scaling laws, has been also tested confronting tsunami synthetics and observations.

I have also analyzed the synthetics generated using the Ye (Ye et al., 2016) catalog of kinematic slip models. This catalog contains 114 interplate megathrust earthquakes (with Mw ≥ 7.0) occurred between 1990 and 2015 on the circum-Pacific subduction zones with source depth less than 60 km. The source characteristics of these events were determined using global broadband body wave observations (for frequencies below 1 Hz). The 26 December

2004 Mw 9.2 Sumatra earthquake is not included in the catalog due to the extremely long source duration.

In the study of Davies (2019), different slip models are tested by comparing tsunami modelling results with the deep ocean tsunami observations of 18 events (2006–2016) in the Global Centroid Moment Tensor (GCMT) catalogue (Ekström et al. 2012) with magnitude M_w >7.7 and hypocentral depths ≤ 71 km. 2006/07/17 Mw 7.7 Java earthquake and the 2016/11/13 Mw 7.9 Kaikoura earthquake are not included in the test since a tsunami record is not identified for those events. Davies (2019) made use of three scenario generation techniques, heterogeneous slip (HS), variable area- uniform slip (VAUS) and fixed area-uniform slip (FAUS), which are considered to generate stochastic scenarios using both depth-dependent and depth-independent rigidity models. Stochastic scenarios are constructed assuming an earthquake location and magnitude similar to that of the actual event, while subduction interface geometry is considered known. This study also proposes some statistics to make comparisons, identifying and partially correcting biases of these scenarios, and providing better justification for their use in applications. According to Davies (2019), observed events should behave like a randomly selected tsunami scenario for an ideal model. To test that, it is proposed to compare the modelled tsunami sizes with the observations. For each event, the fraction of scenarios according to the difference between the maximum and minimum water level is less than the observed value, is calculated at each DART location. For an ideal model, this fraction should be like an independent random sample from a uniform distribution, which is tested also statistically using null-hypothesis significance tests. The fraction distribution can also show if there is any inter-event dependency which is an indicator of model bias. The scenario goodness-of-fit is another statistic that analyze the agreement of

model scenario time series with the observed time series at each DART location for each event. It is assumed that best fitting scenarios also should behave like a randomly selected scenario if the model is ideal. Model bias can be checked comparing the earthquake properties (maximum slip and rupture area) of best fitting scenarios against the random scenarios and these comparisons can also be generalized to make bias adjustment of each model.

In this study, we have compared synthetic tsunamis produced by kinematic slip models generated by the Scala et al. (2020) stochastic slip technique, against tsunami observations at open ocean buoys, for 15 earthquakes as listed in Table 3.1. Given the magnitude and location of the real earthquakes, we consider ensembles of consistent slipping areas and slip distributions, accounting for both a constant and a depth-dependent rigidity profile. Kinematic slip models on planar faults obtained with teleseismic inversion for 10 of 15 events are also present in the earthquake catalog of Ye et al. (2016) and tsunami generated by these models have been also compared with observations.

We have first extracted tsunami records of these 15 events from deep ocean tsunameter (DART buoy) measurements (Figure 3.1.1). DART (Deep-ocean Assessment and Reporting of Tsunami) buoys have been developed for early detection, measurement, and real-time reporting of tsunamis in the open ocean by Project DART® at NOAA's Pacific Marine Environmental Laboratory (PMEL). A DART system contains a seafloor bottom pressure recording (BPR) system, that is able to measure pressure with a resolution of approximately 1mm of sea water and a moored surface buoy for real-time data transmission (https://nctr.pmel.noaa.gov/Dart/dart_pb1.html). The data from the BPR is transmitted by an acoustic modem to the moored surface buoy which then sends the tsunami information to a ground station via satellite telecommunication (Figure 3.1.2). The BPR uses a pressure

transducer which uses a very thin quartz crystal beam, electrically induced to oscillate at its lowest resonant mode. The vertical movement of the seafloor, due to the earthquake, compresses the water column above, causing a decrease in pressure as the seafloor falls, or an increase in pressure as the seafloor rises (Meinig et al., 2005). When a tsunami wave passes above the instrument, quartz crystals stretch and the vibration frequency increases with the increased pressure. Frequency changes on quartz crystals can be measured precisely and converted to corresponding tsunami wave height changes using a constant conversion of 1 psi (pounds per square inch) = 670 mm of water height. BPR uses the temperature data to compensate for the thermal effects on the pressure-sensing element (Eblea and González, 1991; Meinig et al., 2005). The system is triggered to 'Event mode' when a detection threshold is exceeded and the sampling rate of the data set to 15-sec, while the sampling rate is fixed to 15-min when the system is in standard mode. The sampling rate of the data in event mode gradually increases from 15-sec to 1-min values (González et al., 1998).

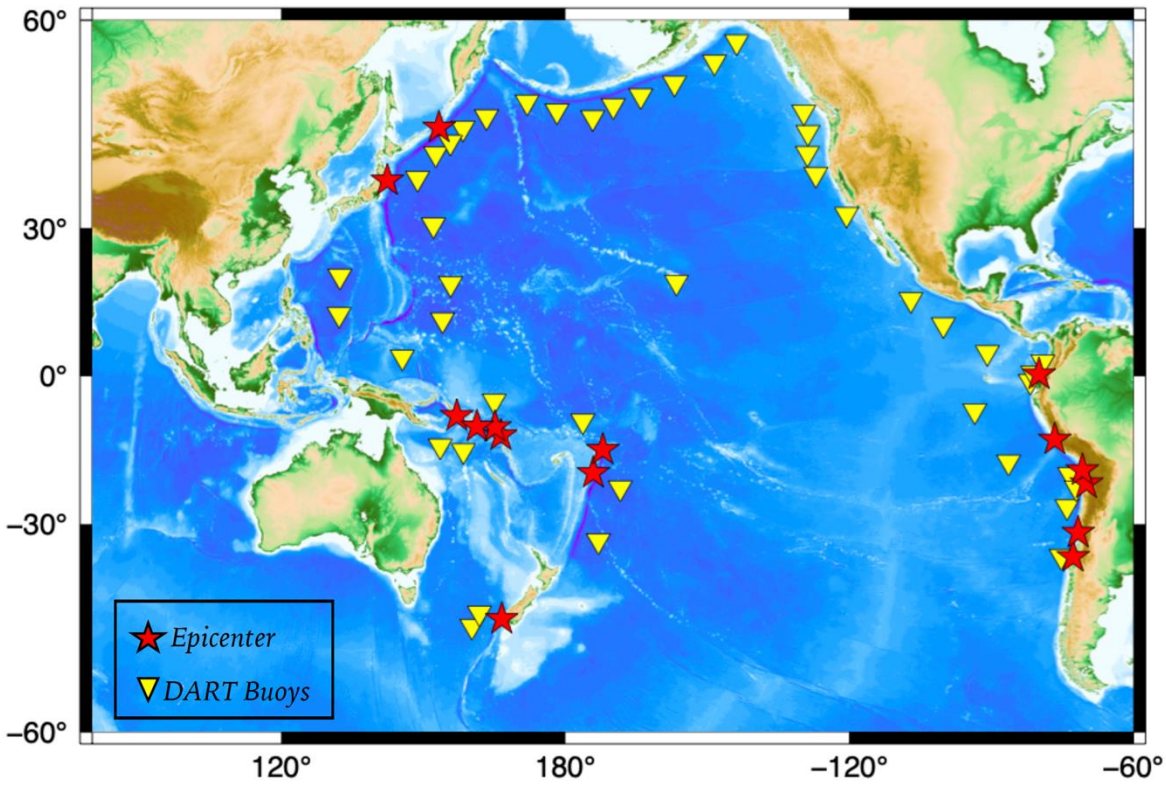

Figure 3.1.1: *The location of 15 events used in this study and DART buoys*

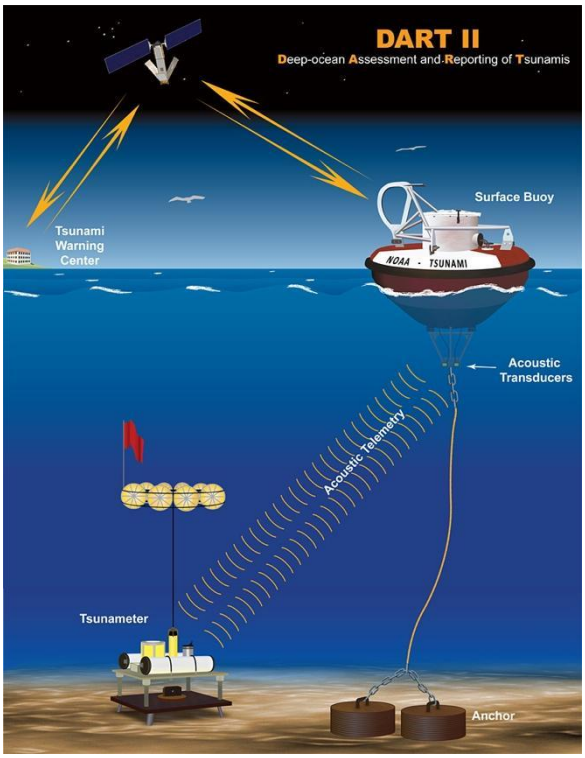

Figure 3.1.2: *DART II system (from https://www.weather.gov/jetstream/dart_max)*

Tsunami records have been detrended, removing the tide from the original signal using the LOWESS procedure, which is a local operation based on a weighted regression, defined over a subset of neighboring data points in a given window (Barbosa et al., 2004; Romano et al. 2015; Davies & Griffin 2018).

Moment magnitude of each event has been calculated by Davies (2019) from the GCMT catalogue seismic moment, using the seismic moment-magnitude relation proposed by Hanks & Kanamori (1979). Since all the events are thrust events, rake angle is fixed to 90° degrees for each model. The adopted relation is the following

$$M_w = \frac{2}{3} * (log\,(M_0) - 9.05) \qquad \text{(Eq.3.1.1)}$$

Event Name	ID	Date	Number of DARTs	Mw	Longitude	Latitude	Depth (km)
Pangai, Tonga	KT1	2006/05/03 15:26:40.3	1	8.0	−174.12	−20.19	55.0
Kuril Islands	KJ1	2006/11/15 11:14:17.8	12	8.3	153.29	46.57	38.9
Solomon Islands	So1	2007/04/01 20:39:56.4	2	8.1	157.04	-8.46	10.0
Peru	SA1	2007/08/15 23:40:57.9	3	8	-76.60	-13.39	39.0
Tocopilla, Chile	SA2	2007/11/14 15:40:50.5	2	7.8	-69.89	-22.25	40.0
New Zealand	Pu1	2009/07/15 09:22:29.0	2	7.8	166.56	-45.76	12.0
Matavai, Samoa	KT2	2009/09/29 17:48:11.0	5	8.1	−172.10	−15.49	18.0
Vanuatu	NH1	2009/10/07 22:18:51.2	1	7.8	166.38	-12.52	35.0
Maule, Chile	SA3	2010/02/27 06:34:15.6	16	8.8	-72.71	-35.85	44.8
Tohoku	KJ2	2011/03/11 05:46:23.0	28	9.1	142.37	38.32	24.4
Solomon Islands	NH2	2013/02/06 01:12:25.8	5	7.9	165.11	-10.80	24.0
Iquique, Chile	SA4	2014/04/01 23:46:47.3	7	8.2	-70.77	-19.61	25.0
Illapel, Chile	SA5	2015/09/16 22:54:32.9	18	8.3	−71.67	−31.57	22.4
Ecuador	SA6	2016/04/16 23:58:36.9	2	7.8	−79.93	0.35	21.0
Solomon Islands	So2	2016/12/08 17:38:46.3	3	7.8	161.32	-10.68	40.0

Table 3.1.1: *List of events modelled in this study. The Latitude, Longitude and depth columns belong to the hypocenter of the event. The 'Number of DARTs' column gives the number of DART buoys at which a tsunami signal was obtained.*

3.2. Generation of synthetic slipping areas and earthquake scenarios

The approach proposed in Scala et al. (2020), adopting a similar strategy as in Davies (2019), is used for generating several sets of scenarios for the 15 events selected. For each of the source's models in these 15 sets, a tsunami numerical simulation is performed. The modelling results are tested and compared to the observations at the DARTs following the methodology proposed by Davies (2019).

Stochastic slip models are generated using the tool ANTI-FASc (https://github.com/antonioscalaunina/ANTI-FASc). This tool accounts for complex geometries in the description of the subduction zone. Here, pre-modelled subduction slab triangular elements in Pacific have been included (Figure A1 and A2 in the appendix). The triangular mesh for each slab is obtained from the Slab 2.0 model which describes 3D geometries of all seismically active subduction zones worldwide (Hayes et al., 2018) or from the modelling proposed by the Geoscience Australia (https://github.com/GeoscienceAustralia/ptha) which uses either Slab 1.0 or Slab 2.0 models (Hayes et al. 2012, 2018) to define fault plane geometries. The Slab 2.0 model uses a variety of data, such as local and regional seismicity catalogs, seismic tomography models etc., to define the slab geometry. The Slab 2.0 model gives contour lines of the depth along the slab, that can be parameterized depending on the purpose. Tonini et al. (2020) present one case in which, when simplifying the earthquake source geometry in a subduction zone, considering planar instead than 3D faults, we get significant differences in tsunami waveforms that may affect the tsunami impact. Therefore, as in Davies (2019), we have avoided the simplification of the source geometry and used a triangular mesh to be able to represent the curvature of

the slab geometry properly. We selected the size of the mesh assuming that each side of the triangular element is approximately 12 km (those of Davies are approximately 50 km x 50 km squares). We tested this mesh discretization and verified that it is able to model k^{-2} stochastic slip distributions efficiently for events of magnitude between M_w 7.0 and 10.0 (Zhang et al. 1994; Ruiz et al., 2011) having a minimum wavelength to be modelled of tens of kilometers.

In the definition of the scenario, we have considered the active barycenters, which are the centroids of each scenario event. They are selected among the centers of the pre-defined subduction elements assuming similar earthquake location and magnitude (Davies, 2019) for each of the 15 selected events. Specifically, for a single event we have assumed that its magnitude can range in an interval of ±0.15 units, around the effective event magnitude. Possible earthquake locations, on the other hand, are defined as those positions having a distance smaller than one rupture length from the real hypocenter to be able to consider all possible rupture areas and shapes that contain the hypocenter of the related event. It is assumed that the number of scenarios is decreased with increasing magnitude, as different from Davies (2019).

ANTI-FASc uses a pre-defined general magnitude discretization (Table 3.2.1). Scenario magnitudes are selected from the discretization, according to the limits imposed for each event. For instance, if the event has the magnitude M_w 8.0, the scenario magnitudes are 7.928 and 8.0933 since these are the values from the discretization within the magnitude interval of ±0.15 units (7.85, 8.15).

Here we consider two different earthquake scaling relations (Strasser et al., 2010; Murotani et al., 2013) to define rupture areas and consequently average slip for each event scenario. Both studies derive these scaling relations for subduction events. Moreover, Strasser

et al. (2010) divide these events into two groups as interface and intraslab events. Through these selected scaling laws, the rupture area A and the rupture length L for each magnitude are computed (Table 3.2.1). The width of the rupture area is also computed as the ratio between the area and the length. However, there is not any direct relation represented by Murotani et al. (2013) between magnitude and rupture length. Therefore, we assumed that amplification due to the ratio between the area calculated by Murotani et al. (2013) and the one by Strasser et al. (2010) is separated between the rupture length and the width

$$A_{MRT} = L_{MRT} * W_{MRT}$$

$$A_{MRT} = \left(L_{STR} * \sqrt{\frac{A_{MRT}}{A_{STR}}} \right) * \left(W_{STR} * \sqrt{\frac{A_{MRT}}{A_{STR}}} \right)$$

$$L_{MRT} = L_{STR} * \sqrt{\frac{A_{MRT}}{A_{STR}}}$$

where A, L and W are respectively the rupture area, length and width for Murotani et al. (2013) with 'MRT' subscript and for Strasser et al. (2010) with 'STR' subscript. Using this principle, L_{MRT} is calculated.

M_w	Rupture Length (Murotani et al., 2013) (km)	Rupture Length (Strasser et al., 2010) (km)	Rupture Area (Murotani et al., 2013) (km^2)	Rupture Area (Strasser et al., 2010) (km^2)
7.5435	89.5	86.3	5460.9	5074.7
7.7453	118.8	113.2	8691.0	7898.1
7.9280	153.5	144.8	13236.4	11788.4
8.0933	193.	180.9	19367.4	16936.4
8.2429	238.7	221.3	27332.0	23509.3
8.3782	288.5	265.6	37322.5	31626.1
8.5007	342.6	313.2	49484.7	41368.1
8.6115	400.2	363.7	63866.2	52740.9
8.7118	460.6	416.3	80458.4	65710.3
8.8025	523.1	470.4	99145.1	80164.1
8.8846	586.9	525.4	119776.4	95970.8
8.9588	651.3	580.6	142092.6	112921.7
9.0260	715.7	635.6	165871.4	130843.4
9.0869	779.4	689.9	190821.6	149515.8
9.1419	841.9	743.0	216599.4	168684.5
9.1917	902.8	794.5	242912.9	188138.9
9.2367	961.7	844.3	269467.2	207668.8
9.2775	1018.3	891.9	295988.0	227081.9

Table 3.2.1: *Magnitude discretization of events and rupture dimensions calculated using Murotani et al. (2013) and Strasser et al. (2010) scaling relations.*

After the calculation of rupture dimensions, the active barycenters are selected (Figure 3.2.1a). This selection has been done for the whole slab for each considered subduction zone, among the pre-defined barycenter of each mesh cell, through a two-step procedure:

1. The barycenters having a distance from the slab boundary smaller than half the width are eliminated to avoid selection of barycenters very close to the slab boundary, which can be critical, especially for the parts of the slab where the width is very small. Also, the rupture area corresponding to these points can exceed the slab boundary.

2. Among the remaining barycenters, a further selection is applied making the average inter-distance among the active barycenters larger than 10% of the rupture length to avoid

generating too numerous similar scenarios. This is important particularly for the events with large magnitude since they can generate large rupture areas.

Four different rupture areas are defined for each selected active barycenter to account for the epistemic uncertainty on the geometrical properties. We used two different scaling relations, as mentioned in the previous part of the section, and two different rupture shapes. We selected a circular rupture and a rectangular one with an aspect ratio controlled by the ratio between length and width as prescribed by the scaling relations. Each ruptured surface is built starting from an active barycenter, which is selected through the procedure previously explained; a circular rupture surface is generated by iteratively adding more and more neighbor mesh cells up to the expected width, without considering the aspect ratio. For a rectangular rupture surface, on the other hand, as soon as the shallowest or/and the deepest points of the temporary area exceed the expected width, the rupture area starts to grow along the length to keep the aspect ratio.

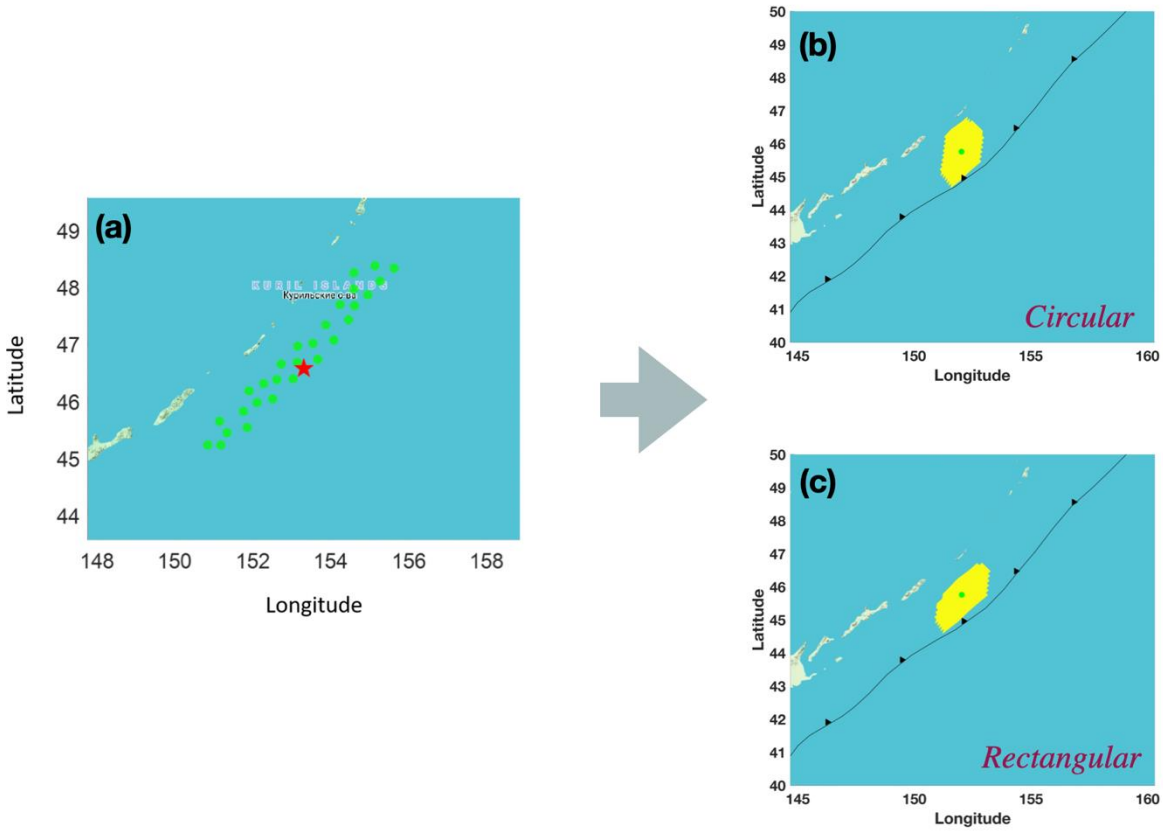

Figure 3.2.1: *(a) Selected active barycenters (green dots) and hypocenter of the real event (red star), (b) Circular shaped (c) Rectangular shaped rupture areas for one of the selected active barycenters, black lines indicate the location of the trench.*

For the generation of slip models, we used two different rigidity models, namely depth-independent and depth-dependent ones, as proposed by Scala et al. (2020). In the depth-independent model, rigidity is homogenous and it is fixed to 30 GPa while in the depth-dependent model rigidity changes with depth and coupling to result into shallow slip amplification. In the depth-dependent model, we used a rigidity profile which is the average between the PREM model and the end-member case of Bilek and Lay (1999) (Figure 3.2.2a). Aseismic slip contribution on the subduction faults should also be considered to evaluate the long-term slip accumulation. The balance between the seismic and aseismic slip can be

defined as a function of the seismic coupling factor. The total long-term slip released at the position x can be given by:

$$D_T = \delta_T(x) + d_T(x) = k(x) \cdot D_T + [1 - k(x)] \cdot D_T$$

where D_T is the total long-term slip, δ_T (**x**) is the seismic and d_T(**x**) the aseismic contributions to the slip at location **x**, and $k(x)$ is the coupling factor and it is given by $k(x) = \widetilde{K} \cdot K(x)$. Here $\widetilde{K}$ is the absolute coupling value of the specific subduction zone and $K(x)$ is the relative coupling variation at **x** (Figure 3.2.2b).

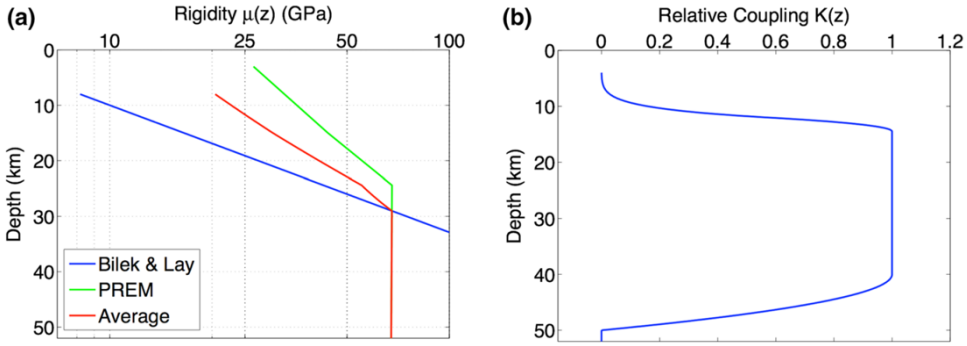

Figure 3.2.2: *(a) Rigidity profiles as a function of depth. (b) Relative coupling as a function of depth (from Scala et al., 2020).*

Slip distributions are generated for each pre-defined slipping surface assuming that sub-asperities are randomly distributed over the identified rupture area by following the power law distribution of sizes (Zheng et al. 1994; Ruiz et al. 2011). Using this self-similar model and different rigidity models, ten different slip models are generated for each rupture surface. The spatial variability of slip in the ensemble is described by a slip probability density function. The method proposed by Murphy et al. (2016) is used to modify stochastic models, integrating a probability distribution that is derived from dynamic features of the rupture. Moreover, we followed the strategy presented by Herrero and Murphy (2018) to generate self-similar slip

distributions calculating accurately the distance between two points of the complex non-planar fault surface.

For each rupture area, 10 stochastic slip distributions are generated using depth-dependent and depth-independent rigidity models. Figure 3.2.3 indicates the amplification and the movement of the slip towards the surface from depth-independent model to depth-dependent model. Table 3.2.2 shows the total number of scenarios for each event and model classes. The number of scenarios is the same in the model classes specified according to the shape of rupture area and rigidity model. However, it is different for the scaling laws. The number of scenarios is higher for Strasser model. Since the rupture length is smaller for this scaling relation, during the elimination of active barycenters according to rupture length (Step 2 explained above) fewer active barycenters are eliminated and therefore the number of scenarios is higher than the Murotani model.

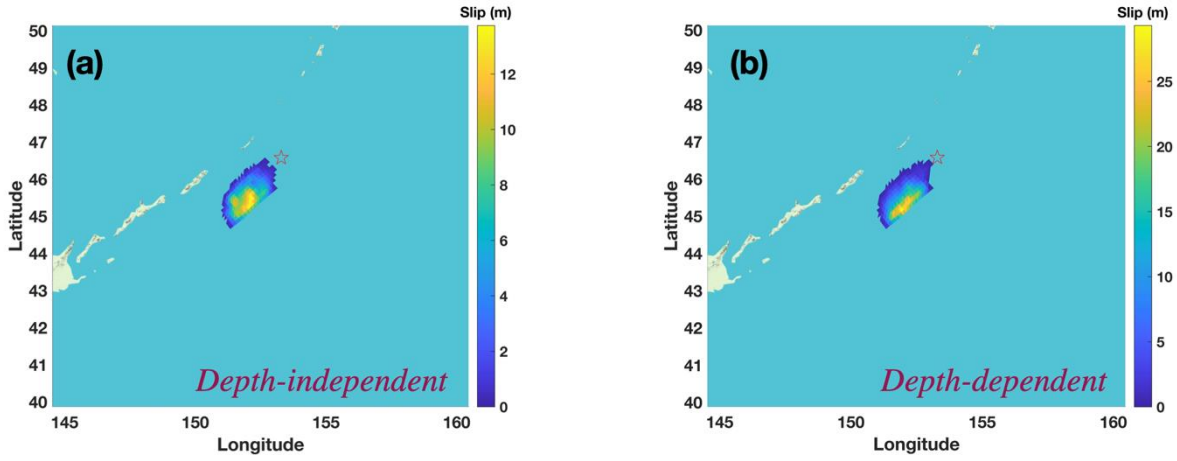

***Figure 3.2.3**: Examples for slip distributions with (a) constant rigidity model and (b) rigidity changes with depth and coupling*

EVENT NAME	**NUMBER OF SCENARIOS PER MODEL**				**TOTAL NUMBER OF SCENARIOS PER EVENT** (with both homogeneous and variable rigidity)
	CIRCULAR		RECTANGULAR		
	MUROTANI	STRASSER	MUROTANI	STRASSER	
Pangai, Tonga	295	315	295	315	2440
Kuril Islands	680	695	680	695	5500
Solomon Islands	345	355	345	355	2800
Peru	1295	1300	1295	1300	10380
Tocopilla, Chile	1055	1065	1055	1065	8480
New Zealand	320	370	320	370	2760
Matavai, Samoa	245	280	245	280	2100
Sola, Vanuatu	555	580	555	580	4540
Maule, Chile	710	790	710	790	6000
Tohoku	565	815	565	815	5520
Solomon Islands	135	160	135	160	1180
Iquique, Chile	895	905	895	905	7200
Illapel, Chile	705	810	705	810	6060
Ecuador	1185	1240	1185	1240	9700
Solomon Islands	610	630	610	630	4960

Table 3.2.2: *List of events and number of scenarios for each event.*

3.3. Teleseismic Finite-fault models

The finite-fault inversion results of Ye et al. (2016) have been also used as further initial conditions for tsunami simulations since 10 out of 15 events, considered here, are also present in this earthquake catalog. The Ye catalog contains kinematic slip models for 114 interplate megathrust earthquakes with Mw ≥ 7.0, occurred between 1990 and 2015 on the circum-Pacific subduction zones. This catalog provides slip maps of each event on a regular grid with cells along strike and dip (Figure 3.3.1(a)). Depth information is also provided for the center of each cell. However, the latitude and longitude information for cells are unknown, the only assigned location information is the hypocenter of the event. Since geographical coordinates of each cell center are required parameters for tsunami modelling code, using the latitude and longitude information of hypocenter and the distance between the central points of the cells, geographical coordinates have been calculated for each center following these steps:

1-The distance along dip and strike are calculated by projecting the fault plane onto the Earth surface with the dip angle and the fault plane is then rotated according to the strike angle.

2-The distance between two points is converted from kilometers to degrees and geographical coordinates are assigned to each cell point (Figure 3.3.1(b)). During this calculation, the elliptical shape of the Earth is also considered since the distance between two points along a meridian, changes from equator to the poles.

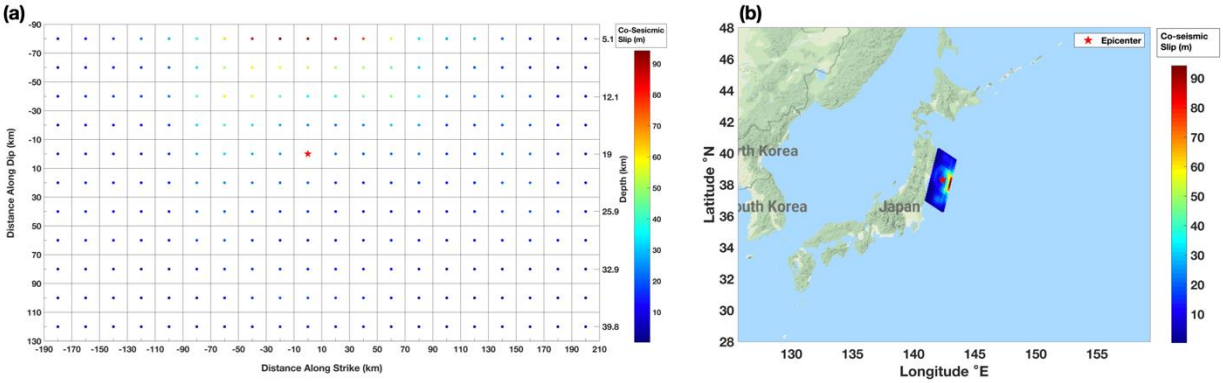

Figure 3.3.1: *An example of conversion of a gridded slip model from Ye et al. (2016) (a) to geographical coordinates (b).*

3.4. Tsunami Numerical Modelling

In this study, Tsunami-HySEA software is used to perform tsunami numerical simulations for each earthquake scenario, either generated from the stochastic slip tool ANTI-FASc or belonging to the Ye teleseismic inversion catalog. These models are then used to evaluate the seafloor deformation and to provide the initial conditions for the tsunami. Tsunami time series of each scenario are recorded at synthetic gauge points where the corresponding event is recorded by a DART buoy. Then, these time records are analyzed to understand to what extent synthetic tsunami waveforms are consistent with available observations.

Tsunami-HySEA is a specific version of HySEA (Hyperbolic Systems and Efficient Algorithms) software that is based on a single-layer, two-layer or multi-layer shallow water system, for tsunami modelling. It is developed by the EDANYA Group (https://edanya.uma.es) from the Universidad de Málaga (UMA) for tsunami simulations. The model is able to simulate the generation, the propagation and the coastal inundation of an earthquake generated tsunami in the same code, for both single and nested domains. Tsunami-HySEA can compute the initial condition using a simple Okada (Okada, 1985) model for a seismic source or Meade (2007) for more complex sea floor deformations. The code is also capable to model time-dependent, multi-segment rupture geometries by defining a series of fault parameters, such as strike, dip and rake angles, coordinates of the center of the fault, fault dimensions and depth. The code also allows to apply filters to the sea surface response of the seafloor deformation (Kajiura, 1963).

The code allows to perform simulations faster than real time on GPU and multi-GPU architectures (de la Asunción et al., 2011, 2013; Castro et al., 2011). This is a crucial factor in

terms of rapid post-disaster management and for application of tsunami early warning systems. Besides benchmarking tests mentioned previously, a specific HySEA code is developed for Tsunami Early Warning Systems (TEWS). This version of the Tsunami-HySEA is currently used as the main tsunami numerical code at the INGV (Istituto Nazionale di Geofisica e Vulcanologia) after passing a detailed one-year validation process to test robustness, computational speed-up, and suitable numerical results. The JRC (Joint Research Centre of the European Commission) also adopted this code in their Tsunami Alert System as one of its numerical codes. The Spanish National TEWS is currently using the test mode of the code in its system.

Tsunami-HySEA solves non-linear, one-layer shallow water equations in both spherical and Cartesian coordinates using the finite volume method. The model equations can be given in Cartesian coordinates

$$\frac{\partial h}{\partial t} + \frac{\partial (hu)}{\partial x} + \frac{\partial (hv)}{\partial y} = 0$$

$$\frac{\partial (hu)}{\partial t} + \frac{\partial}{\partial x}\left(hu^2 + \frac{1}{2}gh^2\right) + \frac{\partial (huv)}{\partial y} = gh\frac{\partial H}{\partial x} + S_x$$

$$\frac{\partial (hv)}{\partial t} + \frac{\partial}{\partial y}\left(hv^2 + \frac{1}{2}gh^2\right) + \frac{\partial (huv)}{\partial x} = gh\frac{\partial H}{\partial y} + S_y$$

where h(**x**,t) is the thickness of water level at point **x** and time t, u(**x**,t) and v(**x**,t) are the depth-averaged velocities along x and y directions, respectively, and H(**x**) is the depth of the sea bottom at point **x** measured from a fixed level of reference. The terms S_x and S_y parametrize the friction effects and two different laws, the Manning law and a quadratic law are

considered. The SWE derived in Chapter 1 (Eq. 1.1.14) are the same equations without the consideration of these two laws. The Manning law is given by

$$S_x = -ghM_n^2 u_x \frac{\|u\|}{h^{4/3}}$$

$$S_y = -ghM_n^2 u_y \frac{\|u\|}{h^{4/3}}$$

where M_n is the Manning coefficient (M_n>0). A quadratic law is given by:

$$S_x = -c_f u_x \|u\|$$

$$S_y = -c_f u_y \|u\|$$

where c_f is the friction coefficient and c_f >0.

Due to the large number of scenario simulations (Table 3.4.1), high computational resources are required to perform tsunami modelling for each scenario. In this study, we used one fraction of the resources of the Project TSU-CAST (TSUnami-ForeCASTing), within PRACE Project Access Call 20 (https://prace-ri.eu/hpcaccess/project-access/project-access-awarded-projects/projects-awarded-under-praceproject-access-call-20/), which provided in total with 30 000 000 core hours on the MARCONI100 supercomputer hosted at CINECA, Italy. MARCONI100 has 4 Nvidia V100 GPUs per node. Individual scenario runs use a single GPU for each scenario, grouped in ensembles of up to 1024 scenarios on MARCONI100. However, before lunching massive number of scenarios, Tsunami-HySEA model is calibrated and validated according to preliminary simulations that are performed in the framework of ChEESE Deliverable D4.8 using some selected scenarios from Ye catalog.

Since computational resources are limited, one of the main difficulties is to reach enough accuracy while still modelling a sufficient number of scenarios within a reasonable time. Therefore, a proper setup should be set to balance accuracy and time (core hours that are necessary to conduct the entire numerical experiment). For this purpose, a convergence test is performed to investigate if relatively coarser data can converge to the finer reference resolution, that can be implemented as a bathymetry-topography data for the tsunami modelling. During this test, we have analyzed the accuracy of simulations using bathymetry-topography data with 2 arc-minute and 1 arc-minute resolutions, with respect to the (assumed as a) reference 30 arc-second resolution. 2 arc-minute and 1 arc-minute data are down-sampled from 30 arc-sec bathymetry model SRTM30+ (Becker et al., 2009). Table 3.4.1 shows the size of each bathymetry data in terms of number of column and rows and approximate run time.

Resolution	Number of Columns	Number of Rows	Run Time (min)
30 arc-sec	14400	7800	108
1 arc-min	7200	3900	14.7
2 arc-min	3600	1950	2.25

Table 3.4.1: *The number of cells and approximate run time for the different resolutions.*

In the test, two different earthquakes, the Maule-Chile (2010), Mw 8.8 event (the rupture length is about 460 km and width is about 174.6 km), and the Tocopilla, Chile (2007), Mw 7.8 event (the rupture length is about 118.8 km and width is about 73.15 km) are considered as a reference to build tsunami sources, to explore the effect of different wavelengths on the convergence. We have used two random synthetic stochastic slip distributions of the same magnitude and at about the same location of the real events, along with realistic scaling relations. The limits of the computational domain are set to (-45°, 20°) in latitude and (80°, 300°) in longitude and several synthetic gauge points are located in the study domain to

record tsunami wave heights at these points for two sources mentioned above (Figure 3.4.1). The propagation time is set to 40 hours on 1 arc-min bathymetric grid for the Pacific Ocean. During the simulations, tsunami wave height is saved each 30 seconds.

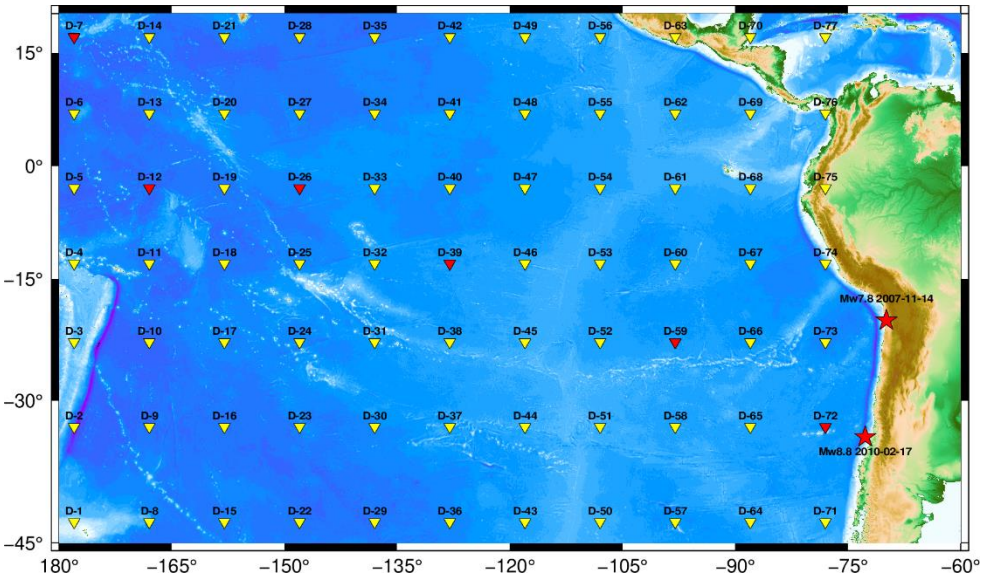

Figure 3.4. 1: *Study domain for the test, the location of synthetic gauge points (yellow and red triangles) and the epicenters of source events (red stars).*

Figure 3.4.2 represents the maximum tsunami wave amplitude of the tsunamis generated by the two sources. It is clear that the maximum wave amplitude is quite high for the event with the bigger magnitude, and that waves show a directivity towards the north-west direction with a higher amplitude.

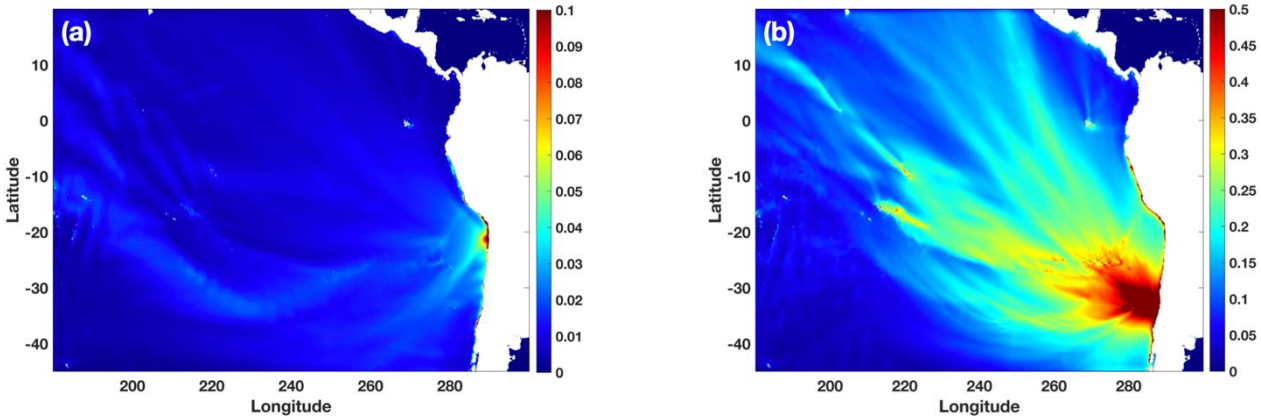

Figure 3.4.2: *Distribution of Max. Tsunami Wave Height (m) generated by synthetic earthquakes at the same location and with similar magnitude to the Tocopilla, Chile 2007 event (a) and Maule, Chile 2010 event (b).*

Figure 3.4.3 and Figure 3.4.4 (high resolution versions are in the appendix) show tsunami time series at synthetic stations D-72, D-59, D-39, D-26, D-12 and D-7, which are located at increasing distances from the source (red triangles in Figure 3.4.1), calculated using different data resolutions, for Tocopilla, 2007 and Maule, 2010 events. We see that the wave amplitudes change with the event and the distance from the source. It can be also observed that the initial part of the waveform has almost the same amplitude but the amplitude and shape change with time, which is more evident on the closest gauge point (D-72), for both events. The fluctuation of the time series is also similar for the 30 arc-sec and 1 arc-min (red and green lines) model while it can be quite different for the 2 arc-min (blue line).

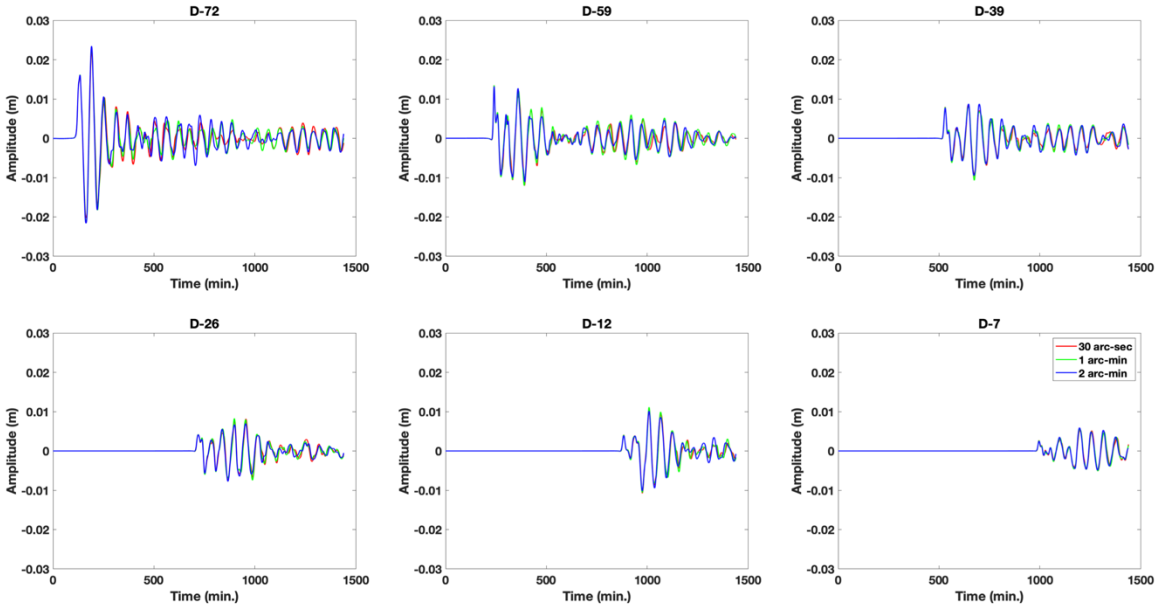

Figure 3.4.3: *Tsunami time-series at different synthetic gauge points for the Tocopilla, Chile 2007 event.*

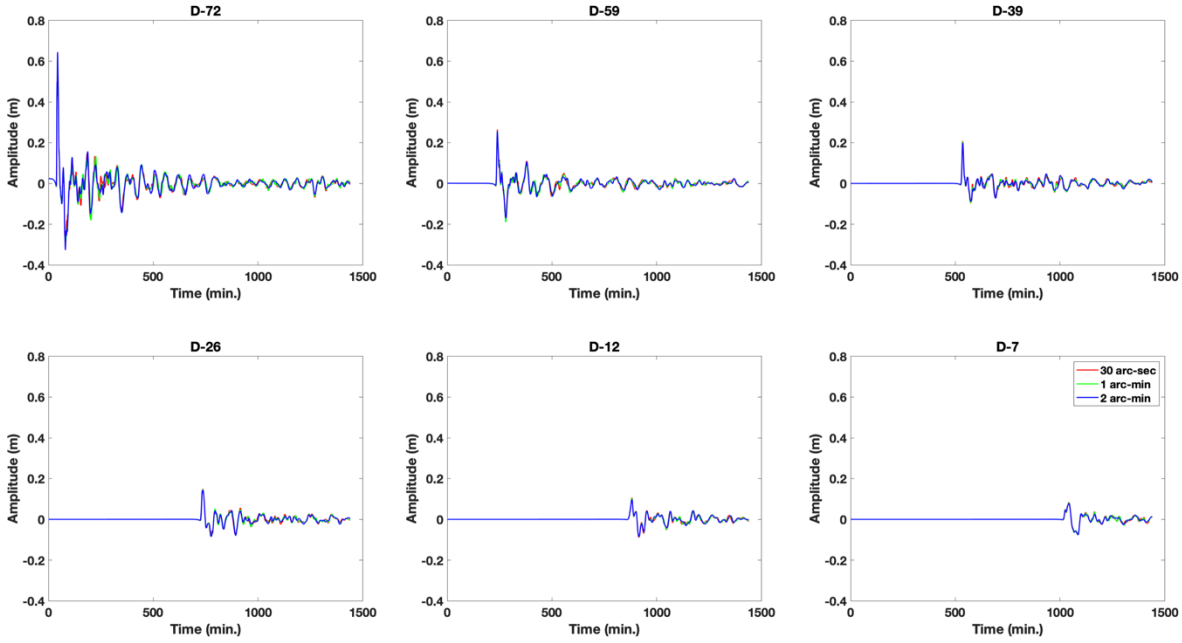

Figure 3.4.4: *Tsunami time-series at different synthetic gauge points for Maule, Chile, 2010 event.*

The modelling results are analyzed in terms of absolute maxima of tsunami wave height with both scatter plots and histograms by comparing one resolution to another. All modelling

results show that a sufficient convergence is achieved for 1 arc-min data when 30 arc-sec is considered as a reference. Figure 3.4.5 and Figure 3.4.6 show the distribution of the absolute maxima at each buoy for two resolutions and residuals of the absolute maximum differences, respectively, for both sources. For both events, the distributions are better aligned along the 1:1 straight line in the first quadrant for the distribution of 1 arc-min with respect to the 30 arc-sec, and the residuals are smaller than the other case. The mean difference of absolute maximum, between the 2 arc-min and 30 arc-sec, is 0.04% and the difference of the absolute maximum between 1 arc-min and 30 arc-sec is 0.03% for Tocopilla, Chile (2007) Mw 7.8 event. These differences are 0.6% and 0.3% for Maule, Chile (2010) Mw 8.8 event.

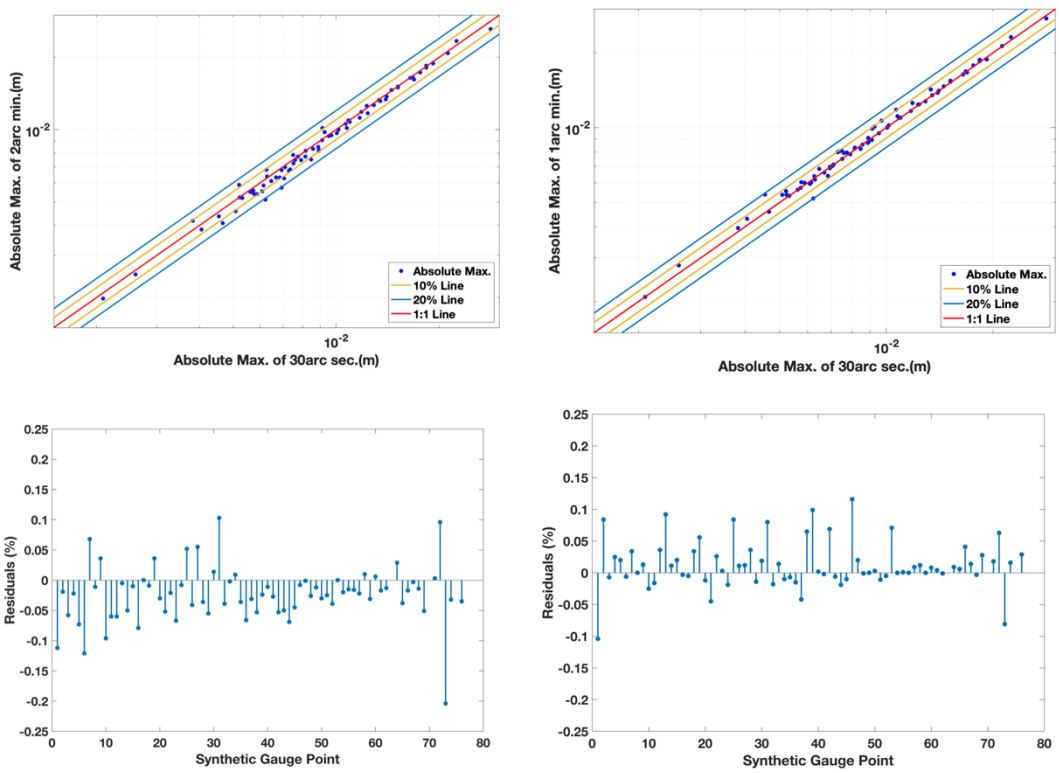

Figure 3.4.5: *Distribution of absolute maximum one resolution to another and residuals of the absolute maximum differences for the Tocopilla, Chile 2007 event.*

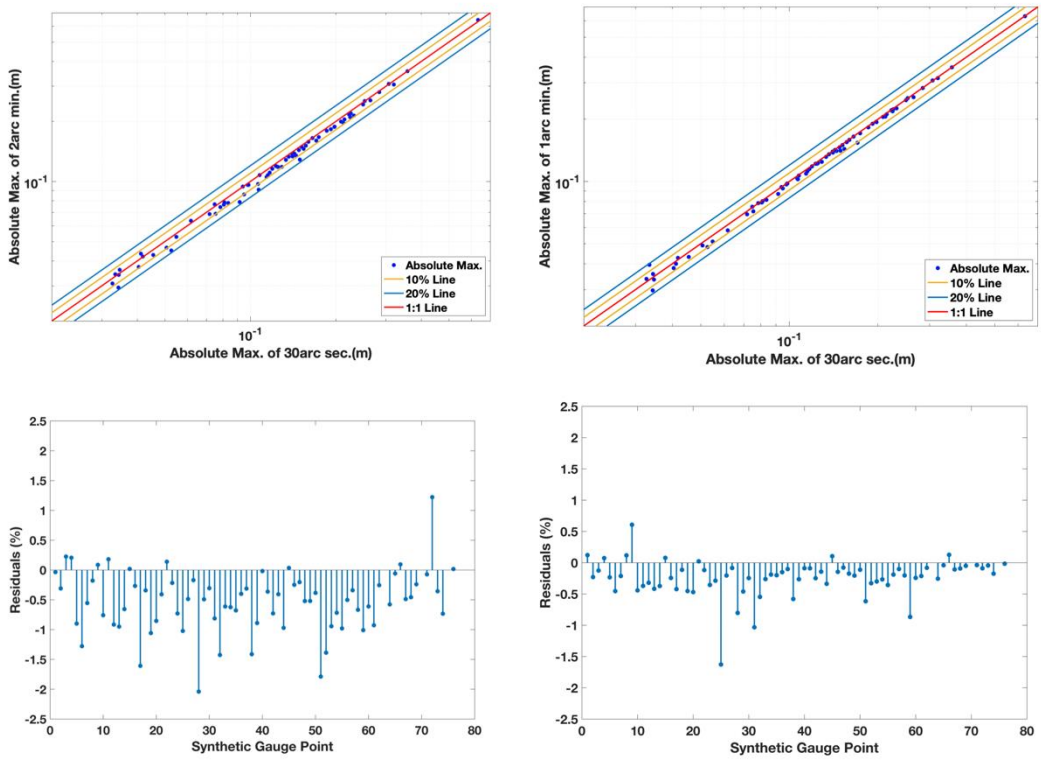

Figure 3.4. 6: *Distribution of absolute maximum one resolution to another and residuals of the absolute maximum differences for the Maule, Chile 2010 event.*

The histograms (Figure 3.4.7 and Figure 3.4.8) also support the result of scatter plots, showing that the mean of the ratio of maxima is closer to 1 for the ratio between the 1 arc-min and 30 arc-sec. The 43% of the data is enclosed inside the (0.975-1.025) interval for the ratio of absolute maximum 2 arc-min over the 30 arc-sec for the Tocopilla, Chile 2007 event, and this percentile increases to the 64% for the ratio of absolute maximum 1 arc-min over the 30 arc-sec. The difference of these percentiles is more relevant for the Maule, Chile 2010 event. While the 20.5% of the data is enclosed inside the same interval for the ratio of absolute maximum 2 arc-min over the 30 arc-sec and 61% for the ratio of absolute maximum 1 arc-min over the 30 arc-sec.

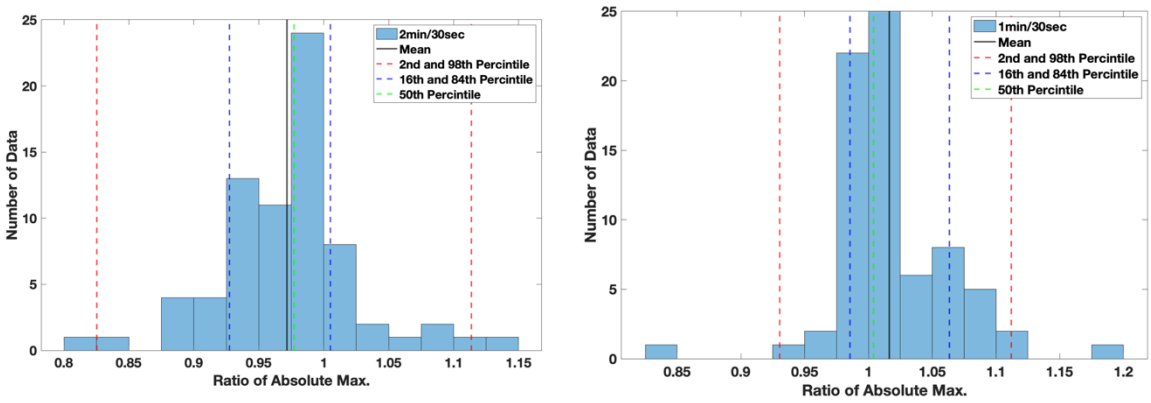

Figure 3.4. 7: *Histograms of the ratio of absolute maximum one resolution to another for the Tocopilla, Chile 2007 event.*

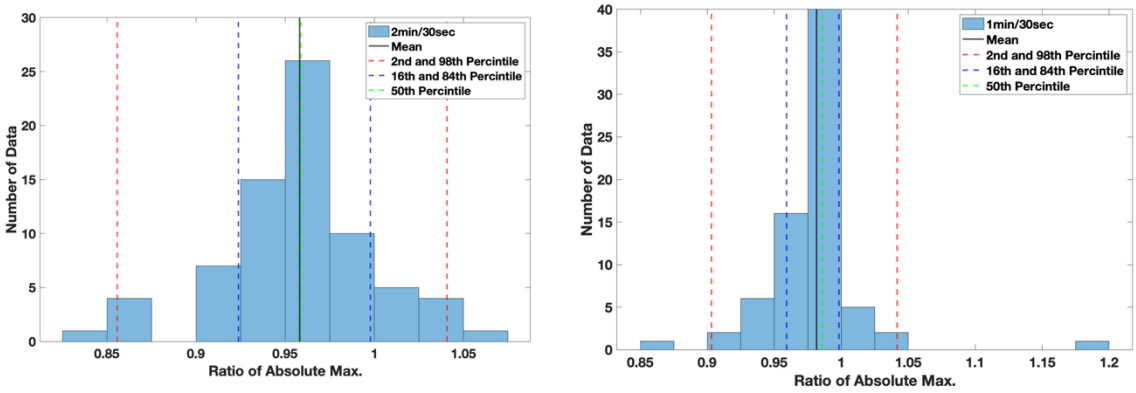

Figure 3.4. 8: *Histograms of the ratio of absolute maximum one resolution to another for the Maule, Chile 2010 event*

The result of the convergence test showed that 1 arc-min bathymetry-topography data are able to model tsunami with sufficient accuracy (generally less than 10%) and this choice will help to decrease run time for simulations.

3.5. Synthetic Waveforms

In the previous section, details of the tsunami numerical modelling have been presented. Here, we will discuss the general features of the synthetic waveforms using the Tohoku event as an example.

The limits of the study domain are set to (-60°,60°) in latitude and (80°,300°) in longitude (Figure 3.5.1). The propagation time is set to 40 hours for each simulation; however, time series have been cut within the limits of the high-frequency part of the de-tided DART signal. Figure 3.5.2 and 3.5.3 (high resolution versions are in the appendix) show the synthetic waveforms of a random scenario for the four model types and tsunami observations of 2011 Tohoku event at each DART buoy location. At some DART locations, there is a delay of the synthetic time series possibly due to unmodeled processes which includes the finite rupture duration, wave dispersion, elastic loading, and seawater compressibility (Baba et al. 2017). For some models, waveforms have a quite different behavior as compared to the observation. For instance, the Strasser model waveforms at DART-21414 and 21419 have a different shape, with two peaks, and smaller amplitude compared to observation. However, it should be considered that these synthetic waveforms are representing one model among the hundreds of scenarios in the ensemble. The maximum wave amplitude of the observations varies from about 2.0 m (DART-21418) to 0.04 m (DART-55023) moving away from the source.

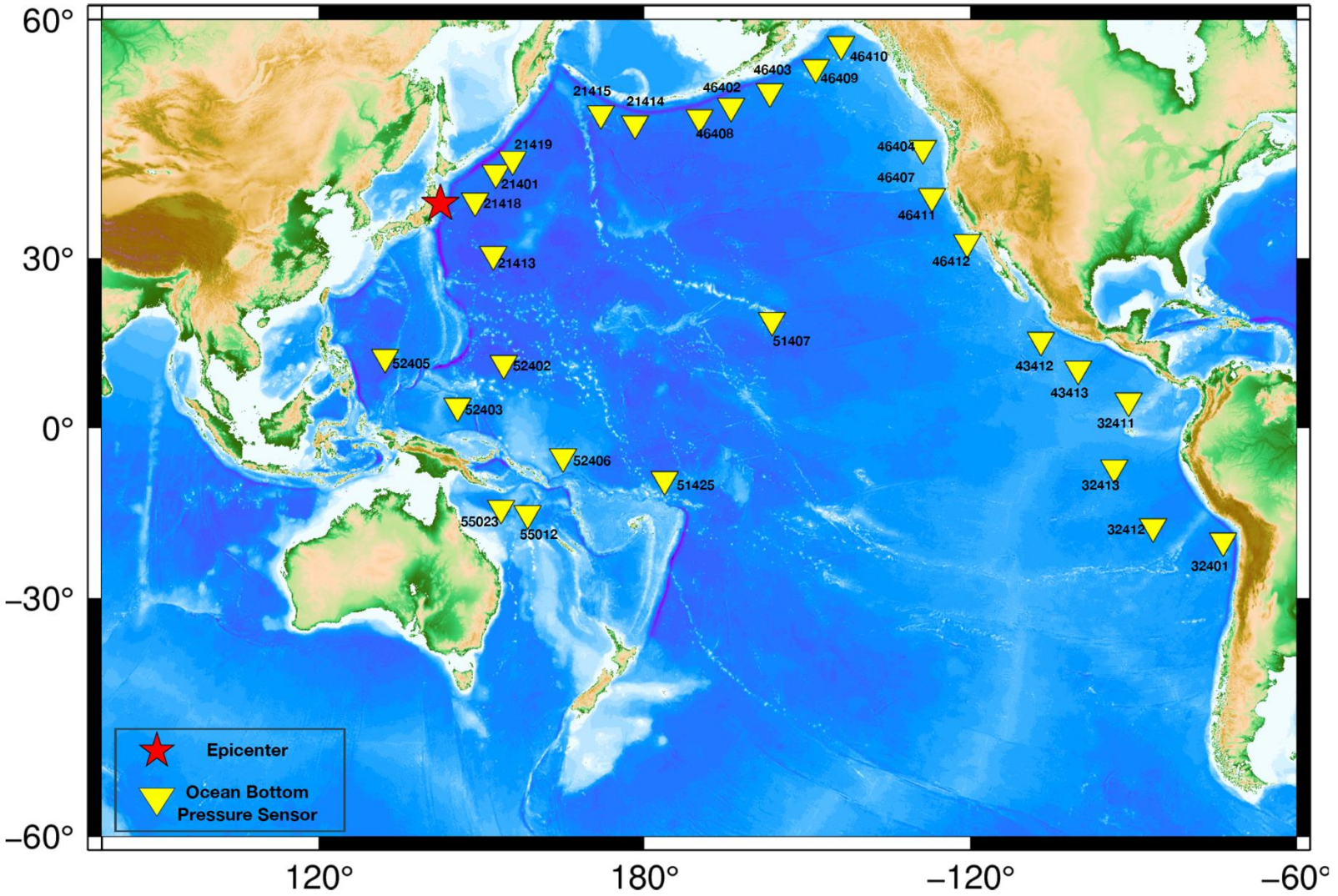

Figure 3.5. 1: *The location of 2011 Tohoku event and DART buoys where ensuing tsunamis are recorded.*

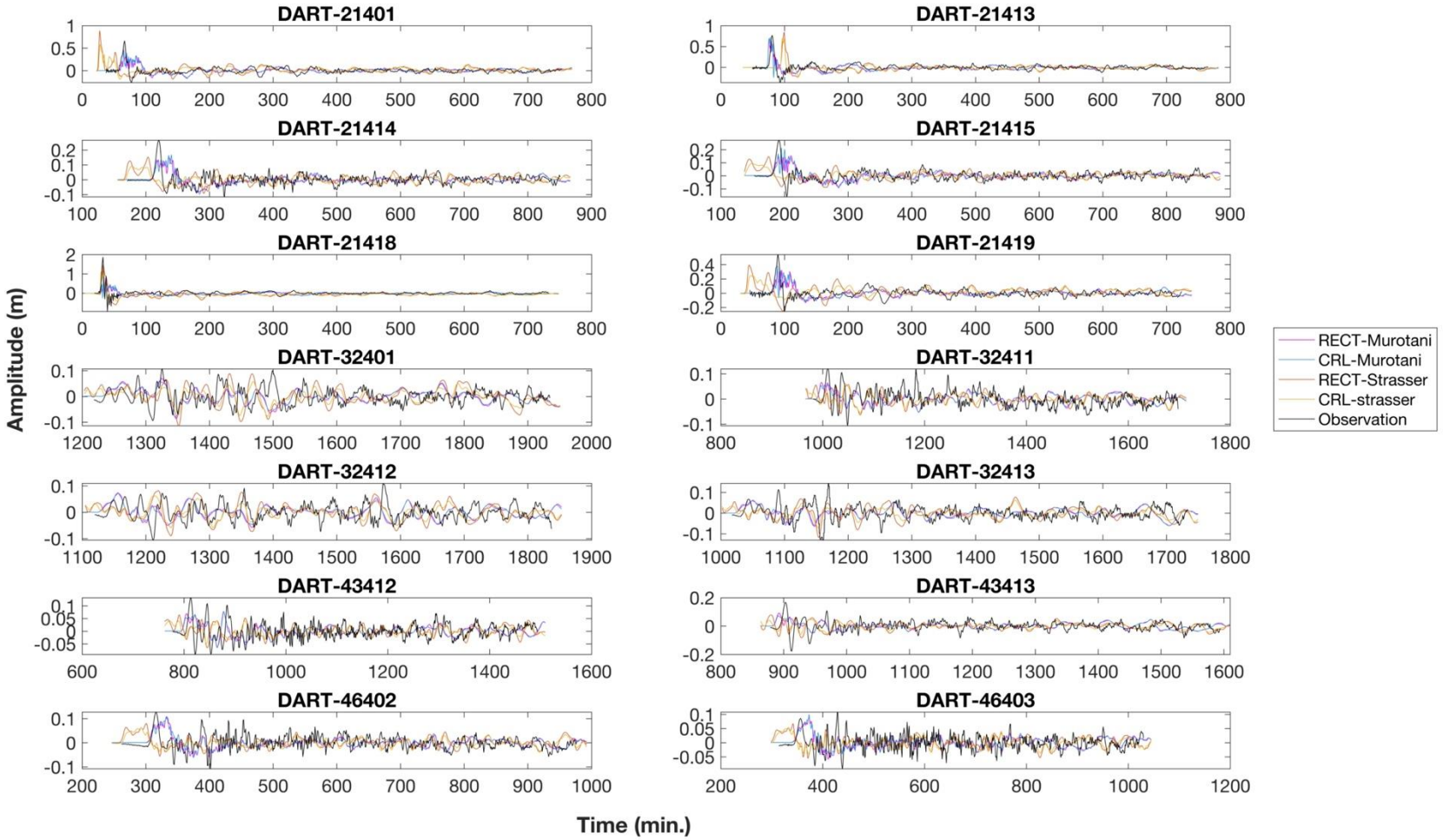

Figure 3.5. 2: *Synthetic tsunami waveforms of a random scenario from 2011 Tohoku event for different model types.*

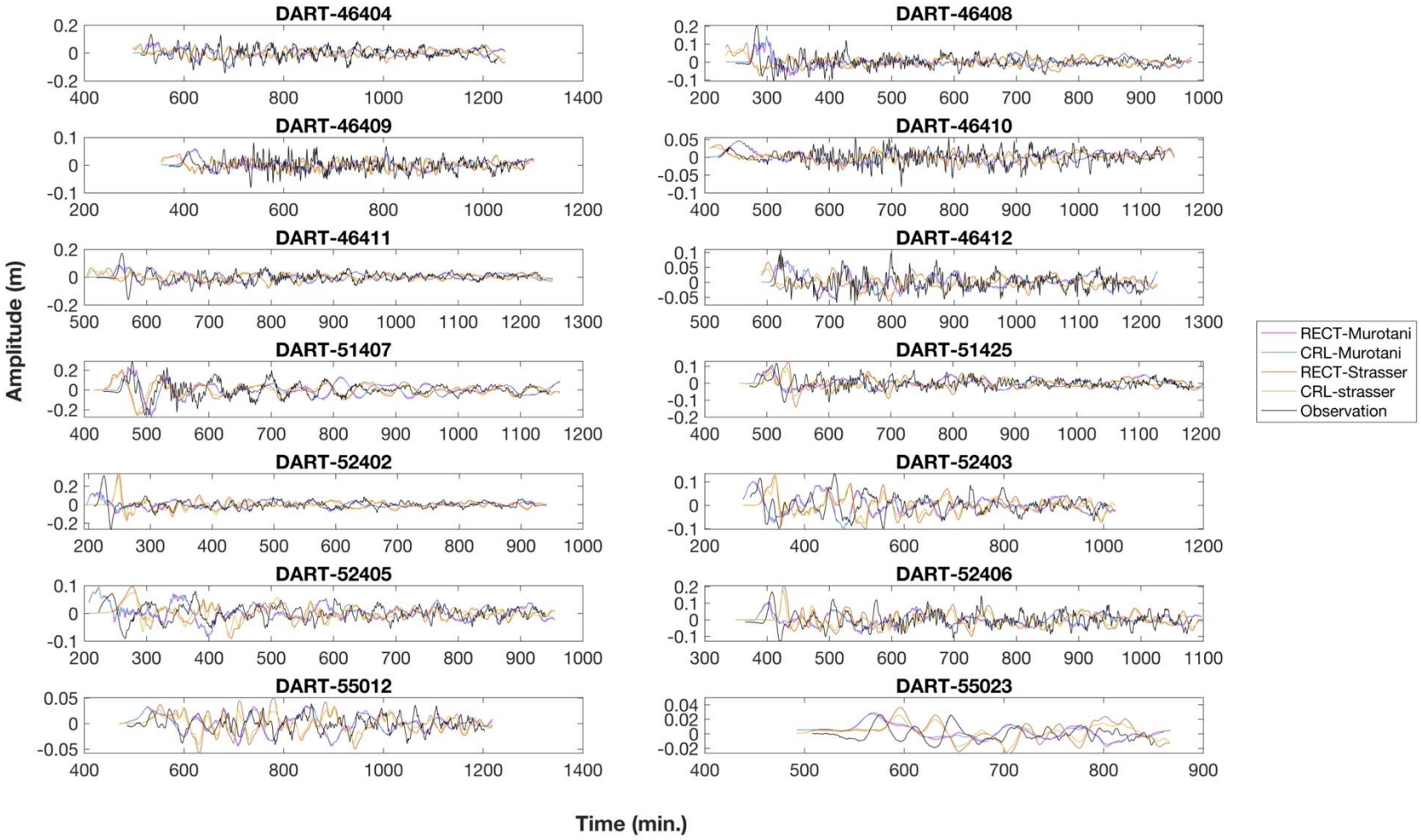

Figure 3.5. 3: *Synthetic tsunami waveforms of a random scenario from 2011 Tohoku event for different model types.*

3.6 Comparison of models in the ensemble with real waveforms

In the study of Davies (2019), different slip models are tested by comparing tsunami modelling results with tsunami observations. This study also proposes some statistics to make comparisons, to identify and partially correct biases of these scenarios, and provide better justification for their use in applications. One of these statistics is the scenario goodness-of-fit ($\mathrm{G_e^s}$). Here, we will discuss the goodness-of-fit of our ensemble, for depth-independent scenarios, in comparison with both kinematic slip models from Ye et al. (2016) catalog and Davies (2019) models.

For each scenario, a scenario goodness-of-fit statistic is defined to summarize agreement with DART buoy observations from event. This statistics can be defined with the following function

$$G_{e,d}^{s} = 1 - 2 * \left(\frac{\left(\sum_i w_i^2 * obs(t_i) * syn(t_i + \delta t_i) \right)}{\sum_i (w_i * obs(t_i))^2 + \sum_i (w_i * syn(t_i + \delta t_i))^2} \right) \qquad \text{(Eq.3.6.1)}$$

where *obs(t_i)* and *syn(t_i)* define the time-series of observations and synthetics, respectively. t_i is the time limited by the high-frequency part of the DART signal. δt is a small-time delay which may observed between the synthetic and observed record due to the delayed rupture process. The allowed time delay starts from 10 s and its end can vary as depending on the arrival time of the initial tsunami wave. When 1/50 of tsunami arrival time to the DART is smaller than 2 min, the maximum allowed delay is 2 min. If this value is higher than 15 min, the maximum delay is set to 15 min. If 1/50 of the arrival time of the tsunami to the DART is between 2 min

and 15 min, the maximum allowed delay is 1/50 of the arrival time (Watada et al. 2014). w_i is the weight which enables to focus on large amplitude wavelets. It is equal to the absolute value of *obs(t_i)*. However, when *obs(t_i)* is smaller than the one-third of the maximum value of the *obs(t_i)*, the weight is equal to one-third of the maximum value of the *obs(t_i)*. Both observed and modeled time series are interpolated to evaluate *obs(t_i)* and *syn(t_i)* at any time t_i. $G^S_{e,d}$ ranges between 0 and 2 with lower values indicating a better fit.

Since most events are recorded at multiple DART buoys, each scenario has its own goodness-of-fit ($G^S_{e,d}$) and some of these scenarios have a better agreement at some DART locations with the observations than the others. Therefore, scenario goodness-of-fit statistic G^S_e is defined to set up the overall fit of each scenario

$$G^S_e = median\left(G^S_{e,d}\right) \qquad \text{(Eq.3.6.2)}$$

Before starting to analyze the scenario goodness-of-fit statistics, the algorithm is built and benchmarked using the data considered by Davies (2019). At the first stage, a test is performed to see if the algorithm correctly calculates the goodness-of-fit with consideration of the time delay of the synthetic time series.

For the test, the following equation is used, since the aim is to test the correctness of the algorithm with time delay only, weights of scenarios are not included in the function at this stage

$$G^S_{e,d} = 1 - 2 * \left(\frac{\left(\sum_i obs(t_i) * syn(t_i + \delta_i)\right)}{\sum_i obs(t_i)^2 + \sum_i syn(t_i + \delta_i)^2}\right) \qquad \text{(Eq.3.6.3)}$$

The idea is to test the calculation considering one single synthetic tsunami time series and using its 10 min delayed version as the observed time series. The time offset (δ_i) is considered for each minute from 2 to 15 min. Since the goodness-of-fit changes from 0 to 2 and smaller values mean a better fit, we expect to see smaller goodness-of-fit values while approaching the 10 min delay and it should be 0 at 10 min delay where the synthetic and observed times series are the same. Then, the goodness-of-fit should increase again when the time delay moves toward 15 min.

The right panel of Figure 3.6.1 shows the distribution of goodness-of-fit for each time delay. It is observed that the goodness-of-fit improves going from time delays 2 min to 10 min and it is zero at 10 min. Also, the goodness-of-fit starts to increase after 10 min delay, as expected.

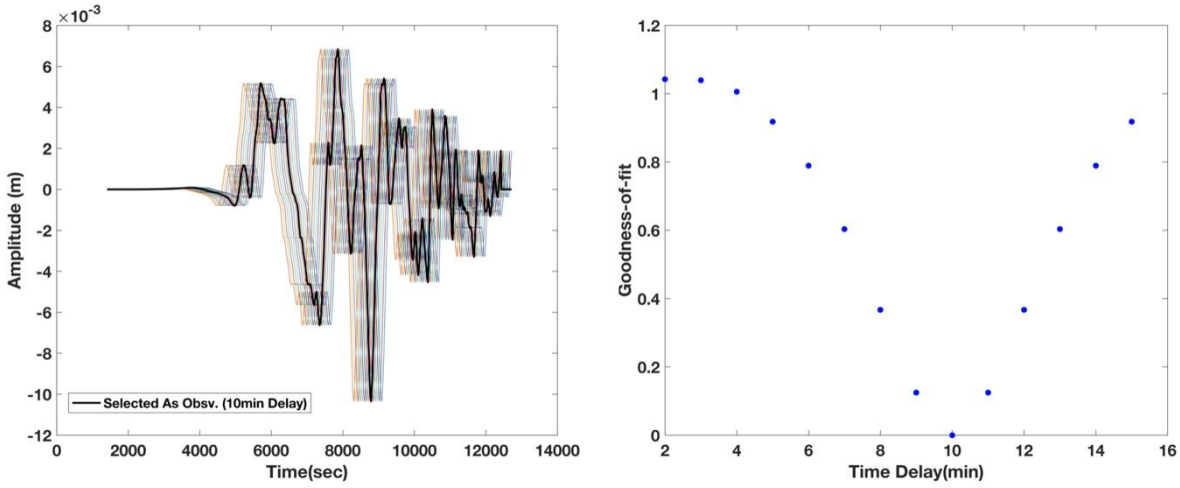

Figure 3.6.1: *Time series of synthetic data for each time delay (left-side). Distribution of goodness-of-fit for each step of time delay (right-side).*

As a further test for the algorithm, scenario weights are considered for the calculation of goodness-of-fit (Eq.3.6.1). The weight allows focusing on large amplitude waveforms and it is

equal to $max(abs(obs/3))$, if $abs\big(obs(t_i)\big) < max(abs(obs/3))$, otherwise it is equal to $abs\big(obs(t_i)\big)$.

The goodness-of-fit value is calculated for each scenario at each DART buoy using Eq.3.6.1 for Mw 8.8 Maule event to show the improvement of the fit including the weight in the calculation. The next figure (Figure 3.6.2) shows the distribution of the best goodness-of-fit at each DART buoy with and without consideration of the weights in the equation. It is observed that the goodness-of-fit improves when the weights of the scenarios are included in the equation.

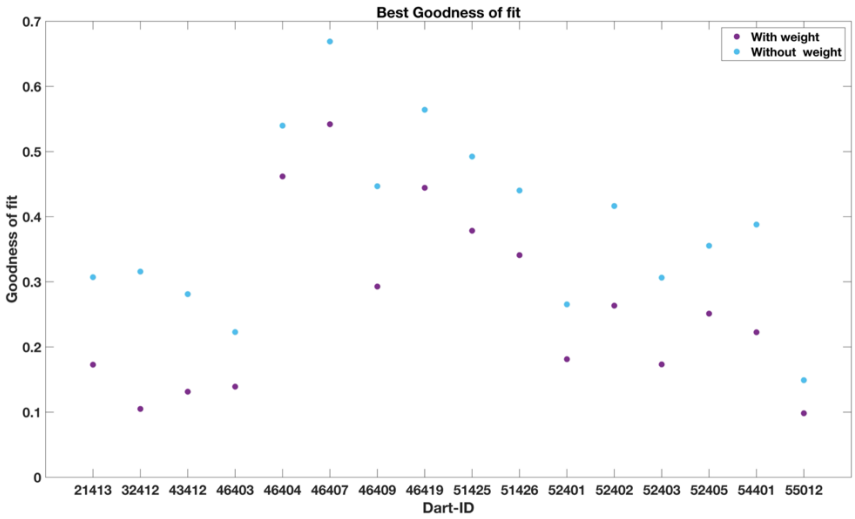

Figure 3.6.2: *Time series of synthetic data for each time delay (left-side). Distribution of goodness-of-fit for each step of time delay (right-side).*

After validating the computation of the goodness-of-fit procedure with these tests, applied it to compute the "best scenario goodness-of-fit" using the scenario time series of Davies (2019).

During the calculation of best scenario goodness-of-fit statistics, some scenarios have been eliminated according to their peak slip value. If the maximum slip of the scenario exceeds

7.5 times the mean slip of the event according to the magnitude and a median scaling-relation area, this scenario should be eliminated (Goda et al. 2014).

During this stage, expected average slip is calculated using following formulas for depth-independent scenarios,

$$M_o = 10^{(1.5*M_w)+9.05}$$

$$\hat{S} = \frac{M_o}{\mu * A_s}$$

where μ is rigidity (we used μ =30 GPa, $\hat{S}$ is the average slip and A_s is the area as obtained from the scaling relations as a function of the magnitude).

For scenarios where rigidity varies with depth, average slip is calculated by considering cells with non-zero slip value using following formulas,

$$M_o = \sum_{i=1}^{N_c} \mu_i(S>0) * S_i(S>0) * A_i(S>0)$$

$$\hat{\mu} = \frac{\sum_{i=1}^{N_c} \mu_i(S>0) * A_i(S>0)}{\sum_{i=1}^{N_c} A_i(S>0)}$$

$$\hat{S} = \frac{M_o}{\hat{\mu} * A_s}$$

where N_c is the number of ruptured cells (where slip is non-zero), μ_i is the rigidity, S_i is the slip, A_i is the area on the i-th cell and $\hat{\mu}$ is the mean rigidity. After the calculation of expected average slip for each scenario, this value is compared with the peak slip value and ruled out if the maximum slip is at least 7.5 times higher than the average slip.

3.6.1. Comparison with kinematic slip models

Figure 3.6.1.1 shows the best scenario goodness-of-fit values for our model ensembles and kinematic slip models. From now on, we will simplify the names of the models and we indicate the kinds of models as RECT-Murotani, RECT-Strasser, CIRL-Murotani and CIRL-Strasser, according to the rupture shape and scaling laws we have used to generate them: RECT stands for rectangular and CIRL for Circular. Panel (a) in the Figure 3.6.1.1 shows that scenarios following the Strasser scaling law tend to have a better fit, while Murotani models show best-fitting more rarely. It can be seen that events in South America show relatively better agreement than the others, possibly due to the larger accuracy in the description of the slab geometry, which is extracted from teleseismic tomography (Scire et al., 2017; Hayes et al., 2018). The events with largest goodness-of-fit values, such as 2009 Samoa (KT2) and the 2006 Kuril (KJ1) events, show relatively short-period tsunami waveforms, which make these events more difficult to model (Kowalik et al. 2008; Zhou et al. 2012; Hossen et al. 2018).

Panel (b) in Figure 3.6.1.1 shows the scenario goodness-of-fit values of events from Ye et al. (2016) catalog. Since there is only one scenario for each event, best scenario defines the scenario with best time delay. Best-fitting value varies between 0.90-1.05 for kinematic models. When we compare our model results with kinematic models, it can be argued that our modelling results show much better agreement with observations than the kinematic models, even if they are random sources which weren't specifically calibrated using tsunami observations. The main reason of these differences could be associated with the simplified Earth models, band-limited signals, kinematic constraints imposed on the rupture process, and limitations of the observation geometry, in the teleseismic inversion method (Lay, 2018).

Since tsunami waves and tsunami hazard are highly sensitive to the uncertainty of the slip and fault geometry (Goda et al., 2014), simplified source models may cause under-estimation of the possible tsunami affects (Tonini, et al., 2020).

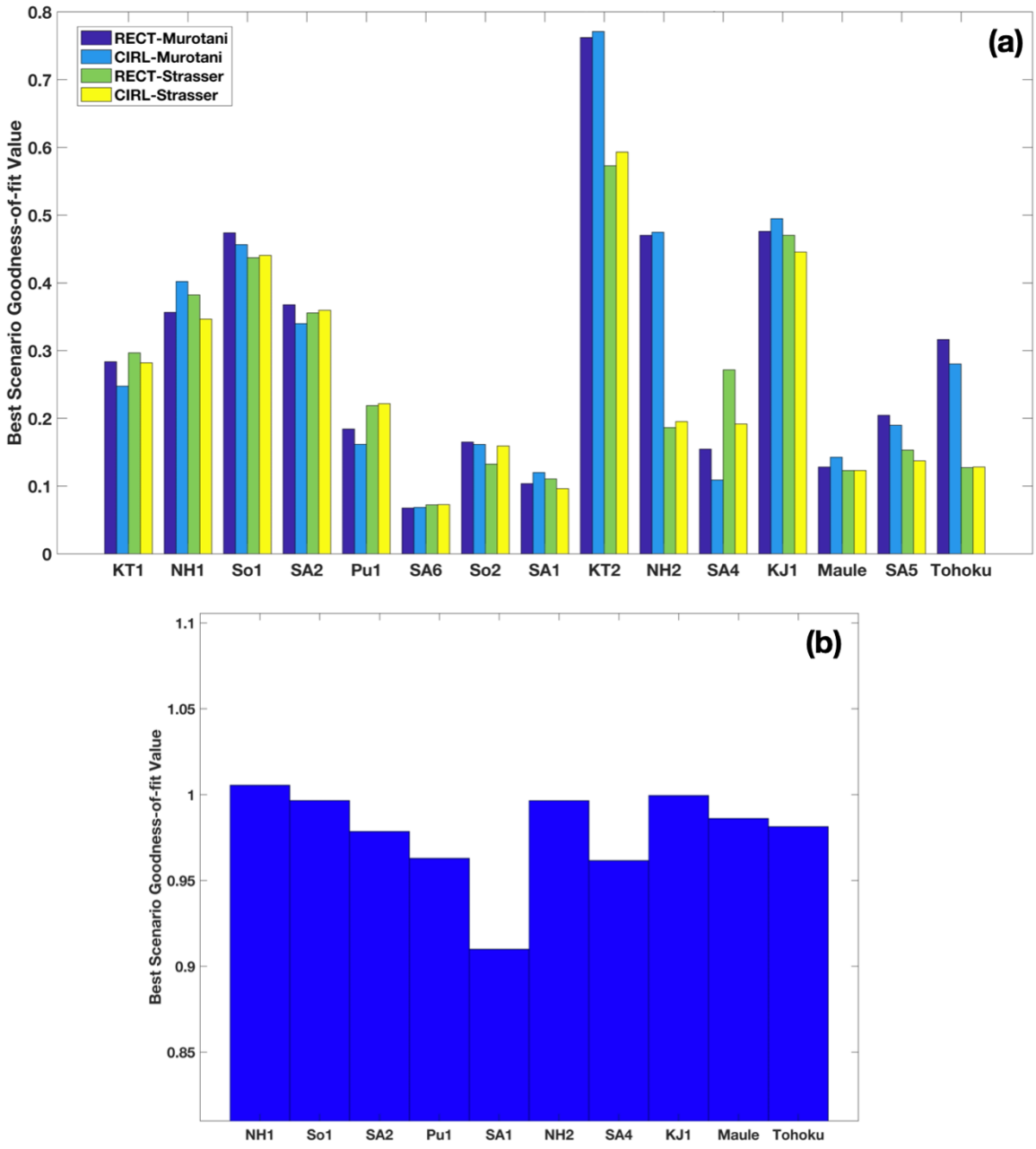

Figure 3.6.1. 1: *Best scenario goodness-of-fit statistics for each event scenario (a) generated in this study (b) extracted from Ye et al. (2016) kinematic model catalog.*

3.6.2. Comparison with Davies (2019) models

The second comparison of the ensemble is done with Davies (2019) models. Although, model scenarios are generated with magnitude and location similar to the real events in the same way as in Davies (2019), there are several different assumptions to generate heterogeneous slip models in this study. First of all, the size of the source mesh in this study is almost one-fourth finer than the one used in the Davies (2019). Besides that, we have made diverse physical assumptions on the fault rupture, considering circular ruptures and including Murotani et al. (2013) scaling law. Moreover, we have used a different magnitude discretization and depth-dependent scenarios are generated considering also the coupling.

The results from these two approaches are compared in terms of ratio of the summation of the best scenario goodness-of-fit. For each kind of model, we have calculated the summation of best scenario goodness-of-fit values (Eq. 3.6.2.1) to eliminate event dependency, and then we have calculated the ratio of those summations (Eq. 3.6.2.2). If the ratio is smaller than 1, this means the best fitting of our model is better than the Davies (2019) model.

$$S = \sum_{i=1}^{n} \min(SGOF)_i \qquad \text{(Eq.3.6.2.1)}$$

$$R = \frac{S_B}{S_D} \qquad \text{(Eq.3.6.2.2)}$$

where n is total number of events, SGOF defines the scenario goodness-of-fit, S_B and S_D are the summations of best scenario goodness-of-fits for our model ensemble and Davies (2019), respectively.

Figure 3.6.2.1 shows the ratio of best SGOF of each model from our ensemble with the HS, FAUS and VAUS models from Davies (2019). According to these results, it can be argued that all of the models from ensemble have better agreement than the FAUS model of the Davies (2019). Considering best-fit models, Strasser models from the ensemble can be individuated as the model that always have better fit than the all Davies (2019) models. However, the performance of Murotani models is close to one and not distant from the ones of the Strasser model, in terms of best-fitting.

Since the number of models considered in the Davies (2019) ensemble (232.000) is much larger than the models in this study (79.620), which may cause low accuracy of models regarding to observed event, we can conclude that, looking to the representation of the observation, in the sense of the best-fitting, we almost get the same results as obtained by Davies (2019), irrespective of the specific models, with a larger preference for the Strasser et al. (2010) scaling laws.

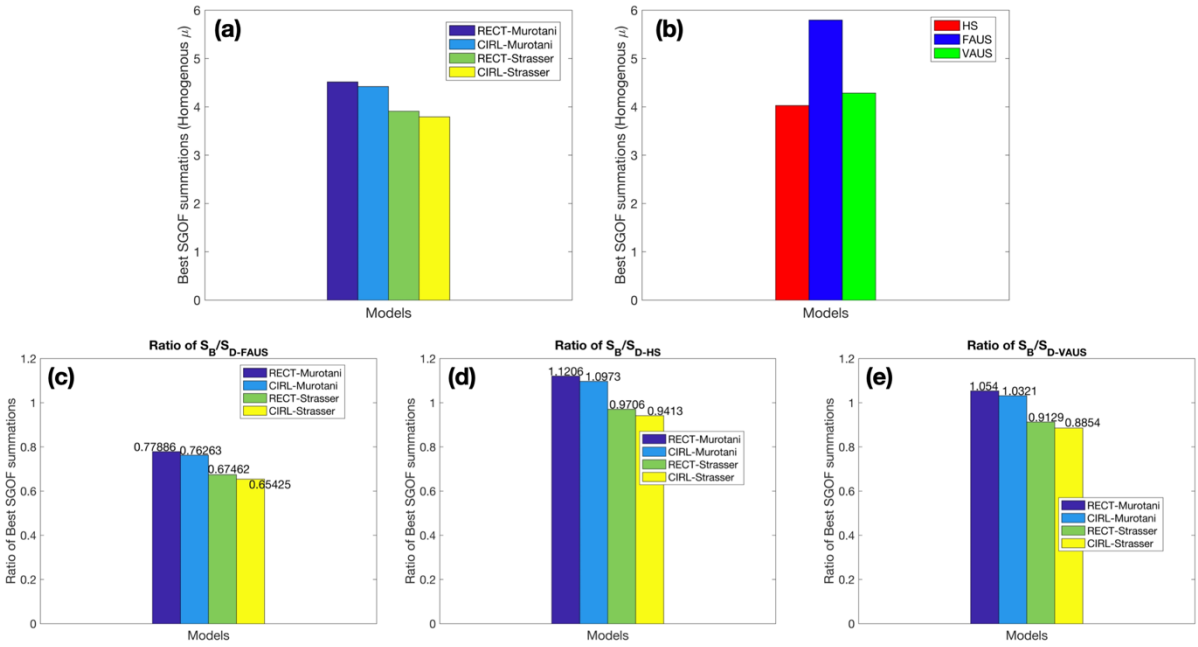

Figure 3.6.2. 1: *Summation of best SGOF for our model ensemble (a) and Davies (2019) (b), the ratio of best SGOF for each model of our ensemble with FAUS (c), HS (d) and VAUS (e) model of Davies (2019).*

3.7 Coverage Statistics ($F^{m}_{e,d}$)

While the comparison between our ensemble and Davies's one show similar best-fitting with real observations, despite the smaller number of models in our case, we are now checking the quality of the whole ensemble as representative of the 15 events selected for modelling. For this comparison, we selected as a parameter the coverage statistics. This statistics defines how big the observed tsunami at a DART is compared to synthetic scenarios. Each scenario is compared with the de-tided stage-range of observed tsunami time series during the associated event, where the tsunami stage-range is the difference between the maximum and minimum water-level of the time series. $F^{m}_{e,d}$ is the fraction of scenarios, which has a stage-range value smaller than the observed stage range at a specific DART point. Values near 1 indicate that the observation is relatively large and that all the scenarios underestimate the observation at that buoy, values near zero indicate that the observation is relatively small and that all the scenarios overestimate the observation. Finally, values close to 0.5 indicate that the observation is mid-sized with respect to the scenarios.

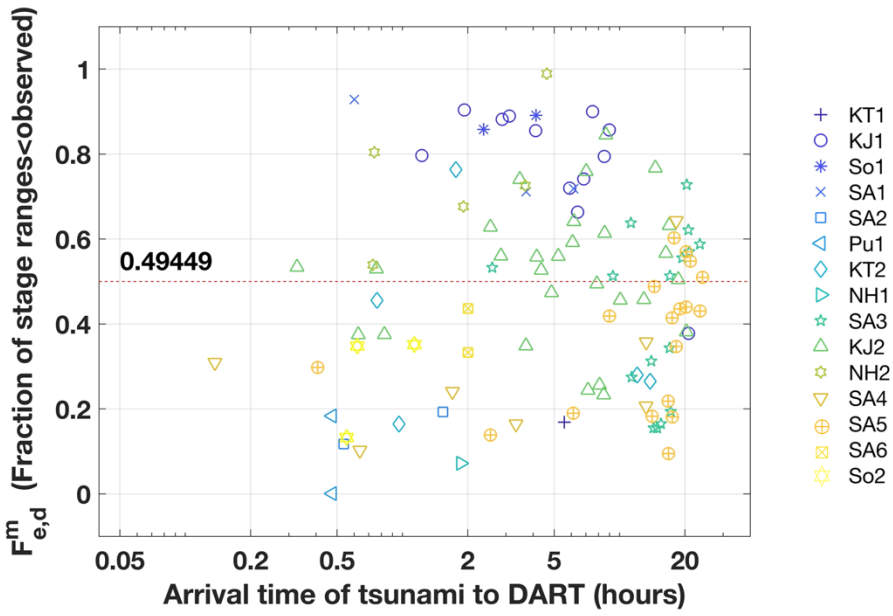

Figure 3.7.1: *Distribution of* $\boldsymbol{F^m_{e,d}}$ *with respect to the tsunami arrival time to DART, each color and shape represent different events.*

Figure 3.7.1 shows the distribution of the $F^m_{e,d}$ putting together all classes. It can be seen that, $F^m_{e,d}$ is uniformly distributed with 0.49 mean value. Coverage statistics should be distributed uniformly if there is not any intra-event dependency. In other words, for the same event $F^m_{e,d}$ might preference towards higher or smaller values due to the spatial relationships among the DART buoy locations and depending on the earthquake depth, magnitude, slip distribution and etc., some earthquakes can generate more efficient tsunamis which can be recorded at several DART locations. If the $F^m_{e,d}$ distribution shows high values, that means the model is biased and there is an under-estimation of the variability of observed tsunami size. Conversely, if the distribution shows a preference for too few $F^m_{e,d}$, the model overestimates the variability of observed tsunami size.

To account for intra-event dependency, the $F^m_{e,d}$ is collapsed to a single median coverage statistics parameter, F^m_e, which is given by

$$F_e^m = median\left(F_{e,d}^m\right) \quad \text{(Eq.3.7.1)}$$

The sampling distribution of F_e^m should be uniformly distributed and symmetric around 0.5 for an ideal model. However, although F_e^m is uniform, there will be a dependency on the number of DART buoys and their relative intra-event stage-range. We can estimate a parent distribution directly from the scenarios, by defining the statistics F_s^m. This is calculated again using the Eq. 3.7.1, but real observations are replaced one by one by the single scenario. In other words, each scenario is considered as an observation at each DART location; then, we compute the fraction of each scenario which have stage-range less than the selected scenario ($F_{s,d}^m$). Finally, the median (F_s^m) of these fractions is calculated.

In conclusion, we compute the distribution of R_e^m , calculated by considering the fraction of scenarios with $F_s^m < F_e^m$. Since F_s^m is calculated among the scenarios, it does not have any DART dependency, consequently R_e^m will be DART independent. The R_e^m should be uniformly distributed under the null hypothesis that *m* is an ideal model and we may test this hypothesis using the Anderson–Darling test (Marsaglia & Marsaglia 2004). This test should verify that the p value of the distribution is lower than the selected threshold, which is generally taken as 0.05. In addition to Anderson–Darling test, the standard deviation of the 15 R_e^m values, one for each event, can be compared with the expected standard deviation of a uniform distribution with 15 samples of size. The 95 percent interval of the expected standard deviation from a sample of size 15 is calculated as 0.21-0.35, using the standard deviations of the 10 million random datasets.

Figure 3.7.2 shows the distribution of R_e^m values. The Anderson-Darling test show that the p value of the distribution of R_e^m is 0.51, and the standard deviation is 0.28, which is within

the 95 percent of random uniform samples. The uniformity of $F_{e,d}^{m}$ distribution and the tests on R_e^m indicate that the model ensemble is unbiased.

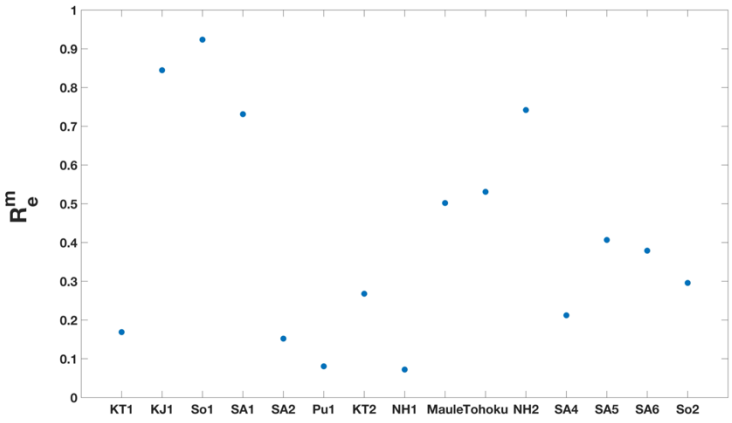

Figure 3.7.2: *Distribution of* $\boldsymbol{R_e^m}$ *values.*

Let us look now to the fraction distribution of each class separately. Figure 3.7.3 shows the distribution of $F_{e,d}^{m}$ for each model class, RECT-Murotani, CIRL-Murotani, RECT-Strasser and CIRL-Strasser. We can see that there are biases in singles classes: Murotani models underestimate the variability of observed tsunami size with higher values, Strasser models show preference to lower values. These models generate larger tsunamis and overestimate the variability of observed tsunami size. The Anderson-Darling test also confirms such biases with very small p values, indicating that the null-hypothesis of uniform $F_{e,d}^{m}$ is rejected. These values come from events having F_e^m zero or one (usually with small number of DART buoys).

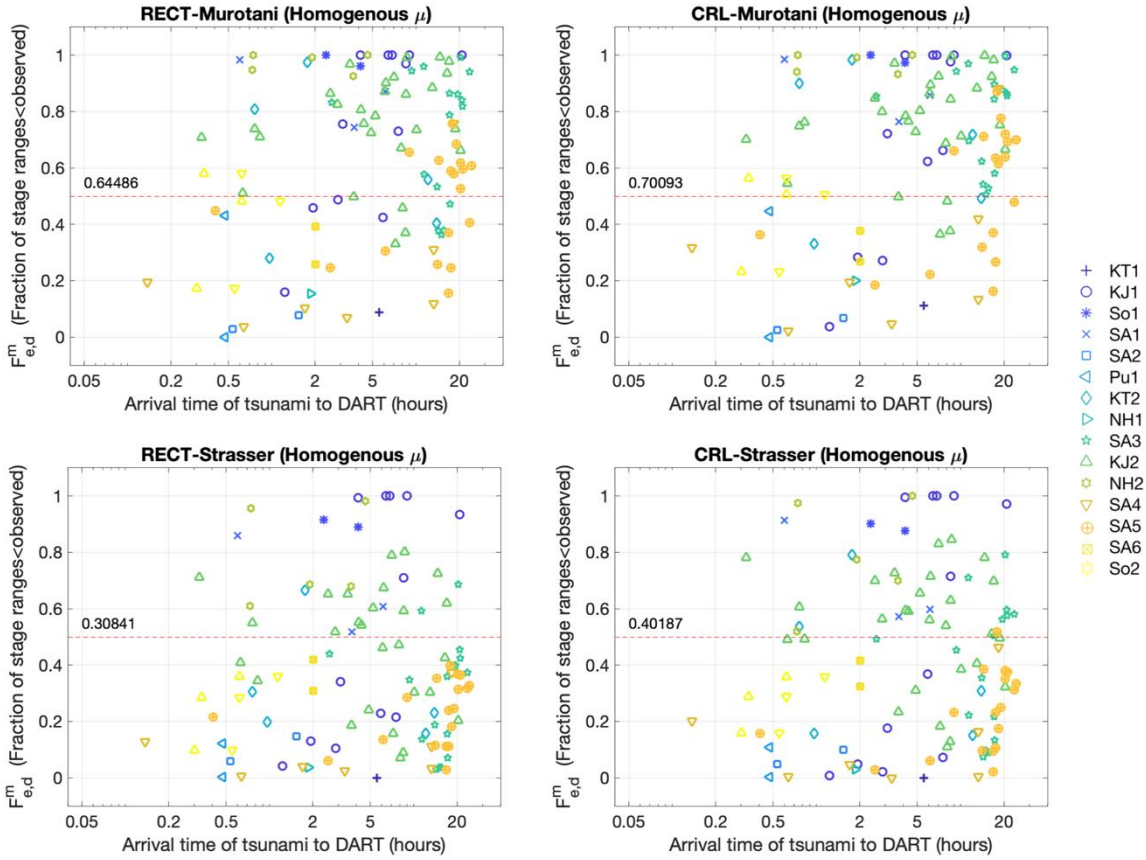

Figure 3.7.3: *Distribution of* $F^{m}_{e,d}$ *with respect to the tsunami arrival time to DART for each model class, each color and shape represent different event.*

Another indicator of unbiased modes is the uniform distribution of the median coverage statistics with respect to magnitude. Figure 3.7.4 shows this distribution for each of 4 models and for each event. Although there is not direct relation between the median-coverage statistics and magnitude, Strasser models overestimate the observation as observed in the previous figure (Figure 3.7.3), with several values below 0.5. However, median-coverage-statistic of Murotani models are almost uniformly distributed. The number of events that have median-coverage-statistics above 0.5 is 7 for CIRL-Murotani model and 8 for the RECT-Murotani models for overall 15 events.

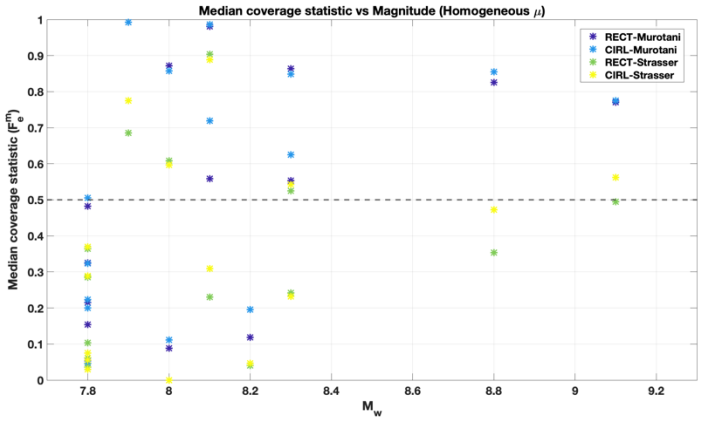

Figure 3.7.4: *Distribution of* $\boldsymbol{F_e^m}$ *with respect to the magnitude. Each color represents different model.*

3.8 Characteristics of the ensemble models

Comparison of the statistical properties of random model scenarios with good fitting scenarios can be used to better understand the dynamics of the model bias (Davies, 2019). If the model is biased but still be able to generate some scenarios which agree with observations reasonably, the earthquake properties of good fitting scenarios should behave different than the properties of random scenarios over the 15 test events.

Figure 3.8.1. shows the distribution of maximum slip and rupture area with respect to magnitude. Good fitting scenarios are defined as the best 3 scenarios that have minimum scenario goodness-of-fit value and these scenarios are plotted with red dots. Overall the 4 models, good fitting scenarios are generally distributed within the 80 percent confidence boundaries. There is not any tendency of good fitting scenarios toward the lower or upper limits but they show similar variability as random scenarios. Therefore, we can say that although our single models are biased, they generate reasonable maximum slip and rupture area.

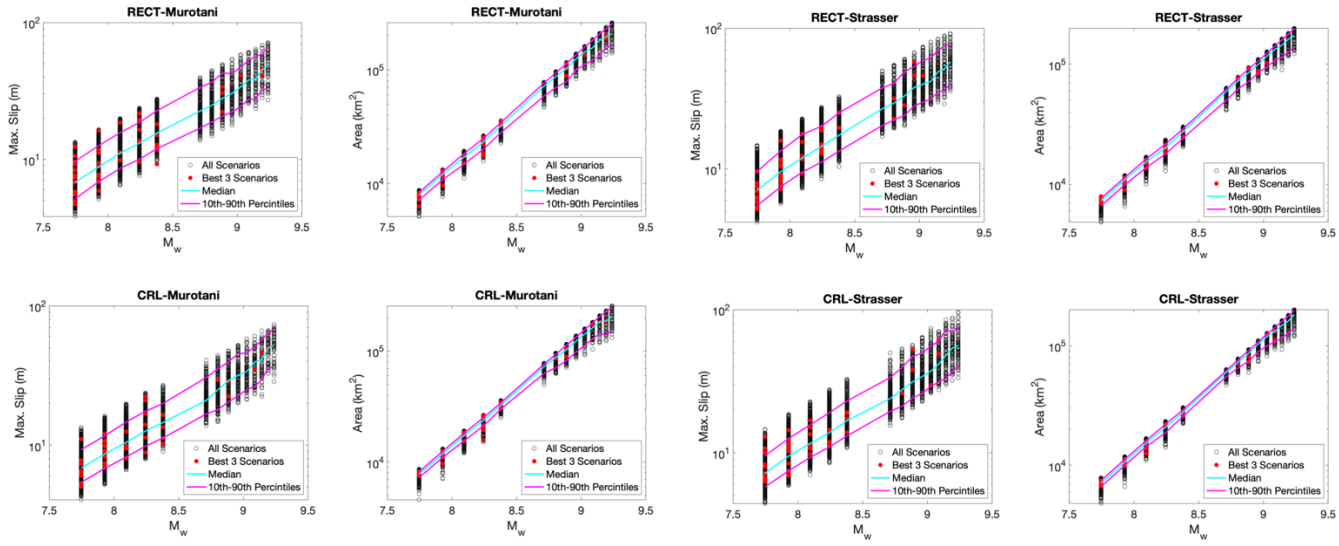

Figure 3.8.1: *Mw versus Maximum slip and rupture area for each model. Best 3 scenarios are showed with red dots.*

The model biases can be adjusted by assigning non-uniform weights to scenarios (Davies, 2019). These scenario weights can be calculated using quantile matching techniques which includes quantile matching of the percentiles of maximum-slip for the good fitting scenario scenarios with a uniform distribution. Figure 3.8.2 shows Quantile-Quantile plots (QQ-plots) for each model to compare percentiles of maximum slip for the three best fitting scenarios, which are calculated event by event, with uniformly distributed percentiles of random events. If the model is unbiased, the best fitting scenario percentiles should be uniformly distributed, maximum slip of best fitting scenario should not have any tendency toward to lower or higher values. Therefore, the data and fitted line should be around the 1:1 line.

Let us consider RECT-Murotani model as an example of non-uniform weighting of scenarios. QQ-plot indicates that, 60% of the 'best scenario' have maximum slip below the 50% percentile, while the rest of the data is distributed around the 1:1 line. Therefore, bias

adjustment should be done putting 60% of the weight on scenarios with maximum slip below the 50th percentiles for this model.

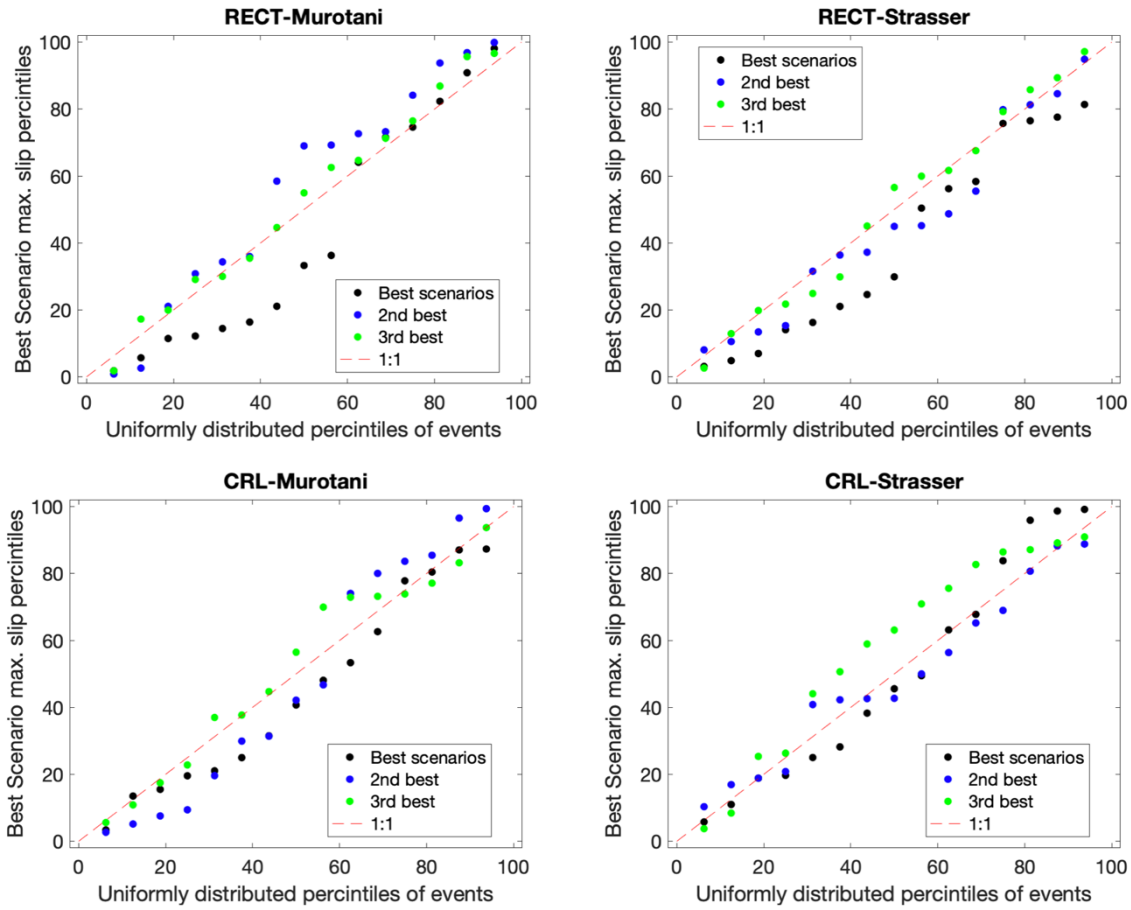

Figure 3.8.2: *QQ-plots for the average percentile of maximum slip for the best three scenarios against the uniformly distributed percentiles of each of the 15 events.*

3.9 Variable mu models

Models scenarios are generated for both depth-independent and depth-dependent rigidity profiles since observation of events in megathrust environment reveals that some rupture characteristics of these events, such as slip and frequency radiation, are related to the depth-dependent frictional properties of the slab interface (Wang and Mori, 2011; Bilek and Lay 2002; Lay et al., 2012; Yao et al., 2013). The tendency of shallow subduction events to have longer duration can be explained with the variation of rigidity or stress drop with depth (Bilek and Lay 1999; Geist and Bilek 2001). Details of the generation of depth-dependent models with rigidity profiles are already explained in the previous sections. Here, we would like to show the results of these models in terms of the same statistical parameters, described in the analysis of the depth-independent case.

Figure 3.9.1 shows the best SGOF values for each event depth-dependent scenario model. The results of best SGOF are similar to the ones obtained with the depth-independent rigidity assumption except for few cases, such as NH1 and Pu1 events, where the fit is poorer.

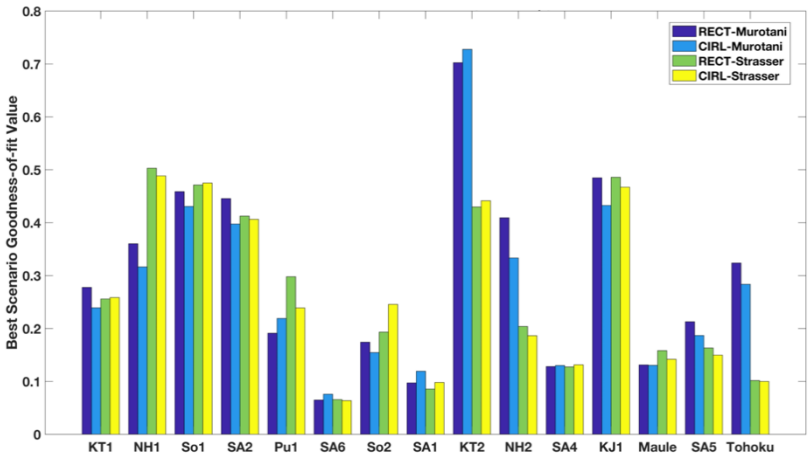

Figure 3.9.1: *Best scenario goodness-of-fit statistics for each event depth- dependent scenario model.*

The comparison of each model with the depth-varying-rigidity models of Davies (2019) indicates that all of the models from ensemble have better agreement than the FAUS model of Davies (2019), as observed in depth-independent models (Figure 3.9.2). However, the performance of Strasser models is poorer as compared to the HS models, while they still have better agreement than the VAUS model. Ratio with HS model shows that, there is not any model from our ensemble that is able to improve the fit with respect to the HS model. However, values close to one, for the smaller number of events, show that we almost catch the same best fitting as in the ensemble of Davies (2019).

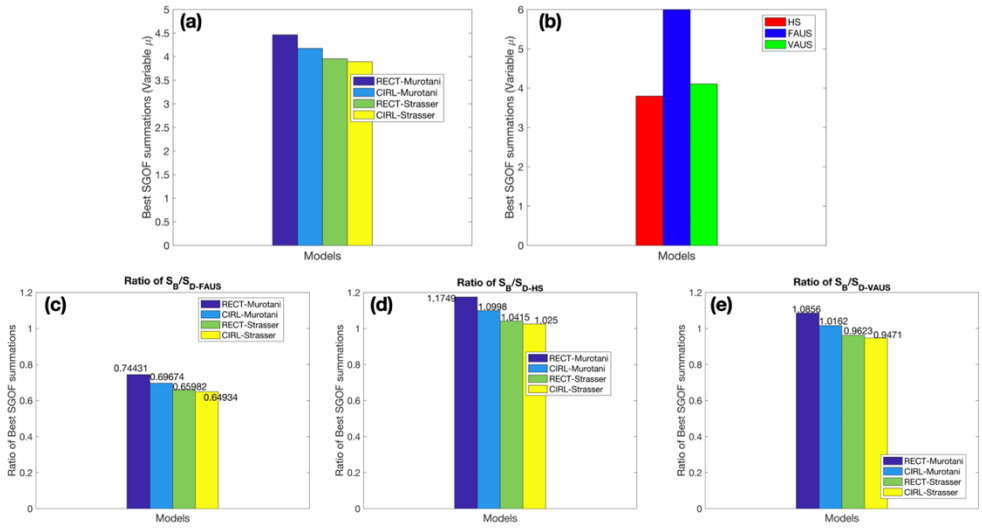

***Figure 3.9.2**: Summation of best SGOF for our model ensemble (a) and Davies (2019) (b), the ratio of best SGOF for each model of our ensemble with FAUS (c), HS (d) and VAUS (e) model of Davies (2019).*

Figure 3.9.3 shows the distribution of $F_{e,d}^{m}$ for each class. Strasser models show again a larger number of values below 0.5, indicating an overestimation of the variability of observed tsunami size also for depth-dependent case. In this case, also Murotani models overestimate the observations while the situation was the opposite for the depth-independent scenarios. The Anderson-Darling test features very small p values indicating that the null-hypothesis of uniform $F_{e,d}^{m}$ is rejected also for these scenarios.

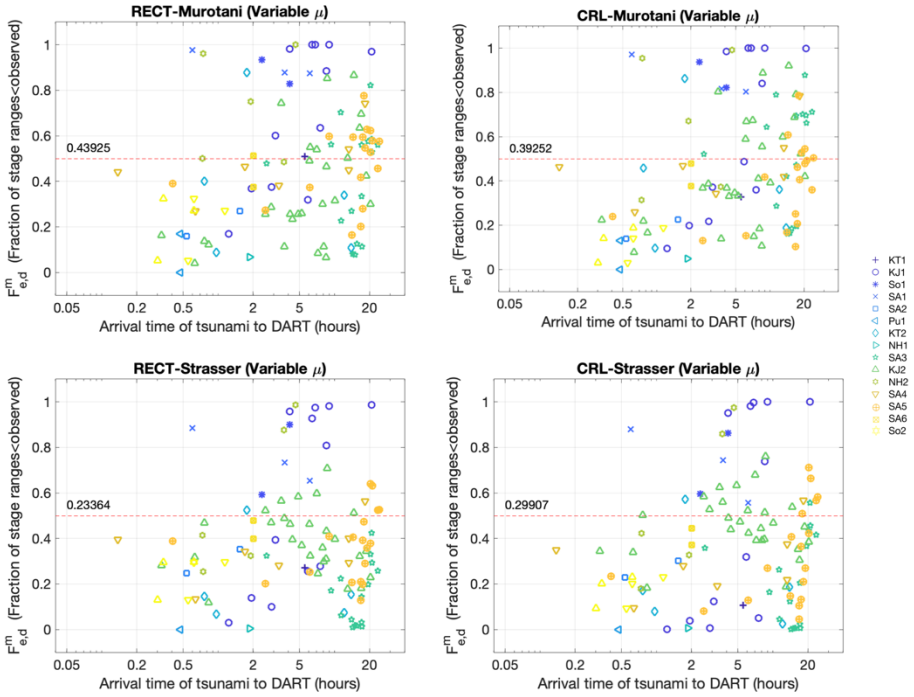

Figure 3.9.3: *Distribution of* $F_{e,d}^{m}$ *with respect to the tsunami arrival time to DART for each depth-dependent model class, each color and shape represent different event.*

The distribution of median coverage statistics with respect to magnitude (Figure 3.9.4) indicates that all the models show a preference for lower median coverage statistics. All model scenarios are biased towards generating larger tsunamis.

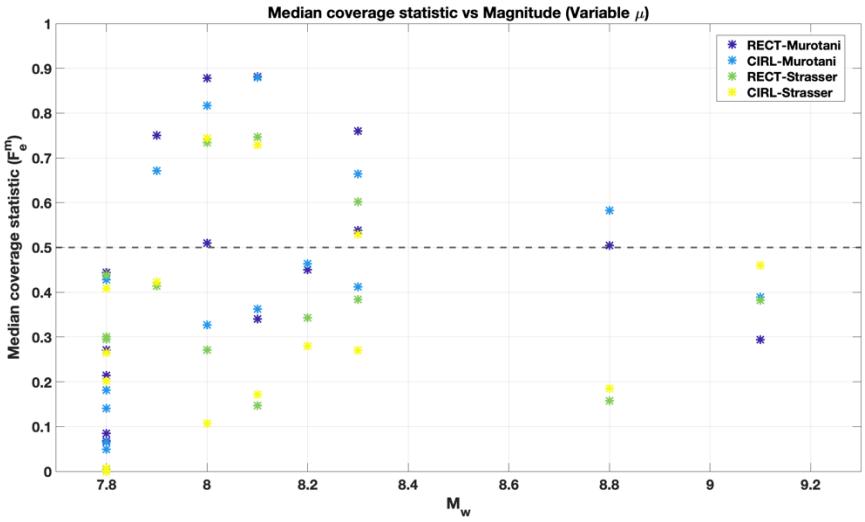

Figure 3.9.4: *Distribution of F_e^m with respect to the magnitude. Each color represents different model.*

Figure 3.9.5. shows the change of maximum slip and rupture area as a function of magnitude. Overall the 4 models, good fitting scenarios show higher maximum slip values while they still remain in the 80 confidence boundaries. These higher values on maximum slip is expectable since maximum slip of scenarios is increased in these models. This preference can be clearly observed especially for Murotani models. Figure 3.9.6 also shows that, best scenario is distributed around the 1:1: line for those models. As described in previous parts, QQ-plots (Figure 3.9.6) can be used to weight scenarios for the bias adjustment of the model.

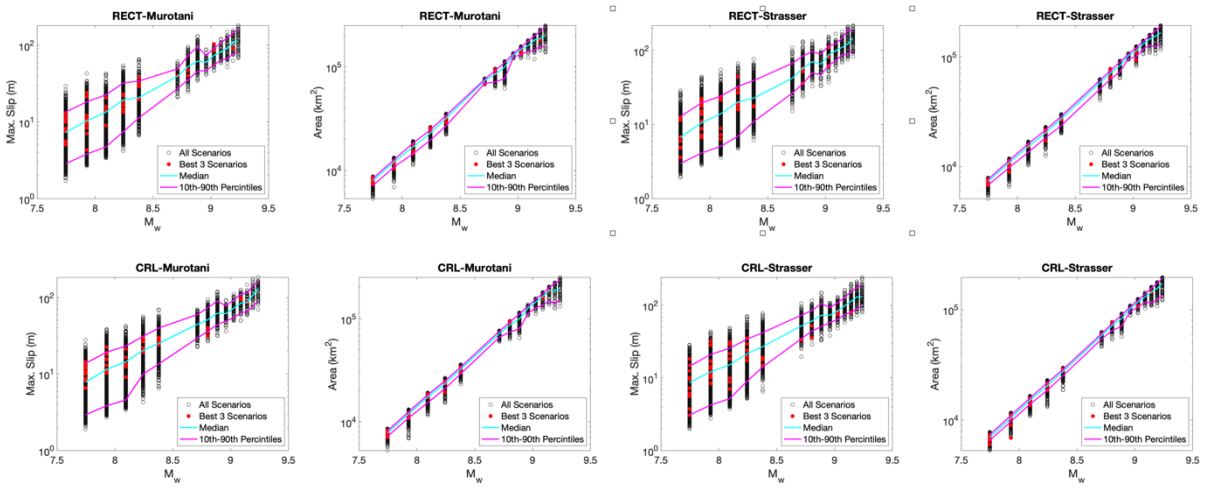

Figure 3.9.5: *Mw versus Maximum slip and rupture area for each depth-dependent model. Best 3 scenarios are showed with red dots.*

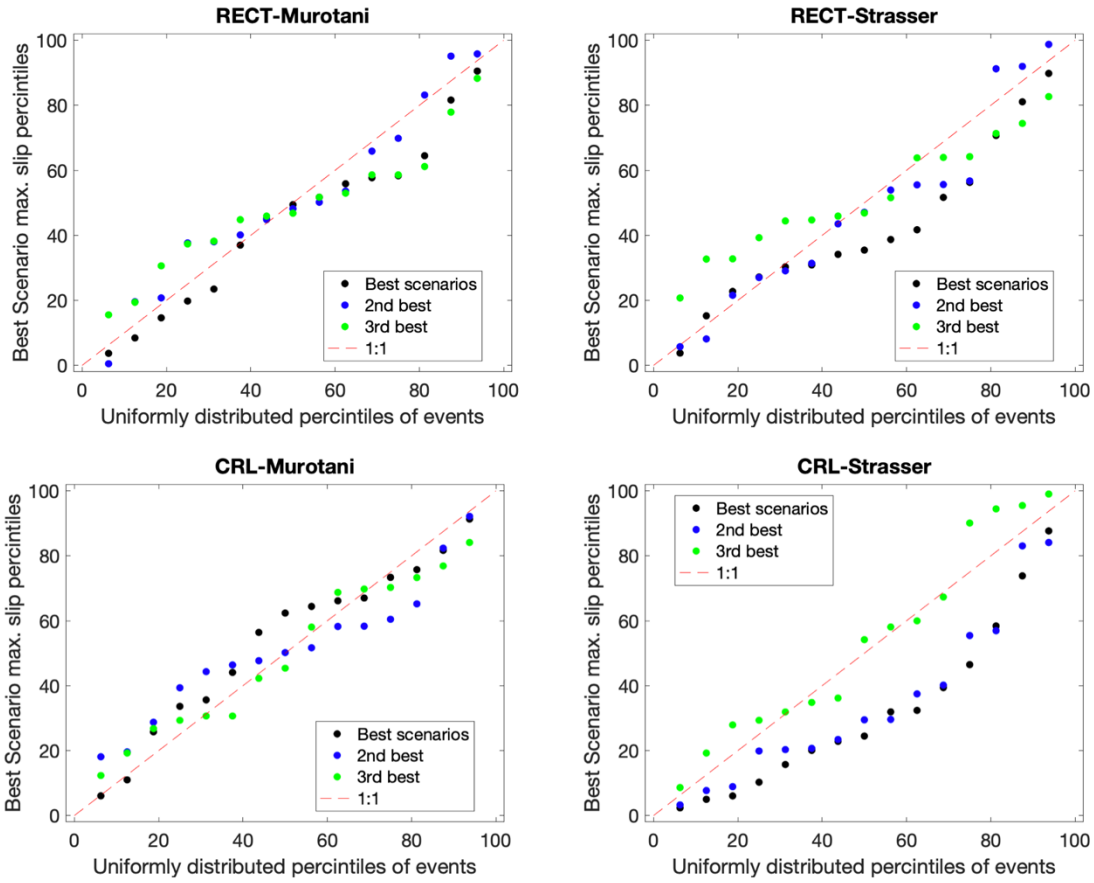

Figure 3.9.6: *QQ-plots for the average percentile of maximum slip for the best three scenarios against the uniformly distributed percentiles of each of the 15 events.*

3.10. Conclusions

There have been plenty of tsunami scenario generation techniques proposed and used for hazard analysis in the literature. However, it is not certain to what extent tsunami waveforms generated by these models are consistent with available tsunami observations, to be used as a forecasting tool in a variety of hazard studies. Also, it is not possible to test PTHA results directly, therefore it is crucial to test stochastic models directly with the observations.

In this study, we have compared different slip generation techniques with observations from open ocean bottom pressure sensors. A set of stochastic scenarios is generated using the approach proposed by Scala et al. (2020) for both constant and variable rigidity for 15 events occurred in the Pacific region. We have used similar earthquake location and magnitude following the scheme suggested by Davies (2019). We made different physical assumptions on the fault rupture, defining circular and rectangular shaped ruptures and using two different scaling relations, Strasser et al. (2010) and Murotani et al. (2013), for the calculation of the rupture area. Besides the stochastic slip models, we also considered kinematic source models of Ye et al. (2016) in our comparisons. Tsunami numerical modelling has been performed for each scenario, using Tsunami-HySEA package, and tsunamis generated by these slip models are tested and compared with the same approach and statistical parameters as in Davies (2019).

Scenario goodness-of-fit statistics reveals that each of the eight ensembles, considering depth-dependent and depth-independent classes, shows comparably good fit to the observed data, while few events poorly modelled, probably due to their short-period tsunami

waveforms. On the other hand, the performance of the kinematic source models from inversion is quite poor in terms of good fitting.

The model ensemble is compared with each of the classes explored by Davies (2019) in terms of ratio of the best SGOF summations. It has been observed that scenarios generated by all depth-independent models show better fit than the FAUS model of Davies (2019). Depth-independent Strasser models are generating better fit than all the 3 models of Davies (2019). However, depth-dependent Strasser models are not able to generate scenarios with better fit as compared to the HS model of Davies (2019). Murotani models, on the other hand, only improve the FAUS model, for both depth-independent and depth-dependent cases. Besides those improvements, differences are within 10% in the best fitting as compared to the best models of Davies (2019), despite the much smaller number of scenarios represented in the ensemble.

Using the coverage statistics, we have tested biases of each model from ensemble. For an unbiased model, the distribution of coverage statistics should be uniform. The uniformity of the distribution is tested analyzing the fraction distribution of scenarios with Anderson-Darling null-hypothesis significance test. In addition to this test, the standard deviation of the distribution is also compared with the standard deviation expected from a sample of 15 events from a uniform distribution. The distribution of coverage statistics for whole ensemble shows that the distribution is uniform and Anderson-Darling test supports that with a high p value. The standard deviation of the fraction distribution is also generated between the 95 per cent of values that is derived by simulating 10 million random datasets.

Distribution of coverage statistics for each model class, on the other hand, shows some biases for both depth-dependent and depth-independent models. Strasser models show a

preference to lower values indicating an overestimation of the variability of observed tsunami size, by generating more frequently larger tsunamis. Murotani models have the opposite tendency, at least for depth-independent rigidity profile. In the case of depth-dependent rigidity, also these latter models overestimate the observations. The Anderson-Darling test of coverage statistics distributions showed very small p values for each model class which implying that the null-hypothesis of uniform $F_{e,d}^{m}$ is rejected.

Comparison of the statistical properties of random model scenarios with good fitting scenarios can be used to better understand the dynamics of the model bias (Davies, 2019). Along the four models of depth-dependent case, there is not any tendency for the maximum slip and the rupture area of best fitting scenarios toward the lower or upper limits, but they show similar variability as random scenarios. Therefore, we can say that although our models are biased, they feature reasonable kinematic properties in slip and size. However, good fitting scenarios show higher maximum slip values for models from the depth-independent case. These higher values on maximum slip is expectable since shallow slip amplification is enhanced in depth-independent model scenarios.

The model biases can be adjusted by assigning non-uniform weights to scenarios (Davies, 2019). This weight can be calculated using quantile matching techniques which include matching of the percentiles of maximum-slip for the good fitting scenarios with a uniform distribution.

CHAPTER 4 – RESEARCH ACTIVITIES

PTHA has become a widely used procedure for estimating tsunami hazard from earthquakes; nevertheless, uncertainties arising from source representation and hydrodynamic modelling are still large and require further research. Moreover, procedures for their estimation are far from being established by the community. In the previous chapter, we have focused on the use of ensemble models to catch the variability of earthquake sources. In the work of Bayraktar and Ozer Sozdinler (2020), presented in this chapter, we have simplified the source description to a homogeneous slip map on a specific fixed-size fault, while we have exploited the non-linearity in the inundation computation for time-dependent PTHA at Tuzla, Istanbul, in Marmara Sea. In this study, we tried to investigate the probability of having tsunami inundation following a seismic event occurring on the Prince Island Fault (PIF). The study considered a characteristic earthquake that ruptures the entire fault all at once. Tsunami modelling is done considering a homogeneous slip distribution. Using the Monte Carlo simulation technique, a synthetic earthquake catalogue, which includes earthquakes having moment magnitudes between Mw 6.5 and 7.1, is generated. Based on this catalogue, probabilities of occurrence and associated tsunami wave heights are calculated for each event at the Tuzla coast. Tsunami numerical modelling is performed for each event from the synthetic catalog using the NAMI-DANCE code which can solve both linear and nonlinear shallow water equations. The code can model tsunami generation, propagation and inundation in one code and it calculates the initial water surface elevation using Okada (1985) equations. Since NAMI DANCE can perform nested grid analyses, four nested domains are generated having the coarsest grid size as 81m and the finest grid size as 3m. Results are

represented as distribution of probability of occurrence corresponding to tsunami hydrodynamic parameters, probabilistic inundation maps and the probability map of exceedance of threshold wave heights at synthetic gauge points.

The recent study of Selva et al. (2021), included later in this chapter, uses the probabilistic approach for tsunami forecasting at the short time scale of an early warning. The information related with the seismic source of an earthquake is limited and uncertain just after the tsunami generation. Therefore, the study mainly aims to project this uncertainty from the source to the alert level using probabilistic methods. The uncertainty quantification is treated using an ensemble of tsunami scenarios from a set of sources weighted by the probability of being consistent with available real-time observations (seismic, geodetic, tsunami) and pre-computed local long-term tsunami hazard information. The long-term hazard contains two seismicity types which are predominant seismicity (PS) and background seismicity (BS). For the BS, each tsunami source is considered as planar fault with uniform slip and the fault size is defined using empirical relations. For the PS, only the source model of subduction earthquakes is included in the ensemble. Since the hazard estimations are sensitive to the slip distribution variability, as it has been discussed also in the previous chapters, for the scenario ensemble of BS, stochastic slip distributions of these events are generated using the approach proposed by Scala et al. (2020), considering earthquake magnitude and hypocenter estimation from real-time observations and adopting a realistic 3D subduction geometry.

We have been discussing about the source uncertainties of the earthquake generated tsunamis by now. In addition to uncertainties of other tsunami sources, there is lack of information theoretical foundation, or commonly accepted methods in the many steps of the assessment. AGITHAR (Accelerating Global science In Tsunami HAzard and Risk analysis) is a

network which aims to improve, standardize and document methods to analyze tsunami hazard and risk. Within the scope of producing a report on research gaps in probabilistic hazard and risk analysis methods and current state-of-the-art, a workshop of a scientific network is held. Behrens et al. (2021) represents the results of this collective work and details recent gaps and open research questions related to PTHA and PTRA. Variety, complexity, and dynamics of fault mechanics and empirical scaling relations are one of the identified gaps in earthquake generated tsunamis on Behrens et al. (2021). In this study, we also tried to cover those gaps using complex fault geometries, depth-varying rigidity models, different scaling relations and rupture shapes.

Nat. Hazards Earth Syst. Sci., 20, 1741–1764, 2020
https://doi.org/10.5194/nhess-20-1741-2020

Natural Hazards and Earth System Sciences
Open Access
EGU

Probabilistic tsunami hazard analysis for Tuzla test site using Monte Carlo simulations

Hafize Basak Bayraktar[1,2] **and Ceren Ozer Sozdinler**[3]

[1]Department of Physics "Ettore Pancini", University of Naples Federico II, Naples, 80126, Italy
[2]Istituto Nazionale di Geofisica e Vulcanologia, Rome, Italy
[3]Institute of Education, Research and Regional Cooperation for Crisis Management Shikoku, Kagawa University, Takamatsu, 760-8521, Japan

Correspondence: Hafize Basak Bayraktar (hafizebasak.bayraktar@unina.it)

Received: 24 July 2019 – Discussion started: 5 September 2019
Revised: 10 January 2020 – Accepted: 9 February 2020 – Published: 15 June 2020

Abstract. In this study, time-dependent probabilistic tsunami hazard analysis (PTHA) is performed for Tuzla, Istanbul, in the Sea of Marmara, Turkey, using various earthquake scenarios of Prince Island Fault (PIF) within the next 50 and 100 years. The Monte Carlo (MC) simulation technique is used to generate a synthetic earthquake catalogue, which includes earthquakes having moment magnitudes between M_w6.5 and 7.1. This interval defines the minimum and maximum magnitudes for the fault in the case of an entire fault rupture, which depends on the characteristic fault model. Based on this catalogue, probability of occurrence and associated tsunami wave heights are calculated for each event. The study associates the probabilistic approach with tsunami numerical modeling. The tsunami numerical code NAMI DANCE was used for tsunami simulations. According to the results of the analysis, distribution of probability of occurrence corresponding to tsunami hydrodynamic parameters is represented. Maximum positive and negative wave amplitudes show that tsunami wave heights up to 1 m have 65 % probability of exceedance for the next 50 years and this value increases by 85 % in the Tuzla region for the next 100 years. Inundation depth also exceeds 1 m in the region with probabilities of occurrence of 60 % and 80 % for the next 50 and 100 years, respectively. Moreover, probabilistic inundation maps are generated to investigate inundated zones and the amount of water penetrated inland. Probability of exceedance of 0.3 m wave height ranges between 10 % and 75 % according to these probabilistic inundation maps, and the maximum inundation distance calculated in the entire earthquake catalogue is 60 m in this test site. Furthermore, synthetic gauge points are selected along the western coast of Istanbul by including Tuzla coasts. Tuzla is one of the areas that shows high probability exceedance of 0.3 m wave height, which is around 90 %, for the next 50 years while this probability reaches up to more than 95 % for the next 100 years.

1 Introduction

The Marmara region, especially highly populated cities along the coasts of the Marmara Sea, is the heart of the Turkish economy in terms of having a great number of industrial facilities with the largest capacity and potential, refineries, ports and harbors. The Marmara Sea and surrounding area is one of the most seismically active areas in Turkey. Main active faults of the region pass through the Marmara Sea. Thus, coastal cities in the Marmara region, especially Istanbul, which has significant importance in terms of the economy and historical and sociocultural heritage with a population of more than 15 million, are under the threat of high damage due to possible big earthquakes and also triggered tsunamis. Recent studies and evaluation of earthquake recurrence periods revealed that there is a high possibility of having an earthquake with a magnitude larger than M_w7.0 in the Prince Island Fault (PIF). According to Ambraseys (2002), the last earthquake on this fault system occurred in 1766 and since that time this fault has been accumulating a huge amount of energy. According to Parsons (2004), the probability of occurrence of a $M > 7$ earthquake beneath the Marmara Sea was estimated to be 35 %–70 % in the following

30 years. The region has distinctive characteristics in terms of its complex tectonic structure and the high possibility of an earthquake occurrence with a magnitude larger than 7.0 offshore of Istanbul. Therefore, there has been a wide range of studies in the Marmara Sea region regarding the fault mechanisms, seismic activities, earthquakes, and triggered tsunamis (Armijo et al., 2002, 2005; Okay et al., 1999; Le Pichon et al., 2001; Yaltırak, 2002; McNeill et al., 2004; Aksu et al., 2000; Imren et al., 2001; Pondard et al., 2007; Yalçıner et al., 1999, 2000, 2002; Aytore et al., 2016; Hébert et al., 2005; Altınok et al., 2003, 2011; Guler et al., 2015; Cankaya et al., 2016; Tufekci et al., 2018; Latcharote et al., 2016).

The North Anatolian Fault Zone (NAFZ) controls a great part of the seismic activity in the Marmara Sea region. The fault zone sets apart Anatolia (Asian part of Turkey) and Eurasia due to the northward migration of the Arabian Plate in the east and southward rollback of the Hellenic subduction zone in the west as seen in Fig. 1 (Armijo et al., 1999; Flerit et al., 2004; Le Pichon et al., 2015).

The Marmara Sea region is a transition zone between the strike-slip regime of the NAFZ and the extension regime of the Aegean Sea area (top left of Fig 1). The northern branch of the NAFZ forms a major transtensional NW–SE right bend under the Sea of Marmara at the Çınarcık trough (Murru et al., 2016). The fault trace is attached to the complex Central Marmara and Tekirdağ pull-apart basins, before joining the NE–SW-striking Ganos fault on land by following the northern margin of the Marmara Sea. Finally, the fault exits into the Aegean Sea by way of Saros Gulf (Wong et al., 1995; Armijo et al., 1999, 2002; Okay et al., 1999; Le Pichon et al., 2001; Yaltırak, 2002; McNeill et al., 2004). The fault trace beneath the Marmara Sea is not directly observable. Therefore, making a segmentation model for the offshore parts of the NAFZ is quite challenging, which causes the fault dimensions, such as its length and width, to include a sum of error margin (Aksu et al., 2000; Imren et al., 2001; Le Pichon et al., 2001; Armijo et al., 2002, 2005; Pondard et al., 2007).

The current right-lateral slip rate along the NAFZ is about $25\,\mathrm{mm\,yr^{-1}}$ (Meade et al., 2002; Reilinger et al., 2006). On the western side, the motion between the Anatolian and Eurasian plates is accommodated across the Marmara region by $\sim 19\,\mathrm{mm\,yr^{-1}}$ of right-lateral slip and $8\,\mathrm{mm\,yr^{-1}}$ of extension (Flerit et al., 2003, 2004). Slip rates of the main Marmara fault range between 17 and $28\,\mathrm{mm\,yr^{-1}}$ (Le Pichon et al., 2003; Reilinger et al., 2006). On the other hand, Hergert and Heidbach (2010) suggest that the right-lateral slip rate on the main Marmara fault is between 12.8 and $17.8\,\mathrm{mm\,yr^{-1}}$ due to slip partitioning and internal deformation. The right-lateral slip rate for the PIF and Çınarcık basin is $15 \pm 2\,\mathrm{mm\,yr^{-1}}$ and in addition to this the fault has $6 \pm 2\,\mathrm{mm\,yr^{-1}}$ of extension (Ergintav et al., 2014).

The main characteristic of the NAFZ is that the earthquakes systematically propagate westward, and historical records show that the northern strand of the NAFZ generates earthquakes with the recurrence interval of about 250 years beneath the Marmara Sea; the last event occurred in 1766 (Ambraseys, 2002; Bohnhoff et al., 2013). This event caused the rupture of the 58 km long northern part of the NAFZ from İzmit to Tekirdağ (Ambraseys and Finkel, 1995; Ambraseys and Jackson, 2000). However, the earthquake that happened on 2 September 1754 can be considered the last characteristic event for the PIF segment, and it caused the rupture of a 36 km long fault segment (Ambraseys and Jackson, 2000). The NAFZ has experienced two $M > 7$ earthquakes: in August 1912 in Ganos and August 1999 at İzmit. After the 1999 İzmit event, seismic energy along the 150 km long northern part of the NAFZ has been accumulating continuously since the 22 May 1766 earthquake. This fault zone extends right to the south of Istanbul beneath the Marmara Sea, and this situation increases the rupture possibility of the PIF and the risk for Istanbul (Stein et al., 1997; Barka, 1999; Bohnhoff et al., 2013). Ergintav et al. (2014) also indicated that the PIF segment accumulates stress $15 \pm 2\,\mathrm{mm\,yr^{-1}}$, and the 3.7 m slip deficit has been accumulating since the 1766 events. This makes the PIF most likely to generate the next $M > 7$ earthquake along the Sea of Marmara segment of the NAF.

Besides these seismic activities in the region, studies of the historical tsunami records show that 35 tsunami events happened between 330 BCE and 1999 BCE in the Marmara Sea region, and the majority of them are earthquake-related tsunami events (Altinok et al., 2011; Yalçıner et al., 2002). The 1509 earthquake, with an estimated magnitude around 7.5 (Ambraseys, 2002), is one of the examples for these events. This earthquake triggered a tsunami and the tsunami waves inundated the Istanbul coast, reaching the city walls and killing around 4000–5000 people in the city (Ambraseys and Finkel, 1995). The 1894 earthquake is also one of the important events that happened in the Marmara Sea. The earthquake triggered a tsunami and the sea inundated 200 m of coast in Istanbul (Altinok et al., 2011). The most recent event happened after the 17 August 1999 İzmit earthquake, and after the earthquake E–W-trending tectonic deformation along the basin and submarine failures generated a tsunami. The International Tsunami Survey Team (Yalciner et al., 1999, 2000) investigated the region and they observed 2.66 m run-up along the coast from Tütünçiftlik to Hereke and 2.9 m run-up at Değirmendere (Yalçıner et al., 2002).

Several tsunami hazard estimation studies (Ozer Sozdinler et al., 2020; Hancilar, 2012; Aytore et al., 2016; Hébert et al., 2005) were also conducted in the region. These tsunami analyses were mostly performed in a deterministic manner using various earthquake scenarios depending on the combinations of different fault parameters without considering probability of occurrences. The 40 km long fault in the eastern basin of the Marmara Sea, with a significant normal component, may generate tsunami waves which can reach maximum 2 m heights along the Istanbul coast with considerable local inundation (Hébert et al., 2005). The rupture of the Yalova Fault,

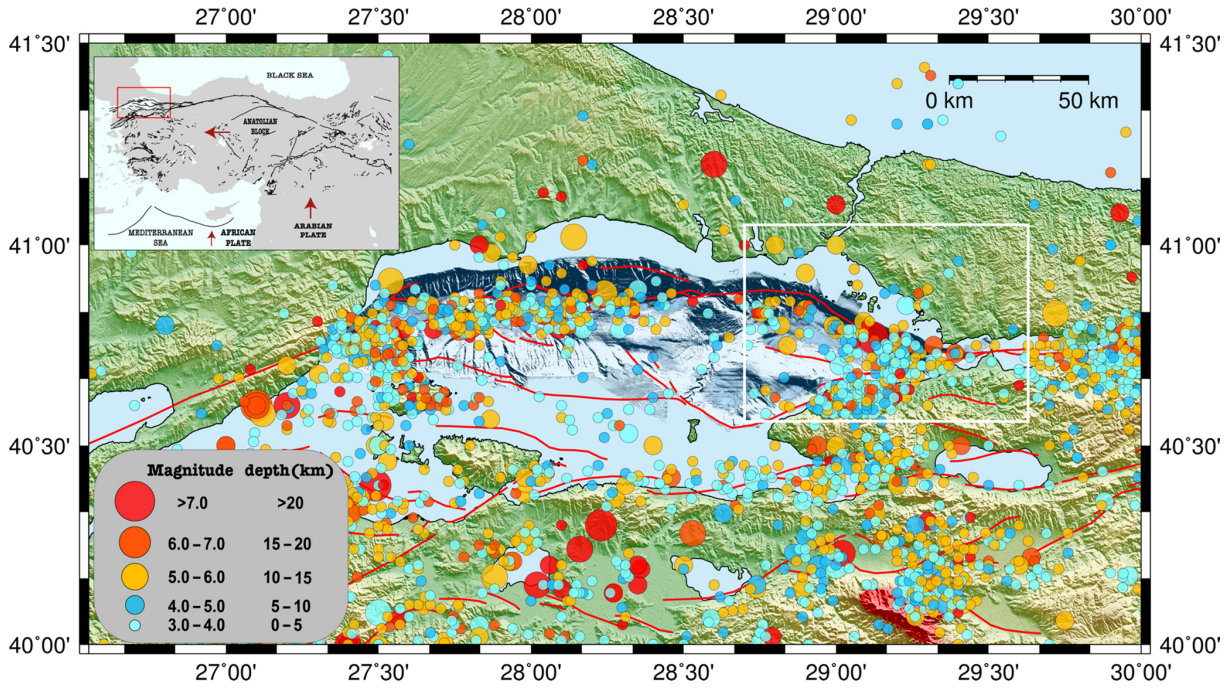

Figure 1. Seismicity map of the Marmara region and general tectonic map of Turkey at the top left. In the seismicity map, the size of the circles changes with magnitude of the earthquakes, and the color of the circles defines the depth change of the earthquakes. Red lines show the known active faults (modified from Emre et al., 2013) in the region, and the white square is the area with the PIF. In the general tectonic map of Turkey, red arrows show the direction of the plate motion, black lines show the active faults in the region (modified from Emre et al., 2013), and the red rectangle shows the Marmara region (created using The Generic Mapping Tools, version 5.4.1). The duration of the catalog, used for the seismicity map, is 05 April 1905–31 December 2018 (KOERI, 2001).

PIF, or Central Marmara Fault can also cause serious damage along the coast of Istanbul. Tsunami wave heights can reach 4.8 m and can penetrate 340 m inwards from the coast in Haydarpaşa Port (Aytore et al., 2016).

A few probabilistic seismic and tsunami hazard analyses (Murru et al., 2016; Erdik et al., 2004; Hancilar, 2012) were also performed in this region. Seismic hazard maps were prepared in the Marmara Sea region by describing fault segments and peak ground accelerations with the periods corresponding to 10 % and 2 % probabilities of exceedance in 50 years (Erdik et al., 2004). In addition, tsunami inundation maps are prepared based on probabilistic and deterministic analyses by depending on these segmentations (Hancilar, 2012). Time-dependent and time-independent earthquake ruptures are also estimated in the Marmara Sea region for the next 30 years (Murru et al., 2016). These previous studies have been conducted for entire Marmara Sea region and therefore they give general and rough information about probability of occurrence in the region without focusing on any specific region in high resolution. However, probabilistic tsunami hazard assessment is important to calculate the tsunami exposure and risk on human populations and infrastructures, since probability calculations consider all possible earthquakes in a fault even if they occur with very low probability (Løvholt et al., 2012, 2015; Grezio et al., 2017). The results of probabilistic studies should be considered when decision makers design coastal zones and structures, especially critical ones. Different from previous probabilistic approaches in the Marmara Sea, the probability of earthquake occurrences in one fault segment, PIF, are taken into account for the preparation of high-resolution tsunami inundation maps and distribution of hydrodynamic parameters due to the probability of occurrence of associated earthquakes on the PIF determined by Monte Carlo (MC) simulations.

This probabilistic tsunami hazard analysis (PTHA) study depends on the fully characteristic fault model, and the main purpose is to perform PTHA for selected test sites. The Tuzla test site is one of the coastal districts of Istanbul and located on the southernmost part of the city (Fig. 2). The region includes several residential areas, but the most critical point about the region is that Tuzla has the biggest shipyard area not only in the Marmara Sea but also in Turkey (Fig. 3). In this study we mainly focused on this region because it is about 20 km away from the PIF and therefore has a high risk of both earthquake and tsunami damage.

2 Probabilistic analysis

Probabilistic tsunami hazard analysis (PTHA), as it is recently becoming a widely used procedure for coastal zones,

Figure 2. The Marmara Sea region, Tuzla test site, and the location of the PIF segment which is used in the analysis like a straight line (created using ArcMap version 10.5).

is performed for the Tuzla region, Istanbul. This method has been applied for various tsunami sources, such as earthquakes, landslides, volcanic activities, etc., on various scales, local, regional, and global (Grezio et al., 2017). For earthquake-generated tsunamis, the method is generally adapted from seismic hazard assessment methods (González et al., 2009). Such kinds of studies consider the events that are generated by coseismic seafloor displacement, using seismic probabilistic hazard analysis (SPTHA), but numerous tsunami simulations are required to consider all expected combinations of seismic sources. This problem can be solved by applying a simplified event tree approach and a two-stage filtering procedure to reduce the number of required source scenarios without decreasing the quality and accuracy of inundation maps (Lorito et al., 2015). The earthquake source itself is very uncertain and the investigation of this uncertainty can be carried out by building an event tree instead of using a logic tree and hazard integrals (Selva et al., 2016). The logic tree approach can be applied to the generation of tsunami hazard curves to decrease the uncertainties by including branches, which are the combination of tsunami sources, magnitude distribution of characteristic tsunamigenic earthquakes, their recurrence interval, and the tsunami height estimation procedure based on a numerical simulation (Annaka et al., 2007). For regional studies, hazard curves can be generated by empirical analysis using available tsunami run-up data. However, if such data are not available, MC simulations, a computationally based method widely used in probabilistic seismic hazard analysis (PSHA), can be considered as a primary method to generate tsunami hazard curves (Geist and Parsons, 2006; Horspool et al., 2014). Submarine landslides, on the other hand, are the major tsunami source for passive margins, which are the transition zone between the oceanic and continental lithosphere that is not an active plate boundary, and they have been included in PTHA methodologies (Geist and Lynett, 2014). Probabilistic studies are also applied to develop multi-hazard loss estimation methodology for coastal regions that are exposed to cascading shaking-tsunami hazards due to offshore mega-thrust subduction earthquakes (Goda and De Risi, 2018).

In this study, a characteristic earthquake model is used to estimate the earthquake recurrence on the PIF. Paleoseismologic studies (Ryall et al., 1966; Allen, 1968; Schwartz and Coppersmith, 1984) suggest that an individual fault tends to generate characteristic earthquakes having a very narrow range of magnitudes. These individual faults have a different frequency distribution than the log linear Gutenberg–Richter frequency–magnitude relationship (Aki, 1984; Schwartz and Coppersmith, 1984; Youngs and Coppersmith, 1985). According to Aki (1984), a characteristic earthquake is generated as a result of constancy of barriers to rupture through repeated seismic cycles.

PIF is fully characteristic and a characteristic earthquake will rupture an entire fault as a whole and release all the energy. Therefore, while performing MC simulations, the area of the fault and fault parameters (strike, dip, and rake angles) are used as constants referring to the outcomes of EU Seventh Framework Programme project MARSITE (Ozer Sozdinler et al., 2020). One of the work packages of this project aimed to define the geometry of the possible tsunamigenic faults in the Marmara Sea and 30 different earthquake scenarios with the different rupture combinations of 32 possible fault segments. Based on these 30 different earthquake scenarios, tsunami numerical modeling is performed. The definition of fault segments depends on extensive review of the literature (Alpar and Yaltırak, 2002; Altınok and Alpar, 2006; Armijo et al., 2005; Ergintav et al., 2014; Gasperini et al., 2011; Hébert et al., 2005; Hergert et al., 2011; Hergert and Heidbach, 2010; Imren et al., 2001; Kaneko, 2009; Le Pichon et al., 2001, 2003, 2014; Oglesby

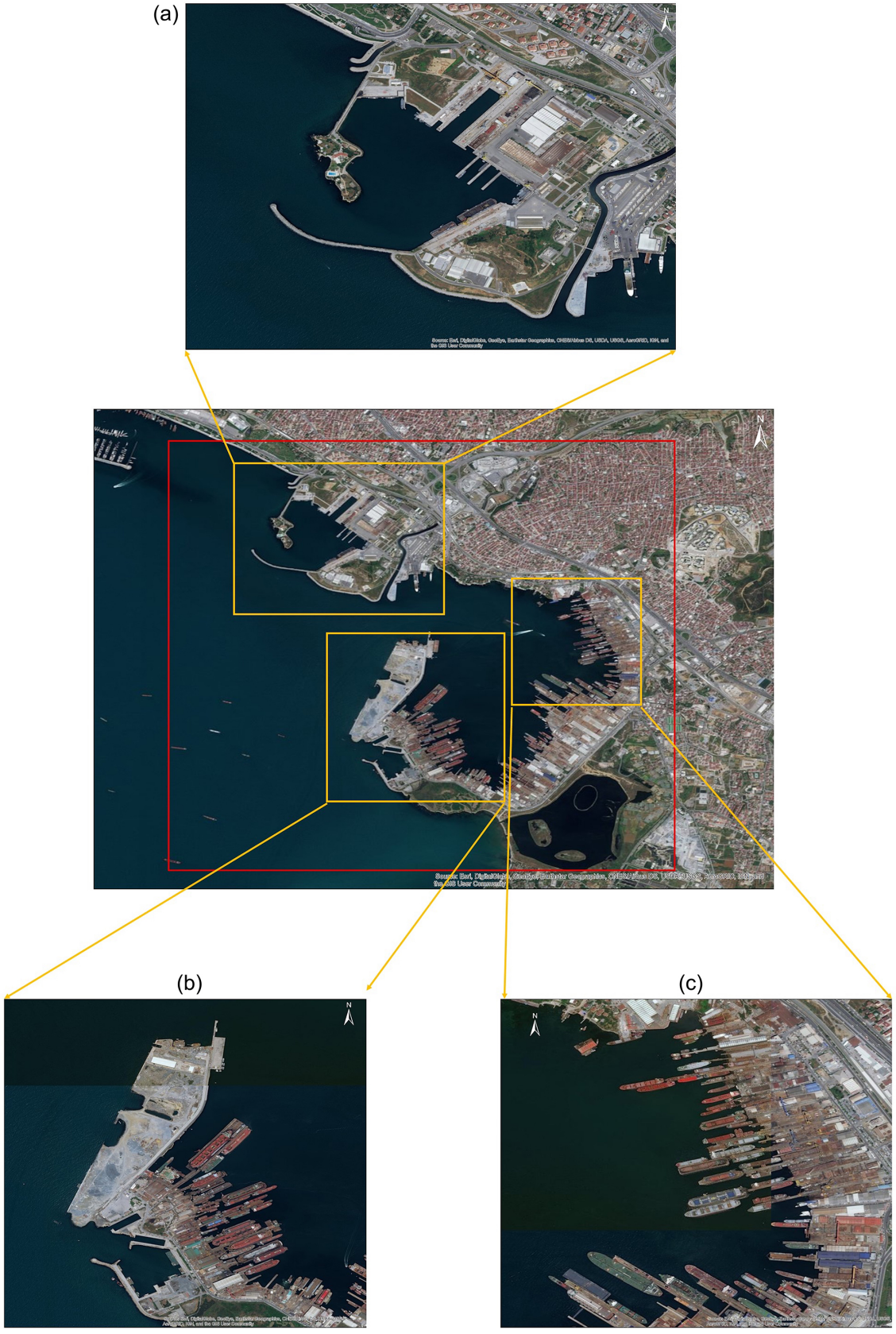

Figure 3. Some important locations at the Tuzla domain. **(a)** Northern part of the Tuzla domain. **(b)** Southern part of the Tuzla domain. **(c)** Tuzla shipyard (created using ArcMap version 10.5).

Table 1. The area and the focal mechanism of the PIF zone. These are the constant parameters during the MC simulation application.

Fault length (km)	Fault width (km)	Strike	Dip	Rake
33.5	14	119	80	210

and Mai, 2012; Şengör et al., 2014; Tinti et al., 2006; Utkucu et al., 2009). As a result of this review, each fault segment is defined as a rectangular area with hypothetical uniform slip. According to the results of the project, the fault parameters of the PIF are given in Table 1. The 3-D fault configuration given by Armijo et al. (2002), which explains fault segmentation in the region depending on morphology, geology, and long-term displacement fields, also fits with the PIF parameters that are used in the project. These parameters are used as constants in this study while assessing probability of occurrence of each earthquake to allow full fault rupture at different depths with different magnitudes.

The MC simulation technique is generally applied to generate an earthquake catalogue of a given length of time. In this technique, a list of earthquakes can be generated using the frequency–magnitude relationship for each seismic source (Zolfaghari, 2015). Seismic zonation should be performed by considering regions that have relatively homogeneous earthquake activity and faulting regimes (Sørensen et al., 2012). In this study, the fault segment model proposed in Ozer Sozdinler et al. (2020) is used and PIF is the only segment that is a seismic source. After that, tsunami numerical modeling is performed for each event of this synthetic catalogue, and tsunami hydrodynamic parameters, mainly maximum wave heights, inundation depth, current velocities, and tsunami inundation zones, are estimated. Tsunami risk assessment will serve the needs of societies best when regional studies are associated with the local ones (Sørensen et al., 2012).

The MC simulation technique allows the generation of a list of earthquakes based on a frequency–magnitude relationship. This technique depends on a uniformly distributed source model and it provides an equal likelihood to each earthquake source. As a result, the synthetic earthquake catalogue will have uniformly randomly distributed earthquake sources (Zolfaghari, 2015).

Using MC simulation, a synthetic earthquake catalogue is generated by selecting earthquake magnitude and depth as uniformly distributed random numbers in a given interval and using area and directivity of the fault as a constant variable (Table 1). We performed MC simulations 100 times for 100 different earthquake scenarios. The number of earthquakes in the catalog is selected as a reasonable number that represents the number of iterations randomly performed in MC simulations for having a synthetic earthquake scenario. As mentioned earlier, NAFZ generates an earthquake with the recurrence interval of about 250 years beneath the Marmara Sea. Therefore, selecting 100 earthquake scenarios would cover a time period of $100 \times 250\,\mathrm{yr} = 25\,000\,\mathrm{yr}$, which is considered as an adequate catalog duration in this study. However, because of having time-dependent probabilistic analyses, this catalog duration is not used for PTHA in this study.

Earthquake magnitude is one of the parameters randomly selected by the MC technique. Based on a characteristic earthquake model, individual faults tend to rupture the entire fault when a large earthquake occurs. This model assumes that a characteristic earthquake releases all of the seismic energy during the fault rupture, and the magnitude of the earthquake depends on the dimension of the fault (Abrahamson and Bommer, 2005).

As mentioned previously, only the PIF is considered an earthquake source approximately 34 km in length and 14 km in width (Ozer Sozdinler et al., 2020; Karabulut et al., 2002). This fault zone is assumed to have the potential to generate a characteristic earthquake and rupture the entire fault. According to the Wells and Coppersmith (1994) scaling relation between fault area and magnitude (Eq. 1), this fault can generate a characteristic earthquake with magnitude varying between $M_\mathrm{w}6.5$ and 7.1.

$$M_\mathrm{w} = a + b \cdot \log(L \cdot W) \tag{1}$$

In this equation, a and b are coefficients, which are 4.33 and 0.9, respectively, L is fault length, and W is the fault width.

Displacement on the fault surface calculations is carried out for each randomly selected magnitude using the formulation of Aki (1966),

$$D = \frac{M_0}{\mu A} = \frac{10^{(M_\mathrm{w}+6.07)\cdot 1.5}}{\mu A}, \tag{2}$$

where D is displacement on the fault surface, M_w is moment magnitude, μ is the shear modulus ($\mu = 30\,\mathrm{GPa}$), and A is the fault area.

Seismogenic thickness and the location of the earthquake is another important parameter required for earthquake and tsunami source. At first, the PIF zone is accepted as fully characteristic and an earthquake should rupture the entire fault area. Therefore, it is assumed that if the rupture starts at the center of the fault and continues in both directions, the fault will rupture entirely. For this reason, the locations of the earthquakes are accepted as the midpoint of the PIF zone for each earthquake scenario (Ozer Sozdinler et al., 2020).

For the seismogenic thickness, the seismic activity of the northern segment of NAFZ starts at the depth of 5 km (Karabulut et al., 2003). The bottom of the seismogenic thickness can be determined based on the aftershock activity of the 17 August 1999 İzmit earthquake. The earthquakes on the northern scarp of the Çınarcık basin are observed between

the depths of 5 and 14 km. The mechanism of events between the depth of 5 and 10 km shows the behavior of normal faulting. On the other hand, the strike-slip mechanism dominates the depths below 10 to 14 km. As a result, seismic activity can be observed between the depths of 5 and 14 km, and fault plane solutions show normal and strike-slip mechanisms in this area (Karabulut et al., 2002). Therefore, the depth of events varies between 5 and 14 km in MC simulations.

In time-independent earthquake occurrence models, probability of an event occurrence follows a Poisson distribution in a given period of time. Therefore, the result of this model does not vary in time. However, probability of an earthquake occurrence is based on the time that has passed since the occurrence of the last event and it follows a Brownian passage time (BPT), lognormal, or other probability distribution (Matthews et al., 2002; Ellsworth et al., 1999; Davis et al., 1989; Rikitake, 1974). In this model, in addition to the recurrence time of earthquakes, variability of the frequency of events and the elapsed time from the last characteristic event are the additional required information and the longer elapsed time causes an increase in probability of an event occurrence (Cramer et al., 2000; Petersen et al., 2007).

Calculation of probability in multi-segment ruptures and more complicated models includes the Gutenberg–Richter magnitude–frequency relationship (Gutenberg and Richter, 1944). The application of time-dependent models is based on a characteristic earthquake model, which assumes all large events occurring along a particular fault segment would have similar magnitudes, rupture area, and average displacements (Schwartz and Coppersmith, 1984). Therefore, this model is suitable for calculating the probability of occurrence of an earthquake on a single fault.

It should be noted that, in this study, PIF is considered to be the only source for the earthquake and tsunami. A time-dependent probabilistic model is followed for the probability calculations because this probabilistic model allows us to consider only one fault instead of using multi-segment rupture scenarios through a characteristic earthquake model.

In the time-dependent approach, the BPT probability model is used to obtain the recurrence time probability of the earthquake in the fault segment. This model does not show a significant difference with the lognormal distribution except for consideration of very long elapsed times from the last characteristic event (Petersen et al., 2007). A characteristic event occurs when the load-state process reaches the failure threshold; an earthquake releases all energy loaded on the fault and then starts the new failure cycle. The time interval between consecutive earthquakes shows a Brownian passage time distribution and that can be useful to forecast long-term seismic events by generating a time-dependent model (Matthews et al., 2002). The Working Group on California Earthquake Probabilities (1999) and the Earthquake Research Committee (2001) have already implemented this time-dependent approach in the San Francisco Bay area and Japan, respectively, for the prediction of long-term events (Petersen et al., 2007). This model depends on the time period passed since the last characteristic event and recurrence time of the earthquake. The probability density function for the BPT model (Matthews et al., 2002) is given by

$$f\left(t, T_{\mathrm{r}}, \propto\right) = \left(\frac{T_{\mathrm{r}}}{2\pi\alpha^2 t^3}\right)^{1/2} \exp\left(\frac{(t-T_{\mathrm{r}})^{1/2}}{2T_{\mathrm{r}}\alpha^2 t}\right), \tag{3}$$

where t is the elapsed time from the last characteristic event and α is the aperiodicity (also known as the coefficient of variation). Aperiodicity defines the regularity of the expected characteristic earthquakes on the fault and varies between 0.3 and 0.7. This parameter, which is known as the parameter defining how much an expected characteristic earthquake occurs regularly or irregularly on any fault segment (Murru et al., 2016), was taken as 0.5 in this study (Parsons, 2004). The mean recurrence interval of earthquakes (T_{r}) can be defined as the ratio between the mean moment of repeating earthquakes (seismic moment) and the long-term moment accumulation rate on the fault (moment rate) (Ren and Zhang, 2013). Seismic moment can be obtained using the formulation of Kanamori (2004), and the moment rate of the fault is calculated from fault area and long-term slip rate of the fault (WGCEP, 2003).

$$T_{\mathrm{r}} = \frac{M_0}{\dot{M}_0} = \frac{10^{(M_{\mathrm{w}}+6.07)\cdot 1.5}}{\mu V A} \tag{4}$$

In this equation, M_{w} is moment magnitude, μ is the shear modulus, V is long-term slip rate in millimeters per year, and A is the fault area. The moment magnitude value in Eq. (4) was selected randomly using MC simulations. Thus, seismic moment (M_0) and the mean recurrence time (T_{r}) were calculated for each earthquake scenario. Long-term slip rate is also selected as 17 mm yr^{-1} for this equation (Ergintav et al., 2014).

Probability of the earthquake occurrence on the fault is calculated based on the probability density function approach. The probability of occurrence of an event in the next ΔT years, given that it has not occurred in the last t years, is given by (Erdik et al., 2004)

$$P(t, \Delta T) = \frac{\int_{t}^{t+\Delta T} f(t)\mathrm{d}t}{\int_{t}^{t+\infty} f(t)\mathrm{d}t}. \tag{5}$$

In this case, probability of a characteristic earthquake was calculated using ΔT as 50 and 100 years.

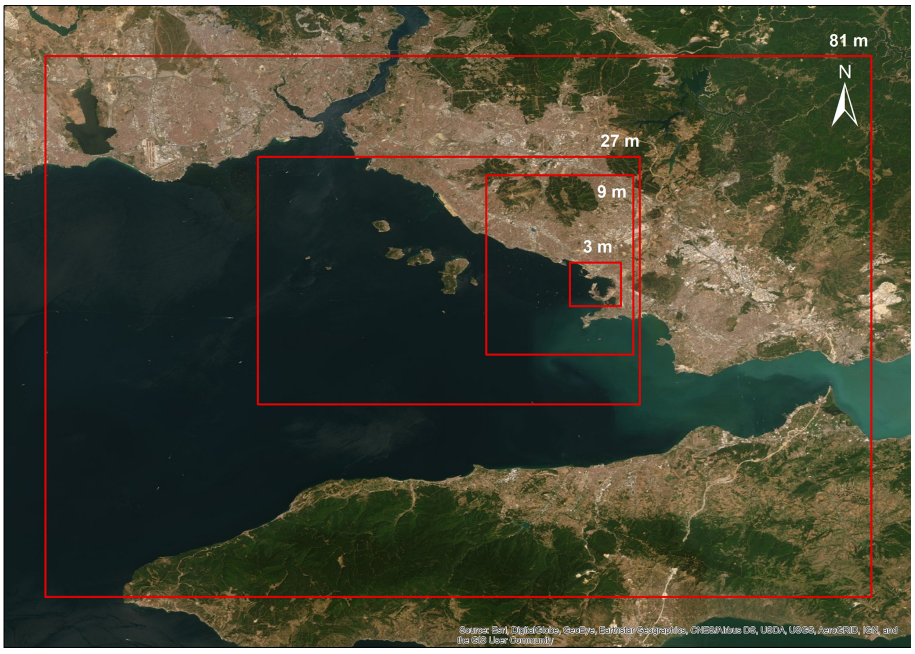

Figure 4. Nested domains for tsunami numerical modeling. Red rectangles show the limits of these domains. Grid size of these domains have a certain 1 : 3 ratio between each other (created using ArcMap version 10.5).

3 Tsunami numerical modeling

Tsunami simulations are performed for each earthquake in the synthetic catalogue using the tsunami numerical model NAMI DANCE (NAMI DANCE, 2011). The code is the user-friendly version of TUNAMI-N2 (Imamura et al., 2001) developed in C++ language, which computes all fundamental parameters of tsunami motion in shallow water and in the inundation zone. It uses an explicit numerical solution of shallow water wave equations with the finite-difference technique and allows for better understanding of the effect of the tsunami waves (Shuto et al., 1990; Imamura, 1989). NAMI DANCE can solve both linear and nonlinear shallow water (NSW) equations with a selected coordinate system (Cartesian or spherical) and calculates the tsunami motion. Linear shallow water (LSW) equations are preferable in deep water because of reasonable computer time and memory, and they calculate the results at an acceptable error limit (Insel, 2009). NAMI DANCE is validated and verified using NOAA standards and criteria for tsunami currents and inundation (Synolakis et al., 2007, 2008). The numerical solutions of NAMI DANCE are also tested, validated and verified against analytical solutions, laboratory measurements, and field observations (NTHMP, 2015; Lynett et al., 2017; Velioglu, 2009).

NAMI DANCE calculates tsunami generation using Okada (1985) equations. In this study, water surface distribution of tsunami source (initial wave amplitude) is calculated with this method for 100 earthquakes of the synthetic earthquake catalogue prepared by MC simulations. As an example, Fig. 5 shows the initial water surface calculated due to one of 100 tsunami sources generated by MC simulations (Fig. 5).

Before starting tsunami simulations, the necessary inputs should be prepared precisely in order to obtain reliable results. Bathymetry–topography data are one of the most important inputs in NAMI DANCE that significantly effects the reliability of results, especially in the shallow water zone due to the nature of the NSW equations. NAMI DANCE can perform nested analyses under the condition that the grid sizes of the study domains have a certain 1 : 3 ratio between each other. Therefore, we generated four nested domains having the coarsest grid size as 81 m and the finest grid size as 3 m with a 1 : 3 ratio in the GIS environment. Bathymetric data for the biggest domain are the combination of the 30 arcsec resolution General Bathymetric Chart of the Oceans (GEBCO) and data produced by navigational charts in shallow zones. Topographic data, on the other hand, are at a high resolution, which is obtained from the Department of Housing and Urban Development of Istanbul Metropolitan Municipality digital elevation model (DEM) and vector data with resolution of 5 and 1 m, respectively. The bathymetry–topography data in the smaller domains are the downscaled version of the 81 m grid bathymetry–topography data; however high-resolution digitized coastline and sea and land structures are also included in the data to generate the smallest grid domain of 3 m (Fig. 4).

The synthetic gauge point file is another required input of NAMI DANCE. In addition to the calculation of principal tsunami hydrodynamic parameters, the program can

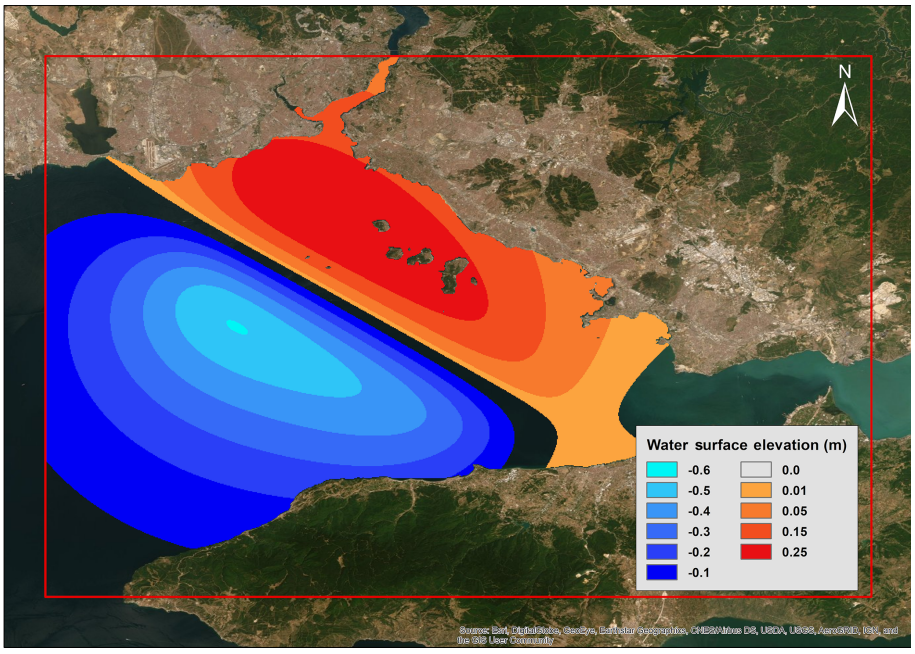

Figure 5. Initial water surface distribution of one of the 100 tsunami sources. The red frame indicates the boundary of the largest nested domain with an 81 m grid size (plotted using ArcMap version 10.5).

also calculate the change of water level, current velocity, and flow depth over time in every gauge point. Therefore, various gauge points are selected along the coast of nested domains, nearshore and offshore and close to some critical structures on land.

During the inundation of tsunami waves, current velocity is an important tsunami parameter in land and sea, especially in ports and bays. Strong current velocities may cause sea vessels to be dragged offshore by undertow or to ground inland. This parameter as well as tsunami wave amplitude, inundation depth, and Froude number can be calculated by NAMI DANCE. However, in this study, the results are represented based on only the probability of exceedance of threshold values for water surface elevation and inundation depth.

4 Results and discussion

In this study, tsunami hydrodynamic parameters are calculated in both the coarsest domain (whole Marmara Sea) and finest domain (Tuzla region). The main parameters focused in this study are the tsunami wave heights and inundation depths, and the results are shown in terms of probability of exceedance of threshold wave height and inundation depth values within the next 50 and 100 years. The situation for the next 500 years is not considered because the return period of the fault rupture is about 250 years, which means this fault generates at least one earthquake within the next 500 years. In other words, probability of exceedance for the next 500 years will be about 99 %.

We present the results of the PTHA for the Tuzla test site in terms of three different visualization categories for the next 50 and 100 years. First, distribution of probability of occurrence of the tsunami hydrodynamic parameters, which are minimum and maximum water surface elevation and inundation depth, is shown. Second, tsunami inundation maps that show the probability of exceedance of 0.3 m inundation depth for different time periods are generated for the Tuzla region in order to observe flooded areas and their probabilities clearly. Finally, the probability map of exceedance of 0.3 m wave heights at synthetic gauge points is represented as a bar chart.

4.1 Probability of exceedance for the entire synthetic earthquake catalogue

The graphics are generated to demonstrate the probabilities of occurrences corresponding to the minimum and maximum water surface elevations and inundation depth calculated from tsunami sources of each earthquake in the synthetic earthquake catalogue.

It should be noted that in the case of having same magnitude of earthquakes in two different earthquake scenarios of the catalogue, the probability of occurrences of these scenarios would be the same. However, since they would have different focal depths, the tsunami initial wave height calculated by Okada (1985) will be different, which results in the calculation of different hydrodynamic parameters. As a result, the graphs show different maximum water surface elevations having the same probability of occurrences.

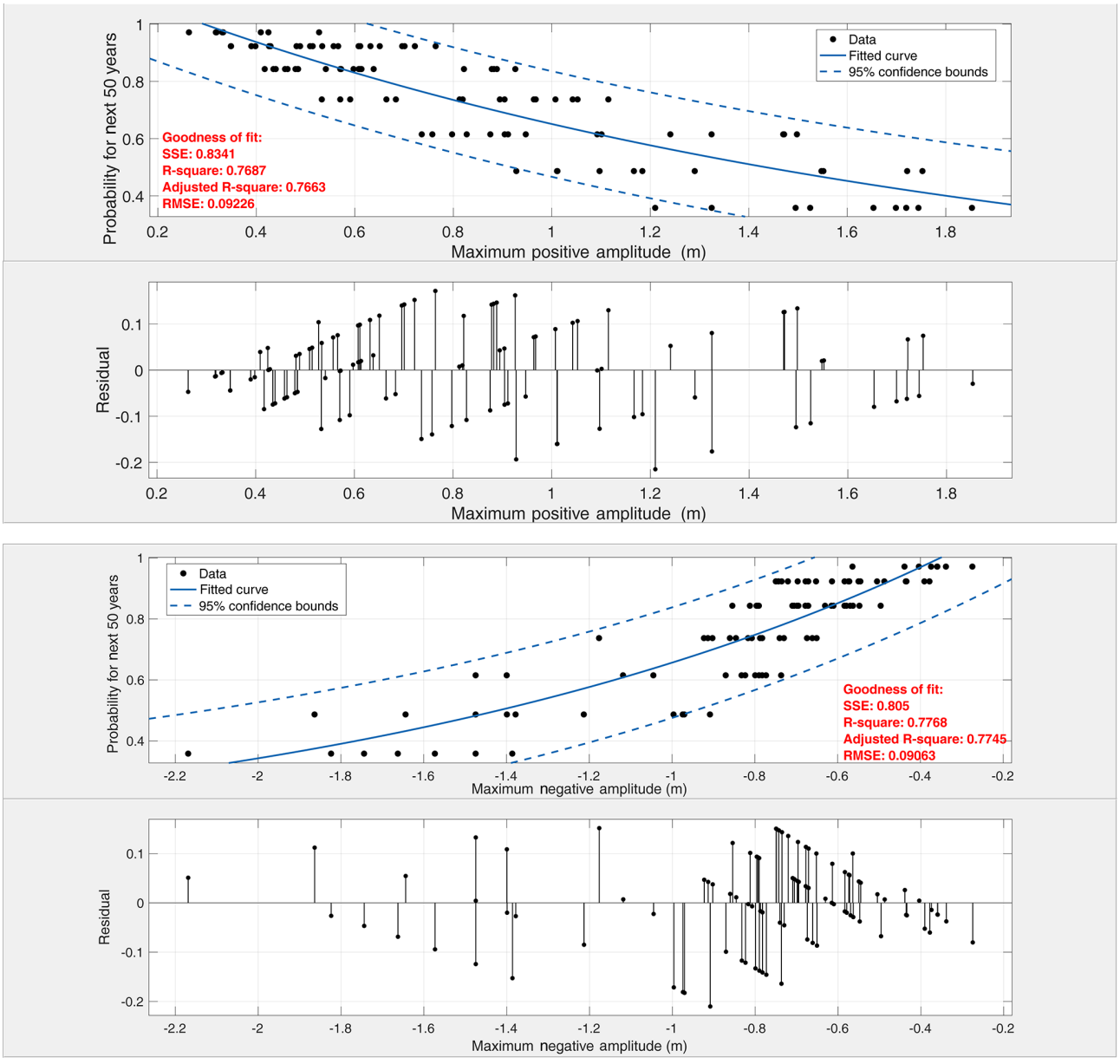

Figure 6.

In Fig. 6, graphics of probabilities of occurrences according to maximum and minimum water surface elevation (maximum water withdraw) and inundation depth for the next 50 years are represented. According to these graphs, tsunami wave heights up to 1 m and withdrawal of the waves around 1 m have approximately 65 % ± 15 % probability of occurrence. The Tuzla region includes various shipyards, ports, and other important facilities. Therefore, the probability of the withdrawal of the water is as important as maximum water surface elevation. The 1 m height of wave withdrawal may cause the ships to be stranded at the ports and results in extreme financial losses as observed in the 20 July 2017 Bodrum–Kos earthquake and tsunami (Yalçıner et al., 2017). The probability of having 1 m inundation depth, on the other hand, can be predicted as about 60 % ± 10 %. The residual of probability with respect to the fitted curve for each data point is demonstrated right after the percentage of probability with the ± sign.

The situation for the next 100 years (Fig. 7) obviously shows that probability of occurrences would increase with time. The probability of exceedance of 1 m water surface elevation and 1 m wave withdrawal reaches up to 85 % ± 10 %. Probability of exceedance of inundation depth also changes significantly. The probability of exceedance of 1 m inundation depth is found to be around 80 % ± 10 %.

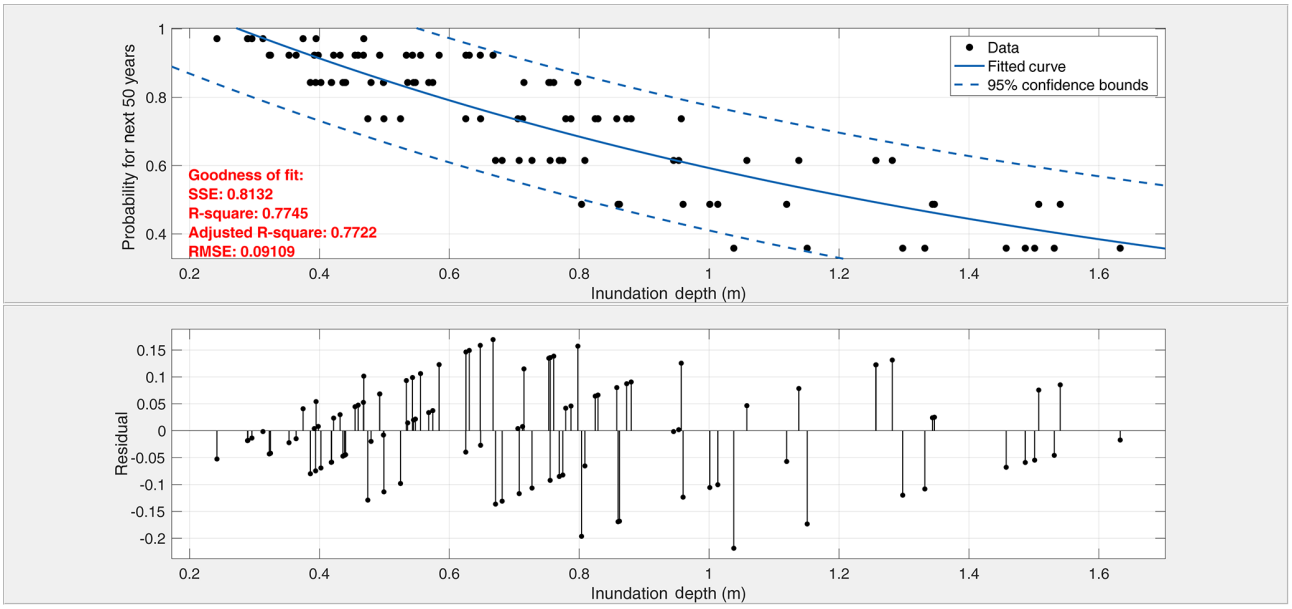

Figure 6. Probabilities of exceedance corresponding to maximum water surface elevation, minimum water surface elevation, and inundation depth for the next 50 years. Black dots represent the probability of exceedance of the tsunami hydrodynamic parameter for each event in the catalog. The blue line is the best fit curve to the data and the dashed blue line is the 95 % confidence boundary of the fitted curve. The residual of the fit is represented for each probability curve.

Considering the results of the whole simulation, the worst-case earthquake scenario generated tsunami waves with maximum water surface elevation equal to 1.8 m, minimum water surface elevation (maximum withdraw) equal to −2.1 m, and inundation depth equal to 1.6 m. The probability of occurrence of this event is 35 % for the next 50 years and 60 % for the next 100 years.

4.2 Probabilistic tsunami inundation maps for the Tuzla test site

Inundation maps of the Tuzla domain are also prepared for the next 50 and 100 years in the GIS environment. Even if inundation depth is on the order of a few centimeters, it can lead to people being dragged by undertow in coastal regions due to the high current velocities of the waves (Jonkman and Penning-Rowsell, 2008). Therefore, these inundation maps have a great significance for understanding the flooded areas in the study domain and the amount of water penetrated inland.

Generation of inundation maps is based on the probability of exceedance of 0.3 m inundation depth. There are several studies in the literature proving both experimentally and numerically that tsunami waves with an order of 0.3 m height have the potential to crush a human body (Jonkman and Penning-Rowsell, 2008; Takagi et al., 2016). For this reason, only the earthquake scenarios that generated inundation depths larger than or equal to the 0.3 m threshold value are considered.

Inundation depth files, which are one of the outputs of the NAMI DANCE, are used for the calculation.

The inundation depth values at each grid node are replaced with the probability of occurrence of the respective earthquake scenario. We repeated this procedure for all earthquake scenarios, which has inundation depths larger than or equal to the 0.3 m threshold.

The mean (average) probability of occurrence is calculated at each grid node. Thus, the spatial distribution of probability of exceedance of 0.3 m inundation depth in the inundation zone is obtained for a specific time interval (Fig. 8).

Figure 8 shows the inundation maps of Tuzla shipyard for the next 50 and 100 years. Most of the area in the Tuzla shipyard region has a probability of exceedance between 10 % and 20 % for the next 50 and 100 years. However, some places in the northern and southern parts of the area and inside the bay show larger than 75 % probability of inundation within the next 100 years. Maximum inundation distance is observed at around 60 m at the test site.

In Fig. 9, probabilistic inundation maps of one of the most important facilities in the study region are represented for the next 50 and 100 years. The area has high potential to be exposed to tsunami waves with a probability larger than 50 % for the next 50 years. In 100 years, this probability increases and varies between 75 % and 90 %. No significant inundation zone is observed along the coast of the seawall and the peninsula. This may be due to the high ground elevation of these zones. Tsunami waves are inundated up to 45 m inside the small bay. This inundation distance could cause severe dam-

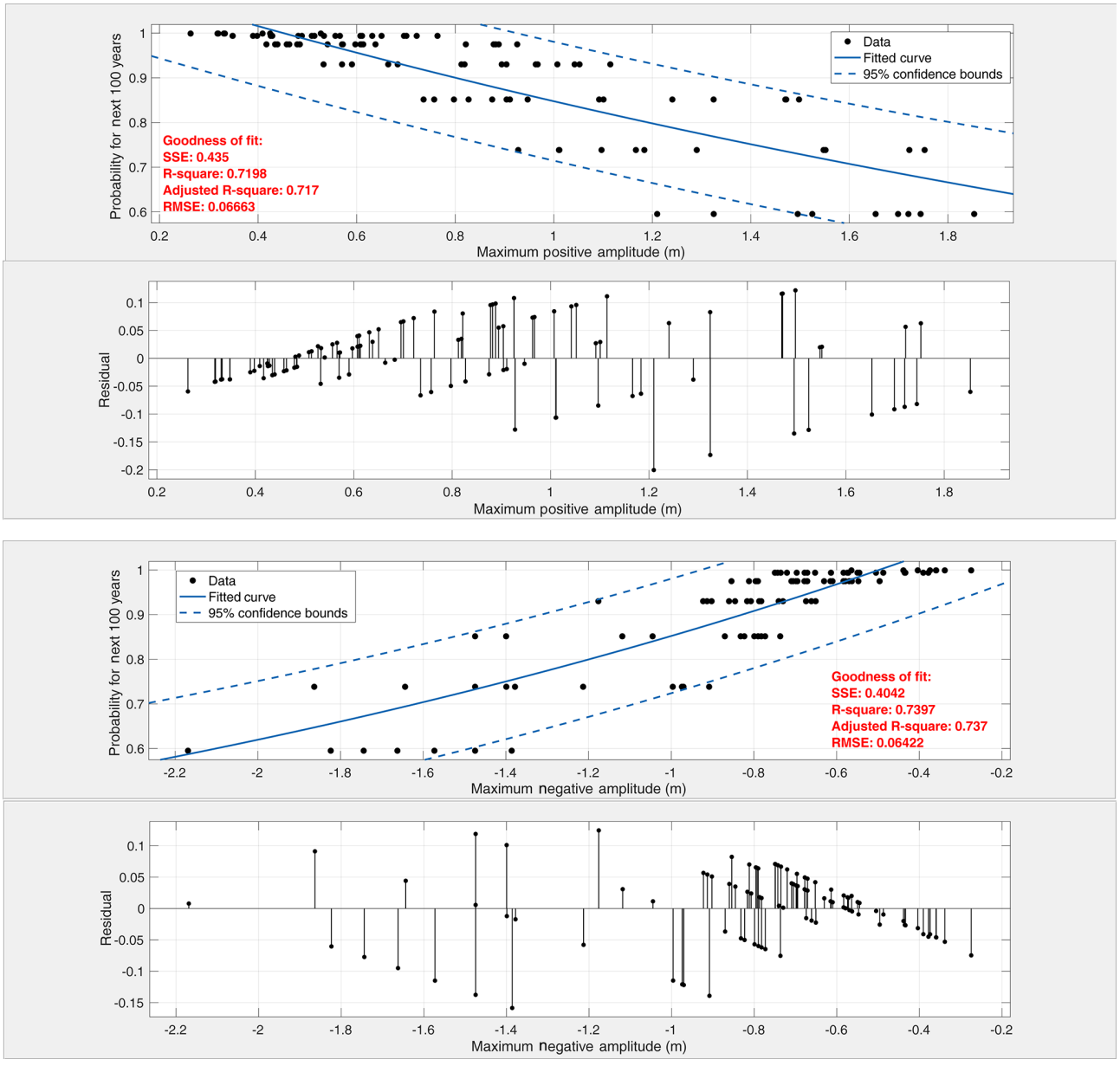

Figure 7.

age to the shipyard and other constructions if corresponding current velocities are also significant.

In the next figure (Fig. 10), the southern part of the Tuzla shipyard is seen according to probabilities of inundation for the next 50 and 100 years. Very limited area in the coastal zone is inundated with the probability between 30 % and 50 % within the next 50 years. The probability decreases up to 10 % at some inner locations from the coastline. For 100-year recurrence time, the situation is almost the same. Only minor parts of the region in the south approach the 75 %–90 % probability of exceedance of 0.3 m inundation depth threshold. The maximum inundation distance is calculated at about 60 m. The inundated region does not include any important facility or structure, and the effect of the tsunami will be minimal. The inundation distance decreases to 10 m in the other parts of the region.

The region indicated in Fig. 11 is located inside the bay and includes a large part of the shipyard area. This area includes lots of large and small piers and ship construction facilities. The situation is more or less the same as the previous region (Fig. 9). The probability of having larger than 0.3 m inundation depth changes between 30 % and 50 % within the next 50 years, while only a few places show 75 %–90 % probability for the next 100 years along the coast. Moreover, the maximum inundation distance is calculated as 25 m for this zone. Even if the probability of inundation is low, these zones

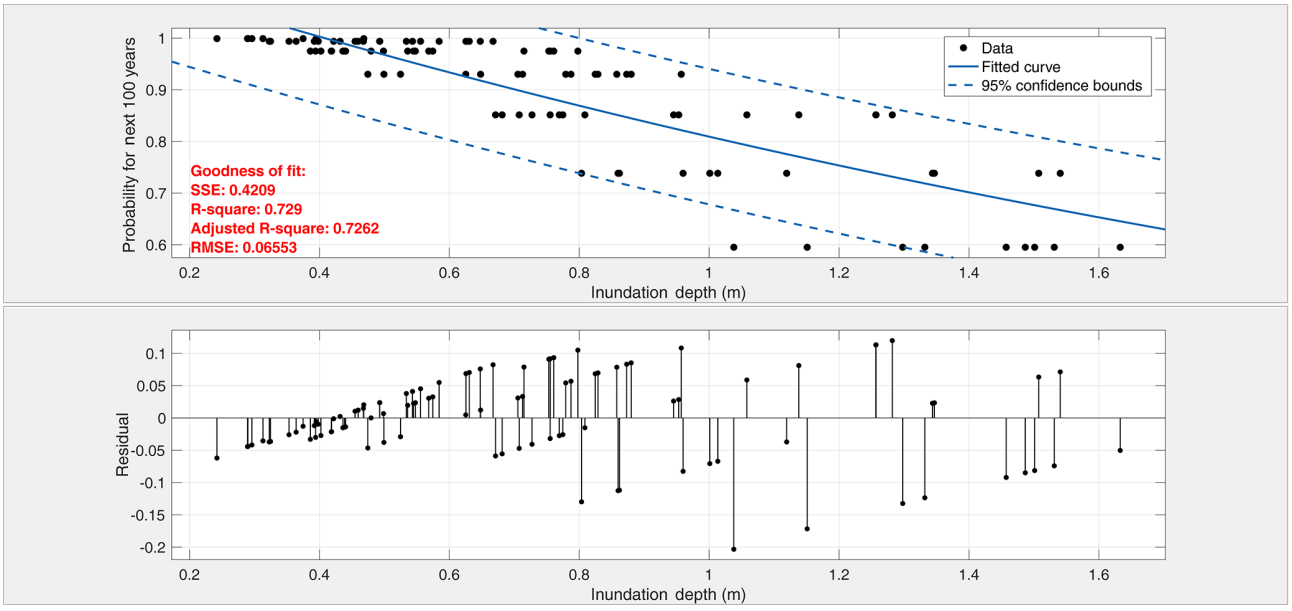

Figure 7. Probabilities of exceedance corresponding to maximum water surface elevation, minimum water surface elevation, and inundation depth for the next 100 years. Black dots represent the probability of exceedance of the tsunami hydrodynamic parameter for each event in the catalog. The blue line is the best fit curve to the data and the dashed blue line is the 95 % confidence boundary of the fitted curve. The residual of the fit is represented for each probability curve.

should be taken into consideration before constructing a new structure.

4.3 Synthetic gauges

Finally, the probability of exceedance of 0.3 m wave heights at synthetic gauge points is presented by bar charts to consider the nearshore effect of tsunami waves along the western coast of Istanbul. Because of the closeness to the fault zone, the southeast coasts of the city are under threat of significant tsunami damage. Similar to the method applied during the preparation of probabilistic inundation maps, the earthquake scenarios with wave heights at synthetic gauge points larger than or equal to 0.3 m are selected and replaced with the probability of each scenario according to wave heights, and after that the average probabilities at each synthetic gauge point are obtained accordingly.

Figure 12 demonstrates the probability of exceedance of 0.3 m wave height at synthetic gauge points, which are about 350 m apart from each other, along the western coast of Istanbul within the next 50 and 100 years. The probability increases while color scale changes from green to purple. According to this figure, minimum probability of exceedance is shown as 75 % at some points. Except for a few of the 228 synthetic gauge points, all points have larger than 90 % probability of exceedance of 0.3 m wave height within the next 50 years.

This condition is very serious since there are so many residential areas and important spots such as ports and recreational facilities in this region. The minimum probability of occurrence, which can generate tsunami waves with at least 0.3 m wave heights, reaches up to 90 % for the next 100-year time period. However, 95 % probability of exceedance of 0.3 m wave height dominates the region for this timescale.

4.4 Uncertainties

PTHA studies include some uncertainties because of the rare occurrence of the large events. Quantification of these uncertainties generally includes the mixture of empirical analyses and subjective judgment.

Uncertainties of PTHA can be divided into two: as aleatory and epistemic variability. Aleatoric uncertainty is the natural randomness of the physical process. Including more data in the analyses does not contribute to the reduction of the aleatoric uncertainty. However, knowledge about the modeling process may decrease this unpredictability. The occurrence time of the earthquake is one of the most fundamental aleatory variables in PTHA. This parameter is generally assumed to be a time-independent variable. However, in this study we used a time-dependent probability model, which reduces the uncertainty on this parameter. The mechanism of the source is considered to be another aleatory variable for PTHA studies. The majority of earthquakes around the world occur at well-defined plate boundaries. However, some unidentified low-activity intraplate faults exist, which were recently included in PTHA studies (Selva et al., 2016). Moreover, the fault volume, which is used in scaling relations to calculate the source magnitude, is another aleatory term. Although homogenous slip distribution is a common imple-

Figure 8. Probabilistic tsunami inundation maps for the Tuzla study domain representing the probability of exceedance of 0.3 m inundation depth within the next 50 and 100 years. Change of colors from green to red represents the increasing probability of exceedance (created using ArcMap version 10.5).

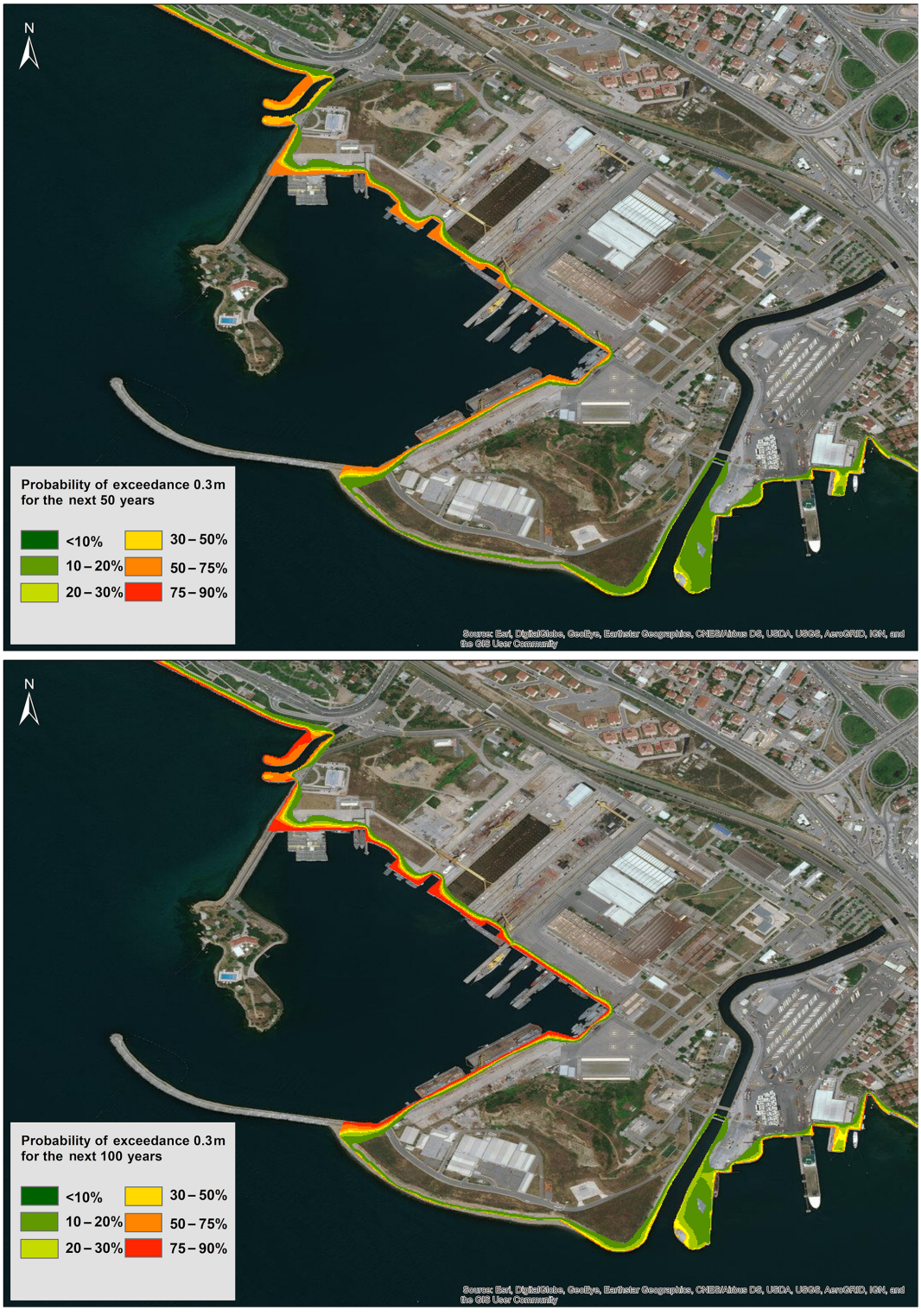

Figure 9. Probabilistic tsunami inundation maps of the northern part of the Tuzla study domain representing the probability of exceedance of 0.3 m inundation depth for the next 50 and 100 years. Change of colors from green to red represents the increasing probability of exceedance (created using ArcMap version 10.5).

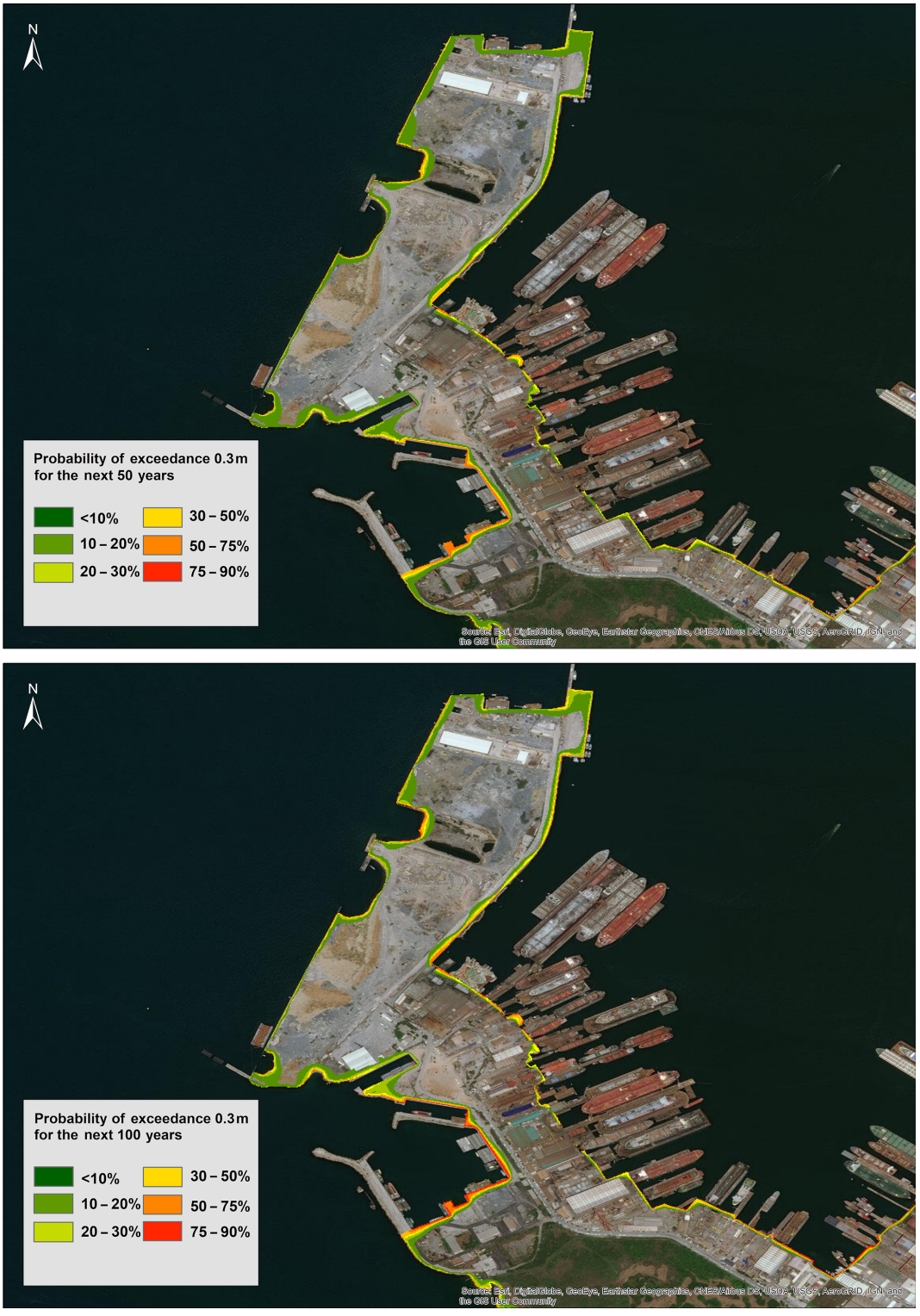

Figure 10. Probabilistic tsunami inundation maps for the southern part of the Tuzla study domain representing the probability of exceedance of 0.3 m inundation depth for the next 50 and 100 years. Change of colors from green to red represents the increasing probability of exceedance (created using ArcMap version 10.5).

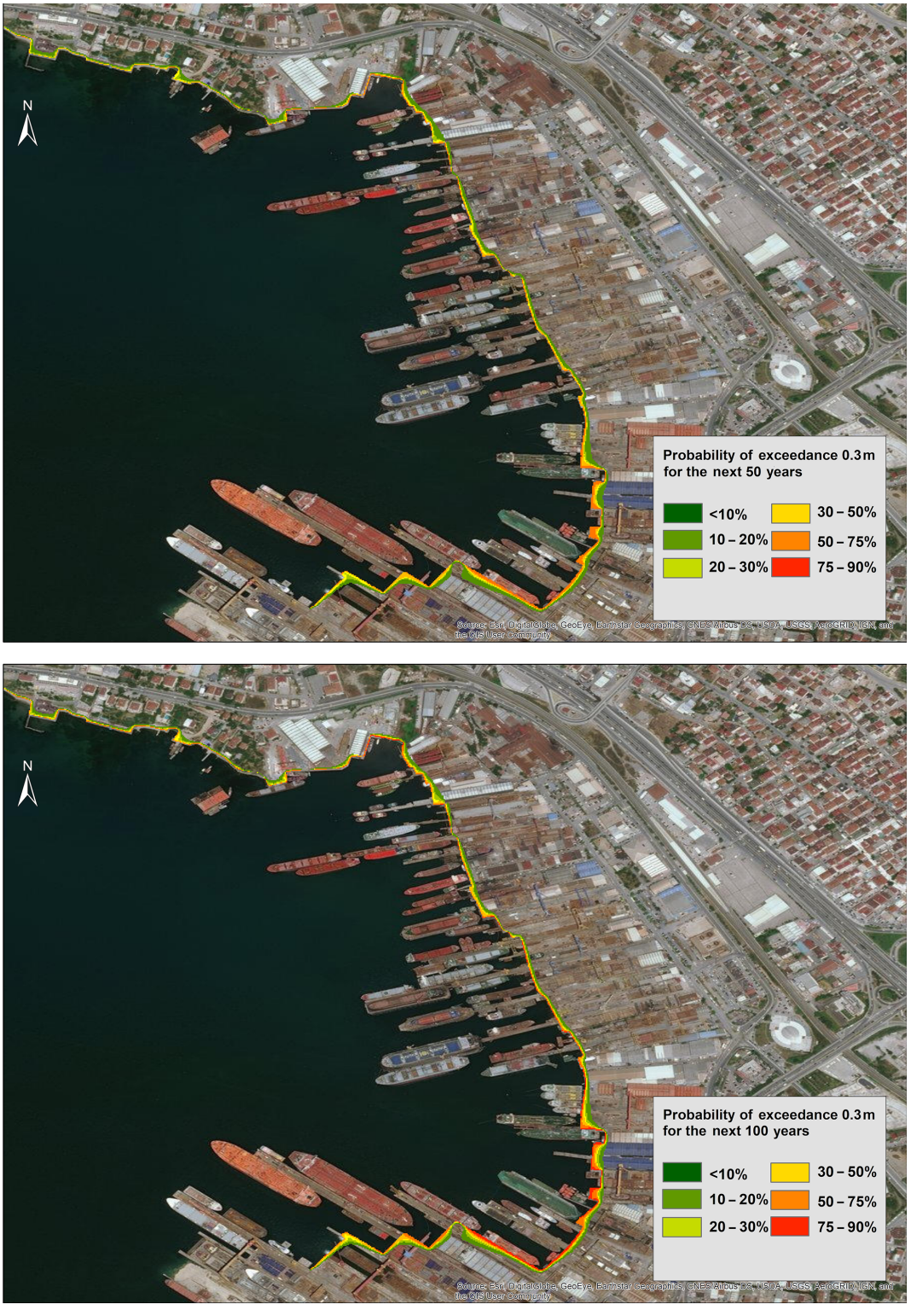

Figure 11. Probabilistic tsunami inundation maps of the shipyard area in the Tuzla study domain representing the probability of exceedance of 0.3 m inundation depth for the next 50 and 100 years. Change of colors from green to red represents the increasing probability of exceedance (created using ArcMap version 10.5).

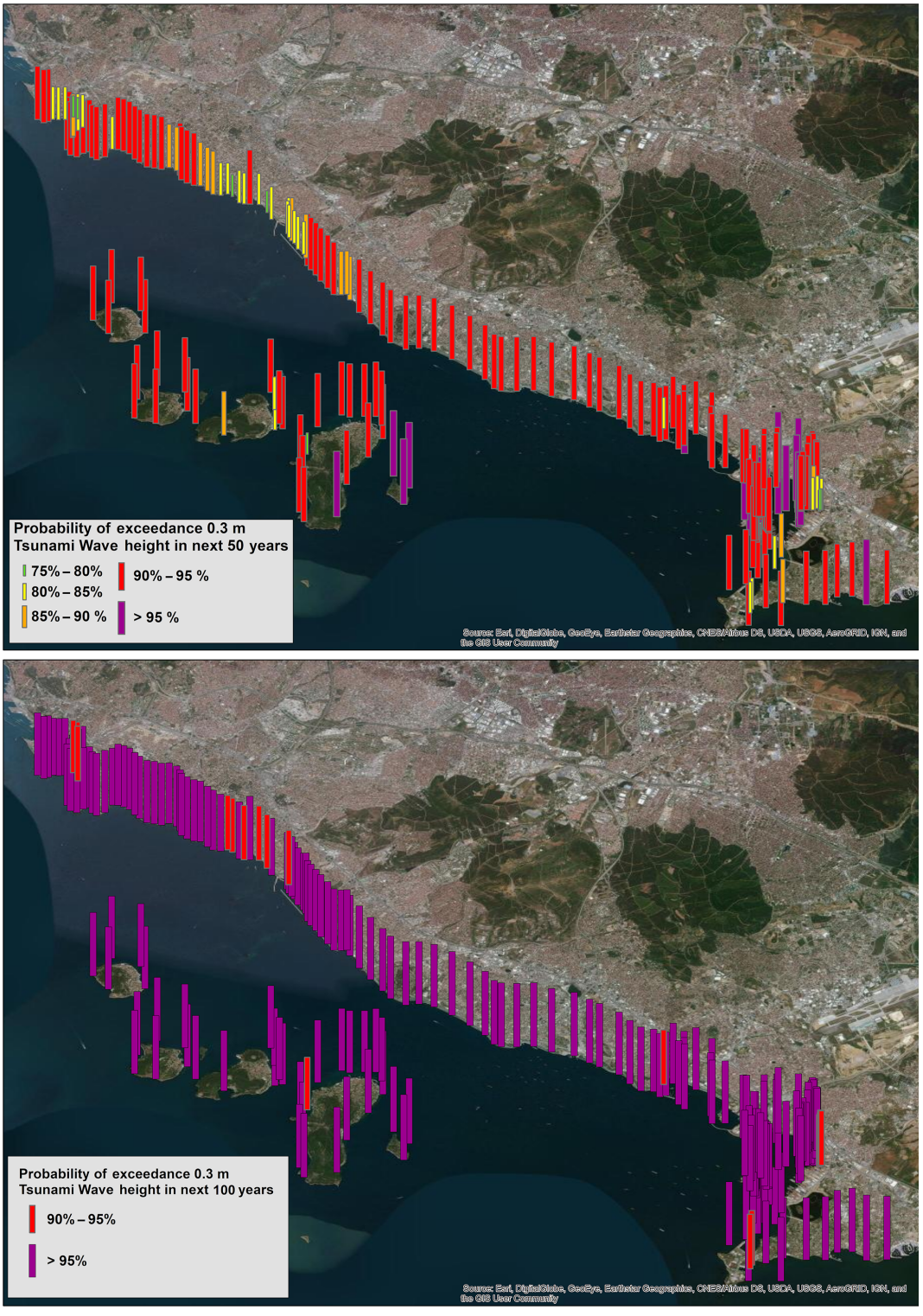

Figure 12. Probability of exceedance of the 0.3 m tsunami wave height within the next 50 and 100 years at synthetic gauge points. The yellow rectangles show the Tuzla study domain; change of colors from purple to green on the bars represents the decreasing probability of exceedance (created using ArcMap version 10.5).

mentation in PTHA, slip distribution of large events does not show homogenous behavior. Therefore, definition of asperities on the fault is another aleatoric variable which should be considered. Tsunami numerical modeling, itself, is also another aleatoric variable since they do not show correlation with real observations, which are more variable than earthquake scenarios incorporated in PTHA (Grezio et al., 2017). The aleatory variable affects the results because it is incorporated directly into the hazard calculations (Abrahamson and Bommer, 2005).

Epistemic uncertainty, on the other hand, consists of the lack of knowledge of the physical process and data. Segmentation of the fault system is one of the epistemic variables since it is not certain where the rupture will be generated and which segments will be triggered. In addition, there are many different scaling relations, which cause another epistemic uncertainty, between the fault area and magnitude. It is also important for tsunami generation whether the fault rupture reaches the surface or not. Thus, updip and downdip limits of the fault rupture can be considered another epistemic variable (Grezio et al., 2017). Accurate probability distributions of input cannot be known. For example, one cannot assume that probability of occurrence of an event follows Poisson distribution. However, return periods of events do not simply fit this distribution (Gonzalez et al., 2013). Unlike aleatoric uncertainty, epistemic uncertainty can be decreased when more information is available (Godinho, 2007). Different techniques, such as logic tree, the Bayesian method, etc., have been developed to reduce these uncertainties.

In this study, a probabilistic model is established based on the characteristic fault model of PIF, which is a segment of NAF, one of the best studied fault zones in the world. It is also assumed that the entire fault area is ruptured, reaching the surface and generating a homogenous slip for each event. The maximum magnitude range of the fault is calculated with the Wells and Coppersmith (1994) scaling relation. All these assumptions naturally include uncertainties which are naturally reflected in this PTHA study. In addition, MC simulation itself also includes uncertainty as being performed 100 times to create synthetic earthquake scenarios. The effect of uncertainty in the aperiodicity parameter also exists and can be reduced by including different parameters for MC simulation. Therefore, the tsunami hydrodynamic parameters associated with the probability of occurrence of the corresponding scenario preserve the same uncertainty.

5 Conclusion

In this study, time-dependent PTHA is performed in the Tuzla region of Istanbul for the purpose of understanding the probability of having tsunami inundation after the PIF rupture. The study combines tsunami numerical modeling with a probabilistic approach, which is modified by probabilistic seismic hazard analysis. Probability calculations have been done based on the time-dependent BPT model, which depends on the time period passed since the last characteristic event and the recurrence time of the earthquake. After that, the synthetic earthquake catalogue is generated using the MC simulation technique, and tsunami numerical modeling was performed depending on this earthquake catalogue using NAMI DANCE code in a GPU environment.

Results of this PTHA study were presented in three different ways for the next 50 and 100 years. The first one was the graphs showing the change of probability with the maximum and minimum water surface elevation and inundation depth for different time intervals. Secondly, the probabilistic tsunami inundation maps are generated for the Tuzla region. Finally, the probability maps of exceedance of 0.3 m wave heights at synthetic gauge points are represented with bar charts.

The main results of this study can be summarized as follows.

- According to the distribution of probability with respect to tsunami hydrodynamic parameters, the probability of exceedance of 1 m maximum positive and negative water surface elevation is 65 % within the next 50 years. The probability for 1 m inundation depth is 60 %.

- Considering probabilities for the next 100 years, 85 % probability of exceedance of 1 m was calculated. For 1 m inundation depth, probability of exceedance of about 80 % is obtained.

- As a result of the whole simulation, 1.8, −2.1, and 1.6 m were calculated for maximum and minimum water surface elevation and inundation depth, with the probability of 35 % for the next 50 years and 60 % for the next 100 years.

- Inundation maps indicate that inundation of tsunami waves that are equal to or larger than 0.3 m have probability mostly higher than 10 % and 20 % for the next 50 years and 100 years, respectively. The probability of occurrence of 0.3 m inundation depth was calculated as a maximum of 75 % for the next 100 years. Maximum inundation distance is calculated as 60 m and observed in the southern part of the finest 3 m grid-sized study area.

- Probabilistic results for the exceedance of 0.3 m wave height at synthetic gauge points demonstrate that only a few of them have a probability between 75 % and 85 %; however several points have more than 90 % probability for the next 50 years. Probability of exceedance increases by more than 95 % for the next 100 years.

The tsunami impact of the PIF rupture along the Tuzla coast is very important as proposed by the results of this study. However, as further steps of this study, PTHA can be done for the other critical test sites along the Marmara Sea that

are close to the PIF segment. In addition, it is also advantageous to consider the other fault segments, with their various rupture combinations and complex rupture probabilities in Marmara Sea, as further studies. Previously in the framework of the MARSITE project, tsunami arrival times and maximum wave amplitudes were calculated along the coast of the Marmara Sea using different earthquake scenarios, and a tsunami scenario database was obtained with a deterministic approach (Ozer Sozdinler et al., 2020). Results of this study show that arrival time of tsunami waves is very short in Marmara Sea for most of the scenarios, which complicates the tsunami early warning operations and evacuation actions. However, due to the short arrival times of the first tsunami waves along the Marmara coast, the tsunami inundation scenario databases would be of great importance in such conditions. It would be the best option for the decision makers and civil protection authorities to also have the inundation maps prepared with a probabilistic approach in order to realize the possibility of exceedance of selected threshold inundation depth for certain critical coastal locations.

This study shows a methodology for PTHA with a time-dependent probabilistic model using only one fault (PIF) as the earthquake and tsunami source. Furthermore, this study can be developed including some faults connected to the PIF in both time-dependent and time-independent probability calculations, and BPT probability can be combined with static Coulomb stress changes on the faults. The BPT model can also be improved by including different aperiodicity parameters. The probability of occurrence of earthquakes is the main focus of this study to perform tsunami hazard analyses. However, submarine landslides are other critically important sources for tsunami generation in the Marmara Sea. Probabilities of sliding areas and the sliding volumes can be considered in the analyses. Submarine landslide-generated tsunamis can be coupled with the earthquake-triggered tsunamis in order to obtain integrated PTHA in the Marmara Sea.

Data availability. Data of scenarios used in tsunami numerical modeling, inputs for probabilistic tsunami inundation map for 50 and 100 years, and *.kml files for probability of exceedance in bar charts can be accessed at https://doi.org/10.6084/m9.figshare.12033789 (last access: 27 March 2020) (Bayraktar, 2020). Further information can be made available upon request to the corresponding author.

Author contributions. HBB performed background research, constructed the database, carried out tsunami simulations, mapped the tsunami inundation maps, and wrote the paper. COS supervised the entire study in all stages and contributed to writing the paper.

Competing interests. The authors declare that they have no conflict of interest.

Acknowledgements. The authors would like to acknowledge the project MARSITE – New Directions in Seismic Hazard assessment through Focused Earth Observation in the Marmara Supersite (FP7-ENV.2012 6.4-2, grant 308417) and the SATREPS project. The authors would like to especially thank Ahmet Cevdet Yalçıner for his valuable feedback and effort during this study and Bora Yalçıner and Andrey Zaitsev for their great support in the development and improvement of the NAMI DANCE numerical code. We would also like to thank Öcal Necmioğlu, Maura Murru, Giuseppe Falcone, Semih Ergintav, Sinan Akkar, Mine Demircioğlu, and Mustafa Erdik for their valuable support and feedback. The Generic Mapping Tools (GMT; Wessel and Smith, 1998) was used for plotting a tectonic map of Turkey and bathymetric map of the Marmara fault system. Other maps throughout this paper were created using ArcGIS® software by Esri. ArcGIS® and ArcMap™ are the intellectual property of Esri and are used herein under license. Copyright © Esri. All rights reserved. For more information about Esri® software, please visit https://www.esri.com/en-us/home (last access: 16 February 2020).

Financial support. This research has been supported by the project MARSITE – New Directions in Seismic Hazard assessment through Focused Earth Observation in the Marmara Supersite (grant no. 308417).

Review statement. This paper was edited by Ira Didenkulova and reviewed by two anonymous referees.

References

Abrahamson, N. A. and Bommer, J. J.: Probability and uncertainty in seismic hazard analysis, Earthq. Spect., 21, 603–607, https://doi.org/10.1193/1.1899158, 2005.

Aki, K.: Asperities, barriers, characteristic earthquakes and strong motion prediction, J. Geophys. Res.-Solid, 89, 5867–5872, https://doi.org/10.1029/JB089iB07p05867, 1984.

Aki, K.: Generation and propagation of G waves from the Niigata Earthquake of June 16 1964. Part 2. Estimation of earthquake movement, released energy, and stress-strain drop from the G wave spectrum, Bull. Earthq. Res. Inst., 44, 73–88, 1966.

Aksu, A. E., Calon, T. J., Hiscott, R. N., and Yasar, D.: Anatomy of the North Anatolian Fault Zone in the Marmara Sea, Western Turkey: extensional basins above a continental transform, GSA Today, 10, 3–7, 2000.

Allen, C. R.: The tectonic environments of seismically active and inactive areas along the San Andreas fault system, Stanford University Publications, Geol. Sci., 11, 70–80, 1968.

Alpar, B. and Yaltırak, C.: Characteristic features of the North Anatolian Fault in the eastern Marmara region and its tectonic evolution, Mar. Geol., 190, 329–350, https://doi.org/10.1016/S0025-3227(02)00353-5, 2002.

Altınok, Y. and Alpar, B.: Marmara Island earthquakes, of 1265 and 1935; Turkey, Nat. Hazards Earth Syst. Sci., 6, 999–1006, https://doi.org/10.5194/nhess-6-999-2006, 2006.

Altınok, Y., Alpar, B., and Yaltırak, C.: Şarköy-Mürefte 1912 earthquake's tsunami, extension of the associated faulting

in the Marmara Sea, Turkey, J. Seismol., 7, 329–346, https://doi.org/10.1023/A:1024581022222, 2003.

Altinok, Y., Alpar, B., Özer, N., and Aykurt, H.: Revision of the tsunami catalogue affecting Turkish coasts and surrounding regions, Nat. Hazards Earth Syst. Sci., 11, 273–291, https://doi.org/10.5194/nhess-11-273-2011, 2011.

Ambraseys, N.: The seismic activity of the Marmara Sea region over the last 2000 years, Bull. Seismol. Soc. Am., 92, 1–18, https://doi.org/10.1785/0120000843, 2002.

Ambraseys, N. N. and Jackson, J. A.: Seismicity of the Sea of Marmara (Turkey) since 1500, Geophys. J. Int., 141, F1–F6, https://doi.org/10.1046/j.1365-246x.2000.00137.x, 2000.

Ambraseys, N. N. N. and Finkel, C. F.: Seismicity of Turkey and Adjacent Areas: A Historical Review 1500–1800, MS Eren, Istanbul, Turkey, 1995.

Annaka, T., Satake, K., Sakakiyama, T., Yanagisawa, K., and Shuto, N.: Logic-tree approach for probabilistic tsunami hazard analysis and its applications to the Japanese coasts, in: Tsunami and its hazards in the indian and pacific oceans, Birkhäuser, Basel, 577–592, https://doi.org/10.1007/978-3-7643-8364-0_17, 2007.

Armijo, R., Meyer, B., Hubert, A., and Barka, A.: Westward propagation of the North Anatolian fault into the northern Aegean: Timing and kinematics, Geology, 27, 267–270, https://doi.org/10.1130/0091-7613(1999)027<0267:WPOTNA>2.3.CO;2, 1999.

Armijo, R., Meyer, B., Navarro, S., King, G., and Barka, A.: Asymmetric slip partitioning in the Sea of Marmara pull-apart: A clue to propagation processes of the North Anatolian fault?, Terra Nova, 14, 80–86, https://doi.org/10.1046/j.1365-3121.2002.00397.x, 2002.

Armijo, R., Pondard, N., Meyer, B., Uçarkus, G., de Lépinay, B. M., Malavieille, J., Dominguez, S., Gustcher, M. A., Schmidt, S., Beck, C., Cagatay, N., Çakır, Z., Imren, C., Eris, K., Natalin, B., Özalaybey, S., Tolun, L., Lefèvre, I., Seeber, L., Gasperini, L., Rangin, C., Emre, O., and Sarikavak, K.: Submarine fault scarps in the Sea of Marmara pull-apart (North Anatolian Fault): Implications for seismic hazard in Istanbul, Geochem. Geophy., Geosy., 6, Q06009, https://doi.org/10.1029/2004GC000896, 2005.

Aytore, B., Yalciner, A. C., Zaytsev, A., Cankaya, Z. C., and Suzen, M. L.: Assessment of tsunami resilience of Haydarpaşa Port in the Sea of Marmara by high-resolution numerical modeling, Earth Planets Space, 68, 139, https://doi.org/10.1186/s40623-016-0508-z, 2016.

Barka, A.: The 17 august 1999 Izmit earthquake, Science, 285, 1858–1859, https://doi.org/10.1126/science.285.5435.1858, 1999.

Bayraktar, H. B.: Tuzla-PTHA, https://doi.org/10.6084/m9.figshare.12033789, 2020.

Bohnhoff, M., Bulut, F., Dresen, G., Malin, P. E., Eken, T., and Aktar, M.: An earthquake gap south of Istanbul, Nat. Commun., 4, 1999, https://doi.org/10.1038/ncomms2999, 2013.

Cankaya, Z. C., Suzen, M. L., Yalciner, A. C., Kolat, C., Zaytsev, A., and Aytore, B.: A new GIS-based tsunami risk evaluation: MeTHuVA (METU tsunami human vulnerability assessment) at Yenikapı, Istanbul, Earth Planets Space, 68, 133, https://doi.org/10.1186/s40623-016-0507-0, 2016.

Cramer, C. H., Petersen, M. D., Cao, T., Toppozada, T. R., and Reichle, M.: A time-dependent probabilistic seismic-hazard model for California, Bull. Seismol. Soc. Am., 90, 1–21, https://doi.org/10.1785/0119980087, 2000.

Davis, P. M., Jackson, D. D., and Kagan, Y. Y.: The longer it has been since the last earthquake, the longer the expected time till the next?, Bull. Seismol. Soc. Am., 79, 1439–1456, 1989.

Earthquake Research Committee: Evaluation method and its application for the probability of long-term earthquke occurrence, Headquarters for Earthquake Research Promotion, Tokyo, 2001.

Ellsworth, W. L., Matthews, M. V., Nadeau, R. M., Nishenko, S. P., Reasenberg, P. A., and Simpson, R. W.: A physically-based earthquake recurrence model for estimation of long-term earthquake probabilities, US Geol. Surv. Open-File Rept. 99, US Geological Survey, Menlo Park, CA, 23 pp., 1999.

Emre, Ö., Duman, T. Y., Özalp, S., Elmacı, H., Olgun, Ş., and Şaroğlu, F.: Active fault map of Turkey with explanatory text, General Directorate of Mineral Research and Exploration Special Publication Series, Ankara, Turkey, p. 30, 2013.

Erdik, M., Demircioglu, M., Sesetyan, K., Durukal, E., and Siyahi, B.: Earthquake hazard in Marmara region, Turkey, Soil Dynam. Earthq. Eng., 24, 605–631, https://doi.org/10.1016/j.soildyn.2004.04.003, 2004.

Ergintav, S., Reilinger, R. E., Çakmak, R., Floyd, M., Cakir, Z., Doğan, U., and Özener, H.: Istanbul's earthquake hot spots: Geodetic constraints on strain accumulation along faults in the Marmara seismic gap, Geophys. Res. Lett., 41, 5783–5788, https://doi.org/10.1002/2014GL060985, 2014.

Flerit, F., Armijo, R., King, G. C. P., Meyer, B., and Barka, A.: Slip partitioning in the Sea of Marmara pull-apart determined from GPS velocity vectors, Geophys. J. Int., 154, 1–7, https://doi.org/10.1046/j.1365-246X.2003.01899.x, 2003.

Flerit, F., Armijo, R., King, G., and Meyer, B.: The mechanical interaction between the propagating North Anatolian Fault and the back-arc extension in the Aegean, Earth Planet. Sc. Lett., 224, 347–362, https://doi.org/10.1016/j.epsl.2004.05.028, 2004.

Gasperini, L., Polonia, A., Çağatay, M. N., Bortoluzzi, G., and Ferrante, V.: Geological slip rates along the North Anatolian Fault in the Marmara region, Tectonics, 30, TC6001, https://doi.org/10.1029/2011TC002906, 2011.

Geist, E. L. and Lynett, P. J.: Source processes for the probabilistic assessment of tsunami hazards, Oceanography, 27, 86–93, https://doi.org/10.5670/oceanog.2014.43, 2014.

Geist, E. L. and Parsons, T.: Probabilistic analysis of tsunami hazards, Nat. Hazards, 37, 277–314, https://doi.org/10.1007/s11069-005-4646-z, 2006.

Goda, K. and De Risi, R.: Multi-hazard loss estimation for shaking and tsunami using stochastic rupture sources, Int. J. Disast. Risk Reduct., 28, 539–554, https://doi.org/10.1016/j.ijdrr.2018.01.002, 2018.

Godinho, J.: Probabilistic Seismic Hazard Analysis an Introduction to Theoretical Basis and Applied Methodology, Msc thesis, University of Patras, Greece, 2007.

González, F. I., Geist, E. L., Jaffe, B., Kânoğlu, U., Mofjeld, H., Synolakis, C. E., Titov, V. V., Arcas, D., Bellomo, D., Carlton, D., Horning, T., Johnson, J., Newman, J., Parsons, T., Peters, R., Peterson, C., Priest, G., Venturato, A., Weber, J., Wong, F., and Yalciner, A.: Probabilistic tsunami hazard assessment at seaside, Oregon, for near-and far-field seismic sources, J. Geophys. Res.-Oceans, 114, C11023, https://doi.org/10.1029/2008JC005132, 2009.

Gonzalez, F. I., LeVeque, R. J., and Adams, L. M.: Probabilistic Tsunami Hazard Assessment (PTHA) for Crescent City, CA, Final Report for Phase I, University of Washington, Department of Applied Mathmatics, Washington, available at: http://hdl.handle.net/1773/25916 (last access: 18 April 2019), 2013.

Grezio, A., Babeyko, A., Baptista, M. A., Behrens, J., Costa, A., Davies, G., Geist, E. L., Glimsdal, S., González, F. I., Griffin, J., Harbitz, C. B., LeVeque, R. J., Lorito, S., Løvholt, F., Omira, R., Mueller, C., Paris, R., Parsons, T., Polet, J., Power, W., Selva, J., Sørensen, M. B., Thio, H. K., and Harbitz, C. B.: Probabilistic tsunami hazard analysis: Multiple sources and global applications, Rev. Geophys., 55, 1158–1198, https://doi.org/10.1002/2017RG000579, 2017.

Guler, H. G., Arikawa, T., Oei, T., and Yalciner, A. C.: Performance of rubble mound breakwaters under tsunami attack, a case study: Haydarpasa Port, Istanbul, Turkey, Coast. Eng., 104, 43–53, https://doi.org/10.1016/j.coastaleng.2015.07.007, 2015.

Gutenberg, B. and Richter, C. F.: Frequency of earthquakes in California, Bull. Seismol. Soc. Am., 34, 185–188, 1944.

Hancilar, U.: Identification of elements at risk for a credible tsunami event for Istanbul, Nat. Hazards Earth Syst. Sci., 12, 107–119, https://doi.org/10.5194/nhess-12-107-2012, 2012.

Hébert, H., Schindele, F., Altinok, Y., Alpar, B., and Gazioglu, C.: Tsunami hazard in the Marmara Sea (Turkey): a numerical approach to discuss active faulting and impact on the Istanbul coastal areas, Mar. Geol., 215, 23–43, https://doi.org/10.1016/j.margeo.2004.11.006 ,2005.

Hergert, T. and Heidbach, O.: Slip-rate variability and distributed deformation in the Marmara Sea fault system, Nat. Geosci., 3, 132–135, https://doi.org/10.1038/ngeo739, 2010.

Hergert, T., Heidbach, O., Bécel, A., and Laigle, M.: Geomechanical model of the Marmara Sea region – I. 3-D contemporary kinematics, Geophys. J. Int., 185, 1073–1089, https://doi.org/10.1111/j.1365-246X.2011.04991.x, 2011.

Horspool, N., Pranantyo, I., Griffin, J., Latief, H., Natawidjaja, D. H., Kongko, W., Cipta, A., Bustaman, B., Anugrah, S. D., and Thio, H. K.: A probabilistic tsunami hazard assessment for Indonesia, Nat. Hazards Earth Syst. Sci., 14, 3105–3122, https://doi.org/10.5194/nhess-14-3105-2014, 2014.

Imamura, F.: Tsunami Numerical Simulation with the Staggered Leap-frog Scheme (Numerical code of TUNAMI-N1), School of Civil Engineering, Asian Institute Technical and Disaster Control Research Center, Tohoku University, Tohoku, 1989.

Imamura, F., Yalçıner, A. C., and Özyurt, G.: TUNAMI-N2: Tsunami Modelling Manual, available at: http://www.tsunami.civil.tohoku.ac.jp/hokusai3/J/projects/manual-ver-3.1.pdf (last access: 20 March 2019), 2001.

Imren, C., Le Pichon, X., Rangin, C., Demirbağ, E., Ecevitoğlu, B., and Görür, N.: The North Anatolian Fault within the Sea of Marmara: a new interpretation based on multi-channel seismic and multi-beam bathymetry data, Earth Planet. Sc. Lett., 186, 143–158, https://doi.org/10.1016/S0012-821X(01)00241-2, 2001.

Insel, I.: The Effects of the Material Density and Dimensions of the Landslide on the Generated Tsunamis, Msc Thesis, Middle East Technical University, Ankara, Turkey, 2009.

Jonkman, S. N. and Penning-Rowsell, E.: Human instability in Flood Flows, J. Am. Water Resour. Assoc., 44, 1208–1218, https://doi.org/10.1111/j.1752-1688.2008.00217.x, 2008.

Kanamori, H.: The diversity of the physics of earthquakes, Proc. Japan Acad. Ser. B, 80, 297–316, https://doi.org/10.2183/pjab.80.297, 2004.

Kaneko, F.: A simulation analysis of possible tsunami affecting the Istanbul coast, Turkey, in: International Workshop on Tsunami Hazard Assessment and Management in Bangladesh, 21–22 January 2009, Dhaka, Bangladesh, 2009.

Karabulut, H., Bouin, M. P., Bouchon, M., Dietrich, M., Cornou, C., and Aktar, M.: The seismicity in the eastern Marmara Sea after the 17 August 1999 Izmit earthquake, Bull. Seismol. Soc. Am., 92, 387–393, https://doi.org/10.1785/0120000820, 2002.

Karabulut, H., Özalaybey, S., Taymaz, T., Aktar, M., Selvi, O., and Kocaoğlu, A.: A tomographic image of the shallow crustal structure in the Eastern Marmara, Geophys. Res. Lett, 30, 2277, https://doi.org/10.1029/2003GL018074, 2003.

KOERI – Kandilli Observatory and Earthquake Research Institute: Bosphorus Univercity: Bogazici University Kandilli Observatory And Earthquake Research Institute, International Federation of Digital Seismograph Networks, Dataset/Seismic Network, https://doi.org/10.7914/SN/KO, 2001.

Latcharote, P., Suppasri, A., Imamura, F., Aytore, B., and Yalciner, A. C.: Possible worst-case tsunami scenarios around the Marmara Sea from combined earthquake and landslide sources, in: Global Tsunami Science: Past and Future, Vol. I, Birkhäuser, Cham, 3823–3846, https://doi.org/10.1007/s00024-016-1411-z, 2016.

Le Pichon, X., Şengör, A. M. C., Demirbağ, E., Rangin, C., Imren, C., Armijo, R., Görür, N., Çağatay, N., de Lépinay, B. M., Meyer, B., Saatçılar, R., and Tok, B.: The active main Marmara fault, Earth Planet. Sc. Lett., 192, 595–616, https://doi.org/10.1016/S0012-821X(01)00449-6, 2001.

Le Pichon, X., Chamot-Rooke, N., Rangin, C., and Sengör, A. M. C.: The North Anatolian fault in the sea of Marmara, J. Geophys. Res.-Solid, 108, 2179, https://doi.org/10.1029/2002JB001862, 2003.

Le Pichon, X., Imren, C., Rangin, C., Şengör, A. C., and Siyako, M.: The South Marmara Fault, Int. J. Earth Sci., 103, 219–231, https://doi.org/10.1007/s00531-013-0950-0, 2014.

Le Pichon, X., Şengör, A. C., Kende, J., İmren, C., Henry, P., Grall, C., and Karabulut, H.: Propagation of a strike-slip plate boundary within an extensional environment: the westward propagation of the North Anatolian Fault, Can. J. Earth Sci., 53, 1416–1439, https://doi.org/10.1139/cjes-2015-0129, 2015.

Lorito, S., Selva, J., Basili, R., Romano, F., Tiberti, M. M., and Piatanesi, A.: Probabilistic hazard for seismically induced tsunamis: accuracy and feasibility of inundation maps, Geophys. J. Int., 200, 574–588, https://doi.org/10.1093/gji/ggu408, 2015.

Løvholt, F., Glimsdal, S., Harbitz, C. B., Zamora, N., Nadim, F., Peduzzi, P., and Smebye, H.: Tsunami hazard and exposure on the global scale, Earth-Sci. Rev., 110, 58–73, https://doi.org/10.1016/j.earscirev.2011.10.002, 2012.

Løvholt, F., Griffin, J., and Salgado-Gálvez, M.: Tsunami hazard and risk assessment at a global scale, Encyclopedia of complexity and systems science, 1–34, https://doi.org/10.1007/978-3-642-27737-5_642-1, 2015.

Lynett, P. J., Gately, K., Wilson, R., Montoya, L., Arcas, D., Aytore, B., and David, C. G.: Inter-model analysis of tsunami-induced coastal currents, Ocean Model., 114, 14–32, https://doi.org/10.1016/j.ocemod.2017.04.003, 2017.

Matthews, M. V., Ellsworth, W. L., and Reasenberg, P. A.: A Brownian model for recurrent earthquakes, Bull. Seismol. Soc. Am., 92, 2233–2250, https://doi.org/10.1785/0120010267, 2002.

McNeill, L. C., Mille, A., Minshull, T. A., Bull, J. M., Kenyon, N. H., and Ivanov, M.: Extension of the North Anatolian Fault into the North Aegean Trough: Evidence for transtension, strain partitioning, and analogues for Sea of Marmara basin models, Tectonics, 23, TC2016, https://doi.org/10.1029/2002TC001490, 2004.

Meade, B. J., Hager, B. H., McClusky, S. C., Reilinger, R. E., Ergintav, S., Lenk, O., Barka, A., and Özener, H.: Estimates of seismic potential in the Marmara Sea region from block models of secular deformation constrained by Global Positioning System measurements, Bull. Seismol. Soc. Am., 92, 208–215, https://doi.org/10.1785/0120000837, 2002.

Murru, M., Akinci, A., Falcone, G., Pucci, S., Console, R., and Parsons, T.: $M \geq 7$ earthquake rupture forecast and time-dependent probability for the Sea of Marmara region Turkey, J. Geophys. Res.-Solid, 121, 2679–2707, https://doi.org/10.1002/2015JB012595, 2016.

NAMI DANCE: Manual of Numerical Code NAMI DANCE, available at: http://namidance.ce.metu.edu.tr (last access: 12 October 2018), 2011.

NTHMP: Proceedings and Results of the National Tsunami Hazard Mitigation Program 2015 Tsunami Current Modeling Workshop, Portland, Oregon, 2015.

Oglesby, D. D. and Mai, P. M.: Fault geometry, rupture dynamics and ground motion from potential earthquakes on the North Anatolian Fault under the Sea of Marmara, Geophys. J. Int., 188, 1071–1087, https://doi.org/10.1111/j.1365-246X.2011.05289.x, 2012.

Okada, Y.: Surface deformation due to shear and tensile faults in a half-space, Bull. Seismol. Soc. Am., 75, 1135–1154, 1985.

Okay, A. I., Demirbağ, E., Kurt, H., Okay, N., and Kuşçu, İ.: An active, deep marine strike-slip basin along the North Anatolian fault in Turkey, Tectonics, 18, 129–147, https://doi.org/10.1029/1998TC900017, 1999.

Ozer Sozdinler, C., Necmioglu, O., Bayraktar, H. B., and Ozel, N. M.: Tectonic Origin Tsunami Scenario Database for the Marmara Region, Nat. Hazards Earth Syst. Sci. Discuss., https://doi.org/10.5194/nhess-2019-186, in review, 2019.

Parsons, T.: Recalculated probability of $M \geq 7$ earthquakes beneath the Sea of Marmara, Turkey, J. Geophys. Res.-Solid, 109, B05304, https://doi.org/10.1029/2003JB002667, 2004.

Petersen, M. D., Cao, T., Campbell, K. W., and Frankel, A. D.: Time-independent and time-dependent seismic hazard assessment for the State of California: Uniform California Earthquake Rupture Forecast Model 1.0, Seismol. Res. Lett., 78, 99–109, https://doi.org/10.1785/gssrl.78.1.99, 2007.

Pondard, N., Armijo, R., King, G. C., Meyer, B., and Flerit, F.: Fault interactions in the Sea of Marmara pull-apart (North Anatolian Fault): earthquake clustering and propagating earthquake sequences, Geophys. J. Int., 171, 1185–1197, https://doi.org/10.1111/j.1365-246X.2007.03580.x, 2007.

Reilinger, R., McClusky, S., Vernant, P., Lawrence, S., Ergintav, S., Cakmak, R., Ozener, H., Kadirov, F., Guliev, I., Stepanyan, R., Nadariya, M., Hahubia, G., Mahmoud, S., Sakr, K. ArRajehi, A., Paradissis, D., Al-Aydrus, A., Prilepin, M., Guseva, T., Evren, E., Dmitrotsa, A., Filikov, S. V., Gomez, F., Al-Ghazzi, R., and Karam, G. : GPS constraints on continental deformation in the Africa-Arabia-Eurasia continental collision zone and implications for the dynamics of plate interactions, J. Geophys. Res.-Solid, 111, B05411, https://doi.org/10.1029/2005JB004051, 2006.

Ren, J. and Zhang, S.: Estimation of recurrence interval of large earthquakes on the Central Longmen Shan fault zone based on seismic moment accumulation/release model, Scient. World J., 2013, 458341, https://doi.org/10.1155/2013/458341, 2013.

Rikitake, T.: Probability of earthquake occurrence as estimated from crustal strain, Tectonophysics, 23, 299–312, https://doi.org/10.1016/0040-1951(74)90029-8, 1974.

Ryall, A., Slemmons, D. B., and Gedney, L. D.: Seismicity, tectonism, and surface faulting in the western United States during historic time, Bull. Seismol. Soc. Am., 56, 1105–1135, 1966.

Schwartz, D. P. and Coppersmith, K. J.: Fault behavior and characteristic earthquakes: Examples from the Wasatch and San Andreas fault zones, J. Geophys. Res.-Solid, 89, 5681–5698, https://doi.org/10.1029/JB089iB07p05681, 1984.

Selva, J., Tonini, R., Molinari, I., Tiberti, M. M., Romano, F., Grezio, A., and Lorito, S.: Quantification of source uncertainties in seismic probabilistic tsunami hazard analysis (SPTHA), Geophys. J. Int., 205, 1780–1803, https://doi.org/10.1093/gji/ggw107, 2016.

Şengör, A. C., Grall, C., İmren, C., Le Pichon, X., Görür, N., Henry, P., and Siyako, M.: The geometry of the North Anatolian transform fault in the Sea of Marmara and its temporal evolution: implications for the development of intracontinental transform faults, Can. J. Earth Sci., 51, 222–242, https://doi.org/10.1139/cjes-2013-0160, 2014.

Shuto, N., Goto, C., and Imamura, F.: Numerical simulation as a means of warning for near-field tsunamis, Coast. Eng. Japan, 33, 173–193, https://doi.org/10.1080/05785634.1990.11924532, 1990.

Sørensen, M. B., Spada, M., Babeyko, A., Wiemer, S., and Grünthal, G.: Probabilistic tsunami hazard in the Mediterranean Sea, J. Geophys. Res.-Solid, 117, B01305, https://doi.org/10.1029/2010JB008169, 2012.

Stein, R. S., Barka, A. A., and Dieterich, J. H.: Progressive failure on the North Anatolian fault since 1939 by earthquake stress triggering, Geophys. J. Int., 128, 594–604, https://doi.org/10.1111/j.1365-246X.1997.tb05321.x, 1997.

Synolakis, C. E., Bernard, E. N., Titov, V. V., Kânoğlu, U., and González, F. I.: Standards, Criteria, and Procedures for NOAA Evaluation of Tsunami Numerical Models, NOAA OAR Special Report, Contribution No. 3053, NOAA/OAR/PMEL, Seattle, Washington, 55 pp., 2007.

Synolakis, C. E., Bernard, E. N., Titov, V. V., Kânoğlu, U., and Gonzalez, F. I.: Validation and verification of tsunami numerical models, in: Tsunami Science Four Years after the 2004 Indian Ocean Tsunami, Birkhäuser, Basel, 2197–2228, 2008.

Takagi, H., Mikami, T., Fujii, D., Esteban, M., and Kurobe, S.: Mangrove forest against dyke-break-induced tsunami on rapidly subsiding coasts, Nat. Hazards Earth Syst. Sci., 16, 1629–1638, https://doi.org/10.5194/nhess-16-1629-2016, 2016.

Tinti, S., Armigliato, A., Manucci, A., Pagnoni, G., Zaniboni, F., Yalçiner, A. C., and Altinok, Y.: The generating mechanisms of the August 17, 1999 Izmit bay (Turkey) tsunami: regional (tec-

tonic) and local (mass instabilities) causes, Mar. Geol., 225, 311–330, https://doi.org/10.1016/j.margeo.2005.09.010, 2006.

Tufekci, D., Suzen, M. L., Yalciner, A. C., and Zaytsev, A.: Revised MeTHuVA method for assessment of tsunami human vulnerability of Bakirkoy district, Istanbul, Nat. Hazards, 90, 943–974, https://doi.org/10.1007/s11069-017-3082-1, 2018.

Utkucu, M., Kanbur, Z., Alptekin, Ö., and Sünbül, F.: Seismic behaviour of the North Anatolian Fault beneath the Sea of Marmara (NW Turkey): implications for earthquake recurrence times and future seismic hazard, Nat. Hazards, 50, 45–71, https://doi.org/10.1007/s11069-008-9317-4, 2009.

Velioglu, D.: Advanced Two and Three Dimensional Tsunami Models: Benchmarking and Validation, Msc. Thesis, Middle East Technical University, Ankara, Turkey, 2009.

Wells, D. L. and Coppersmith, K. J.: New empirical relationships among magnitude, rupture length, rupture width, rupture area, and surface displacement, Bull. Seismol. Soc. Am., 84, 974–1002, 1994.

Wessel, P. and Smith, W. H.: New, improved version of Generic Mapping Tools released, Eos Trans. Am. Geophys. Union, 79, 579–579, https://doi.org/10.1029/98EO00426, 1998.

WGCEP – Working Group on California Earthquake Probabilities: Earthquake probabilities in the San Francisco Bay region: 2002–2031, US Geological Survey Open-File Report 03-214, US Geological Survey, Menlo Park, CA, 2003.

Wong, H. K., Lüdmann, T., Ulug, A., and Görür, N.: The Sea of Marmara: a plate boundary sea in an escape tectonic regime, Tectonophysics, 244, 231–250, https://doi.org/10.1016/0040-1951(94)00245-5, 1995.

Working Group on California Earthquake Probabilities: Earthquake probabilities in the San Francisco Bay Region: 2000 to 2030 a summary of findings, US Geol. Surv. Open-File Rept. 99-517, US Geological Survey, Menlo Park, CA, 1999.

Yalciner, A. C., Synolakis, C., Borrero, J., Altinok, Y., Watts, P., Imamura, F., Kuran, U., Ersoy, Ş. S., Kanoğlu, U., and Tinti, S.: Tsunami generation in Izmit Bay by the 1999 Izmit earthquake, Conferance on the 1999 Kocaeli Earthquake, Istanbul Technical University, Istanbul, Turkey, 217–221, 1999.

Yalciner, A. C., Altinok, Y., Synolakis, C. E., Borrero, J., Imamura, F., Ersoy, S., Kuran, U., Tinti, S., Eskijian, M., Freikman, J., Yuksel, Y., Alpar, B., Watts, P., Kanoglu, U., and Bardet, J.-P.: Tsunami waves in İzmit Bay, Earthq. Spect., 16, 55–62, 2000.

Yalçıner, A. C., Alpar, B., Altınok, Y., Özbay, İ., and Imamura, F.: Tsunamis in the Sea of Marmara: Historical documents for the past, models for the future, Mar. Geol., 190, 445–463, https://doi.org/10.1016/S0025-3227(02)00358-4, 2002.

Yalçıner, A., Annunziato, A., Papadopoulos, G., Dogan, G. G., Guler, H. G., Cakir, T. E., and Kanoglu, U.: The 20th July 2017 (22: 31 UTC) Bodrum-Kos Earthquake and Tsunami: Post Tsunami Field Survey Report, available at: http://users.metu.edu.tr/yalciner/july-21-2017-tsunami-report/Report-Field-Survey-of-July-20-2017-Bodrum-Kos-Tsunami.pdf (last access: 11 December 2019), 2017.

Yaltırak, C.: Tectonic evolution of the Marmara Sea and its surroundings, Mar. Geol., 190, 493–529, https://doi.org/10.1016/S0025-3227(02)00360-2, 2002.

Youngs, R. R. and Coppersmith, K. J.: Implications of fault slip rates and earthquake recurrence models to probabilistic seismic hazard estimates, Bull. Seismol. Soc. Am., 75, 939–964, 1985.

Zolfaghari, M. R.: Development of a synthetically generated earthquake catalogue towards assessment of probabilistic seismic hazard for Tehran, Nat. Hazards, 76, 497–514, https://doi.org/10.1007/s11069-014-1500-1, 2015.

nature COMMUNICATIONS

ARTICLE

https://doi.org/10.1038/s41467-021-25815-w OPEN

Probabilistic tsunami forecasting for early warning

J. Selva[1✉], S. Lorito[2], M. Volpe[2], F. Romano[2], R. Tonini[2], P. Perfetti[1], F. Bernardi[2], M. Taroni[2], A. Scala[3], A. Babeyko[4], F. Løvholt[5], S. J. Gibbons[5], J. Macías[6], M. J. Castro[6], J. M. González-Vida[6], C. Sánchez-Linares[6], H. B. Bayraktar[2,3], R. Basili[2], F. E. Maesano[2], M. M. Tiberti[2], F. Mele[2], A. Piatanesi[2] & A. Amato[2]

Tsunami warning centres face the challenging task of rapidly forecasting tsunami threat immediately after an earthquake, when there is high uncertainty due to data deficiency. Here we introduce Probabilistic Tsunami Forecasting (PTF) for tsunami early warning. PTF explicitly treats data- and forecast-uncertainties, enabling alert level definitions according to any predefined level of conservatism, which is connected to the average balance of missed-vs-false-alarms. Impact forecasts and resulting recommendations become progressively less uncertain as new data become available. Here we report an implementation for near-source early warning and test it systematically by hindcasting the great 2010 M8.8 Maule (Chile) and the well-studied 2003 M6.8 Zemmouri-Boumerdes (Algeria) tsunamis, as well as all the Mediterranean earthquakes that triggered alert messages at the Italian Tsunami Warning Centre since its inception in 2015, demonstrating forecasting accuracy over a wide range of magnitudes and earthquake types.

[1] Istituto Nazionale di Geofisica e Vulcanologia, Bologna, Italy. [2] Istituto Nazionale di Geofisica e Vulcanologia, Rome, Italy. [3] Department of Physics "Ettore Pancini", University of Naples, Naples, Italy. [4] German Research Centre for Geosciences (GFZ), Potsdam, Germany. [5] Norwegian Geotechnical Institute (NGI), Oslo, Norway. [6] Grupo EDANYA, Universidad de Málaga, Málaga, Spain. ✉email: jacopo.selva@ingv.it

Tsunamis may strike a coastal population close to the earthquake location within minutes after its origin time. Tsunami Early Warning Systems (TEWS) must forecast the tsunami threat rapidly following any potentially tsunamigenic earthquake. Tsunami impact prediction immediately after the event is subject to large uncertainty stemming mainly from the unknown details of the earthquake source, which implies large variability in the estimated tsunami inundation[1]. The uncertainty is amplified by the necessity to act rapidly to maximize the evacuation lead time. Given the available information, a vast number of different forecast outcomes are possible. The forecasts should assign a probability to each of these outcomes (like in, for example, weather forecasting[2,3]). Present-day tsunami forecasts are non-probabilistic, producing single-outcome forecasts. The uncertainty is often accommodated only implicitly through conservative choices (e.g. safety factors) to minimize missed alarms, at the cost of increasing the rate of false alarms[4]. Supplementary Table 1 summarizes all the symbols and acronyms used.

For sufficiently distant earthquakes, tsunami forecasts can be constrained with moment tensors[5], yet these forecasts are still characterized by significant uncertainty. Deep-sea sensors, where available, can further help constraining the tsunami through inversion and data assimilation techniques[4,6–10]. However, locally, the tsunami may inundate after minutes[11] and initial tsunami forecast must be performed solely from basic earthquake parameters. Innovative rapid source estimation techniques are steadily progressing[12–19], and next-generation sensors and methods could bring dramatic improvements to reduce uncertainties[7,20–23]. Yet, some uncertainty sources are intrinsic[24,25], and the earthquake and tsunami characteristics may be surprising and remain elusive even years after the event[26–28]. Therefore, uncertainty quantification and reduction efforts must be synergistically undertaken.

The need to deal with uncertainty in early warnings has been long recognized[29,30] and recently emphasized also for TEWS[31,32]. Following the 2004 Indian Ocean tsunami, the cost of "insist(ing) on certainty" was highlighted[33]. Despite subsequent attempts to define methods to quantify tsunami forecast uncertainty[34–38], operational tsunami forecasting in TEWSs is still non-probabilistic (http://www.ioc-tsunami.org/). Specifically, Tsunami Service Providers (TSPs) worldwide adopt Decision Matrices (DMs, look-up tables linking earthquake parameters with alert levels) or Envelopes (ENVs, selecting a local maximum over a selection of scenarios), or consider one or a few Best-Matching Scenarios (BMSs, scenarios matching the seismic and/or tsunami data available at the time of the estimation) to define initial alert levels[16,32,39–45]. Specific strategies (e.g. maximum credible magnitude, safety factors, etc.), usually rooted in the analysis of past events, are sometimes adopted to implicitly replace uncertainty quantification[16,32], but TSPs do not yet apply any formal probabilistic method. For example, a proxy of existing uncertainty is sometimes derived from the statistics of the scenarios selected with ENV methods [e.g. [44]) or of the along-coast variability of the forecast [e.g. [45]). However, in this way, the tsunami forecast cannot be tested quantitatively against observations and consequently the procedure cannot be calibrated[46,47]. In addition, the commonly adopted safety measures generally tend to overestimate the forecasts, although underestimations may still occur[43].

The use of a single estimation of the tsunami intensity to define alert levels, typical of non-probabilistic forecasts, also mixes to some extent scientific tsunami forecasts with political decision making. For example, a safety factor introduces a positive bias in the forecast to reduce the missed alarms rate: this is not done to improve the accuracy of the forecast, but to reduce potential societal consequences, which is a typical decision-making task. The decision-making process requires competences beyond the field of tsunami science. It is therefore considered fundamental to have effective and transparent uncertainty communication from scientists to decision makers[48–51] to make the process more traceable and to optimize the risk-reduction management[33,51–56]. For fast evolving phenomena like tsunamis, this can be realized adopting pre-defined rules, to be used automatically during an emergency.

An effective and transparent communication of uncertainty may be realized through Probabilistic Tsunami Forecasting (PTF). The PTF workflow should allow for a full propagation of uncertainty, from the earthquake hypocentre and magnitude estimation to alert-level definition, accounting for all the available information at the time of the estimate. This also clarifies the separation between scientific components (uncertain tsunami forecast through hazard curves) and political duties (alert-level definition for risk mitigation), following the hazard-risk separation principle[57,58]. This strategy is similar to the one used for seismic risk reduction: scientists determine the probability of different shaking intensities in the target area in a given time window (e.g. 50 years), and decision makers define seismic building codes selecting a design exceedance probability[59]. Similarly, the rule of conversion from PTF to alert levels can be defined by the authorities-in-charge by selecting a target probability value (e.g. one particular percentile), corresponding to a pre-defined level of conservatism for risk-reduction actions. This separation, enabled by the uncertainty quantification, is becoming a standard also for long-term coastal planning against tsunamis[60–63] and tsunami building code definition[64].

In this work, PTF is introduced and applied to a wide range of past events to discuss the feasibility of its real-time application and to test it against observations. To illustrate its potentiality for tsunami warning, we define alert levels from PTF based on different probability thresholds corresponding to different levels of conservatism, and we compare the results with the alert levels that would have been obtained applying a range of current-practice non-probabilistic methods. We demonstrate that PTF is statistically accurate in its forecasts for a wide range of events, from relatively small crustal events to large magnitude subduction zone earthquakes. We show that PTF can be timely produced also for near-field tsunami warning and that, adopting real-time conversion rules established in advance, probabilistic forecasts accounting for real-time uncertainty can be transparently transformed into alert levels, allowing to implement any desired level of conservatism based on all the available information at the time of the estimation.

Results

The PTF workflow. The procedure introduced here, coined Probabilistic Tsunami Forecasting (PTF), explicitly quantifies the uncertainty in real-time forecasts and enables uncertainty-informed alert-level definition in operational tsunami early warning (Fig. 1). PTF can provide the probability distribution of a Tsunami Intensity Measure (TIM, e.g. maximum run-up or near-coast wave amplitude) at multiple forecast points almost immediately, as soon as an earthquake location and magnitude estimates are available, typically few minutes after origin time (Fig. 1a). The method rigorously embeds uncertainty in tsunami forecast at the time of the estimate by quantifying the probability distribution for one (or more) TIM at each forecast point (Fig. 1c). The quantification is managed through an ensemble of tsunami scenarios defined by a set of sources weighted by the probability of being consistent with available real-time observations (Fig. 1a; e.g. seismic, geodetic, tsunami), as well as with local

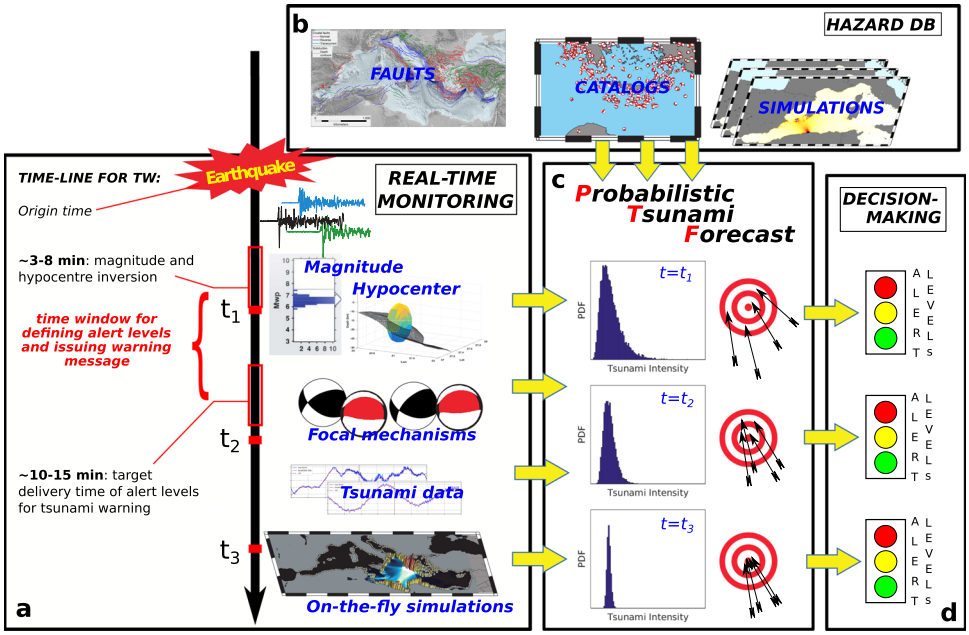

Fig. 1 PTF concept. a Timeline for tsunami warning: real-time information from an earthquake that just occurred and from the ongoing tsunami gradually integrates **b** local long-term hazard information, **c** progressively increasing the precision of the probabilistic forecasts (hazard curves) produced by the Probabilistic Tsunami Forecasting (PTF). **d** At any time, PTF can be transformed into alert levels (here represented as traffic lights) useful for decision making. In the current study, implementation refers to the time t_1, when only earthquake magnitude and hypocentre estimates are available from real-time observations.

earthquake and tsunami hazard information (Fig. 1b; e.g., pre-computed tsunami scenarios, long-term frequencies) derived from hazard and/or other long-term forecast models. PTF can be refined continuously with updated information (i.e., seismic moment tensor, tsunami data, Fig. 1a) to reduce the uncertainty in the forecasts (Fig. 1c). The evolving probability distributions can be used to define at any time, according to pre-defined rules, alert levels for specific points/areas (Fig. 1d), which in turn correspond to actions for risk reduction (for example, evacuation).

We implement PTF for near-field tsunami warning, that is, for sites proximal to the earthquake epicentre. This is a challenging task for TEWS[16]. To define the needs for near-field tsunami warning, we take as reference tsunami warning in the Mediterranean Sea. Here, seismically induced tsunamis always originate relatively close to some coastline, and tsunami inundation often occurs minutes after the earthquake. To maximize lead times, TSPs in the NEAMTWS (North-eastern Atlantic, the Mediterranean and connected seas Tsunami Warning System) currently adopt Decision Matrices (DMs, e.g., http://www.ioc-tsunami.org/), with a target delivery time of 10–15 min after earthquake occurrence (Fig. 1a). With this tight temporal constraint, while the seismic hypocentre and magnitude probabilities can be computed from real-time earthquake data to input PTF, faulting geometry and mechanism probabilities are not yet available. However, this missing information can be derived from long-term seismo-tectonic constraints. Considering that hypocentre and magnitude solutions are typically available in 3–8 min[42], the target delivery time of alert-levels can be matched by PTF with computational times on the order of a few minutes (e.g. <2 min, Fig. 1a).

For the Mediterranean Sea, long-term source information is derived from the regional hazard database NEAMTHM18[65–67], which assumed that earthquakes may occur in principle everywhere in the Earth's crust. Thus, NEAMTHM18 provides a database of sources covering the entire Mediterranean Sea with any potential mechanism. For any given target event, an ensemble of sources and corresponding probability consistent with both real-time and past observations (as expressed by NEAMTHM18 focal mechanism probability[66,68]) can be defined starting from real-time information. Using the NEAMTHM18 pre-computed database of tsunami simulations, the sources in the ensemble are propagated to the forecast points (Supplementary Fig. 1) through numerical tsunami simulations. The hazard is quantified combining source probabilities and tsunami propagation, including an additional basic treatment of tsunami modelling uncertainty accounting for approximations in source, propagation, and inundation[39]. Maximum wave amplitude extrapolated at 1 m depth (hereinafter near-coast wave amplitude) is selected as the TIM. The PTF computational time correlates with the ensemble size, which can be controlled by adopting cut-offs on source probabilities. Testing four different cut-offs, we found that a cut-off of 2 standard deviations offered a good compromise between stability of the results and computational time (<2 minutes, see Supplementary Table 4), matching the target response time for the warning (Fig. 1a). So, while computation times can be lowered further by code optimization, PTF can be applied in its present configuration to any possible source in the Mediterranean Sea, satisfying response-time demands for its operational use for NEAMTWS.

This PTF implementation can be extended to any other source area by (i) defining a database of potential sources covering the selected target area adopting the same strategy used in NEAMTHM18 for the Mediterranean, and (ii) using a workflow for high-performance computing[69] to produce all the simulations required in the ensemble of sources. The details of the PTF implementation can be found in Methods.

PTF for the 2003 Mw 6.8 Zemmouri-Boumerdes earthquake. To illustrate the PTF workflow, we first consider the 2003 Mw 6.8 Zemmouri-Boumerdes earthquake (Fig. 2) that occurred on the Tell-Atlas fold-and-thrust belt (likely on a south-dipping fault), triggering a tsunami causing damage at several harbours in the

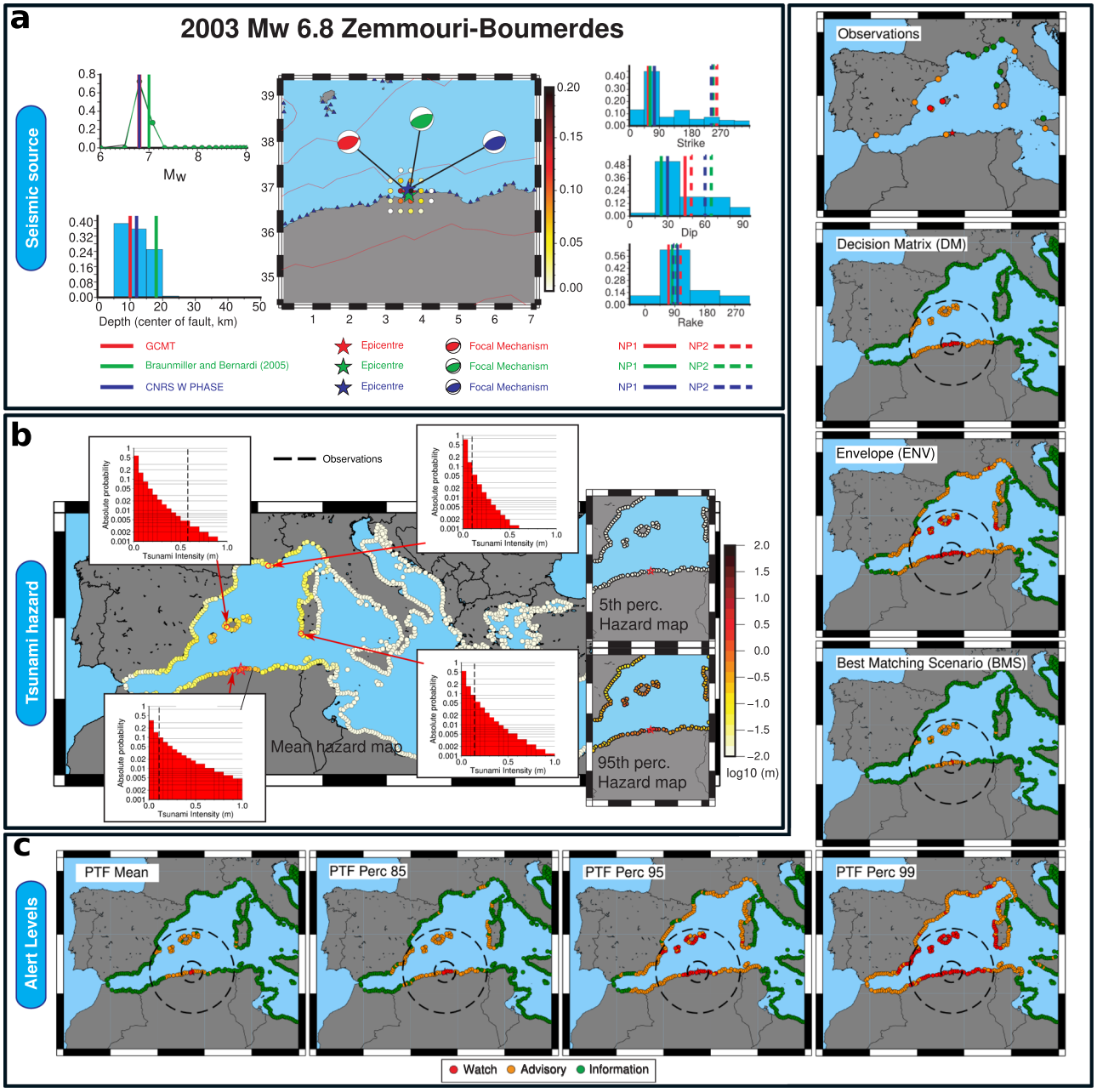

Fig. 2 PTF workflow: example for the 2003 Zemmouri-Boumerdes tsunami. a PTF source model: marginal distributions for earthquake magnitude and depth (left), location (centre), and fault parameters (right) for the ensemble describing source variability. Several revised moment tensor solutions are plotted as vertical lines for comparison. Distributions are consistent with seismic observations. For example, the ~30° southern-dipping realistic fault plane is strongly emphasized in the PTF source ensemble. **b** PTF results: tsunami intensity measure distribution (hazard curve) at four selected coastal locations in the western Mediterranean compared with observations (dashed vertical lines), and hazard maps involving all forecast points derived from different PTF's statistics (mean, 5–95th percentiles), showing uncertainty and spatial pattern of the tsunami forecast. **c** NEAMTWS Alert levels assigned from observations[40], decision matrix (DM), best-matching-scenario (BMS), envelope (ENV), and PTF mean, and 85, 95, and 99th percentiles; dashed lines indicate local and regional areas, as defined in the DM (Supplementary Table 8). NEAMTWS considers three alert levels (Information, Advisory, and Watch), each corresponding to off-coast tsunami wave amplitudes intervals: alert levels are assigned comparing tsunami near-coast wave amplitude with alert-level intervals.

western Mediterranean[9,70–72]. PTF is implemented in hindcasting mode, retrospectively simulating a real-time application. Real-time data (hypocentre and magnitude; Supplementary Table 2) are reconstructed using standard CAT-INGV operating procedures[42] on archived data (details in Supplementary Note 1). The resulting discrete joint distributions (Fig. 2a) for hypocentre, faulting geometry and mechanism are consistent with the most recent moment tensor estimations (Supplementary Table 3, refs. [5,19,73–75]). Marginal distributions for strike, dip, and rake angles emphasize the expected geometry and mechanism for an event at that location, based on the local seismotectonics derived from the long-term hazard model[66–68]. The fault plane ambiguity is correctly resolved with the south-dipping reverse fault more probable than the conjugate plane.

For this event, the ensemble of sources is composed of approximately 15,000 scenarios (Supplementary Table 4). The

results are visualized through probability density functions for the selected TIM at each forecast point (Fig. 2b). TIMs and relative uncertainties are visualized through conditional hazard maps, whereby the mean or percentiles of the probability distributions are mapped. Despite combining a large number of scenarios, the forecast impact pattern is largely controlled by the dominant source orientation and by the tsunami propagation and generally agrees with observations. The specific observations can be compared with PTF distributions summarizing the expectations at each specific point. For the four locations reported Fig. 2b, all observations fall inside the PTF distributions. The tsunami observed in the Balearic Islands was relatively larger than expected and thus is in the right tail of the PTF distribution.

Alert levels are then assigned directly from PTF distributions (Fig. 2c). Different methods can be defined based on PTF statistics and/or on evaluating the probability of pre-defined TIM intervals (see Supplementary Note 2). In the NEAMTWS, three alert levels (Information, Advisory, and Watch) are defined corresponding to near-coast tsunami wave amplitudes that are negligible (we here assume <10 cm), 10–50 cm, >50 cm respectively (or twice these values for maximum run-up). Alert levels for each location are here assigned by comparing a TIM derived from the PTF with the relevant amplitude intervals. Different statistics of the PTF (e.g. the mean or a given percentile) can be used to extract this value, leading to alternative definitions of alert levels. Overall, we adopt the simplest method for illustrative purposes: mapping PTF statistics into alert levels' reference intensity intervals, which is equivalent to the definition of probability thresholds for long-term hazard (see Supplementary Note 2)[60–64].

To discuss PTF alert-level assignments, we take as reference three methods representative of standard non-probabilistic operational procedures to define alert levels. As reference for conservative methods, we consider (i) the Decision Matrix (DM) adopted by the Italian tsunami warning centre CAT-INGV (representative for the NEAMTWS operational procedures, see Supplementary Note 3), and (ii) an envelope (ENV) method resembling the one described in Catalan et al.[44], in which the maximum tsunami wave amplitude is selected at each coastal site from a set of scenarios compatible with the ongoing event. We consider all scenarios within half fault length (derived from[76,77]) from the epicentre and with magnitude best approximating the available magnitude incremented by 0.5. As reference for single simulation methods (current practice in many TSPs worldwide[32,39–41]), we consider a single Best-Matching Scenario (BMS) selected as the most likely source in the PTF ensemble, whose simulation results are used to define alert levels.

For 2003 Zemmouri-Boumerdes, DM and ENV-based alert levels tend to be more conservative than those based on the PTF mean or on the BMS (Fig. 2c). DMs associate alert levels with forecast points depending on earthquake location and magnitude through a discontinuous, decreasing function of the distance from the epicentre (see Supplementary Note 3). Thus, DMs do not consider that both source orientation and bathymetry control the tsunami propagation pattern and features, which is evident also for this event[70,71]. ENV, BMS, and PTF-based alert levels on the other hand embed the tsunami propagation footprint through numerical simulations. BMS results are comparable to PTF central values (e.g. the mean, Fig. 2c), ENV results to the high percentiles of the PTF. All non-probabilistic methods produce specific alert-levels, while PTF allows specification of a desired level of caution through choosing higher or lower percentiles, corresponding to TIMs with a high or low probability of exceedance. Consequently, the overall spatial extent of and the number of high alert levels (i.e. advisory/watch) is controlled by the selected percentile (the higher the percentile, the larger the affected area), with high percentiles including less likely larger TIMs from the tail of PTF distributions. Figure 2c shows that several observations correlate better with conservative simulation-based methods like ENV and high-percentile PTF alert levels (e.g. 95th percentile): the reason is that this event challenged numerical modellers due to basin and harbour-related amplifications that occurred for instance in the Balearic Islands harbours[71]. Either higher resolution tsunami modelling is introduced, or only a conservative definition of alert levels can then include these values.

To examine more closely the reliability of PTF TIM forecasts, we compare PTF distributions directly with all the available observations (Fig. 3). Direct observations for this tsunami include data from several coastal sea-level stations (hereinafter, tide-gauge data) in the western Mediterranean[70–72]. The time-series are, however, few and coarsely sampled[40–42]. To enrich the comparison, we also consider other indirect observations and hind-casted models. Several moment tensors and finite-fault model estimates are available in the literature (Supplementary Table 3). A spatially homogeneous tsunami dataset for the test can be obtained simulating the tsunami from such available finite-fault models[78–84], retrieved by separate or joint seismic and geodetic data inversion (details in Supplementary Note 4). These data collectively sample our best assessment of the epistemic uncertainty of the source process almost two decades after the earthquake. The numerical simulations map this source uncertainty onto a synthetic tsunami dataset.

The maximum near-coast wave amplitude simulated from finite-faults models (red lines) generally falls within PTF's inner confidence intervals (defined through the 5–95th percentile interval), and the means (red and black solid lines) are highly clustered (we note that PTF distributions are not necessarily Gaussians and percentiles are here used to define confidence intervals). This agreement indicates that, while our PTF implementation simplifies the source representation (since NEAMTHM18 scenarios use uniform slip for crustal faults), the source variability in the PTF ensemble and the log-normal distribution we use to quantify the uncertainty embed the tsunami source uncertainty, as quantified by the range of available finite-fault models[46,78–84].

Conversely, observations at the tide-gauges are more scattered (yellow squares in Fig. 3). Several observations from Eastern Spain, the Balearic Islands, and western Italy fall into the tails of the PTF distributions. The misfits of some local maxima of the observations are present for both the PTF's central values and numerical simulations from best-fit source models. These misfits are probably due to the above-mentioned basin and harbour-related amplifications that likely occurred in several areas[71], and that cannot be reproduced without high-resolution tsunami numerical modelling. As they fall inside the upper tail of the PTF distributions, only the alert level corresponding to conservative choices (high percentiles of the PTF) include such maxima, resulting in a better correlation with the observations noted above (Fig. 2c). This demonstrates that even the relatively simple uncertainty model implemented to manage uncertainty in tsunami generation and propagation (see "Quantification of PTF's propagation factor" in Methods) can deal to some extent with these hard-to-predict amplifications, leading to forecasts that can encompass observations within uncertainty bounds. In the future, forecast precision may be improved through more advanced techniques to better quantify local amplifications and related uncertainty[63,85–91]. Notably, also other potential sources of local deviations exist, for example, the contribution of seismically induced landslides. While significant efforts in these directions are ongoing, research is still required to fully implement such methods in near-field real-time forecasts[92,93].

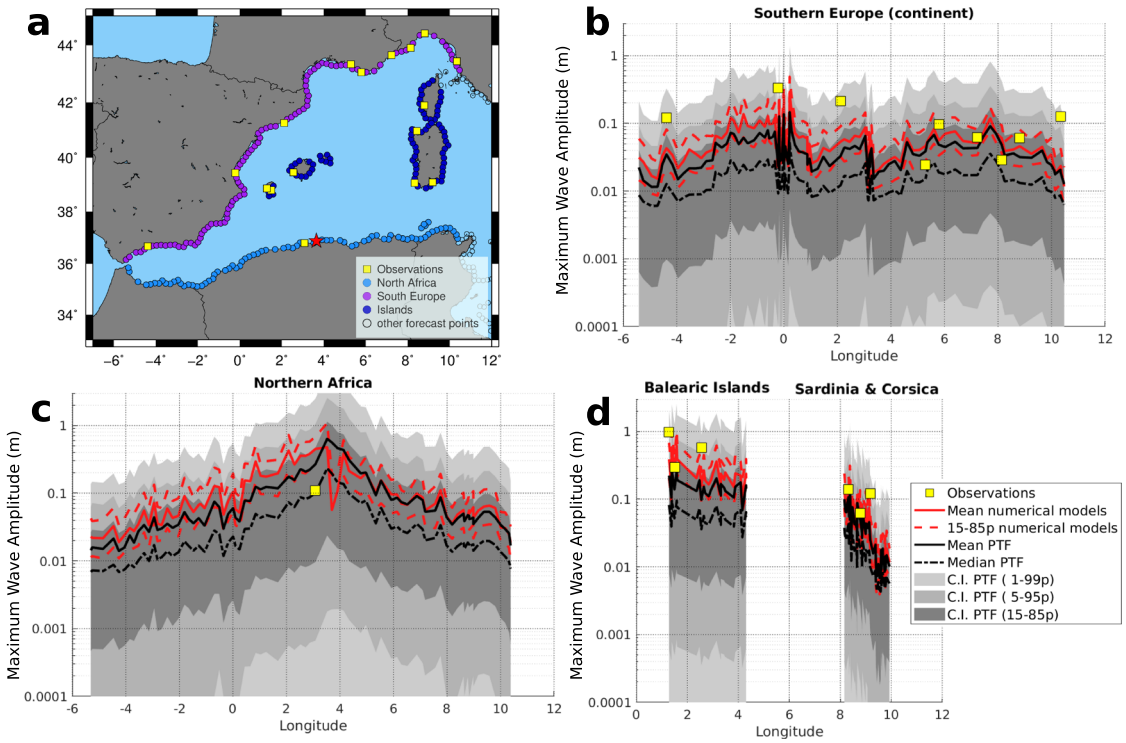

Fig. 3 PTF for the 2003 Zemmouri-Boumerdes tsunami. a selection of forecast points for specific comparison and **b–d** graphical comparison between tsunami observations (yellow squares) and maximum wave amplitudes evaluated from numerical models (red lines: mean and 15–85 percentiles with solid and dashed lines, respectively), and PTF statistics (black lines: mean and percentiles with solid and dashed lines, respectively) at all forecast points in **b** northwest Africa, **c** southwest Europe, and **d** the main islands.

PTF for the 2010 Maule Mw 8.8 earthquake. To illustrate PTF behaviour for larger magnitudes, we implement the PTF also to the NEAMWave17 ICG/NEAMTWS exercise scenario, a synthetic Mw 8.5 earthquake on the Hellenic Arc in southwestern Greece (see Supplementary Note 6), and to the 2010 Maule, Chile, Mw 8.8 earthquake[94] (Fig. 4). The latter required the extension of PTF implementation to cover the Chilean subduction zone (see Methods)[95]. For such large magnitudes, the source model includes in the ensemble only subduction earthquakes (Supplementary Table 4) with heterogeneous slip distributions also featuring shallow slip amplification[65–67,95,96], mimicking to some extent tsunami earthquakes (events generating a tsunami larger than expected from seismic magnitude[96,97]).

The 2010 Maule event provides the opportunity to compare PTF results with a larger and higher-quality dataset of tsunami observations, including coastal and deep-sea tsunami sensors (DART and tide-gauges) and run-up data[98,99] (Fig. 4). To compare with tsunami amplitude at the coast, run-up data are halved ([100] and reference therein). The results for this event show that PTF inner confidence intervals (15–85th percentiles) encompass all the observations, including run-ups (Fig. 4e,f), despite their possibly relatively large measurement errors. This result is coherent with the results of Catalan et al.[44], who show that the scenario envelope includes observations. The prediction at tide-gauges (Fig. 4c,d) shows a slight tendency towards overestimation, which remains within the uncertainty bounds. For the much smaller Mw 6.8 Zemmouri-Boumerdes event in the Mediterranean, we observed an opposite tendency towards underestimation. A possible reason is that, for smaller earthquakes on steeper faults like this, local resonances and amplification play a more important relative role due poorly modelled smaller tsunami wavelengths; for the Mw 8.8 Maule event, shelf and basin resonances occur also at longer periods[101], but they are well-captured on a 30 arc-sec grid (see Methods). Moreover, the scenarios in the PTF ensemble of large magnitudes ($Mw > 8.1$[66]) are modelled on the 3D subduction geometry and with randomly sampled slip distributions (see Methods; the smaller crustal scenarios discussed above are instead modelled with simplified planar-fault uniform-slip sources). Consequently, the tsunami modelling uncertainty (accounting for tsunami generation, propagation, and inundation simplifications[102,103]) might be slightly overestimated in this case, as source representation is more advanced for such magnitudes, then compensating some underestimation due to local tsunami effects. This possible slight overestimation is also present when focussing on DART, even if may be less pronounced due to the larger source-target distance (Fig. 4a,b). Notably, a systematic extension to more case studies with extended high-quality observations may allow, in the future, a finer tuning of the adopted uncertainty modelling in each of the PTF factors, for example, using the large set of tsunami observations that is available in the Pacific Ocean[46,47].

Testing PTF. To quantitatively test PTF performance for operational use in TEWS, we should define an unbiased set of events for which a tsunami warning issuance is required, regardless of whether a detectable tsunami was actually generated or not (the Gutenberg-Richter distribution of earthquake magnitudes implies that most of tsunami warnings will be issued close to this condition). To this end, we built a testing dataset (Fig. 5a) composed of all Mediterranean earthquakes that triggered alert messages from the CAT-INGV TSP, without any filter or selection. This includes all the twelve seismic events with initial magnitude estimate $Mw \geq 6.0$ that occurred since CAT-INGV became operational in 2015. We added the 2003 Zemmouri-Boumerdes event, to enrich the set of events in the western Mediterranean, reaching a total of thirteen events (Fig. 5a).

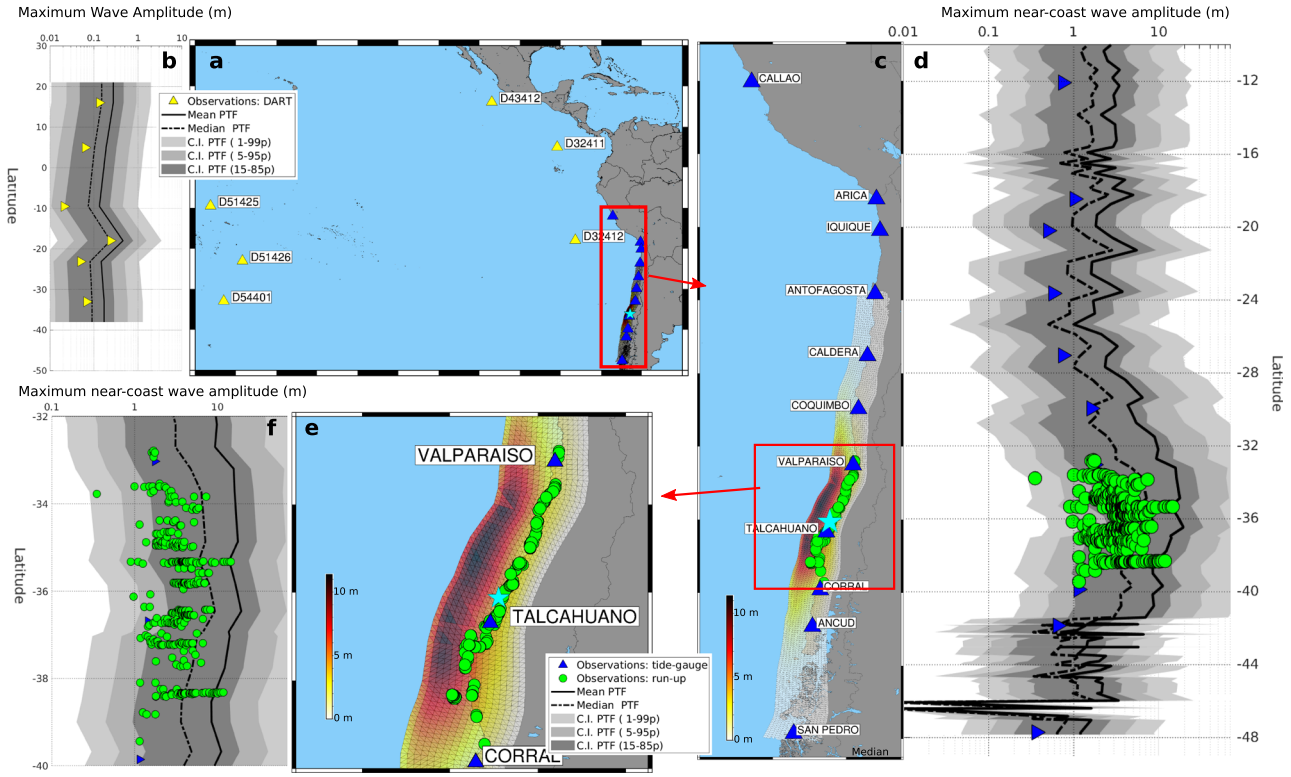

Fig. 4 PTF for the 2010 M8.8 Maule tsunami. a Epicentre and location of deep-sea (DART) observations (yellow triangles) and **b** corresponding comparison between deep-sea observations and PTF forecasts (black lines and grey areas). **c** Epicentre (star), average of the slip distributions used in the ensemble, and location of coastal observations (tide-gauges and run-up as blue triangles and green circles, respectively; run-up is halved to compare with wave amplitude, see Supplementary Note 6). **d** Graphical comparison between coastal observations and PTF forecasts (black lines and grey areas). **e**, **f** Same as **b**, **c** zoomed over the area with run-up measures.

Observations for the tests include rapid and revised moment tensor estimates, and tsunami observations from the available tide-gauges and from run-up surveys, when available (more details in Supplementary Note 6).

PTF accuracy is evaluated through formal hypothesis testing to assess the consistency between forecasts and available data and, if need be, to reject the PTF uncertainty model (see Methods). Both intermediate (source mechanism) and final (tsunami intensity) forecasts are tested. Results indicate that overall focal mechanism forecasts are accurate, such that the PTF source model is never rejected (results in Supplementary Table 7). Tsunami data and forecasts are compared simultaneously at all forecast points with observations, and spatial correlations are accounted for (see Methods). Although tsunami observations in many cases are limited, and sometimes with a poor signal-to-noise ratio due to the small event sizes, statistical tests confirm PTF accuracy also regarding tsunami forecasts, both for the events generating an observable tsunami (e.g. the October 30, 2020 Mw 7.0 Samos-Izmir event, Fig. 5b; results for all the six events of this type in Supplementary Fig. 4) and the ones for which a tsunami has not been observed (e.g. the 2017 Mw 6.5 Lesbos event, Fig. 5c; the results for all the seven events of this type in Supplementary Fig. 5). The tsunami generated by the Mw 7.0 Samos-Izmir earthquake (maximum run-up ~3.8 m[104]), as well as by the May 2, 2020 Mw 6.7 Ierapetra event, offered us a unique opportunity to perform a blind test for PTF, since the complete evaluation system was in place before the events occurred. The same test can be applied to the 2010 Maule tsunami, using both deep-sea and coastal observations as well as near-field and far-field observations; the results confirm the overall accuracy of PTF also for large magnitude event (Supplementary Fig. 4). On the other hand, for all the events that did not generate any measurable tsunami, PTF consistently forecasts an essentially negligible tsunami (<0.10 m) at all the observation points (Supplementary Fig. 5). While specific events may tend toward over/underestimation, altogether they pass the statistical test (accuracy level of 0.05). More details in testing results are discussed in Supplementary Note 7.

PTF and alert levels. Using the same testing dataset, we finally compare the PTF alert levels with those produced by the reference non-probabilistic methods (DM and BMS, Fig. 6). The comparison with data (Fig. 6a) is limited to the forecast points where observations are available. Comparisons are grouped in three categories as: correct-assignment (assigned = observed); false-alarm (assigned > observed); and missed-alarm (assigned < observed).

The three non-probabilistic methods give significantly different results (Fig. 6a and Supplementary Table 9). DM and ENV produces relatively few missed alarms (about 3%) but generates many false alarms (about 55%). This high percentage is in line with other conservative methods worldwide[4]. Conversely, BMS optimizes the correct assignments (about 86%), minimizing false alarms but increasing the missed alarms (11%). This reflects the fact that DM and ENV are worst case oriented to reduce missed alarms. On the contrary, the aim of BMS is to stay as close as possible to the actual event.

The alert levels computed from PTF shows a large variability, which depends on the selected percentile. High percentiles of PTF compare with conservative non-probabilistic methods (DM and ENV). The highest PTF percentiles (e.g. the 99th) are even more conservative than DM and ENV, further reducing missed alarms at the cost of further increasing false alarms. Decreasing the PTF

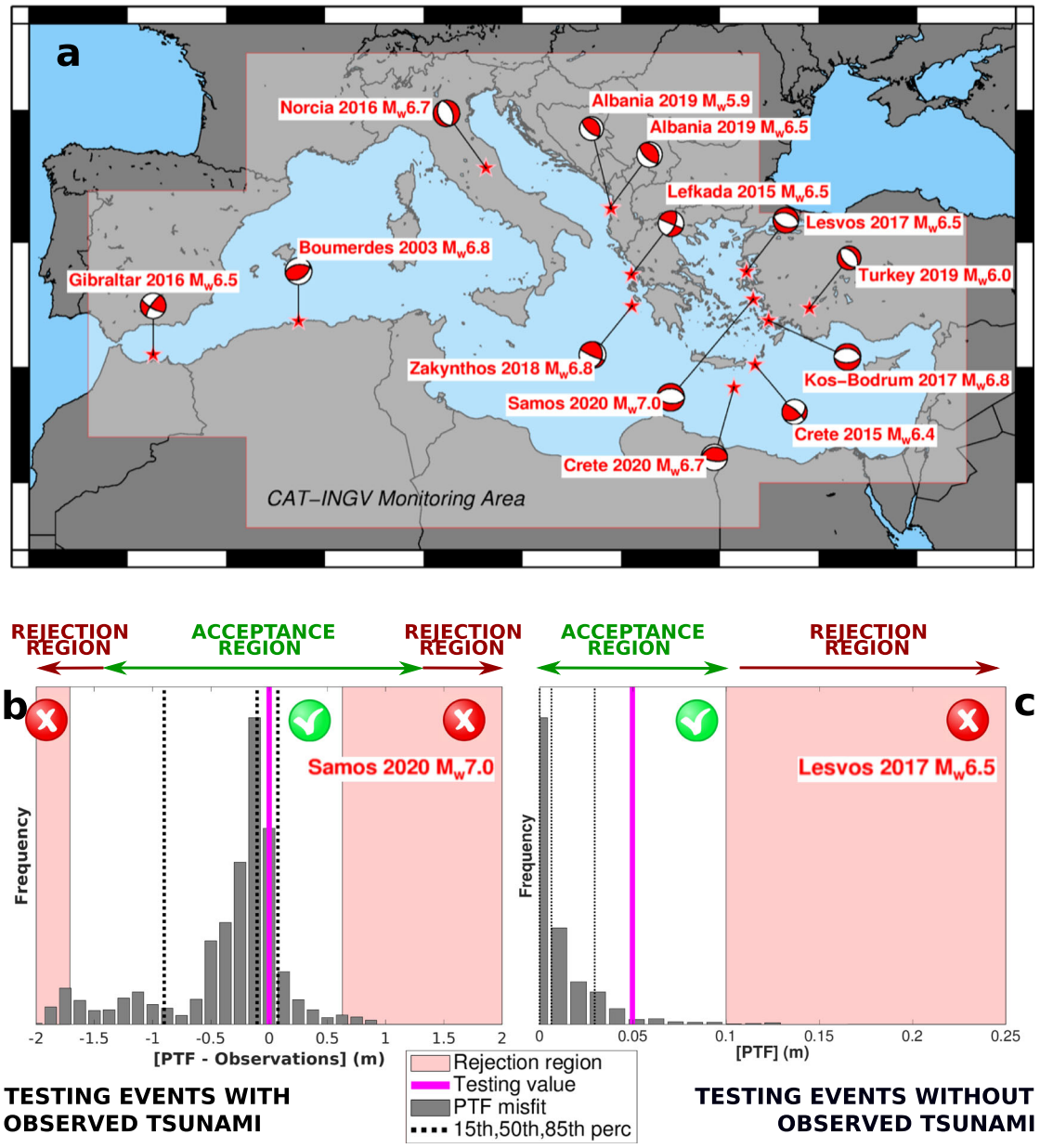

Fig. 5 Testing PTF. a Testing dataset and monitoring area of CAT-INGV; additional details are reported in Supplementary Table 2. **b** Example of test for events with observed tsunami: the case of 2020 Mw 7.0 Samos-Izmir earthquake. PTF misfit distribution (*[PTF-Observations]*) is evaluated as the difference between near-coast wave amplitudes sampled from the PTF source ensemble and observations and staked for all observation points (see Methods). Gray bars report the misfit distribution, along with its 15, 50, and 85 percentiles (dashed lines). The model is rejected if the testing value (null misfit, purple line) falls in the rejection area (light red area); otherwise, the test is passed. **c** Example of test for events without observed tsunami: the case of 2017 Mw 6.5 Lesbos earthquake. The PTF distribution (*[PTF]*), obtained sampling from the PTF source ensemble, is expected to encompass small values. The model is rejected if the testing value (the 95th percentile of *[PTF]*, purple line) falls in the rejection area (light red area: near-coast wave amplitude < 0.1 m); otherwise, the test is passed. To keep spatial correlations, in both *[PTF-Observations]* and *[PTF]* the uncertainty in propagation is averaged (see Methods). All the other case studies are reported in Supplementary Figs. 4 and 5.

percentile, the number of correct assignments progressively increases: most false alarms are suppressed, while missed alarms increase. The increase of correct assignments (green bars in Fig. 6a) and the decrease of false alarms (orange bars) are due to a reduction of the overall number of alerted (advisory or watch) forecast points (Fig. 6b), observed at all forecast points independently from the position and number of observations. PTF median and mean match with a best-match method like BMS. The BMS and the PTF median produces a similar percentage of correct alarms (85% vs 86%), while the PTF mean produce a slightly larger percentage of correct alarms, fewer missed alarms, but more false alarms and alerted forecast points (Fig. 6a, b).

Overall, PTF percentiles encompass and go beyond the range of behaviours and associated level of conservatism of DM, ENV, and BMS. The percentage of missed alarms can be strongly reduced with conservative choices (PTF high percentiles), that is from 14% to <1% passing from the median to the 99th percentile, at the cost of an increase in the percentage of false alarms, from <1 to 53%. Intermediate-high PTF percentiles (80th or 85th) are somehow between such extrema, progressively modulating the rates of missed/correct/false alarms.

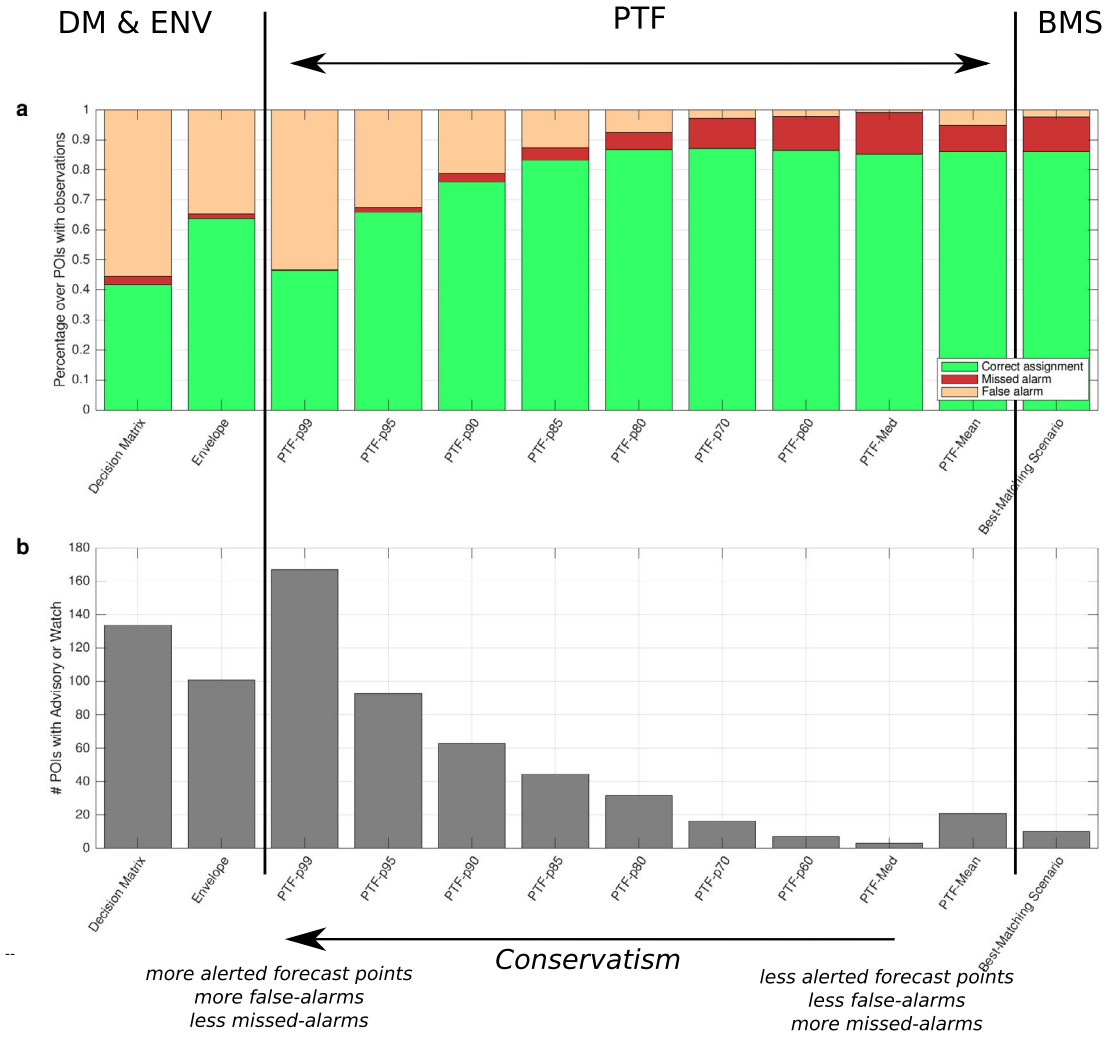

Fig. 6 Alert levels from PTF and non-probabilistic methods. We compare the assigned and observed alert levels based on DM, ENV, BMS, and PTF statistics for the 13 events in the testing dataset considered in this paper (Fig. 5a). **a** Average percentage of correct- (green), false- (yellow) and missed alarms (red) at forecast points with observations. **b** Average total number of forecast points with advisory and watch levels at all forecast points. Note that CAT-INGV DM is less conservative than the original NEAMTWS DM. The different PTF statistics allow covering the full range of conservative choices, encompassing the range defined by existing non-probabilistic methods. The selection of a specific PTF percentile can be explicitly linked to a pre-defined level of conservatism, quantifying the expected rate of false/missed alarms.

Hence, PTF allows better interpretation of the role of conservatism in present-day non-probabilistic methods, for an explicit and systematic selection of the desired level of conservatism.

Finally, we note that PTF helps overcoming the potential instabilities of DMs with events close to the defined magnitude thresholds. This instability can be well illustrated through the recent 2020 Samos-Izmir event. In the first minutes after the event, real-time magnitude estimations oscillated just around the DM threshold of Mw = 7 (with uncertainty bounds ~6.8–7.2, see Supplementary Table 2). As a consequence, small oscillations in the central magnitude could determine a significant change in the alert levels; for example, using the reference DM of CAT-INGV, all regional forecast points (<400 km) would pass from advisory to watch, and regional forecast points (>400 km) from information to advisory (see Supplementary Fig. 6), with a number of alerted forecast points passing from 297 (29 watch) to 1107 (297 watch). On the contrary, PTF solutions are not based on any threshold and they account for estimation uncertainty, then they are stable with respect to such oscillations.

Discussion

We present an approach dealing with uncertainty in real-time tsunami forecasting and linking alert-level definition for tsunami early warning to such uncertainty, coined Probabilistic Tsunami Forecasting (PTF). Current practices do not quantify uncertainty in tsunami forecasting and define alert levels deterministically. To reduce missed alarms, they typically adopt safety factors that increase the number of false alarms. PTF addresses this issue through explicit uncertainty quantification, linking alert levels to the desired level of conservatism.

This approach has been implemented for near-field tsunami warning and tested against all available data in the Mediterranean, including two blind tests (the recent 2020 Mw 6.7 Ierapetra and Mw 7.0 Samos-Izmir earthquakes), as well as for the 2010 Mw 8.8 Maule earthquake and tsunami, one of the largest events ever recorded. The results show that PTF is statistically accurate in its forecasts, ranging from relatively small crustal earthquakes to large magnitude subduction zone events.

We have shown that uncertainty forecasts can be quantitatively and transparently transformed into alert levels, using real-time

conversion rules established in advance. Current practice bases this transformation on some generic rules defined in agreement with authorities, fusing the scientific and political aspects of defining alert levels[16,32,39–45]. As quantitative information about how certain is a forecast is not available, is not based on the effective real-time uncertainty on observations, and is not communicated, it is not possible to be sure regarding the degree of conservatism that is being applied. The formal quantification of uncertainty of PTF allows instead accounting for real-time uncertainty, covering explicitly the full range of possible choices, from conservative methods minimizing missed alarms to best-guess methods maximizing correct alarms. In this way, the desired average performance can be explicitly selected, allowing optimizing choices for each risk-reduction action. Choosing such rules requires competences outside tsunami science, as they depend on decision-makers needs, on acceptable risks, tolerated false/missed alarms rates, and other contextual factors. In any case, not only missed alarms but also false alarms may generate significant economical and societal consequences[4,105]. Considering that both missed and false alarms are due to uncertainty in the forecast, and both exist in current-practice methods, a transparent management of uncertainty is preferable[48–51], for example quantifying the potential socio-economical consequences of alternative choices, as evaluated from the expected long-run rate (over multiple events) of false/missed alarms[33,51–56,106–111]. Real-time uncertainty forecasts could also be exploited in the future by decision makers to define new strategies for risk management. Indeed, a range of different risk-mitigation actions (also beyond evacuation, such as the activation of mitigation procedures in industrial plants or automatic stops in lifelines) can lead to different choices for different targets and/or different actions with different tolerances to missed and false alarms[52–54]. This possibility is prevented in present-day common practice, but is made possible by an explicit quantification of uncertainty in real-time. This approach to tsunami warning would also complement the ongoing efforts towards uncertainty reduction through enhanced real-time tsunami monitoring capability (GNSS, DART, SMART cables[6,21]) and increase of real-time computational capability[23]. These elements have been already emphasized by the United Nation Decade of Ocean Science for Sustainable Development (2021–2030, https://www.oceandecade.org/).

More extensive testing against tsunami data worldwide will allow a thorough calibration of the uncertainty quantification framework, eventually introducing strategies to reduce uncertainty without losing accuracy. Here, by implementing a PTF applicable worldwide, we have set the scene for both hindcasting and blind tests of PTF performance against events of any magnitude, similarly to other testing experiments (http://cseptesting.org/). Further exploiting high-performance computing infrastructures, we can extend quantitative testing of tsunami forecasts and their underlying science worldwide to a larger set of tsunami events[46]. Moreover, several important specific issues are still only partially dealt with, like, for example, tsunami earthquakes[97] or more complex coastal dynamics. Testing and calibration must include these specific aspects to make PTF operational and fully suitable for science-informed decision making.

Methods

Probabilistic Tsunami Forecasting (PTF) evaluation. The uncertainty existing at the time $t>t_E$ on the potential tsunami generated by the event E occurring at the time t_E is summarized through a probability distribution conditional upon E. The corresponding survivor function $h_E(x,p,t) = P(X>x|\,E;p,t)$ describes a hazard curve for a given Tsunami Intensity Measure (TIM) x in the target forecast point p, corresponding to the probability density function $dh_E(x,p,t)$. The function $h_E(x,p,t)$ can be estimated from the uncertain knowledge about E at time t based on an ensemble of tsunami simulations corresponding to tsunami sources compatible with the information about E available at the time t. The available information is constituted by the estimates of the source parameter values (e.g. earthquake location and magnitude) as derived from available seismic, geodetic and/or tsunami records (Fig. 1); different techniques may be applied to obtain this information, ranging from source inversion to data assimilation. The quantity and the quality of the information available may increase through time, eventually reducing uncertainty. Applying the total probability theorem, $h_E(x,p,t)$ reads:

$$h_E(x,p,t) = P(\,X>x|E;p,t) = \int_S P(X>x|s;p)g(s|E;t)ds \approx \sum_i P(X>x|s_i;p)P(s_i\,|\,E;t) \quad (1)$$

where $P(X>x|s;p)$ (propagation factor) is the probability that the earthquake scenario s produces a tsunami exceeding the TIM value x at the location p; $g(s|\,E;t)$ (source factor) is the probability that each scenario s can be considered as a good approximation of E based on the uncertainty on the source parameters at the time t; the set S includes all the possible scenarios s in the area.

In the right-hand side of Eq. 1, we approximate the infinite set S with a discrete set $\{s_i\}$, defining a finite ensemble of source scenarios resembling E. This discretization is possible if the databank $\{s_i\}$ is built to represent all the possible earthquakes in the area, reasonably covering all the natural variability. The probabilities $P(s_i\,|\,E;t)$ can be interpreted as weighting factors for each source within the ensemble. To speed up the evaluation of $h_E(x,p,t)$, the databank $\{s_i\}$ and corresponding propagation factors $\{P(X>x|s_i;p)\}$ can be prepared in advance. As time passes, $\{s_i\}$ and $\{P(X>x|s_i;p)\}$ can be refined accounting for the incoming information about the source and about the tsunami, eventually including data assimilation[7–10]. In addition, $\{s_i\}$ can be enhanced with new and possibly more accurate scenarios better resembling the observations (Fig. 1a). The forecast (Fig. 1c) and the alert level (Fig. 1d) can be updated accordingly.

The best candidate databank $\{s_i\}$ is the source model of a time-independent long-term PTHA (Probabilistic Tsunami Hazard Analysis[102]) for three main reasons. First, PTHA source models, by construction, should guarantee or approximate well enough the source completeness. Second, one of the ingredients of the PTHA is the databank of $\{P(X>x|s_i;p)\}$ used for tsunami propagation. Third, PTHA provides long-term source frequency and conditional probability for all scenarios, which makes it a suitable backup for not yet available real-time information. It may then provide all the elements depicted in Fig. 1b.

Given that $\{P(X>x|s_i;p)\}$ may be pre-calculated and used as a look-up table in real-time, the computational time is dominated by the quantification of $P(s_i\,|\,E;t)$, the retrieval of $\{P(X>x|s_i;p)\}$ from the databank and the aggregation procedure. Being the quantification of $P(s_i\,|\,E;t)$ and the aggregation computationally inexpensive, the main time-consuming step is the retrieval of the scenarios from the databank, which is a problem quite common in informatics that can be further optimized by code engineering with respect to present implementation. Time can be saved by reducing the number of scenarios (the ensemble size), for example, by discarding scenarios with negligible $P(s_i\,|\,E;t)$ through pre-defined cut-offs, whose practical implementation is discussed in the following section. Probabilities must be re-normalized accordingly to avoid biases. The larger the reduction, the larger the loss of accuracy in the tails of $dh_E(x,p,t)$. We stress that by coupling appropriate cut-off and specific code engineering, computational time can be probably reduced to a few seconds.

The presented formulation is in principle valid also for non-seismic tsunami sources. However, source parameters are more difficult to obtain in real-time for non-seismic sources and source variability is less constrained. For the same reason, also the creation of scenario databases is more challenging. As a result, present-day PTHA studies are primarily focused on earthquakes[92,102]. Since TEWSs are nowadays mostly devoted to seismic sources only, as a starting point we will also focus our attention to seismic sources.

Quantification of PTF's source factor. The source factor of Eq. 1 deals with the real-time uncertainty on the source of the event E, quantifying the proximity between the scenarios $\{s_i\}$ and E, based on information available at time $t>t_E$. In principle, $P(s_i|E;t)$ can be estimated using any type of real-time observations, including seismic and geodetic data, as well as tsunami records.

To deal with local tsunamis, delivery time for alert levels should be shorter than, say, 10 min (Fig. 1). For $t-t_E<10'$, no direct measurements of the sea level anomaly associated with the ongoing tsunami are typically available, thus $P(s_i|E;t)$ should be estimated based on source parameters. Each scenario s_i can be parameterized as $\sigma_i = \sigma_i(M_k, c_l, o_m)$, where M_k is the magnitude, c_l the geometrical centre of fault, and o_m a vector with all of the other rupture parameters (e.g. strike, dip, rake, slip, other kinematic rupture parameters). Consequently, $P(s_i|E;t)$ can be factorized as a chain of conditional probabilities:

$$P(s_i(\mathrm{M}_k,c_l,o_m)|E,t) = P(o_m|c_l,\,\mathrm{M}_k;E,t)P(c_l|\mathrm{M}_k;E,t)P(\mathrm{M}_k|E,t) \quad (2)$$

where $P(\mathrm{M}_k|E,t)$ is the probability of the magnitude bin corresponding to M_k, $P(c_l|\mathrm{M}_k;E,t)$ is the probability of the 3D volume bin (lon, lat, z) corresponding to c_l and depending on M_k, and $P(o_m|c_l,\mathrm{M}_k;E,t)$ describes the dependence of all the other unknown earthquake parameters on position and magnitude.

For $t-t_E<10'$, not even a complete seismic source characterization is usually available. Real-time information typically includes only hypocentre and magnitude

estimation, while robust estimates of the other parameters o_m are available only at later times, such as a moment tensor solution. Nevertheless, given an earthquake of a given magnitude at a given location, the possible values of all other seismic parameters o_m are not all equally probable. They depend on the local long-term seismo-tectonic behaviour, and their likelihood can be retrieved from long-term PTHA, conditional to the magnitude and hypocentre real-time estimates. Therefore, $P(s_i(\mathrm{M}_k, c_l, o_m)|E, t)$ turns out to be a mixture of real-time (RT) and long-term (LT) estimations:

$$P(s_i(\mathrm{M}_k, c_l, o_m)|E, t - t_0 < 10') = P(o_m|c_l, \mathrm{M}_k)^{LT} P(c_l|\mathrm{M}_k; E, t)^{RT} P(\mathrm{M}_k|E, t)^{RT} \quad (3)$$

where:

- the magnitude probability $P(\mathrm{M}_k|E, t)^{RT}$ corresponding to the early automatic estimation uncertainty. We assume a normal distribution and integrate it over the magnitude bins corresponding to M_k. The normal distribution is set with the method of moments by setting the mean to the best-guess estimation and the standard deviations as the semi difference between 84 and 16th percentiles, as estimated from the adopted magnitude inversion method (see Supplementary Note 1 and Supplementary Table 2).
- the probability that c_l is the centre of the causative fault can be evaluated as follows. The position of the nucleation ζ can be seen as the (vector) sum of the spatial position of the centre of the fault c_l and the relative position of the nucleation within the fault, χ, that is $\zeta = c_l + \chi$, and thus $c_l = \zeta - \chi$. Consequently, $P(c_l|\mathrm{M}_k; E, t)^{RT}$ can be computed as the convolution between one distribution representing the uncertain position of ζ (from real-time information) and another distribution representing the uncertainty on the position of ζ within the fault. The latter depends on M_k: the larger the magnitude, the higher the probability that a relatively distant c_l can be associated with ζ. We assume a 3D normal distribution for both the uncertainty on ζ and $c_l - \zeta$. The former originates from the hypocentre estimation (see Supplementary Note 1 and Supplementary Table 2), while the latter is set centred in 0 with a covariance matrix with diagonal $\sigma_{xx}^2 = \sigma_{yy}^2 = (L/2)^2$, $\sigma_{zz}^2 = \frac{(W/2)^2}{2}$ (for an average dip of 45 degrees), and $\sigma_{xy} = \sigma_{xz} = \sigma_{yz} = 0$. In other words, this distribution, which describes the uncertainty in the position of nucleation within the fault, is obtained by multiplying three independent Gaussians with a horizontal standard deviation equal to L/2, and a vertical standard deviation $(W/2)\sin(\pi/4) = W/(2\sqrt{2})$. The fault dimensions W and L are evaluated using empirical scaling relations[76,77] for crustal and subduction interface earthquakes, respectively. Note that Murotani et al.[77] is selected to be more conservative since it provides larger expected areas than other empirical scaling laws available for subduction earthquakes. The convolution of these distributions (again a 3D normal distribution) is integrated over 3D volume bins corresponding to c_l.
- the probability $P(o_m|c_l, \mathrm{M}_k)^{LT}$ of the other earthquake parameters o_m is taken from long-term hazard estimations. Most earthquake parameters (e.g. faulting type or rupture details) mainly depend on the tectonic regime around the fault location (as evaluated from seismic catalogues) and on the characteristics of the source zone. For example, c_l may lie on a subduction interface, which has a dominantly reverse slip mechanism, whose exact direction may, in turn, depend on the specific location over the slab interface; or c_l may instead lie on the neighbouring outer-rise, with a higher probability for a normal mechanism. Other parameters (e.g. slip distribution) may depend on both position and magnitude. If this information is not available from previous long-term studies (at the global, regional or local scale), maximum ignorance can be modelled using uniform distributions until real-time information (e.g. focal mechanism and/or moment tensor estimations) become available.

To reduce the computational effort and save time, we implemented cut-off thresholds in the real-time estimations of Eq. 2, that is, the real-time quantification of the uncertainty in magnitude and hypocentral location. Scenarios with marginal probabilities smaller than the cut-off are neglected. For simplicity, the threshold in the hypocentral location has been implemented in 2D that is marginalizing in depth. We implemented thresholds corresponding to 1.5, 2, 2.5, and 3 standard deviations (Supplementary Table 4). On average, passing from 2 to 3 standard deviations increases the number of scenarios by one order of magnitude (from 10^3–10^4 to 10^4–10^5), significantly expanding the computational cost. Percentiles 5th-95th of the PTF remain stable for standard deviations ≥2, and computational times are within 2' (the longest being ~ 100"), which can be considered an acceptable upper-limit for a non-engineered real-time serial application. Hence, the two standard deviations cut-off is taken as a reference for all examples and tests discussed.

In our prototype implementation for the Mediterranean Sea, the real-time earthquake parameter estimations are computed by the Early-Est software (see Supplementary Note 1). The long-term information is instead based on the NEAMTHM18 tsunami hazard model (http://www.tsumaps-neam.eu/[65–67]). NEAMTHM18 includes millions of scenarios completely covering the Mediterranean sea, considering two seismicity types for dealing selectively with epistemic uncertainty: predominant seismicity (PS), constrained to happen inside geometrically well-constrained subduction interfaces, and background seismicity (BS), diffused everywhere within the crust. PS includes the Calabrian, Hellenic, and Cyprus Arcs, while BS covers all the Mediterranean with a regular grid, including the relatively less-constrained seismicity potentially occurring on unmapped offshore faults and the surroundings of subduction zones (e.g. in the outer-rise).

Outside the Mediterranean, the discretization strategy defined by NEAMTHM18 is still used, but PS sources are the subduction zones defined in SLAB2 model[112] and BS sources are modelled over a regular grid with size ~0.2 × 0.2 degree corrected to define approximately equal size cells[113]. Real-time earthquake parameter estimates are taken from the literature (for the Maule case study[114]) and the forecast of focal mechanisms for crustal faults from[113].

Seismic fault parameters are considered less uncertain for PS than for BS. In the BS branch, all fault parameters are set as free parameters, except for few physical constraints: an upper bound is set for magnitude ($M_k \lesssim 8.1$), and depth is limited by the crustal thickness. Faults are planar with uniform slip and fault size determined from empirical scaling relations[76]. For the PS branch instead, only magnitude, position on the slab, and slip distribution are parametrized, as the geometry is specified by the 3D subduction interface, and the rake is forced to comply with the dominant one on the subduction segment. For $M_k \gtrsim 8.0$, heterogeneous slip is imparted using stochastic models suitable for 3D faults[96]. The magnitude is extended up to the magnitude the interfaces may host. Several alternative strategies are considered to model epistemic uncertainty associated with subduction earthquakes, such as different seismogenic depth ranges, scaling relations, rigidity properties, and stochastic shallow slip amplification[66,96].

The separation between PS and BS is implemented by splitting $P(s_i \mid E, t)$ of Eqs. 1 and 3 in two terms, that is:

$$P(s_i|E, t) = P(s_i|E, t, PS)P(PS|\zeta, \mathrm{M}_k) + P(s_i|E, t, BS)(1 - P(PS|\zeta, \mathrm{M}_k)) \quad (4)$$

where $P(PS|\,\zeta, \mathrm{M}_k)$ is the probability that the nucleation started at the point ζ on one of the three subduction interfaces considered in the Mediterranean Sea (the Calabrian, Hellenic and Cyprian Arcs). This is computed from the uncertainty on ζ from the real-time estimation, considering a seismogenic volume corresponding to each interface with a buffer of 10 km. For $M_k > 8.1$, earthquakes are assumed to belong to PS, so $P(PS|\zeta, \mathrm{M}_k) = 1$[66]. $P(s_i|E, t, PS)$ and $P(s_i|\,E, t, BS)$ are both evaluated as in Eq. 2, using the same magnitude distribution. Both the long-term factors (focal mechanism for BS, slip distributions for PS) are taken from NEAMTHM18 (mean of the epistemic uncertainty) for the Mediterranean case studies and, when alternative scenarios were present in NEAMTHM18, they were all included in the databank $\{s_i\}$, weighted by their epistemic credibility. For the Chilean subduction zone, slip distributions were produced, following the same strategy adopted in the NEAMTHM18[95,96].

Quantification of PTF's propagation factor. For each source s_i, the propagation factor in Eq. 1 is based on the results of one numerical tsunami simulation, often obtained as a linear combination of synthetic tsunamis produced by elementary sources.

The NEAMTHM18 propagation database[66,67] is based on dislocations in a homogeneous elastic medium. Seafloor deformations were processed with a low-pass wavenumber filter (modelled as 1/cosh(kH) following Kajiura approach[115], where k is the wavenumber and H is the average sea depth nearby the fault) to obtain the tsunami initial condition, reconstructed as a combination of Gaussian-shaped elementary sea-level elevations. Tsunami simulations are saved at the 50 m isobaths and, in this regime, nonlinear effects are negligible[116]. Gaussian sources were modelled with the benchmarked GPU-based nonlinear shallow water Tsunami-HySEA code (https://edanya.uma.es/hysea)[117], with eight hours of propagation on a regular grid including the whole Mediterranean Sea, using the 30 arc-sec bathymetric model SRTM30+ (http://topex.ucsd.edu/WWW_html/srtm30_plus.html). The results are obtained at the 50 meters isobath almost evenly spaced at ~20 km from each other along the coasts of the Mediterranean Sea (Supplementary Fig. 1 and Supplementary Dataset 1). The time step is computed using the usual CFL stability condition, that for a 2D, 2-step numerical scheme writes as $\Delta t = 1/4 \times \mathrm{CFL} \times \min(\Delta x/\lambda_{\max}, \Delta y/\lambda_{\max})$, where $\lambda_{\max}$ is the maximum eigenvalue of the matrix associated with the hyperbolic system to be approximated[118]. The CFL number retained is 0.95 (must be ≤1), and the resulting time steps depend on the scenario simulated (mesh size and maximum propagation depth).

The NEAMTHM18 propagation database does not cover scenarios outside the NEAM region. For the scenarios within the Chilean subduction zone, we exploit modern high-performance computing infrastructures[69], performing all the individual simulations required to complete the source ensemble. For the Maule case study, the simulation environment has been set as the fault is modelled with a mesh of triangular elements preserving the variable strike and dip of the Nazca subduction zone as in the SLAB2 model. The numerical simulations have been performed using Tsunami-HySEA code with a bathymetric grid for the Pacific Ocean with a spatial resolution of 30 arc-sec[95].

Wave amplitudes in front of the coast are estimated from the offshore simulation results with the basic version of Green's law[119]: $x_{1m} = x_{50m}\sqrt[4]{50}$. Unlike in NEAMTHM18, the uncertainty related to tsunami generation, propagation, and inundation simplifications[102,103] is here modelled as a log-normal distribution, with median equal to the modelled tsunami near-coast wave amplitude, plus an unknown bias and a standard deviation that may be estimated by comparing modelled tsunamis against observations[102,103]. This uncertainty includes unmodeled source variability (realistic earthquakes are usually more variable than

the scenarios in $\{s_i\}$), local topo-bathymetric features, as well as to the variability of the tsunami along the coastline among different forecast points[92,102]. For simplicity, we neglect the bias, and set

$$P(X > x|s_i; p) = 1 - \Phi([\log(x) - \log(\xi(s_i, p))]/1) \quad (5)$$

where $\Phi(x)$ is a standard cumulative normal distribution, and $\xi(s_i, p)$ is the value of the selected TIM (here, near-coast wave amplitude) evaluated at the forecast point p due to the scenario σ_i. Bearing in mind the variability set by other authors[85,96], the variance is here set to 1.

Testing source geometry and focal mechanisms forecasts. To test the Zemmouri-Boumerdes forecast, we considered a total of 12 solutions as reported in Supplementary Table 3, five of them based on seismic moment tensor inversion, and the other seven obtained from geodetic finite-fault inversions (see Supplementary Note 4). The null hypothesis H0 is that the estimations can be considered a sample of our forecast model. To test H0, we randomly sampled groups of 12 focal mechanisms from the distribution $P(o_m|c_l, M_k; E, t)$ of Eq. 3, marginalized for all the parameters except the angles strike, dip, and rake. Then, we computed the log-likelihood of each group, assuming independence, and we compared the obtained distribution with the log-likelihood of the observations. Under H0, the rank of observations should be larger than a pre-defined conventional confidence level (one-tailed test).

The same test is performed for all the 12 events in the testing dataset of Fig. 5a, both collectively (all the events together) and individually (all events taken separately). We tested both preferred fault and double-couple planes, and H0 is evaluated at standard confidence levels. Even if the dependence of a single CMT solution is weak, we repeated the same tests restricting to the nine events that occurred after the production of the method[68] (in September 2016).

All the results are discussed in the Main Text and in Supplementary Note 7.

Testing tsunami forecasts. The test of PTF against tsunami observations is performed simultaneously at all the locations with available data. Considering that they are correlated to each other, we adopted a two-step strategy. First, we sampled scenarios from the source model $P(s_i|E, t = t^*)$ of Eq. 1 and considered the spatially correlated results. Second, we stacked the comparisons at all forecast points by taking the difference between the observations and the expected value (the mean) of $P(X > x|s_i; p)$ (the propagation factor) for the sampled scenarios, allowing us to compare all locations simultaneously. In this way, the uncertainty on the source is fully sampled, while the uncertainty on the propagation is averaged. Under the null hypothesis that PTF source and propagation factors are not significantly and systematically biased (in the sense of a large systematic over/underestimation), we expect that the distribution of the differences will contain the value 0. Where multiple observations associated with the same forecast point are available, the difference is computed against the maximum observation to guarantee a balanced and robust forecast evaluation. We verified that 0 is not in the tails of the distribution, but it is contained between the percentiles 2.5–97.5 for $\alpha = 0.05$. An example of this test is reported in Fig. 5b.

Whenever the available observations are all equal to 0, a bias would be found by the previous test, since PTF always forecasts >0. This occurs for seven events (see Supplementary Notes 6 and 7). In this case, the test described above is modified by verifying that 0.10 m (minimum threshold of Advisory AL) is unlikely at all the locations where observations are available. Adopting as above $\alpha = 0.05$, we tested that 0.10 m falls at percentiles larger than 95th, respectively (one-tailed test). An example of this test is reported in Fig. 5c.

Data availability

All data generated or analysed during this study are included in this published article, in its supplementary information files, and in the referenced datasets (e.g., NEAMTHM18: http://www.tsumaps-neam.eu, IRIS Data Services and Data Management Center: https://ds.iris.edu/ds, Orpheus EIDA data services: https://www.orfeus-eu.org/data, VLIZ-IOC/UNESCO repository: http://www.ioc-sealevelmonitoring.org, Earthquake Sourve Model Database: http://equake-rc.info/SRCMOD).

Code availability

The PTF Matlab code used for this paper is available on Github at https://github.com/INGV/matPTF.

Received: 22 July 2020; Accepted: 23 August 2021;
Published online: 28 September 2021

References

1. Satake, K., Fujii, Y., Harada, T. & Namegaya, Y. Time and space distribution of Coseismic Slip of the 2011 Tohoku earthquake as inferred from tsunami waveform data. *Bull. Seismol. Soc. Am.* **103**, 1473–1492 (2013).
2. Palmer, T. N. et al. Representing model uncertainty in weather and climate prediction. *Annu. Rev. Earth Planet. Sci.* **33**, 163–193 (2005).
3. Leutbecher, M. & Palmer, T. N. Ensemble forecasting. *J. Comput. Phys.* **227**, 3515–3539 (2008).
4. Bernard, E. & Titov, V. Evolution of tsunami warning systems and products. *Philos. Trans. A Math. Phys. Eng. Sci.* **373**, 20140371 (2015).
5. Kanamori, H. & Rivera, L. Source inversion of W phase: speeding up seismic tsunami warning. *Geophys. J. Int.* **175**, 222–238 (2008).
6. Angove, M. et al. Ocean observations required to minimize uncertainty in global tsunami forecasts, warnings, and emergency response. *Front. Mar. Sci.* **6**, 350, https://doi.org/10.3389/fmars.2019.00350 (2019).
7. Wang, Y. et al. Tsunami data assimilation without a dense observation network. *Geophys. Res. Lett.* **46**, 2045–2053 (2019).
8. Wang, Y., Heidarzadeh, M., Satake, K., Mulia, I. E. & Yamada, M. A tsunami warning system based on offshore bottom pressure gauges and data assimilation for Crete Island in the Eastern Mediterranean Basin. *J. Geophys. Res. Solid Earth* **125**, e2020JB020293, https://doi.org/10.1029/2020JB020293 (2020).
9. Heidarzadeh, M., Wang, Y., Satake, K. & Mulia, I. E. Potential deployment of offshore bottom pressure gauges and adoption of data assimilation for tsunami warning system in the western Mediterranean Sea. *Geosci. Lett.* **6**, 19 (2019).
10. Maeda, T., Obara, K., Shinohara, M., Kanazawa, T. & Uehira, K. Successive estimation of a tsunami wavefield without earthquake source data: a data assimilation approach toward real-time tsunami forecasting. *Geophys. Res. Lett.* **42**, 7923–7932 (2015).
11. Carvajal, M., Araya-Cornejo, C., Sepúlveda, I., Melnick, D. & Haase, J. S. Nearly instantaneous tsunamis following the Mw 7.5 2018 Palu earthquake. *Geophys. Res. Lett.* **46**, 5117–5126 (2019).
12. Newman, A. V. & Okal, E. A. Teleseismic estimates of radiated seismic energy: the E/M 0 discriminant for tsunami earthquakes. *J. Geophys. Res. Solid Earth* **103**, 26885–26898 (1998).
13. Blewitt, G. et al. Rapid determination of earthquake magnitude using GPS for tsunami warning systems. *Geophys. Res. Lett.* **33**, L11309, https://doi.org/10.1029/2006GL026145 (2006).
14. Lomax, A. & Michelini, A. Mwpd: A duration–amplitude procedure for rapid determination of earthquake magnitude and tsunamigenic potential from P waveforms. *Geophys. J. Int.* **176**, 200–214 (2009).
15. Hirshorn, B., Weinstein, S. & Tsuboi, S. On the application of Mwp in the near field and the March 11, 2011 Tohoku earthquake. *Pure Appl. Geophys.* **170**, 975–991 (2013).
16. Melgar, D. et al. Local tsunami warnings: perspectives from recent large events. *Geophys. Res. Lett.* **43**, 1109–1117 (2016).
17. Sahakian, V. J., Melgar, D. & Muzli, M. Weak near-field behavior of a tsunami earthquake: toward real-time identification for local warning. *Geophys. Res. Lett.* **46**, 9519–9528 (2019).
18. Lay, T., Liu, C. & Kanamori, H. Enhancing tsunami warning using P wave coda. *J. Geophys. Res. Solid Earth* **124**, 10583–10609 (2019).
19. Duputel, Z., Rivera, L., Kanamori, H. & Hayes, G. W phase source inversion for moderate to large earthquakes (1990–2010). *Geophys. J. Int.* **189**, 1125–1147 (2012).
20. Inoue, M., Tanioka, Y. & Yamanaka, Y. Method for near-real time estimation of tsunami sources using ocean bottom pressure sensor. *Netw. (S-Net.). Geosci.* **9**, 310 (2019).
21. Howe, B. M. et al. SMART cables for observing the global ocean: science and implementation. *Front. Mar. Sci.* **6**, 424, https://doi.org/10.3389/fmars.2019.00424 (2019).
22. Mulia, I. E. & Satake, K. Developments of tsunami observing systems in Japan. *Front. Earth Sci.* **8**, 145, https://doi.org/10.3389/feart.2020.00145 (2020).
23. Makinoshima, F., Oishi, Y., Yamazaki, T., Furumura, T. & Imamura, F. Early forecasting of tsunami inundation from tsunami and geodetic observation data with convolutional neural networks. *Nat. Commun.* **12**, 2253 (2021).
24. Inazu, D. et al. Near-field tsunami forecast system based on near real-time seismic moment tensor estimation in the regions of Indonesia, the Philippines, and Chile. *Earth Planet Space* **68**, 73 (2016).
25. Cienfuegos, R. et al. What can we do to forecast tsunami hazards in the near field given large epistemic uncertainty in rapid seismic source inversions? *Geophys. Res. Lett.* **45**, 4944–4955 (2018).
26. Satake, K. Double trouble at Tonga. *Nature* **466**, 931–932 (2010).
27. Delescluse, M. et al. April 2012 intra-oceanic seismicity off Sumatra boosted by the Banda-Aceh megathrust. *Nature* **490**, 240–244 (2012).
28. Lay, T. et al. The October 28, 2012 Mw 7.8 Haida Gwaii underthrusting earthquake and tsunami: slip partitioning along the Queen Charlotte Fault transpressional plate boundary. *Earth Planet. Sci. Lett.* **375**, 57–70 (2013).
29. Sorensen, J. & Mileti, D. S. Decision-making uncertainties in emergency warning system Organizations. *Int. J. Mass Emergencies Disasters* **5**, 33–61 (1987).
30. WMO. *Guidelines on Ensemble Prediction Systems and Forecasting* (WMO, 2012).

31. IOC/UNESCO. *Intergovernmental Oceanographic Commission / UNESCO] IOC/UNESCO Symposium on Advances in Tsunami Warning to Enhance Community Responses* (Summary Statement, 2018).
32. JMA. *(Japan Meteorological Agency) Lessons learned from the tsunami disaster caused by the 2011 Great East Japan Earthquake and improvements in JMA's tsunami warning system*. http://www.data.jma.go.jp/svd/eqev/data/en/tsunami/LessonsLearned_Improvements_brochure.pdf (2013).
33. Woo, G. & Aspinall, W. Need for a risk-informed tsunami alert system. *Nature* **433**, 457–457 (2005).
34. Behrens, J. et al. A new multi-sensor approach to simulation assisted tsunami early warning. *Nat. Hazards Earth Syst. Sci.* **10**, 1085–1100 (2010).
35. Blaser, L., Ohrnberger, M., Riggelsen, C., Babeyko, A. & Scherbaum, F. Bayesian networks for tsunami early warning. *Geophys. J. Int.* **185**, 1431–1443 (2011).
36. Blaser, L., Ohrnberger, M., Krüger, F. & Scherbaum, F. Probabilistic tsunami threat assessment of 10 recent earthquakes offshore Sumatra. *Geophys. J. Int.* **188**, 1273–1284 (2012).
37. Tatsumi, D., Calder, C. A. & Tomita, T. Bayesian near-field tsunami forecasting with uncertainty estimates. *J. Geophys. Res. Oceans* **119**, 2201–2211 (2014).
38. Giles, D., Gopinathan, D., Guillas, S. & Dias, F. Faster than real time tsunami warning with associated hazard uncertainties. *Front. Earth Sci.* **8**, 597865 (2021).
39. Allen, S. C. R. & Greenslade, D. J. M. Developing tsunami warnings from numerical model output. *Nat. Hazards* **46**, 35–52 (2008).
40. Harig, S. et al. The Tsunami Scenario Database of the Indonesia Tsunami Early Warning System (InaTEWS): evolution of the coverage and the involved modeling approaches. *Pure Appl. Geophys.* **177**, 1379–1401 (2020).
41. Greenslade, D. J. M. et al. *An enhanced tsunami scenario database: t2*. (Bureau of Meteorology, 2009).
42. Amato, A. et al. From seismic monitoring to tsunami warning in the Mediterranean Sea. *Seismol. Res. Lett.* **92**, 1796–1816, https://doi.org/10.1785/0220200437 (2021).
43. Tinti, S., Graziani, L., Brizuela, B., Maramai, A. & Gallazzi, S. Applicability of the decision matrix of North Eastern Atlantic, Mediterranean and connected seas Tsunami Warning System to the Italian tsunamis. *Nat. Hazards Earth Syst. Sci.* **12**, 843–857 (2012).
44. Catalan, P. A. et al. Design and operational implementation of the integrated tsunami forecast and warning system in Chile (SIPAT). *Coast. Eng. J.* **62**, 373–388 (2020).
45. Allen, S. C. R. & Greenslade, D. J. M. Model-based tsunami warnings derived from observed impacts. *Nat. Hazards Earth Syst. Sci.* **10**, 2631–2642 (2010).
46. Davies, G. Tsunami variability from uncalibrated stochastic earthquake models: tests against deep ocean observations 2006–2016. *Geophys. J. Int* **218**, 1939–1960 (2019).
47. Davies, G. & Griffin, J. Sensitivity of probabilistic tsunami hazard assessment to far-field earthquake slip complexity and rigidity depth-dependence: Case Study of Australia. *Pure Appl. Geophys.* **177**, 1521–1548 (2020).
48. Budnitz, R. et al. *Senior Seismic Hazard Analysis Committee (SSHAC): Recommendations for Probabilistic Seismic Hazard Analysis: Guidance on Uncertainty and Use of Experts: Main Report*. https://www.nrc.gov/reading-rm/doc-collections/nuregs/contract/cr6372/vol1/index.html (1997).
49. Fakhruddin, B., Clark, H., Robinson, L. & Hieber-Girardet, L. Should I stay or should I go now? Why risk communication is the critical component in disaster risk reduction. *Prog. Disaster Sci.* **8**, 100139 (2020).
50. Frewer, L. et al. The views of scientific experts on how the public conceptualize uncertainty. *J. Risk Res.* **6**, 75–85 (2003).
51. Woo, G. *Calculating Catastrophe* (IMPERIAL COLLEGE PRESS, 2011).
52. Goltz, J. D. *Introducing Earthquake Early Warning in California: A Summary of Social Science and Public Policy Issues—A Report to OES and the Operational Areas* (Governor's Office of Emergency Services, Sacramento CA, USA, 2002).
53. Iervolino, I., Giorgio, M. & Manfredi, G. Expected loss-based alarm threshold set for earthquake early warning systems. *Earthq. Eng. Struct. Dyn.* **36**, 1151–1168 (2007).
54. Iervolino, I. Performance-based earthquake early warning. *Soil Dyn. Earthq. Eng.* **31**, 209–222 (2011).
55. Fischhoff, B. The realities of risk-cost-benefit analysis. *Science* **350**, aaa6516–aaa6516 (2015).
56. Rogers, D. & Tsirkunov, V. *Global assessment report on disaster risk reduction: costs and benefits of early warning systems*. http://documents1.worldbank.org/curated/en/609951468330279598/pdf/693580ESW0P1230aster0Risk0Reduction.pdf (2010).
57. Jordan, T. H., Marzocchi, W., Michael, A. J. & Gerstenberger, M. C. Operational earthquake forecasting can enhance earthquake preparedness. *Seismol. Res. Lett.* **85**, 955–959 (2014).
58. Field, E. H. et al. The potential uses of operational earthquake forecasting: Table 1. *Seismol. Res. Lett.* **87**, 313–322 (2016).
59. Solomos, G., Pinto, A. & Dimova, S. *A review of the seismic hazard zonation in national building codes in the context of Eurocode 8*. https://eurocodes.jrc.ec.europa.eu/doc/EUR23563EN.pdf (2008).
60. MCDEM. *[New Zealand Ministry of Civil Defence & Emergency Management] Tsunami evacuation zones: director's guideline for Civil Defence Emergency Management Groups* (Ministry of Civil Defence & Emergency Management, 2008).
61. MCDEM. *[New Zealand Ministry of Civil Defence & Emergency Management] Tsunami evacuation zones: director's guideline for Civil Defence Emergency Management Groups* (Ministry of Civil Defence & Emergency Management, 2016).
62. DPC. *[Dipartimento della Protezione Civile] Indicazioni alle Componenti ed alle Strutture operative del Servizio nazionale di protezione civile per l'aggiornamento delle pianificazioni di protezione civile per il rischio maremoto - Normativa. Dipartimento della Protezione Civile* http://www.protezionecivile.gov.it/amministrazione-trasparente/provvedimenti/dettaglio/-/asset_publisher/default/content/indicazioni-alle-componenti-ed-alle-strutture-operative-del-servizio-nazionale-di-protezione-civile-per-l-aggiornamento-delle-pianificazioni-di-prot-1 (2018).
63. Tonini, R. et al. Testing inundation maps for evacuation planning in Italy. *Front. Earth Sci.* **9**, 628061, https://doi.org/10.3389/feart.2021.628061 (2021).
64. Chock, G., Yu, G., Thio, H. K. & Lynett, P. J. Target structural reliability analysis for tsunami hydrodynamic loads of the ASCE 7 Standard. *J. Struct. Eng.* **142**, 04016092 (2016).
65. Basili, R. et al. *NEAM Tsunami Hazard Model 2018 (NEAMTHM18): online data of the Probabilistic Tsunami Hazard Model for the NEAM Region from the TSUMAPS-NEAM project*. https://doi.org/10.13127/tsunami/neamthm18 (2018).
66. Basili, R. et al. The making of the NEAM Tsunami Hazard Model 2018 (NEAMTHM18). *Front. Earth Sci.* **8**, 616594 https://doi.org/10.3389/feart.2020.616594 (2021).
67. Basili, R. et al. *NEAMTHM18 Documentation: the making of the TSUMAPS-NEAM Tsunami Hazard Model 2018*. https://doi.org/10.5281/zenodo.3406625 (2019).
68. Selva, J. et al. Quantification of source uncertainties in Seismic Probabilistic Tsunami Hazard Analysis (SPTHA). *Geophys. J. Int.* **205**, 1780–1803 (2016).
69. Løvholt, F. et al. *Urgent Tsunami Computing. in 2019 IEEE/ACM HPC for Urgent Decision Making (UrgentHPC)* 45–50 (IEEE, 2019).
70. Heidarzadeh, M. & Satake, K. The 21 May 2003 Tsunami in the Western Mediterranean Sea: statistical and wavelet analyses. *Pure Appl. Geophys.* **170**, 1449–1462 (2013).
71. Alasset, P.-J., Hébert, H., Maouche, S., Calbini, V. & Meghraoui, M. The tsunami induced by the 2003 Zemmouri earthquake (MW= 6.9, Algeria): modelling and results. *Geophys. J. Int.* **166**, 213–226 (2006).
72. Sahal, A. et al. The tsunami triggered by the 21 May 2003 Boumerdès-Zemmouri (Algeria) earthquake: field investigations on the French Mediterranean coast and tsunami modelling. *Nat. Hazards Earth Syst. Sci.* **9**, 1823–1834 (2009).
73. Braunmiller, J. & Bernardi, F. The 2003 Boumerdes, Algeria earthquake: regional moment tensor analysis. *Geophys. Res. Lett.* **32**, L06305, https://doi.org/10.1029/2004GL022038 (2005).
74. Dziewonski, A. M., Chou, T.-A. & Woodhouse, J. H. Determination of earthquake source parameters from waveform data for studies of global and regional seismicity. *J. Geophys. Res. Solid Earth* **86**, 2825–2852 (1981).
75. Ekström, G., Nettles, M. & Dziewoński, A. M. The global CMT project 2004–2010: centroid-moment tensors for 13,017 earthquakes. *Phys. Earth Planet. Inter.* **200–201**, 1–9 (2012).
76. Leonard, M. Self-consistent earthquake fault-scaling relations: update and extension to stable continental strike-slip faults self-consistent earthquake fault-scaling relations. *Bull. Seismol. Soc. Am.* **104**, 2953–2965 (2014).
77. Murotani, S., Miyake, H. & Koketsu, K. Scaling of characterized slip models for plate-boundary earthquakes. *Earth Planets Space* **60**, 987–991 (2008).
78. Belabbès, S., Wicks, C., Çakir, Z. & Meghraoui, M. Rupture parameters of the 2003 Zemmouri (Mw 6.8), Algeria, earthquake from joint inversion of interferometric synthetic aperture radar, coastal uplift, and GPS. *J. Geophys. Res. Solid Earth* **114**, B03406, https://doi.org/10.1029/2008JB005912 (2009).
79. Delouis, B. et al. Slip distribution of the 2003 Boumerdes-Zemmouri earthquake, Algeria, from teleseismic, GPS, and coastal uplift data. *Geophys. Res. Lett.* **31**, L18607, https://doi.org/10.1029/2004GL020687 (2004).
80. Meghraoui, M. et al. Coastal uplift and thrust faulting associated with the Mw = 6.8 Zemmouri (Algeria) earthquake of 21 May, 2003. *Geophys. Res. Lett.* **31**, L19605, https://doi.org/10.1029/2004GL020466 (2004).
81. Santos, R., Caldeira, B., Bezzeghoud, M. & Borges, J. F. The Rupture Process and Location of the 2003 Zemmouri–Boumerdes Earthquake (Mw 6.8) Inferred from Seismic and Geodetic Data. *Pure Appl. Geophys.* **172**, 2421–2434 (2015).
82. Semmane, F., Campillo, M. & Cotton, F. Fault location and source process of the Boumerdes, Algeria, earthquake inferred from geodetic and strong motion data. *Geophys. Res. Lett.* **32**, L01305, https://doi.org/10.1029/2004GL021268 (2005).
83. Yagi, Y. & Fukahata, Y. Introduction of uncertainty of Green's function into waveform inversion for seismic source processes. *Geophys. J. Int.* **186**, 711–720 (2011).

84. Yelles, K., Lammali, K., Mahsas, A., Calais, E. & Briole, P. Coseismic deformation of the May 21st, 2003, Mw = 6.8 Boumerdes earthquake, Algeria, from GPS measurements. *Geophys. Res. Lett.* **31**, L13610, https://doi.org/10.1029/2004GL019884 (2004).
85. Davies, G. et al. A global probabilistic tsunami hazard assessment from earthquake sources. *Geol. Soc. Lond. Spec. Publ.* **456**, 219–244 (2018).
86. Glimsdal, S. et al. A new approximate method for quantifying tsunami maximum inundation height probability. *Pure Appl. Geophys.* **176**, 3227–3246 (2019).
87. Griffin, J. et al. An evaluation of onshore digital elevation models for modeling tsunami inundation zones. *Front. Earth Sci.* **3**, 32, https://doi.org/10.3389/feart.2015.00032 (2015).
88. Song, J. & Goda, K. Influence of elevation data resolution on tsunami loss estimation and insurance rate-making. *Front. Earth Sci.* **7**, 246, https://doi.org/10.3389/feart.2019.00246 (2019).
89. Gibbons, S. J. et al. Probabilistic tsunami hazard analysis: high performance computing for massive scale inundation simulations. *Front. Earth Sci.* https://doi.org/10.3389/feart.2020.591549 (2020).
90. Gailler, A., Hébert, H., Schindelé, F. & Reymond, D. Coastal amplification laws for the French tsunami warning center: numerical modeling and fast estimate of tsunami wave heights along the French Riviera. *Pure Appl. Geophys.* **175**, 1429–1444 (2018).
91. Gusman, A. R., Tanioka, Y., MacInnes, B. T. & Tsushima, H. A methodology for near-field tsunami inundation forecasting: Application to the 2011 Tohoku tsunami: Tsunami Inundation Forecasting Method. *J. Geophys. Res. Solid Earth* **119**, 8186–8206 (2014).
92. Behrens, J. et al. Probabilistic tsunami hazard and risk analysis—a review of research gaps. *Front. Earth Sci.* **9**, 628772, https://doi.org/10.3389/feart.2021.628772 (2021).
93. Selva, J. et al. Tsunami risk management for crustal earthquakes and non-seismic sources in Italy. *Riv. Nuovo Cim.* **44**, 69–144 (2021).
94. Romano, F. et al. Benchmarking the optimal time alignment of tsunami waveforms in nonlinear joint inversions for the Mw 8.8 2010 Maule (Chile) Earthquake. *Front. Earth Sci.* **8**, 585429 (2020).
95. Selva, J. et al. *Data for: Probabilistic Tsunami Forecasting for Early Warning.* (2021) https://doi.org/10.6084/m9.figshare.15015132. (2021).
96. Scala, A. et al. Effect of shallow slip amplification uncertainty on probabilistic tsunami hazard analysis in subduction zones: use of long-term balanced stochastic slip models. *Pure Appl. Geophys.* **177**, 1497–1520 (2020).
97. Polet, J. & Kanamori, H. In *Encyclopedia of Complexity and Systems Science* (ed. Meyers, R. A.) 1–22 (Springer, 2016).
98. National Geophysical Data Center. *Global Historical Tsunami Database.* https://doi.org/10.7289/V5PN93H7 (2020).
99. NOAA. [National Oceanic and Atmospheric Administration] National Data Buoy Center. https://www.ndbc.noaa.gov/.
100. Power, W., Downes, G. & Stirling, M. Estimation of tsunami hazard in New Zealand due to South American Earthquakes. *Pure Appl. Geophys.* **164**, 547–564 (2007).
101. Aranguiz, R. et al. Tsunami resonance and spatial pattern of natural oscillation modes with multiple resonators. *J. Geophys. Res. Oceans* **124**, 7797–7816 (2019).
102. Grezio, A. et al. Probabilistic tsunami hazard analysis: multiple sources and global applications. *Rev. Geophys.* **55**, 1158–1198 (2017).
103. Choi, B. H., Pelinovsky, E., Ryabov, I. & Hong, S. J. Distribution functions of tsunami wave heights. *Nat. Hazards* **25**, 1–21 (2002).
104. Dogan, G. G. et al. The 30 October 2020 Aegean Sea Tsunami: Post-Event Field Survey Along Turkish Coast. *Pure Appl. Geophys.* **178**, 785–812, https://doi.org/10.1007/s00024-021-02693-3 (2021).
105. González, F. I. et al. The NTHMP tsunameter network. *Nat. Hazards* **35**, 25–39 (2005).
106. NRC. *(National Research Council) Science and Decisions: Advancing Risk Assessment* (National Academies Press, 2009).
107. Di Bucci, D. & Savadori, L. Defining the acceptable level of risk for civil protection purposes: a behavioral perspective on the decision process. *Nat. Hazards* **90**, 293–324 (2018).
108. Woo, G. Probabilistic criteria for volcano evacuation decisions. *Nat. Hazards* **45**, 87–97 (2008).
109. Marzocchi, W. & Woo, G. Probabilistic eruption forecasting and the call for an evacuation. *Geophys. Res. Lett.* **34**, L22310 (2007).
110. Marzocchi, W., Iervolino, I., Giorgio, M. & Falcone, G. When is the probability of a large earthquake too small? *Seismol. Res. Lett.* **86**, 1674–1678 (2015).
111. Iervolino, I. et al. Operational (Short-Term) earthquake loss forecasting in Italy. *Bull. Seismol. Soc. Am.* **105**, 2286–2298 (2015).
112. Hayes, G. P. et al. Slab2, a comprehensive subduction zone geometry model. *Science* **362**, 58–61 (2018).
113. Taroni, M. & Selva, J. A Testable Worldwide Earthquake Faulting Mechanism Model. *Seismological Research Letters* (2021).
114. U.S. Geological Survey. *Advanced National Seismic System (ANSS) Comprehensive Catalog.* https://doi.org/10.5066/F7MS3QZH. (2017).
115. Kajiura, K. The leading wave of a tsunami. *B. Earthq. Res. Inst.* **41**, 535–571 (1963).
116. Molinari, I. et al. Fast evaluation of tsunami scenarios: uncertainty assessment for a Mediterranean Sea database. *Nat. Hazards Earth Syst. Sci.* **16**, 2593–2602 (2016).
117. de la Asunción, M. et al. Efficient GPU implementation of a two waves TVD-WAF method for the two-dimensional one layer shallow water system on structured meshes. *Computers Fluids* **80**, 441–452 (2013).
118. Macías, J., Mercado, A., González-Vida, J. M., Ortega, S. & Castro, M. J. Comparison and computational performance of tsunami-HySEA and MOST models for LANTEX 2013 scenario: impact assessment on Puerto Rico Coasts. *Pure Appl. Geophys.* **173**, 3973–3997 (2016).
119. Kamigaichi, O. In *Encyclopedia of Complexity and Systems Science* (ed. Meyers, R. A.) 1–38 (Springer, 2014).

Acknowledgements

We thank D. Melini, and S. Cacciaguerra, INGV, and P. Lanucara, CINECA, for their support with the computational infrastructures; F. Hernandez for providing some sea-level data archived at the VLIZ-IOC/UNESCO repository; S. Belabbès, B. Delouis, M. Meghraoui, R. Santos for providing their inversion results for the 2003 Zemmouri-Boumerdes earthquake, and especially Y. Yagi and K. Obara who updated their inversion on purpose. This work benefited from the agreement between Istituto Nazionale di Geofisica e Vulcanologia and the Italian Presidenza del Consiglio dei Ministri, Dipartimento della Protezione Civile (DPC). This paper does not necessarily represent DPC official opinion and policies. The research leading to these results has been also partially funded by the European Union's Horizon 2020 research and innovation programme under the ChEESE project, grant agreement No. 823844, and benefited of the PRACE project TSU-CAST—TSUnami ForeCASTing (Proposal 2019215169, Call 20). Some figures were produced with GMT (Generic Mapping Tools, https://www.generic-mapping-tools.org/) and Inkscape, https://inkscape.org/.

Author contributions

J.S. and S.L., with the support of M.V., F.R., R.T., P.P., F.B., and M.T. developed the Methodology. J.S. implemented the software, with the contribution of P.P., M.V., F.R., R.T., A.B., A.S., B.B., S.L., J.M., M.J.C., J.M.G.V., and C.S.L. A.B., F.L., S.G., F.M., A.P., and A.A. contributed to the conceptualization of the methodology. R.B., F.E.M., M.M.T., F.M., and A.A. developed fundamental Resources in input to the methodology. F.M., A.P., and A.A. supported the development of the methodology from the very early stages. J.S., S.L., and M.V. prepared the original draft, which has been reviewed by all the authors.

Competing interests

The authors declare no competing interests.

Additional information

Supplementary information The online version contains supplementary material available at https://doi.org/10.1038/s41467-021-25815-w.

Correspondence and requests for materials should be addressed to J. Selva.

Peer review information *Nature Communications* thanks Patricio Catalan, Christa von Hillebrandt-Andrade, and Yuchen Wang for their contribution to the peer review of this work. Peer reviewer reports are available.

Reprints and permission information is available at http://www.nature.com/reprints

Publisher's note Springer Nature remains neutral with regard to jurisdictional claims in published maps and institutional affiliations.

frontiers in Earth Science

REVIEW
published: 29 April 2021
doi: 10.3389/feart.2021.628772

Probabilistic Tsunami Hazard and Risk Analysis: A Review of Research Gaps

Jörn Behrens[1], Finn Løvholt[2], Fatemeh Jalayer[3], Stefano Lorito[4], Mario A. Salgado-Gálvez[5,6], Mathilde Sørensen[7], Stephane Abadie[8], Ignacio Aguirre-Ayerbe[9], Iñigo Aniel-Quiroga[9], Andrey Babeyko[10], Marco Baiguera[11], Roberto Basili[4], Stefano Belliazzi[3], Anita Grezio[12], Kendra Johnson[13], Shane Murphy[14], Raphaël Paris[15], Irina Rafliana[16,17], Raffaele De Risi[18], Tiziana Rossetto[11], Jacopo Selva[12], Matteo Taroni[4], Marta Del Zoppo[3], Alberto Armigliato[19], Vladimír Bureš[20], Pavel Cech[20], Claudia Cecioni[21], Paul Christodoulides[22], Gareth Davies[23], Frédéric Dias[24], Hafize Başak Bayraktar[3], Mauricio González[9], Maria Gritsevich[25,26,27], Serge Guillas[11], Carl Bonnevie Harbitz[2], Utku Kânoğlu[28], Jorge Macías[29], Gerassimos A. Papadopoulos[30], Jascha Polet[31], Fabrizio Romano[4], Amos Salamon[32], Antonio Scala[3], Mislav Stepinac[33], David R. Tappin[11,34], Hong Kie Thio[35], Roberto Tonini[4], Ioanna Triantafyllou[36], Thomas Ulrich[37], Elisa Varini[38], Manuela Volpe[4] and Eduardo Vyhmeister[39]*

[1]Department of Mathematics/CEN, Universität Hamburg, Hamburg, Germany, [2]NGI - Norwegian Geotechnical Institute, Oslo, Norway, [3]University of Naples Federico II, Naples, Italy, [4]Istituto Nazionale di Geofisica e Vulcanologia, Rome, Italy, [5]ERN Internacional, Mexico City, Mexico, [6]Centre Internacional de Metodes Numerics en Enginyeria (CIMNE), Barcelona, Spain, [7]University of Bergen, Bergen, Norway, [8]Universite de Pau et des Pays de L'Adour, E2S UPPA, SIAME, France, [9]IHCantabria - Instituto de Hidráulica Ambiental de La Universidad de Cantabria, Santander, Spain, [10]Deutsches GeoForschungsZentrum GFZ, Potsdam, Germany, [11]University College London, London, United Kingdom, [12]Istituto Nazionale di Geofisica e Vulcanologia, Sezione di Bologna, Bologna, Italy, [13]GEM Foundation, Pavia, Italy, [14]Ifremer, Plouzané, France, [15]Laboratoire Magmas and Volcans, Aubière, France, [16]German Development Institute/Deutsches Institut für Entwicklungspolitik (DIE), Bonn, Germany, [17]Indonesian Institute of Sciences (LIPI), Jakarta, Indonesia, [18]University of Bristol, Bristol, United Kingdom, [19]Alma Mater Studiorum - University of Bologna, Bologna, Italy, [20]University of Hradec Kralove, Hradec Kralove, Czech Republic, [21]Università Degli Studi Roma Tre, Rome, Italy, [22]Cyprus University of Technology, Limassol, Cyprus, [23]Geoscience Australia, Canberra, ACT, Australia, [24]University College Dublin, Dublin, Ireland, [25]Finnish Geospatial Research Institute (FGI), Masala, Finland, [26]Department of Physics, University of Helsinki, Helsinki, Finland, [27]Institute of Physics and Technology, Ural Federal University, Ekaterinburg, Russian Federation, [28]Department of Engineering Sciences, Middle East Technical University, Ankara, Turkey, [29]Facultad de Ciencias, Universidad de Málaga, Málaga, Spain, [30]International Society for the Prevention and Mitigation of Natural Hazards, Athens, Greece, [31]Cal Poly Pomona, Pomona, CA, United States, [32]Geological Survey of Israel, Jerusalem, Israel, [33]University of Zagreb, Zagreb, Croatia, [34]British Geological Survey, Nottingham, United Kingdom, [35]AECOM, Los Angeles, CA, United States, [36]Department of Geology and Geoenvironment, National and Kapodistrian University of Athens, Athens, Greece, [37]Department of Earth and Environmental Sciences, Ludwig-Maximilians-Universität München, Munich, Germany, [38]C.N.R. - Institute for Applied Mathematics and Information Technologies, Milano, Italy, [39]Insight Research Centre, University College Cork, Cork, Ireland

Tsunamis are unpredictable and infrequent but potentially large impact natural disasters. To prepare, mitigate and prevent losses from tsunamis, probabilistic hazard and risk analysis methods have been developed and have proved useful. However, large gaps and uncertainties still exist and many steps in the assessment methods lack information, theoretical foundation, or commonly accepted methods. Moreover, applied methods have very different levels of maturity, from already advanced probabilistic tsunami hazard analysis for earthquake sources, to less mature probabilistic risk analysis. In this review we give an overview of the current state of probabilistic tsunami hazard and risk analysis. Identifying research gaps, we offer suggestions for future research directions. An extensive literature list allows for branching into diverse aspects of this scientific approach.

Keywords: tsunami, probabilistic method, hazard, risk, research gap

OPEN ACCESS

Edited by:
Victoria Miller, The University of the West Indies St. Augustine, Trinidad and Tobago

Reviewed by:
Eric Geist, United States Geological Survey (USGS), United States
Patricio Andres Catalan, Federico Santa María Technical University, Chile

****Correspondence:***
Jörn Behrens, joern.behrens@uni-hamburg.de

Specialty section:
This article was submitted to Geohazards and Georisks, a section of the journal Frontiers in Earth Science

Received: *12 November 2020*
Accepted: *10 February 2021*
Published: *29 April 2021*

Citation:
Behrens J, Løvholt F, Jalayer F, Lorito S, Salgado-Gálvez MA, Sørensen M, Abadie S, Aguirre-Ayerbe I, Aniel-Quiroga I, Babeyko A, Baiguera M, Basili R, Belliazzi S, Grezio A, Johnson K, Murphy S, Paris R, Rafliana I, De Risi R, Rossetto T, Selva J, Taroni M, Del Zoppo M, Armigliato A, Bureš V, Cech P, Cecioni C, Christodoulides P, Davies G, Dias F, Bayraktar HB, González M, Gritsevich M, Guillas S, Harbitz CB, Kânoğlu U, Macías J, Papadopoulos GA, Polet J, Romano F, Salamon A, Scala A, Stepinac M, Tappin DR, Thio HK, Tonini R, Triantafyllou I, Ulrich T, Varini E, Volpe M and Vyhmeister E (2021) Probabilistic Tsunami Hazard and Risk Analysis: A Review of Research Gaps. Front. Earth Sci. 9:628772. doi: 10.3389/feart.2021.628772

INTRODUCTION

Tsunamis are rare but potentially devastating natural hazards. With often limited available data, a coherent framework that incorporates data, physical assumptions (i.e., the general model of the system), and statistical methods for hazard and risk analysis is necessary to assess consequences affecting different layers of societies. To further develop, standardize and document such a framework is the underlying objective of COST Action AGITHAR (Accelerating Global Science in Tsunami Hazard and Risk Analysis; AGITHAR, 2020) and this article forms one outcome of the Action.

Probabilistic tsunami hazard and risk analyses (PTHA and PTRA, respectively) offer structured and rigorous procedures that allow for tracing and weighting the key elements in understanding the potential tsunami hazard and risk in globally distributed applications (e.g., Basili et al., 2021). Because of this, PTHA are becoming a standard basis for tsunami risk assessment around the world. Significant challenges in this analysis method are 1) the choice of hypothetical events and assigning "correct" probabilities, and ii) the impact of source regions distributed throughout an ocean basin and, conceivably, unifying distinct types of sources in a homogeneous probabilistic framework with a comprehensive treatment of uncertainty. The great importance of PTHA is due to its practical implications for society providing information for long-term planning and coastal management in areas where potential tsunamis may occur. Conversely, PTRA are still less abundant and standardized than PTHA, as elaborated in this review.

Few mega-tsunamis have been observed in the instrumental period, a timeframe spanning from approximately the 1960s to today. Thus, it is challenging to confidently assess the rate at which consequential tsunamis will occur. Predominantly seismically triggered tsunamis comprise about 80% of all tsunamis worldwide (e.g., Harbitz et al., 2014) with the remainder caused by landslides, volcanoes, or meteorological phenomena.

The sparsity of background data and requirements in engineering applications have driven the development of probabilistic methods for assessing tsunami hazard and risk aiming for unbiased comparisons of different hazards (natural and anthropogenic) as well as their uncertainty quantification. In recent years, the probabilistic framework has been increasingly applied. However, broadly accepted approaches are not yet defined, and potentially incompatible implementations of probabilistic methods are used in different regions across the world, and different tsunami source types are often treated separately and are rarely combined.

In this study, we have documented current gaps and open research questions related to PTHA and PTRA. We have organized this review into two main sections, one focused on tsunami hazard and the other on risk. We preface these topics with a brief introduction to the probabilistic framework underlying both PTHA and PTRA. Note that we grouped the gaps in numerical modeling in the hazard analysis related section, even though modeling may also be considered a cross-cutting topic. We believe, however, that the mentioned gaps are more related and addressed in a similar way as the other hazards related research gaps.

While PTHA and PTRA allow for including uncertainty in a consistent way, it is necessary to point out that it is not always simple to describe the knowledge gaps formally, for example through alternative models, and quantify their impact on hazard and risk models in terms of epistemic uncertainty (i.e., caused by lack of knowledge or data, Kiureghian and Ditlevsen, 2009). Overall, the research gaps identified in this study are "known unknowns" (e.g., Logan, 2009) and deserve more thorough research efforts, in order to determine their influence on the overall outcome of the PTHA or PTRA workflow.

This fact makes it hard to determine quantitatively the importance of each of the research gaps. Nevertheless, we tried to assess—in a qualitative way—the relative priority of research gaps and discuss this in the last section of this report.

PROBABILISTIC FRAMEWORK

In this section, we present a structure for probabilistic hazard and risk analyses. An overview is given in **Figure 1**. More in-depth reviews of identified gaps related to the individual probabilistic framework components are discussed in sections "*Probabilistic Tsunami Hazard Analysis*" and "*Probabilistic Tsunami Risk Assessment*".

The purpose of PTHA is to find the probability for a tsunami intensity measure (*IM*) to exceed a given threshold in a predefined time interval. Note that, in the PTHA framework, "Intensity Measure" is used with a meaning that differs from the "tsunami intensity scale" used, for instance, in tsunami catalogs to define the "size" of a tsunami or the effects it produces inland. In the PTHA context, an *IM* is a physical observable strictly connected to the physics of the process. Common *IM*s are wave amplitude, flow depth, current velocity, momentum flux, or maximum inundation height, depending on the problem setting (Grezio et al., 2017).

Different probabilistic framework alternatives for computational PTRA exist. One option, rooted in seismic risk analysis, is *performance-based* risk assessment, presented by PEER (Pacific Earthquake Engineering Center) in 2000. The term performance-based is often used in contraposition to traditional prescriptive assessment procedures for seismic-resistant building design (Fardis, 2009). The performance-based framework aims to provide a practical yet rigorous workflow and has also been used for risk assessment for hurricanes (e.g., van de Lindt and Dao, 2009; Barbato et al., 2013), floods (De Risi et al., 2013; Jalayer et al., 2016), and tsunamis (Chock et al., 2011; Chock, 2016; Attary et al., 2017). This framework can be organized in different modules; for example, *hazard* and *vulnerability* or *hazard*, *fragility* and *consequence*. Modules communicate with each other through intermediate variables and their conditional probabilities. Examples of intermediate variables are intensity measure (*IM*), damage measure (*DM*) and decision variable (*DV*). *IM* serves as an intermediate variable between hazard and vulnerability. *DM*

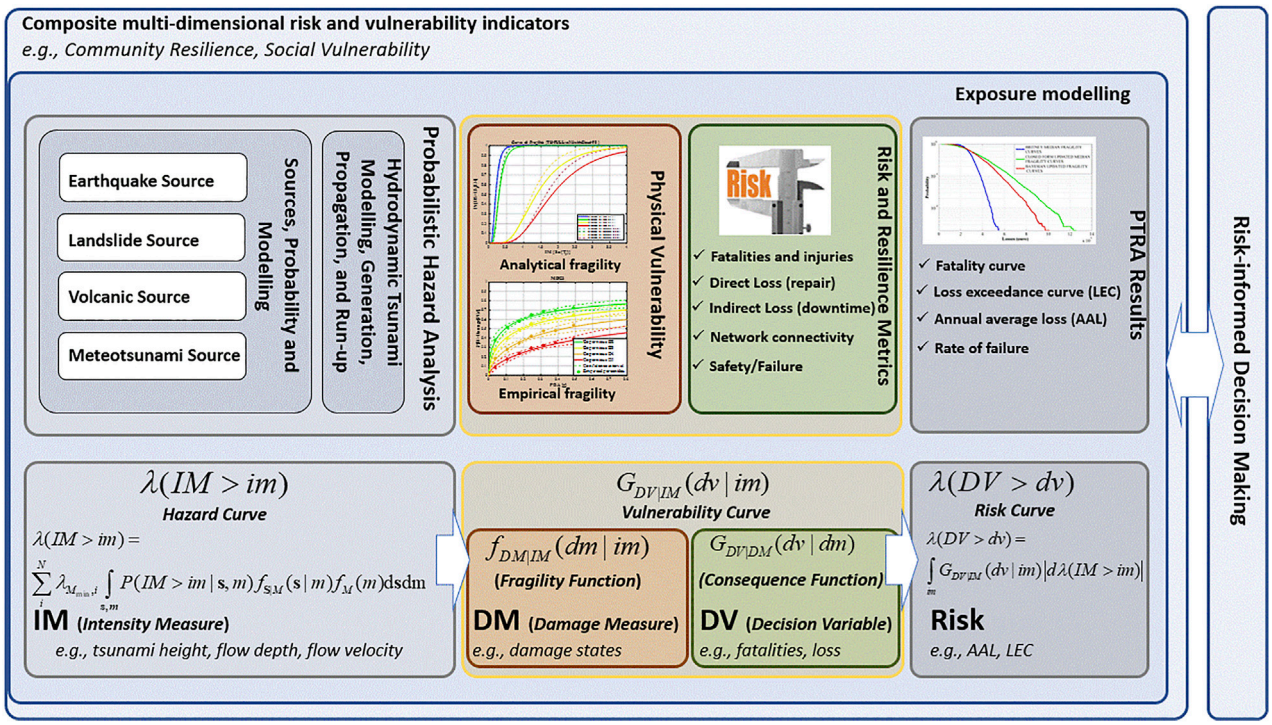

FIGURE 1 | Roadmap of PTHA and PTRA frameworks: The entire process of risk evaluation needs to interact with the (risk-informed) decision-making process. *Composite multi-dimensional risk and vulnerability indicators* ("*Probabilistic Tsunami Hazard Analysis*" section) are shown as defining the context for the complex tsunami risk evaluation. The *exposure modeling* ("*Probabilistic Tsunami Risk Assessment*" section) defines groups of individuals and assets at risk. The horizontal flowchart at the bottom of the figure shows the PEER-like workflow for risk assessment. *Probabilistic hazard analysis* ("*Probabilistic Tsunami Hazard Analysis*" section) discusses estimation of the mean annual frequency (rate) of exceedance of a given value (*im*) of an intensity measure (*IM*, **Eq. 1**) commonly visualized as a hazard curve. The *IM* can be a vector or a scalar that describes the intensity of a tsunami. Examples of IM's are flow depth, maximum tsunami inundation height, etc. *M* refers in a generic manner to the size of various tsunami sources (e.g., earthquake magnitude, landslide volume). The tsunami *sources, probability and modeling* (earthquake, landslide, volcanic and meteotsunami) are discussed in "*Probabilistic Tsunami Hazard Analysis*" section. **s** denotes the vector of source parameters. *N* denotes the number of tsunamigenic sources. $\lambda_{M_{\min,i}}$ denotes the mean annual frequency of tsunamigenic events exceeding $M_{\min}$ from source *i*. "*Gaps in Hydrodynamic Tsunami Modeling, Generation, Propagation, and Run-up*" section discusses *hydrodynamic tsunami modeling, generation, propagation and run-up*. The *physical vulnerability* ("*Gaps in Physical Vulnerability*" section) discusses the estimation of the probability distribution for a damage measure (DM, specific value *dm*) given *IM* (specific value *im*), known as the fragility function. The most common example of a DM is the physical damage state. The *risk and resilience metrics* section ("*Gaps in Risk and Resilience Metrics*" section) discusses the estimation of various decision variables (e.g., fatalities, repair costs, downtime) denoted as DV (specific value *dv*). More specifically, it discusses the probability distribution for DV given DM also known as the consequence function. The vulnerability function (**Eq. 3**) describes the (mean and standard deviation) of the probability distribution for DV given *IM* and is obtained by integrating over the entire domain of DM. One way to show the PTRA results is through visualizing the mean annual frequency of exceeding a specific value *dv* of DV (e.g., the loss exceedance curve (LEC) or the annual average loss (AAC)) shown in **Eq. 2**, referred to generically as the risk curve.

connects vulnerability with fragility and describes physical damage. *DV* connects fragility with consequences and reaches out to decision-makers with numbers of casualties, repair costs, or downtimes. Interestingly, several risk-informed decision-making processes related to tsunamis are based on PTHA information only (e.g., hazard-based evacuation zones, hazard-based land-use planning). As an example, the criterion "flow depth (*IM*) larger than a threshold (*im*)" can be used as a basis for decision-making (e.g., assigning evacuation zones). In other words, an *IM* can act as an intermediate variable (intensity measure) as well as a decision variable.

To illustrate the framework, suppose a finite set of *N* hypothetical tsunamigenic sources representing all possible tsunami events affecting the site of interest. Each event occurs randomly in time and independently of all others (i.e., as a Poisson process). The tsunami hazard curve–the main outcome of PTHA–describes the mean annual rate of a tsunami event affecting location *x* with an intensity measure *IM(x)* greater than some threshold *im*, denoted as $\lambda(IM(x) \geq im)$. This can be expressed as:

$$\lambda\left(IM\left(x\right) \geq im\right) = \sum_{i}^{N} \lambda_{M_{\min,i}} \int P\left(IM\left(x\right) \geq im | s, m\right) f_{S|M}\left(s|m\right) f_{M}\left(m\right) \mathrm{dsd}m \quad (1)$$

where $\lambda_{M_{\min,i}}$ is the mean annual rate of occurrence of tsunamigenic events from source *i* (e.g., earthquakes, landslides, etc.) having magnitudes *M* exceeding $M_{\min}$, f_M is the conditional probability density function for $M \geq M_{\min,i}$, and $f_{S|M}$ is the probability density function of the set of source parameters *S* given magnitude *M*. The aleatoric uncertainty associated with variable source characteristics can be represented by probabilistic prediction models of the source

parameters. Finally, $p(IM(x) \geq im|\boldsymbol{s},m)$ is the complementary cumulative distribution function of IM given $S = s$ and $M = m$, and can be evaluated through tsunami simulations. Note that **Eq. 1** can be used only if sources are independent; a counterexample being a landslide generated from the same earthquake that amplifies the ensuing tsunami's destruction.

Epistemic uncertainty in PTHA is often accounted for using logic trees or, more recently, ensemble modeling, which allow alternative hypotheses for uncertain parameters, each of which is assigned a weight reflecting confidence in the respective parameter value (e.g., Geist and Parsons, 2006; Selva et al., 2016; Grezio et al., 2017). **Equation 1** is computed for each logic tree 'end branch'.

Building on tsunami hazard, the tsunami loss curve at any location is calculated by convolving vulnerability and hazard over the entire span of IM:

$$\lambda(DV \geq \mathrm{d}v) = \int_{im} G_{DV|IM}(\mathrm{d}v|im)|\mathrm{d}\lambda(IM(x) \geq im)| \quad (2)$$

where $\lambda(DV \geq \mathrm{d}v)$ is the mean annual rate of occurrence of DV larger than a threshold $\mathrm{d}v$. Vulnerability is expressed through the complementary probability distribution function denoted as $G_{DV|IM}(\mathrm{d}v|im)$, for DV given IM, and is itself calculated by integrating fragility and consequence functions (see also **Figure 1**):

$$G_{DV|IM}(\mathrm{d}v|im) = \int_{\mathrm{d}m} G_{DV|DM}(dv|dm) f_{DM|IM}(dm|im) ddm, \quad (3)$$

with

- $f_{DM|IM}$, the *tsunami fragility function,* predicts the probability of incurring a particular value (dm) of damage measure DM (e.g., damage states) for a given $IM = im$;
- $G_{DV|DM}(\mathrm{d}v|\mathrm{d}m)$, the *tsunami consequence function* (e.g., the damage-loss function), expressed as the complementary cumulative distribution function of DV given DM.

Strictly speaking, **Eqs. 1** and **2** do not consider multi-hazard and multi-risk aspects such as cascading effects, combined damage due to tsunami loading and earthquake shaking. Assuming a Poisson process, the rate of exceedance λ is often transformed the first excursion of a specific value $\mathrm{d}v$ for a generic decision variable DV in the time Δt (e.g., 1 year, 50 years):

$$P(DV \geq \mathrm{d}v; \Delta t) = 1 - \exp(-\lambda(DV \geq \mathrm{d}v)\Delta t) \quad (4)$$

PROBABILISTIC TSUNAMI HAZARD ANALYSIS

This section discusses gaps in PTHA, focusing on those in tsunami sources and hydrodynamic modeling. Each subsection includes a summary of the present state-of-the-art, followed by an in-depth discussion of the gaps.

Gaps in Earthquake Source Representation

Existing Methods

Seminal Seismic PTHA (SPTHA) was performed using crude source and tsunami representations (Lin and Tung, 1982; Rikitake and Aida, 1988; Tinti, 1991). Since then, the methodology has evolved dramatically (Geist and Parsons., 2006; Annaka et al., 2007; Power et al., 2007; Thio et al., 2007; Burbidge et al., 2008; González et al., 2009; Sørensen et al., 2012; Hoechner et al., 2016; Miyashita et al., 2020), also in the framework of large programs (e.g., Horspool et al., 2014; Davies et al., 2018; Davies and Griffin, 2018; Basili et al., 2021).

SPTHA methodology for spatio-temporal and kinematic source treatment and the basic uncertainty framework were mostly transcribed from Probabilistic Seismic Hazard Analysis (PSHA, Esteva, 1967; Cornell, 1968; a historical perspective: McGuire, 2008). Due to tsunami data scarcity, it is challenging to derive hazard estimates directly from historical records (Geist and Parsons, 2006; Grezio et al., 2017). Consequently, numerical modeling is a distinctive characteristic of SPTHA where seafloor displacement and tsunami evolution from generation to inundation are simulated for each scenario (Geist and Parsons, 2006; Geist and Lynett, 2014). Source parameters can be inferred from past seismicity or from balancing the seismic moment across a fault zone, potentially constrained by geodetic strain rates (Grezio et al., 2017). Often only major subduction zones are considered in SPTHA, assuming that they are the main hazard drivers (e.g., González et al., 2009; Davies et al., 2018). In this case, spatial characterization provides geometrical and kinematic constraints, such as the fault geometry, preferential slip direction, and other source zone properties. Crustal and general seismicity from unconstrained or unknown faults is treated with a larger uncertainty (e.g., Selva et al., 2016; Basili et al., 2021). Earthquakes are usually simplified to having either uniform (e.g., Horspool et al., 2014) or heterogeneous instantaneous slip (e.g., De Risi and Goda, 2017). Seafloor deformation is predominantly computed analytically assuming an elastic homogeneous half-space (Mansinha and Smylie, 1971; Okada, 1992; Meade, 2007; Nikkhoo and Walter, 2015).

State-of-the-art seismic source representation for tsunami simulations is reviewed by Geist and Oglesby (2014) and Geist et al. (2019). Additionally, we note some innovative efforts for complex, yet computationally affordable, approaches to source simulation (Melgar et al., 2016; Murphy et al., 2016; Sepúlveda et al., 2017; Scala et al., 2020), and methods for handling source modeling uncertainties and sensitivity including temporal aspects and recurrence (Grezio et al., 2010; Basili et al., 2013; Lorito et al., 2015; Selva et al., 2016; Lotto et al., 2017; Davies, 2019; Goda, 2019; Davies and Griffin, 2020).

Identified Gaps

Limited Past Events and Data to Inform Hazard Models (S1)

Completeness and quality of historical earthquake data, needed to constrain seismic source parameters, varies greatly depending on the history of the investigated geographical region (Stucchi et al., 2004; Albini et al., 2014). Event catalogs are generally too short to account for the source frequency needed to model large average return periods in PTHA. The description of earthquake

recurrence and of the tail of the frequency-magnitude distribution is highly uncertain (Kagan, 2002; Geist and Parsons, 2014; Rong et al., 2014; Bommer and Stafford, 2016). In the attempt of constraining this uncertainty, seismic source parameters have been estimated globally using seismic or geodetic data or both (e.g., Bird and Kagan, 2004; Bird et al., 2015; Bird and Kreemer, 2015); however, these types of input data are not always considered by PTHAs. Moreover, a framework for constraining PTHA directly from tsunami observations exists (Geist and Parsons, 2006; Grezio et al., 2017), while treatment of incomplete catalogs is described by Smit et al. (2017). Where possible, other data types should also be considered. Paleo-seismic and paleo-tsunami catalogs may help constrain or validate at least large event recurrence (e.g., Priest et al., 2017; Paris et al., 2020), while GPS-constrained strain accumulation can indicate the total seismic moment rate (e.g., Hayes et al., 2018). Care should be taken of potential biases coming from overweighting evidence of large tsunamis in the past (Geist and Parsons, 2006).

Fault Identification, Fault and Source Zone Parameterization and Tsunamigenic Potential Characterization (S2)

Tsunami sources are often constrained from infrequent offshore geologic studies investigating very large areas. Therefore, geologic fault data are often incomplete, causing a wide range of source knowledge levels (Basili et al., 2013). Seismic source characterization for SPTHA generally refers to properties of pre-existing large faults, and often only to great subduction zone sources. All other–mostly crustal–faults are seldomly considered in PTHA, although non-subduction earthquakes may control tsunami hazard, especially when located near the target site (Selva et al., 2016). Despite overall good constraint of subduction interface geometries (e.g., Hayes et al., 2018), along-strike trench segmentation and its impact on rupture propagation remains uncertain, limiting rupture forecasts and hindering estimates of subduction earthquake maximum magnitude (e.g., Bilek, 2010; Kopp, 2013; Grezio et al., 2017). Whenever fault knowledge is incomplete, more randomized "background" seismicity modeling is needed, with less predictable geometry and seismic behavior compared to subduction interfaces (Sørensen et al., 2012; Selva et al., 2016). Fault slip rates can constrain seismicity recurrence parameters; these can vary both spatially (Zechar and Frankel, 2009) and temporally (e.g., Ota and Yamaguchi, 2004; Ramírez-Herrera et al., 2011; Tiberti et al., 2014) but usually only averages are considered due to a lack of information. Kagan and Jackson (2014) pointed out that more research would be needed for focal mechanism forecasting; identifying the prevailing faulting mechanism is a critical task particularly in tectonically complex environments. This is expected, in turn, to exert a strong influence on tsunami hazard.

Variety, Complexity, and Dynamics of Fault Mechanics (S3)

Source simplification represents a dominant uncertainty in SPTHA (Geist and Oglesby, 2014). Its effect on seafloor deformation needs to be investigated better, concerning deformation models that incorporate complex material properties, geometrical complexity, varying depth-dependent fault conditions, dynamic simulations including off-fault damage and near-surface amplification, which all may increase tsunami hazard (Masterlark, 2003; Ma, 2012; Kozdon and Dunham, 2013; Ryan et al., 2015; Murphy et al., 2016; Lotto et al., 2017; Murphy et al., 2018; Scala et al., 2019; Scala et al., 2020; Tonini et al., 2020). Secondary ruptures including splay faulting may happen as an independent source or as part of a large earthquake on the subduction interface (Wendt et al., 2009; Li et al., 2014; Hananto et al., 2020).

Tsunami earthquakes produce excessively large tsunami intensities compared to their moment magnitude (Polet and Kanamori, 2016), and their global and local frequency is unconstrained. A simplified characterization of *tsunami earthquakes*, which is sometimes adopted, assumes larger slip associated with less rigid materials at shallow depths to preserve the seismic moment (e.g., Bilek and Lay, 1999; Geist and Bilek, 2001). These and other very complex ruptures, potentially containing fault branching, rupture jumping, and mixed-mode slip (e.g., Ulrich et al., 2019a; Ulrich et al., 2019b), are not well represented in PTHA. On a larger scale, rupture area may be shared by more than one subduction interface, like in the case of triple junctions (e.g., Solomon event 2007, Lorito et al., 2016). Due to a lack of observations the likelihood of such events is uncertain and quantification of their relative contribution to SPTHA therefore difficult.

Due to all these uncertainties and the extreme computational demand for dynamic computation, numerical simulations are *de facto* replaced with heterogeneous stochastic slip modeling (e.g., Herrero and Bernard, 1994; Mai and Beroza, 2002; Davies et al., 2015; Sepúlveda et al., 2017), and less frequently with stochastic stress modeling (e.g., Wendt et al., 2009). Because source observations are relatively scarce, more statistical tests (Davies and Griffin, 2019) are needed for source model validation.

Empirical Scaling Relations (S4)

Several different empirical scaling relations are used to define earthquake rupture properties, such as length, width, average slip, and earthquake magnitude (e.g., Wells and Coppersmith, 1994; Murotani et al., 2008; Blaser et al., 2010; Strasser et al., 2010; Murotani et al., 2013; Goda et al., 2016; Skarlatoudis et al., 2016; Allen and Hayes, 2017; Thingbaijam et al., 2017). These relationships quantify appreciable uncertainties that are seldomly accounted for in SPTHA. These relations imply stress drop and time-dependent rupture characteristics and self-similarity of earthquakes across scales, but this is apparently violated in some cases. For example, the 2011 Tohoku earthquake released a huge amount of slip in a relatively small portion of the subduction interface compared to the Sumatra 2004 or Chile 1960 earthquakes (Okal, 2015); scaling relations are not directly applicable to abnormally slow and unusually large shallow slip occurring in low-rigidity zones during *tsunami earthquakes*.

Complex, Non-stationary Seismic Cycle (S5)

Even in the simplest subduction environment, the seismic cycle over co-seismic, inter-seismic and post-seismic phases is complex and non-stationary, for example due to visco-elastic rheology and

the role of fluids (Wang et al., 2012; Moreno et al., 2014; Melnick et al., 2017). Time-dependent models could potentially be used to estimate the stress transfer from one earthquake to the neighboring faults (King et al., 1994). Stress transfer from megathrust earthquakes triggering outer-rise ruptures or possibly even the opposite are such examples (e.g., Lorito et al., 2016). Based on seismic catalogs, it is possible to infer non-Poissonian earthquake recurrence, for example earthquake clustering (Kagan and Jackson, 1991). A time-dependent model, which could better describe the probability of earthquake occurrence for some specific applications or timeframes, is taken into account by only a few PTHAs (e.g., Goda et al., 2017; Goda, 2020).

Other Constraints (S6)

It is reasonable to assume that high seismic coupling correlates with future slip location. Under simplifying assumptions, along-strike geodetic coupling variation can be inferred from geodetic strain (Métois et al., 2012). Large uncertainty remains, particularly regarding the near-trench region (Loveless and Meade, 2011). Recent developments in seafloor geodesy and modeling techniques are offering improved constraints (e.g., increasing offshore coupling resolution, Bürgmann and Chadwell, 2014; Foster et al., 2020), and slow slip events and consequently the stress evolution on the fault (e.g., Araki et al., 2017). High seismic coupling combined with stress accumulation in areas of seismic inactivity is described as a seismic gap. The possibility of using seismic gaps to identify zones of enhanced seismic hazard has long been debated (e.g., Bilek and Lay, 2018). Attempts to obtain physically motivated constraints on the maximum magnitude utilizing convergence rate, age of the oceanic crust and sediment thickness have been rather unsuccessful (Okal, 2015). Ongoing research explores these and other controlling factors of subduction zone seismicity, including small- and large-scale roughness of the subduction interface, static friction coefficient, upper plate strain and rigidity, dip angle and curvature (e.g., Heuret et al., 2012; Bletery et al., 2016; Sallarès and Ranero, 2019; Rijsingen, et al., 2019; Muldashev and Sobolev, 2020). Additionally, rupture cycles and supercycles over multiple segments controlled by geological asperities have been proposed (Philibosian and Meltzner, 2020). Similar to some of the previously discussed items in this section, no consensus has been reached on the statistical meaning of such information and on how to frame it within SPTHA.

Gaps in Landslide Source Representation

Existing Methods

Landslide tsunami PTHA (LPTHA) was introduced less than a decade ago (Geist and Lynett, 2014). Its application is often similar to SPTHA (e.g., ten Brink et al., 2006; Lane et al., 2016), but can also be based on geotechnical interpretations with a strong emphasis on expert judgment (e.g., Grilli et al., 2009; Hermanns et al., 2013; Løvholt et al., 2020). Salamon and Di Manna (2019) derive empirical scaling relations for landslides triggered by onshore earthquakes. In LPTHA, the landslide volume is used analogously to the seismic moment in SPTHA as a rate of occurrence. The slide volume is generally also the most influential factor on tsunami genesis (Snelling et al., 2020). Landslide motion has a strong influence too (Løvholt et al., 2015b; Yavari-Ramshe and Ataie-Ashtiani, 2016). LPTHA source models are coupled to numerical tsunami models in Monte Carlo simulations. Methods for simulating both the landslide dynamics and tsunami generation range from block models (Harbitz, 1992; Tinti et al., 1997; Watts, 2000; Grilli and Watts, 2005; Tinti et al., 2006; Løvholt et al., 2015b), depth-averaged rheological models of viscoplastic or granular nature (e.g., Kelfoun and Druitt, 2005; Jop et al., 2006; Løvholt et al., 2017; Kim et al., 2019), to computational fluid dynamics (CFD) based approaches with different landslide complexity (e.g., Crosta et al., 2016; Abadie et al., 2020). Submarine landslide tsunamis are mainly characterized by the Froude number (landslide velocity over wave celerity) measuring the degree of critical landslide velocity, the landslide acceleration, and the rate of landslide mass mobilization (e.g., Ward, 2001; Løvholt et al., 2015b). Subaerial landslides are characterized by the landslide frontal area, along with the Froude number, landslide density, and slope angle (e.g., Fritz et al., 2003; Heller and Hager, 2010; Bullard et al., 2019).

Identified Gaps

Lack of Understanding and Likelihoods for Tsunamigenic Landslide Volumes (L1)

For submarine landslides, we refer to the reviews of Huhn et al. (2019) and Harbitz et al. (2014). The challenge can be attributed to several factors:

- Limited or insufficient mapping of past landslide occurrences. Their characteristics and lack of dating prevent constraining the age of the sediments without excessive uncertainty ranges (e.g., Geist et al., 2013). The new global landslide database initiative (Clare et al., 2019) is a good starting point for standardizing, but not yet complete enough for feeding LPTHA. Good data coverage exists for certain regions such as the Mediterranean (Urgeles and Camerlenghi, 2013), Gulf of Mexico (Pampell-Manis et al., 2016) and the US East Coast (Chaytor et al., 2009, Geist et al., 2014).
- Limited understanding of how past landslide recurrence can be projected into the future hazard, including time and geological context dependency. For example, we cannot yet generally link climatically driven trends to past landslide frequency (Urlaub et al., 2013). However, it is concluded that the last ice age affect present landslide probability offshore US (Lee, 2009) and Norway (Bryn et al., 2005).
- Limited available geological and geotechnical data inhibit identification of failure-prone sediments and discrimination from stable areas, including weak failure zones, pore pressure conditions or fractures, as well as obstacles or structures. When data exist, they may be proprietary, and a challenge is related to the need for covering very large geographical and heterogeneous regions. A methodological gap exists in bridging geotechnical data and slope stability models (e.g., Carlton et al., 2019) to volume-frequency relationships.

- Limited data and knowledge on triggers of landslides, such as meteorological or seismic events, impedes the quantitative assessment of potential landslide magnitude.

Difference of Onshore and Offshore Landslides (L2)
The specific character of subaerial and submarine landslides is often vastly different. Potential direct or indirect trigger mechanisms are sometimes not fully understood or difficult to embed into the probability of failure (e.g., precipitation-induced landslides, weak zones and fluid overpressure, range of failure propagation and cascading failure propagation spread). Understanding and estimating the annual probability of landslide failure in rock slopes with complex fracture patterns and stress conditions is associated with large uncertainty. Extensively monitored rock slopes in Norway (e.g., Blikra et al., 2005) show large motion over decades before failure takes place, rendering assessment of failure probability difficult. Matching expert judgment (e.g., Hermanns et al., 2013) to observed landslide magnitude frequency statistics (e.g., Nes, 2018) will help aggregate understanding of landslide frequencies and help link knowledge on failure-prone areas to probability. While epistemic uncertainties in the described situations are large, current LPTHA models do not incorporate them.

Limited Constraints on Landslide Dynamics and Material Behavior (L3)
The interplay of diverse tsunamigenic landslide parameters makes the generation complex, implying that much less voluminous landslides may be more effective tsunami generators than respectively larger ones. As an example, we note that the approximately 500 km^3 Trænadjupet Slide that occurred 4,500 years BP likely produced a moderate coastal impact possibly of just a few meters (e.g., Løvholt et al., 2017), while the 100 times less voluminous 1998 Papua New Guinea landslide induced more than 10 m run-up locally (e.g., Tappin et al., 2008). Because tsunami genesis is tightly linked to landslide acceleration as well as rate of mobilization of the landslide volume (e.g., Løvholt et al., 2005), quantifying the rate and nature of the slope failure is important. Just a few studies discuss the effect of initial failure rate on tsunami generation (e.g., Trapper et al., 2015; Germanovich et al., 2016; Puzrin et al., 2016) and related aspects such as remoulding and cascading failures on the landslide tsunami generation (e.g., Løvholt et al., 2017; Kim et al., 2019; Zengaffinen et al., 2020). How to include these factors and their associated probabilities in PTHA is not resolved. While advanced numerical models for landslide dynamics exist (e.g., Tinti et al., 1997; Jop et al., 2006; Savage et al., 2014; Si et al., 2018a; Si et al., 2018b; Kim et al., 2019; Wang et al., 2019; Gallotti and Tinti, 2020), their complexity and variety obfuscate understanding on which models are most suitable to be used. Furthermore, some models (e.g., Savage et al., 2014; Si et al., 2018a; Si et al., 2018b) are presently too comprehensive to be used in PTHA. Procedures for linking them to measured material properties and geological settings are not in place. Finally, fluid resistance forces (pressure drag, skin friction, and added mass) may be as important as the landslide properties, in particular for submarine landslides and further investigating physical understanding is necessary to constrain epistemic uncertainty.

Limited Availability of Benchmarks (L4)
Suitable benchmarks have recently been made available (e.g., Huang and Garcia, 1998; NTHMP, 2018; Kim et al., 2019), but are arguably less mature and fewer than their hydrodynamic modeling counterparts (e.g., Pedersen, 2008; Synolakis et al., 2008). A challenge is a transition from simplified laboratory tests to real-world landslide representation. Moreover, while numerous empirical lab experiments exist, they are significantly influenced by scale effects (Heller, 2011). Neither complex rheological behavior nor real-world complexity is covered in the benchmarks. Complex laboratory experiments (e.g., Rondon et al., 2011) can be used for validating CFD models, but CFD models are presently too computationally expensive for tsunami hazard analysis modeling.

Limited Past Events to Inform Hazard Models (L5)
Information about past landslides and tsunamis can be used to infer landslide dynamics uncertainty. This can be done using landslide run-out information alone (e.g., Salmanidou et al., 2017), which consequently yields broad epistemic uncertainties in LPTHA. By using tsunami information, such uncertainties can be drastically reduced (e.g., Gylfadóttir et al., 2017; Kim et al., 2019; Løvholt et al., 2020). In practice, however, very few landslide tsunami data are available.

Gaps in Volcano Source Representation

Existing Methods

Volcanic PTHA, coined VPTHA here, is even less developed than LPTHA (Grezio et al., 2017). Among the few examples are the VPTHA framework developed in Ulvrova et al. (2016) and Paris et al. (2019) for underwater explosions at Campi Flegrei, and Grezio et al. (2020) for pyroclastic flows of Vesuvius. Given that risk reduction measures at volcanoes are often related to the identification of precursory patterns preceding eruptions or to recognizing unrest episodes with increased volcanic activity, the volcanic hazard is often computed conditional to eruptions or unrest, and without an explicit quantification of long-term probability. For example, in Paris et al. (2019), the hazard analysis (Campi Flegrei, Naples, Italy) is confined to conditional tsunami intensity probabilities, due to probabilistic realizations of eruptions with different vent size and location.

Identified Gaps

Variety of Potential Volcanic Sources (V1)
Tsunamigenic volcanic events are diverse and they include both eruptive and non-eruptive triggering phenomena, such as underwater explosions, pyroclastic flows, lahars, slope failures, volcanic earthquakes, shock waves from large explosions, and caldera subsidence (Latter, 1981; Kienle et al., 1987; Begét et al., 2005; Day, 2015; Paris, 2015; Grezio et al., 2017). A large range of wave characteristics is typical for volcano tsunamis, even if most such sources are localized and generate mainly short-period waves with greater dispersion and limited far-field effects compared to earthquake-generated tsunamis (e.g., Yokoyama,

1987; Nomanbhoy and Satake, 1995; Le Méhauté and Wang, 1996; Choi et al., 2003; Watts and Waythomas, 2003; Bellotti et al., 2009; Maeno and Imamura, 2011; Ulvrova et al., 2016; Selva et al., 2019, 2020). However, tsunamis are among the farthest propagating volcanic perils, often generating regional impact (e.g., Krakatau, Stromboli, Ischia, etc., see for example Paris et al., 2014; Rosi et al., 2018; Selva et al., 2019; Gallotti et al., 2020). Notably, some of the tsunamigenic volcanic events overlap with those recorded for seismic and landslide tsunami: flank collapse, slope failure and even pyroclastic flows are related to landslides (Løvholt et al., 2015b; Paris, 2015); volcano-tectonic earthquakes occur with high frequency in volcanic areas (Paris, 2015). Such frequency information as well as understanding material properties and transformation during flow should draw upon volcanological expertise. It is often difficult to define a single generation phenomenon since different potentially tsunamigenic processes can occur during the same volcanic episode, especially during large caldera-forming eruptions (Paris, 2015).

Difficulties in Constraining Recurrence Rates (V2)

Since volcanic tsunami generation is so diverse, constraining recurrence rates for the different source types as eruptive phenomena (Walter et al., 2019), unrest episodes (Tinti et al., 1999; Selva et al., 2020), and triggered subaerial landslides (Selva et al., 2019) is difficult. The integration into a multi-source VPTHA is further complicated by the need for accounting for the complex interdependencies that may exist among the different source mechanisms. The hazard is often nonstationary through time (e.g., Bebbinghton, 2008; Bebbinghton, 2010), which represents another challenge.

Gaps in Modeling Tsunami Generation and Propagation (V3)

Extensive reviews on existing strategies to model volcanic sources are found in Paris, (2015), Grezio et al. (2017) and Paris et al. (2019). Given the complexity, an important part of the hazard analysis is oriented toward understanding the physical mechanism of generation, and how to represent this probabilistically. Similar to landslide generated tsunamis, volcano tsunami modeling suffers from the difficulty of coupling the complex dynamics of the generating event and its interaction with wave propagation. For example, pyroclastic flows are complex, multi-phase phenomena involving the interaction of high-temperature gases and volcanic clasts covering a very large range of granulometric dimensions (Freundt, 2003; Bougouin et al., 2020). This difficulty leads to simplified modeling schemes (e.g., Bevilacqua et al., 2017; Sandri et al., 2018). These simplified strategies may be too reduced for an effective constraint of their tsunami potential (Grezio et al., 2020). Some phenomena may be represented by empirical models (for submarine explosions, see Paris et al., 2019, and for caldera collapse, see Ulvrova et al., 2016). Experimental and numerical simulations coupled with field data increased understanding of the physics and main parameters of volcanic tsunamis (Grezio et al., 2017).

Lack of Data From the Geological Record (V4)

Tsunami is often not dealt with in the volcanological community, although it may be more fatal than other volcanic hazards such as lava flows or ash falls (Auker et al., 2013; Brown et al., 2017). Consequently, a systematic investigation of tsunami-related data in geological surveys at volcanoes is often missing. Because different volcanic phenomena may trigger tsunamis, even when tsunami data exist, attributing the observation to a specific mechanism is difficult (e.g., Krakatau 1883 eruption: Paris et al., 2014). Therefore, a systematic collection of available volcano-generated tsunami data and linking to potential volcanic generating processes is required. This will imply defining a strategy of tsunami-oriented monitoring around coastal volcanoes. It would be useful to combine such efforts with existing data collections such as the Global Volcanism Program (Global Volcanism Program, 2013).

Limited Availability of Well Recorded Past Events or Benchmark Studies (V5)

Only a few past events are well constrained in terms of both the source and of the subsequent tsunami (e.g., Unzen 1792, Karymskoye Lake 1996; Montserrat 1997 and 2003, Anak Krakatau 2018; Stromboli 2002 and 2019). The lack of consensus in modeling procedures for each type of tsunamigenic volcanic event, along with the tendency to consider all sources as "unique", complicates the task of defining benchmarks for volcano tsunamis.

Gaps in Meteorological Source Representation

Existing Methods

Meteotsunami PTHA, coined MPTHA here, was developed only recently (see Grezio et al., 2017). A framework for MPTHA development is proposed by Geist et al. (2014). The dynamics of meteotsunamis are fairly well-known (e.g., Monserrat et al., 2006; Sibley et al., 2020), related to unusually strong and rapid atmospheric pressure fluctuations and resonance effects causing strong waves closely associated with the behavior of tsunamis. The source mechanisms of meteotsunamis are also well understood (Monserrat et al., 2006; Pattiaratchi and Wijeratne, 2015) with a major driver a Proudman resonance (Proudman, 1929). Because meteotsunamis are strongly linked to (un)favorable combinations of pressure fluctuations, shallow (shelf) bathymetry, and directivity of the weather system, they take place more frequently in specific geographical areas, such as in the Adriatic Sea (Vilibić and Šepić, 2009), the Baltic Sea (Pellikka et al., 2020), and the East Coast of the United States (Pasquet et al., 2013). The main input data for meteotsunamis include meteorological pressure data, preferably with full spatial and temporal characteristics of the pressure field for given meteorological events. Such data can be used to provide synthetic probabilistic source scenarios as input to an MPTHA, where an example for the Northeast US coastline is given by Geist et al. (2014). While this field does

not share the data sparsity issues that are associated with volcanoes and landslides, large uncertainties persist, as briefly discussed below.

Identified Gaps

Lack of Understanding the Potential and Likelihood for Tsunamigenic Meteorological Patterns (M1)

A systematic assessment of potential source areas and exposed coastal regions is not available. Some regional studies can serve as a preliminary indication (e.g., Dusek et al., 2019; Šepić et al., 2012; Šepić et al., 2016), but a rigorous catalog is missing. Climatological information is likely available, but a systematic extraction of data concerning meteotsunami potential has not been performed. It is not clear whether the resolution of available climatological data (e.g., from reanalysis) is sufficiently fine to allow for the extraction of corresponding relevant meteotsunami source patterns.

High Sensitivity to Several Parameters and Lack of Understanding of Local Amplification Factors (M2)

Whitmore and Knight (2014) demonstrate the high sensitivity of typical tsunami impact to source parameters and hence a large gap in knowledge on relevant localized parameters. The size, speed, amplitude, directivity, and duration of an atmospheric disturbance resonating with the water column in a specific topographic setting need to be known to assess the hazard. Therefore, such parameters need to be derived for all tsunamigenic regions, then applied to available climatological data sets, and finally fed into corresponding models for assessment of hazard. An assessment of amplifying tidal conditions in each of such regions is also missing.

Limited Availability of Benchmark Studies (M3)

While there are many individual meteotsunami events described in the literature (e.g., Churchill et al., 1995; González et al., 2001; Pasquet et al., 2013; Vilibić et al., 2014), no truly validated benchmark data are available for meteotsunami benchmarking. In principle, a similar methodology as described in Synolakis et al. (2008) could be followed. However, only very little unification of source modeling has been achieved and except for preliminary simplified tests (as in Vilibić, 2008), there exists no widely accepted test suite. This applies in particular to verification and validation of the probabilistic workflow of MPTHA.

Limited Past Events and Data to Inform Hazard Models (M4)

There is no consistent catalog of occurrences, although regional studies have been performed (e.g., Haslett et al., 2009; Woodruff et al., 2018). As stated before, there are no unified parameterizations of meteotsunami sources, which could be entered into such a catalog. Even though many individual events are described in the literature (see subsection above), these are by no means representative or complete to be used in hazard models. More rigorous collection of data with the special focus on meteotsunamis–background climatology, meteorological situation, ocean state, topo-bathymetry–for the diverse areas of interest would be desirable.

Gaps in Hydrodynamic Tsunami Modeling, Generation, Propagation, and Run-up

Existing Methods

Hydrodynamic tsunami modeling includes numerical simulation of tsunami generation, propagation as well as coastal and onshore impact. It is an essential part of any PTHA or PTRA analysis. Reviews of commonly applied methods are available (e.g., Pedersen, 2008; Synolakis et al., 2008; Behrens and Dias, 2015). The pre-eminent challenge is the need to bridge a broad range of scales. First, in the probabilistic regime, a comprehensive PTRA must consider a very large number of scenarios to cover all relevant tsunamigenic sources, explore wave physics, and quantify uncertainties. Second, for each individual scenario source, large-scale propagation and coastal inundation modeling (optimally at scales of 1–10 m) need to be represented to quantify tsunami-related on-shore damages and losses. However, the fastest HPC simulation workflows (e.g., de la Asunción et al., 2013; Oishi et al., 2015; Macías et al., 2017; Musa et al., 2018) still require typically 10–60 min to simulate tsunami inundation at a scale of tens of meters, rendering them unsuitable for extensive PTRA studies with up to millions of scenarios (Basili et al., 2021). To overcome this "challenge of scales", modeling approximations are presently necessary for PTHA feasibility and can either involve 1) largely reducing the number of inundation scenarios (e.g., González et al., 2009; Lorito et al., 2015; Volpe et al., 2019; Williamson et al., 2020), 2) use of approximate models or statistics such as amplification factors (e.g., Løvholt et al., 2012; Kriebel et al., 2017; Gailler et al., 2018; Glimsdal et al., 2019), or 3) machine learning-based tsunami emulators (e.g., Sarri et al., 2012; Salmanidou et al., 2017; Giles et al., 2020).

Identified Gaps

PTHA Uncertainty Treatment for Tsunami Inundation Processes (H1)

At present, we lack well tested local PTHA benchmarks where the sources of uncertainties are effectively characterized, in a way that allows their formal propagation along the PTHA/PTRA assessment chain. Moreover, the effect of coseismic coastal displacement due to near field sources (e.g., Volpe et al., 2019), which affects tsunami inundation, should be investigated more deeply, especially when using techniques for reducing the number of scenarios. For this purpose, a large number of inundation scenarios are needed to quantify the epistemic uncertainty and bias caused by simplifications introduced through approximate methods. A local PTHA application using more than 40,000 earthquake sources (Gibbons et al., 2020) is only a start.

Tsunami Generation (H2)

Unit source models (Kajiura, 1963; Nosov and Kolesov, 2007; Molinari et al., 2016) of varying computational cost and complexity approximate the volumetric deep-water source displacements. While Lotto et al. (2019) clarified that the horizontal momentum does not effectively contribute to tsunami generation in deep-water sources, an extensive sensitivity analysis of how such simplifications affect PTHA

has not been carried out. Incorporating time-dependent and moving sources, be it earthquakes (e.g., Ulrich et al., 2019a), landslides (e.g., Løvholt et al., 2015b) or volcanoes, will involve much higher computational burden. How to limit the number of source time steps for time-dependent source modeling is sparsely studied (e.g., Zengaffinen et al., 2020). For landslide tsunamis, closed-form models (e.g., Watts et al., 2003; Cecioni and Bellotti, 2010) represent a simple alternative but can introduce biases when conveyed to real geographical settings, due to oversimplification or inadequacy for the real situation. Subaerial landslides and volcanoes are often simplified because the required consideration of full 3D hydrodynamics (e.g., Abadie et al., 2020) into PTHA poses too high computational demand. Hence, more research is needed for developing simplified time-dependent sources compatible with PTHA demands, while quantifying the epistemic uncertainty and bias caused by the simplification. New methods may facilitate more detailed characterization of past inundation scenarios and their sources (e.g., Chagué-Goff et al., 2012; Sugawara et al., 2014; Paris et al., 2020).

Uncertainty and Variability due to Numerical Model for Tsunami Propagation (H3)

Most non-linear shallow water (NLSW) simulation codes produce similar results in the propagation phase, in particular in controlled benchmark cases (e.g., Synolakis et al., 2008). However, clear model differences can appear due to varying components (applied numerical method, workflow, sources, setup etc.) in practical applications. Comparing different numerical forecast models in the Indian Ocean, Greenslade et al. (2014) found large variations, attributed to differences in the workflow and source representation rather than to the tsunami model itself. Testing how such kinds of uncertainty quantification relate to "heterogeneous modeling practices" has not been carried out systematically. Moreover, a rigorous investigation of the performance of far-field propagation is sparse (Dao and Tkalich, 2007; Davies and Griffin, 2020). Differences in numerical dissipation and discretization can also contribute to modeling deviations. As there is no standardized test case for far-field propagation that could reveal the differences in performance of different approaches, it is pressing to address these issues more systematically. Due to the computational burden, most PTHA applications today employ shallow water type models, neglecting frequency dispersion, which can lead to bias. Dispersion can be incorporated through conventional dispersive wave solvers (e.g., Bellotti et al., 2008; Løvholt et al., 2008; Kim et al., 2009; Shi et al., 2012), or through manipulating numerical schemes in NLSW codes (like MOST, e.g., Wei et al., 2008), although the general applicability of the latter is presently not clear. A systematic investigation quantifying the effect of dispersion (as in Glimsdal et al., 2013) on PTHA for practical source configurations would be desirable.

Nonlinearity and Resonances (H4)

Most tsunami simulations to date start from an ocean at rest and assume that interaction of currents with gravity waves is negligible. Androsov et al. (2011) demonstrated that significant alterations of the wave height can be attributed to tidal activity. A quantitative sensitivity analysis of this effect, its dependence on bathymetry, and its correlation to the choice of model (NLSW) is necessary. Huthnance (1975) described the phenomenon of trapped waves on continental shelves that may trigger edge waves and other amplified phenomena. Tsunami resonance effects in Chile and the Balearic Islands are studied in Aranguiz et al. (2019) and Vela et al. (2014). Pattiaratchi and Wijeratne (2015) describe the effect of such phenomena as amplifying factors for meteotsunamis. It is currently unclear how such amplifying phenomena can be represented in the numerical model, nor if the strength is captured adequately.

Quantifying the Influence of Modeling Assumptions and Scaling (H5)

A hierarchy of modeling approaches, from shallow water assumption, over dispersive long wave solvers, to Navier Stokes type models, can be used to numerically treat tsunami hazard analysis in varying complexity. Due to ever-increasing computational resources, a trend toward more involved model equations can be observed. However, a clear quantitative assessment of the difference has only partly been performed. Lynett et al. (2017) use extensive benchmarking to study and compare modeling approaches to currents induced by tsunami waves. While this study is enlightening and provides very good benchmarking tools, further assessment is necessary to quantify the influence of higher fidelity modeling techniques. Generally, we note that current benchmarking (e.g., Synolakis et al., 2008) stays behind current high-fidelity modeling capabilities. Additionally, some benchmarks based on laboratory experiments have issues with scaling (see Heller, 2011; Pedersen et al., 2013), and related bias and accuracy have not been investigated systematically.

Modeling Situations With Complex Tsunami Inundation (H6)

NLSW models are predominantly used to simulate tsunami inundation. However, real inundation situations involve features too complex for NLSW approximate modeling, such as urban structures, or damage and erosion due to debris transport. At present, these topics are only partly represented, often using heuristic model formulations. Examples include spatially variable friction mapping (e.g., Gayer et al., 2010; Kaiser et al., 2011), or porous body equivalent friction models representing buildings (e.g., Yamashita et al., 2018). Bottom friction parameterization is almost insensitive for offshore modeling (see Arcos and LeVeque, 2015). However, variable bottom friction parameterizations may pose a viable tool for simulating detailed inundation, but large uncertainties still prevail (e.g., Griffin et al., 2015; Macías et al., 2020). While small scale laboratory tests exist (Park et al., 2013), the heuristic nature of named models and the difficulty to perform controlled tests, implies potentially large epistemic uncertainties. Debris impact and transport are predominantly addressed through post-disaster surveys and experimental analysis of data so far (e.g., Nistor et al., 2017a; Nistor et al.,

2017b; Stolle et al., 2019), and is mostly embedded in only vulnerability analysis (see below), and not in hydrodynamic modeling or PTHA to our knowledge. Extending the modeling dimensions and physical complexity is desirable (e.g., Marras and Mandli, 2021). Open and related to this issue is the influence and potential bias of the accuracy of topo-bathymetric grids, including filtering of structures and vegetation, on the accuracy of inundation simulations (see Griffin et al., 2015; Goda and Song, 2019). Unphysical bias can also be introduced when coupling high resolution (nested) models to large-scale propagation models as shown in Harig et al. (2008).

PROBABILISTIC TSUNAMI RISK ASSESSMENT

This section discusses identified gaps in PTRA. We go through current state for exposure modeling, physical vulnerability, and risk and resilience metrics, as they naturally follow each other in a consequence-based risk workflow (**Figure 1**). Methods characterizing the complex social, organizational, and economic context in a tsunami risk assessment are discussed subsequently.

Gaps in Exposure Modeling

Existing Methods

Exposure data provide information about the characteristics and location of people and assets at risk. There are several techniques for the acquisition of exposure data, with different degrees of resolution and precision (Pittore et al., 2017). Data from governmental agencies are most commonly used, as they are open and available in most developed countries. These data often provide coverage for the entire building inventory (e.g., physical assets) and are regularly updated for asset management (e.g., national technical maps) and fiscal reasons (e.g., cadastral data). Different exposure databases exist. The Global Exposure Database—GED (De Bono and Mora, 2014; De Bono and Chatenoux, 2015) developed for GAR13 and updated later for GAR15 (UNISDR, 2013; 2015) provides a global dataset at 5 km grid resolution at inland and 1 km at coastal locations, including data for buildings, their use, and exposed value. The 2013 and 2015 versions of the GED served as the exposure databases for the global risk model by the United Nations Office for Disaster Risk Reduction, which considered earthquakes, hurricanes, tsunamis and riverine floods as hazards. The DRMKC Risk Data Hub WebGIS tool (Antofie et al., 2019) has been developed to provide access and sharing of EU-wide information relevant for disaster risk management. Initiatives such as the Open Exposure Data (OED) with roots in proprietary catastrophe modeling and reinsurance industry, provide the opportunity to generate exposure data, including those relevant to tsunami risk, with interoperability between different modeling tools. These databases mainly contain data from census or remote sensing. A recent interview-based approach, relying on local practicing engineers with knowledge of building features, has been adopted for the compilation of building inventories at regional scales (Polese et al., 2020). Careful validation needs to address possible heterogeneity in data. At present, the only guidelines and tools that exist for capturing and classifying exposure data for a tsunami are the multi-hazard exposure taxonomy, and associated tools, provided by GED4ALL (Silva et al., 2018b).

Identified Gaps

Lack of Detail (E1)

Most available exposure data have not been collected for the purpose of tsunami risk assessment and may be missing important information for modeling tsunami fragility or vulnerability. For instance, population cadastral data are often collected at the municipal, district or residential unit level, requiring extra assumptions to determine the geographical distribution. Tsunami hazard intensities can vary considerably between two nearby locations. Accurate geo-localization of the exposed assets and people is needed to obtain robust results, necessitating a minimum resolution level for the exposure databases. While main building construction characteristics are often known, tsunami relevant features (e.g., building lateral load resistance, foundation) are missing (Rivera et al., 2020). Exposure data for critical structures and infrastructure should include functionality information for the exposed asset. This would allow for proper modeling and hence assessment of community resilience, considering different services such as healthcare and education. In other cases, data gaps and uncertainties are associated with regulatory and privacy limitations or outdated sources.

Lack of Exposure Data (E2)

In many developing countries, where cities have rapid urbanization processes and long-term planning is not consistently enforced, exposure data are not always available or updated. Such data may be inferred from satellite and aerial imagery, from freeware data made available from international projects (e.g., NASA's EOSDIS), from volunteered geographic information systems (e.g., Huyck et al., 2011; Huyck and Eguchi, 2017; OpenStreetMap, 2020), or through intergovernmental organizations (e.g., JRC Risk Data Hub, 2020).

Lack of Tsunami Exposure Model and Taxonomy (E3)

Significant efforts have been made in the earthquake risk community to define a common exposure taxonomy (e.g., GED4GEM, Silva et al., 2018a; METEOR, Huyck et al., 2019). However, these taxonomies do not contain all the required structural attributes for estimating tsunami risk such as geomorphological, land use, and land cover datasets, or number and size of openings in buildings. A recent development is GED4ALL, a multi-hazard taxonomy (Silva et al., 2018b), which considers tsunami as a hazard. GED4ALL also discusses multiple asset types like buildings, people, infrastructure systems and crops. Common taxonomy and attributes are fundamental to avoid heterogeneity, especially when considering multiple asset types.

Spatio-Temporal Variability (E4)

Most exposure models are static in time and do not consider the spatio-temporal variability of exposure components. This aspect

is critical when modeling human exposure since there can be daily and seasonal variations. For example, coastal regions often attract tourists, visitors and seasonal workers, leading to significant seasonal fluctuations in the population (Fraser et al., 2014). Spatio-temporal variation in exposure heavily influences the tsunami risk.

Gaps in Physical Vulnerability

Existing Methods

As tsunami losses are closely connected to damages to buildings and infrastructure, the vulnerability component is often cut into two parts: a tsunami-to-damage fragility function, and a damage-to-loss consequence function (**Figure 1**). Advancements in tsunami vulnerability models have significantly lagged behind those of tsunami hazard, with almost no studies found to precede the 2004 Indian Ocean Tsunami (Charvet et al., 2017). However, with the recent devastating tsunamis providing a large quantity of observed damage and loss data to develop and validate fragility and vulnerability models, this field of study has rapidly grown. Several empirical fragility functions for the assessment of buildings (Koshimura et al., 2009; Mas et al., 2012; Suppasri et al., 2014; Charvet et al., 2015; Chock et al., 2016) and infrastructure (Eguchi et al., 2014; Hatayama, 2014) have been derived from observed damage in the 2004 Indian Ocean, 2009 Samoa, 2010 Chile, and 2011 Tohoku tsunamis. Recently, analytical fragility functions were derived from numerical simulations of building response under tsunami inundation (Petrone et al., 2017; Alam et al., 2018; Karafagka et al., 2018; Páez-Ramírez et al., 2020), and under sequential earthquake and tsunami impact (Park et al., 2012; Attary et al., 2019; Petrone et al., 2020). Only a few studies exist that move from fragility to vulnerability modeling (De Risi et al., 2017). There is a lack of consensus on many aspects of physical fragility and vulnerability modeling.

Identified Gaps

Limitation in Asset Types and Geographical Scope (P1)

The vast majority of existing tsunami fragility and vulnerability models relate to buildings, few exist for bridges, fuel tanks, or other types of infrastructure. The main reason is that most fragility functions are empirical, and few observational damage or loss data are available for infrastructure components. Even for buildings, the geographical scope of existing vulnerability and fragility models is limited. Most empirical fragility functions are based on data from the 2004 Indian Ocean and 2011 Tohoku events, and hence represent non-engineered buildings in countries surrounding the Indian Ocean and engineered buildings typical of Japan. With analytical fragility functions only covering a small number of building types, large portions of the world's exposure remain unrepresented by current studies.

Effect of Multiple Hazard on Empirical Tsunami Fragility Mode (P2)

Tsunamis are commonly triggered by large earthquakes. Near-source, observational data on asset damage and loss collected after the tsunami often include the combined effects of earthquake ground shaking and tsunami inundation. Hence, empirical fragility and vulnerability models derived from such data inherently comprise the effects of both hazards. Therefore, corresponding empirical fragility models may be regarded as inappropriate for use in a tsunami-only risk assessment. Pure tsunami damage data is rare and currently limited to non-engineered structures (Charvet et al., 2017).

Lack of Consensus Regarding Best Tsunami Intensity Measure (P3)

The intensity measure *IM* (**Figure 1**) links the hazard and vulnerability components within risk models. Traditionally, tsunami inundation maps are presented in terms of inundation depth. While the majority of fragility and vulnerability models adopt inundation depth as *IM*, other tsunami *IM* have also been used such as the flow velocity or momentum flux. The absence of inundation velocity measurements in field data requires running tsunami inundation simulations to use such *IM* (Koshimura et al., 2009; Song et al., 2017). More recently, force-based *IM* (e.g., flow velocity, momentum flux) were used in fragility functions for engineered buildings yielding better correlation to observed damage than inundation depth (Macabuag et al., 2016). However, no consensus on the most appropriate *IM* could be reached. As a consequence, mismatches between representations of hazard and vulnerability in risk modeling may exist.

Gaps in Building Analysis and Assessment for Use in Analytical Tsunami Fragility (P4)

Buildings are often used as vertical evacuation shelters and an assessment of their structural fragility is therefore an important information in the risk assessment workflow. Tsunami engineering being a younger discipline than earthquake engineering has adopted approaches from the latter community. This was supported by the physical similarity of both hazards applying predominantly horizontal loads to structures. However, there are fundamental differences in how earthquake and tsunami loads are applied to buildings. For example, tsunami loads affect the lower floors of a high-rise building, whereas seismic loads are inertial forces usually causing increasing magnitude for higher floors (Baiguera et al., 2019). Thus, earthquakes induce large bending moments in structural elements, whereas tsunamis typically induce large shear. Since typical structural modeling approaches tend to prioritize flexural effects, the bias in tsunami fragility assessment may be large. Furthermore, seismic loads are dynamic, whereas loads from tsunami inundation can be considered quasi-static, and Rossetto et al. (2018) have shown that building ductility is often not crucial in the tsunami response of structures. Although no consensus has been reached in this regard, more fragility functions based on static rather than time-dependent non-linear approaches are derived now (Petrone et al., 2017; Rossetto et al., 2019). As a tsunami applies direct pressures to a structure, non-structural components like infill walls (and their openings) are seen to play an important role in determining tsunami forces (Del Zoppo et al., 2021). Furthermore, buoyancy, foundation scour and debris impact, which significantly affect building damage from tsunami inundation are rarely modeled (Del Zoppo et al., 2019). These

effects are still to be investigated; therefore, published analytical tsunami fragility functions are subjected to large modeling uncertainties. Progress towards more comprehensive and reliable analytical fragility and vulnerability models is needed.

Gaps in Risk and Resilience Metrics

Existing Methods

Tsunami risk assessments typically reflect the impact on the exposed population and infrastructure. The most commonly used decision variables (or metrics) are the number of fatalities, injuries, affected people, besides the direct and indirect economic losses. Direct economic losses represent the repairing/replacement costs of damaged assets, whereas indirect losses reflect costs as down-time, partial loss of functionality of buildings and infrastructure, loss or reduction in network connectivity, flow and/or capacity. These metrics can be used in alternative approaches such as worst-case scenarios, scenario-based for a prescribed return-period, and fully probabilistic. A review of early methods for tsunami risk assessment can be found in Jelínek and Krausmann (2008).

Fully probabilistic risk assessments require the integration of hazard estimates (PTHA) with vulnerability functions (see **Figure 1**, Løvholt et al., 2015a; 2019). Since the results of PTHA are not always available, tsunami risk assessments are often performed considering selected (worst-case) scenarios as hazard input (e.g., Triantafyllou et al., 2019), which sometimes represent past disasters (e.g., Daniell et al., 2017). Having the results of PTHA available, tsunami risk assessment can also be performed for a limited number of scenarios (e.g., Nadim and Glade, 2006; Okumura et al., 2017). When the PTHA results are available in the form of stochastic event sets, a fully probabilistic tsunami risk assessment (PTRA) can be performed (Ordaz, 2000; Strunz et al., 2011; Salgado-Gálvez et al., 2014), although these types of analyses usually demand an extensive computational effort (e.g., Løvholt et al., 2015a; Jaimes et al., 2016; Goda and Song, 2019; Ordaz et al., 2019).

In a fully probabilistic tsunami risk assessment workflow, risk results are obtained in terms of exceedance frequencies for the above-mentioned metrics (**Figure 1**). For instance, loss exceedance curves (LEC) provide the relationship between loss values and their exceedance frequencies (Løvholt et al., 2015a; Jaimes et al., 2016; Attary et al., 2017; Ordaz et al., 2019). The area under the LEC corresponds to the average annual loss (AAL), a metric that provides a long-term overview of risk and accounts for the contribution of large and infrequent events as well as small and more frequent ones. From the LEC, loss values associated with a given return period can be obtained, such as loss values estimated by Løvholt et al. (2015a) at a global level representing direct losses. The Hazus tsunami loss estimation methodology provides state-of-the-art decision-support software for estimating potential losses from tsunami events (FEMA, 2017a; FEMA, 2017b).

Risk assessment is not necessarily limited to quantifying the direct and indirect impact on exposed populations and infrastructures. The evaluation of safety and reliability of physical systems is of interest too and for this, fragility functions ("*Gaps in Physical Vulnerability*" section) can be integrated with hazard to obtain the frequency of exceeding a given damage level (see **Figure 1**, e.g., Park et al., 2019; Fukutani et al., 2019). The risk metrics provide valuable data also for the assessment of quantitative resilience (also denoted as engineering resilience), which aims to estimate the resilience of a network, an infrastructure, or even an urban ecosystem to a specific natural hazard (see Mebarki et al., 2016 for industrial plants, Akiyama et al., 2020 for bridges). Quantitative resilience should not be confused with coastal community resilience which is discussed in detail in the following section.

Identified Gaps

Gaps Related to Characterization and Propagation of Uncertainties (R1)

Most existing PTRA models rely on a homogeneous Poisson process as the probabilistic backbone for the occurrence process (**Eq. 4**). The Poisson model, strictly speaking, should be used for propagating only those uncertainty sources that renew with the occurrence of each new event (Kiureghian, 2005). This means that propagation of other sources of uncertainties in a PTRA framework (i.e., those that lack renewal properties), such as the uncertainties in modeling, analysis method, and in general epistemic uncertainties, need more research (Goda and De Risi, 2018; Goda, 2020). One possible direction could point to Bayesian methods (Jalayer and Ebrahimian, 2020).

Challenges in Characterizing Vulnerability Functions (R2)

PTRA lacks a clear distinction and definition of the different loss components that are quantified through the vulnerability functions. On the one hand, direct economic losses can be estimated with a good degree of confidence using existing methodologies (Pagnoni et al., 2019). Long-term direct (e.g., cost of maintenance) and indirect losses (e.g., down-time and reduced functionality including business interruption) typically represent a significant component of the total economic loss (direct + indirect) yet require better quantitative approaches.

Lack of a Tsunami Consequences Database (R3)

There is a lack of tsunami-specific consequence databases accounting for casualties and losses (Yamao et al., 2015). These types of databases exist for disasters in general (e.g., EM-DAT) and more specifically for earthquakes (So et al., 2012; Cardona et al., 2018). They are useful not only to keep a consistent record of past events and the affected regions but to disaggregate the impacts of large events in terms of losses (direct and indirect) and casualties (fatalities and injured), besides assessing the consequences in particular sectors (e.g., road networks, heritage sites, etc.) at different resolution levels. The information included in the consequences databases provides valuable data to validate and calibrate different components of the models (e.g., fragility curves, vulnerability functions). Some data can be partially acquired from collections of documented eyewitness accounts (Santos and Koshimura, 2015), or other sources (e.g., ITIC, 2020).

General Lack of Risk Studies for Networks and Lifelines (R4)

Current implementations of PTRA are mainly focused on residential buildings and emergency planning activities such as

the definition of evacuation routes. However, the resilience of coastal areas relies on conventional and strategic infrastructures (Akiyama et al., 2013; Pitilakis et al., 2019). Conventional infrastructure such as roads, bridges, power, water, sanitation and communication networks, underpin economic and social activities in most urban areas (Salgado-Gálvez et al., 2018). Schools and hospitals support the provision of education and health services, which are essential to recovery. Critical infrastructures in coastal areas include harbors (nuclear) power plants, gas and oil storage, and early warning infrastructure, such as tidal buoys and offshore bottom pressure gauges (De Risi et al., 2018). Such infrastructures are complex, often interconnected and geographically distributed systems involving multiple sectors (Duenas-Osorio and Vemuru, 2009; Argyroudis et al., 2019), where further research is needed to quantify their resilience to tsunamis.

Assessing Tsunami Risk in a Multi-Hazard and Multi-Risk Framework (R5)

As triggered events, tsunamis fit naturally within a multi-hazard framework. Moreover, there can be several cascading consequences associated with the occurrence of tsunamis, such as technological disasters induced by natural hazards known as NATECH risks (e.g., the Fukushima Disaster), disruption to supply chains, and societal impacts. Therefore, management and decision-making for tsunami risk should be framed in a multi-risk context. To be able to make risk-informed decisions considering tsunamis, it is important to model the interaction of tsunamis with other phenomena at the level of hazards, vulnerabilities, and socio-economic consequences. An important gap related to risk assessment for tsunamis (and in general) is the lack of a streamlined and standard workflow for modeling the multi-hazard and multi-risk aspects. Currently, most studies consider the different hazards to be independent or "simultaneous" (e.g., earthquake and tsunami as independent events); whereas, few works consider interacting hazards such as coupled simulation of tsunami and earthquake (De Risi and Goda, 2016; Goda et al., 2017; Goda and De Risi, 2018; Ordaz et al., 2019; Park et al., 2019), the cumulation of tsunami and earthquake damages and losses (Ordaz, 2015; Attary et al., 2019; Park et al., 2019; Petrone et al., 2020), and interaction of tsunami and aging infrastructure (Akiyama et al., 2020).

Lack of Understanding and Quantification of Mortality (R6)

Strikingly, the 2004 tsunami with more than 226,000 dead and missing people (EM-DAT, 2020) caused an order of magnitude higher fatalities than the 2011 Tohoku tsunami with 19,846 (EM-DAT, 2020). Hence, past major disasters indicate that the vulnerability to tsunami mortality of a population is much more sensitive to demographic factors (Løvholt et al., 2014) than to physical vulnerabilities ("*Gaps in Physical Vulnerability*" section). Correlations of tsunami flow depth and number of fatalities following the 2004 Indian Ocean, 2006 Java and 2011 Tohoku tsunamis reveal much larger scatter than those observed in physical vulnerability functions, even when derived from the same events (Reese et al., 2007; Koshimura et al., 2009; Suppasri et al., 2016). As human behavior influences mortality strongly (Johnston et al., 2016; Blake et al., 2018), deriving simplified vulnerability charts based on single tsunami intensity measures may not be appropriate. Tsunami awareness and availability of tsunami early warning systems and infrastructure are important (Gregg et al., 2006; Fraser et al., 2014), as well as proximity to source areas. Our understanding and ability to quantify and assess the effect of all these factors on tsunami mortality is still very limited.

The Weakness of Capturing Multi-Faceted Aspects of Vulnerability (R7)

Quantitative risk assessments typically address several socio-economic parameters (e.g., safety, downtime, direct and indirect economic losses, and even human behavior and response) as dimensions of consequences to disruptive tsunami events. However, PTRA falls short in modeling some dimensions of vulnerability that are part of a given context and not directly caused by a disruptive event (e.g., governance-related issues, adaptation and coping capacities, societal inequalities). There are no established methodologies, within the context of the PTRA framework (**Equations 1–4**), for characterizing context-based impacts of tsunami on the social, political and economic dimensions, leaving it unclear how to address these dimensions. Integrated and heuristic approaches such as "MOVE" (Birkmann et al., 2013) or holistic approaches as those proposed by Carreño et al. (2007) or Aguirre-Ayerbe et al. (2018), have strived to address the context-based and multi-dimensional nature of vulnerability and risk and could be adapted to be used as physical risk indicators in the outcomes of PTRA.

Gaps in Social Vulnerability, Multi-Dimensional Vulnerability and Risk Indicators

Existing Methods

Although not directly addressing tsunami risk, Jasanoff (1993) pointed out the urge to bridge the two cultures of quantitative and qualitative risk assessment, stressing the importance to view risk in a larger context of social justice (*who* should we protect, from *which* harm, at *what* cost, and by foregoing *what* other opportunities). The societal factors impacting vulnerability and risk are mainly rooted in a complex and diverse aggregate, which varies over time and space. Qualitative vulnerability investigations use models and frameworks considering several dimensions (e.g., economic, demographic, psychological, political or physical), summarized by composite vulnerability and risk indices. These indicators can be distinguished from the risk and resilience metrics discussed in the previous section ("**Gaps in Risk and Resilience Metrics**" section) since some of them cannot be directly integrated into a computational PTRA procedure. Examples of existing multi-dimensional vulnerability and risk indicators are: The *community resilience* (e.g., Lam et al., 2016; Saja et al., 2019), *the urban disaster risk index* (Carreño et al., 2007; Salgado-Gálvez et al., 2016), the *social vulnerability index* (Cutter et al., 2003; Flanagan et al., 2011), the *Coastal vulnerability index* (McLaughlin and Cooper, 2010), *Metropolitan Tsunami Human Vulnerability Assessment* (Tufekci et al., 2018).

Identified Gaps

The Difficulty of "Quantifying" Social Vulnerability (I1)

Social vulnerability describes combinations of social, cultural, economic, political, and institutional processes that determine differentials in the experience of hazards and recovery from dangerous events (Spielman et al., 2020). Experts may construct meaningful indicators to include a social component in hazard planning, preparation, and response. Integrating social vulnerability research into emergency and disaster risk management is essential, but caution is required to assign quantitative elements. Integration of social factors may allow planners and decision-makers to better identify problems in case of destructive events and provide insights into addressing recovery solutions (Cardona, 2001; Chakraborty et al., 2005; Schmidtlein et al., 2008). Social Vulnerability Index (SoVI) is a single quantitative indicator which was developed through a review of hazard case studies by Cutter et al. (2003) examining the spatial patterns of social vulnerability to natural hazards at the county level in the United States. Because of the complex and multidimensional nature of factors contributing to vulnerability, no variable has yet been identified to fully validate SoVI. An alternative approach to assess its reliability is to identify how the changes in the SoVI algorithm construction may lead to the changes in the outcome. Schmidtlein et al. (2008) investigated the sensitivity of quantitative features of the SoVI such as the scale of application, the set of used variables, and various geographic contexts.

Ambiguities in Definition of Community Resilience (I2)

Resilience is a frequently used term to discuss the capacity of a society or ecosystem to recover quickly from a disaster. The United Nations Office for Disaster Risk Reduction has defined resilience as "*the capacity of a system, community or society potentially exposed to hazards to adapt, by resisting or changing in order to reach and maintain an acceptable level of functioning and structure. This is determined by the degree to which the social system is capable of organizing itself to increase this capacity for learning from past disasters for better future protection and to improve risk reduction measures*" (UNISDR, 2007). A comprehensive review of various definitions of resilience can be found in Davoudi et al. (2012) and Ayyub (2014). The definition of coastal resilience is hindered by varying definitions and non-unified terminology, difficulties in selecting and combining different resilience indicators, and lack of data for validation (Lam et al., 2016). In fact, resilience is still lacking rigorous measurement methods (Bozza et al., 2015), especially in the context of tsunami hazard (Genadt, 2019).

Lack of Tsunami Vulnerability Index (I3)

A specific tsunami Disaster Risk Index (TDRI), similarly to the Disaster Risk Index (DRI) developed by the UN Development Program to compare disaster risk between countries exposed to hazards (UNDP, 2004) or the Urban Seismic Risk Index by Carreño et al. (2007) should be developed.

Integrated Approaches to Consider the Multi-Dimensional Aspects of Tsunami Risk (I4)

Vulnerability and risk are multi-faceted concepts and encompass various assets, physical, organizational, and institutional dimensions (e.g., Herslund et al., 2016). Vulnerability and risk assessment considering these different facets often requires different scientific backgrounds and approaches (Hufschmidt et al., 2005). A consequence-based approach to risk assessment (e.g., the PEER framework, or computational PTRA in general) has its roots in engineering. The approach follows a logical flow from causes associated with a disruptive event toward quantifying its direct and indirect socio-economic consequences. This approach focuses on the physical dimension of vulnerability, acting as a "container" of functions and services and thereby invokes–directly or indirectly–other dimensions of vulnerability such as social, economic and organizational vulnerability. On the other hand, the context-based approach (e.g., approaches based on integrated indicators) has its roots in the humanities and social disciplines. This approach deals with the context and the interactions between different actors, the respective territory, the different drivers (climate, societal changes) and how decisions can affect the overall context and the complex interplay between actors and drivers. Needless to say, the two approaches complement each other and have to be taken into account in policymaking for DRR in an integrated manner (O'Brien et al., 2007).

Considering Community Response and Organizational Capacities (I5)

Recent tsunami events worldwide have highlighted the need to critically revisit how human behavior in tsunami evacuation, and more generally, the human dimension of preparedness for tsunamis is addressed within the risk assessments. The lessons from Japan 2011, Chile 2010 and Indonesia in 2010 and 2018 events highlight such needs. Questions arise on how and if the different and seemingly inconsistent human behavior can be addressed in tsunami risk assessments. Moreover, atypical events such as the Krakatoa, Indonesia 2018, do not allow for conventional prevention, warning and mitigation strategies. In most cases, aid and help arrive late due to limited organizational capacities, leaving the affected communities in even more vulnerable conditions, especially during the first critical hours and days after the event. Events with growing levels of complexity are likely to continue to occur in the future and this calls for a more in-depth consideration of how different communities respond and how those variations can be integrated within the risk assessment framework.

Incorporating Risk Perception in the Formulation and Analysis of Complex Risks (I6)

Perceptions are dynamic and socially constructed. Perceptions can change abruptly or gradually, depending on the context. Understanding evacuation behavior requires an understanding of risk perceptions. This can help explain why the response to tsunami drills may be different than when responding to a real event. It is quite challenging for risk methodologies to consider the dynamic, complex and subjective aspects of risk perception. Only by understanding the subjective meanings of perceived risks allows risk communication to be designed and applied more effectively.

CONCLUSIONS AND DIRECTIONS

In this review, we discuss a large number of research gaps in PTHA and PTRA. It becomes obvious that methods have substantially improved over the past decades, but also that open questions remain in the physical description, conceptualization, modeling, as well as the social and psychological dimensions of the topic.

The physics and geological complexity of tsunamigenic sources are still not captured nor understood adequately, leading to large uncertainties. For SPTHA, neither all earthquake faults nor their exact location, geometry, boundary and initial conditions (e.g., stress, friction) are fully constrained. Statistical models of recurrence constitute the largest uncertainties in large and rare events, including tsunami earthquakes. Uncertainty may become excessive for landslide tsunamis, where statistics on past events often are absent, and our understanding of slope failure probability is limited. The need for covering vast geographical scales, source diversity and related uncertainties, render LPTHA extremely challenging. For VPTHA additional difficulties arise due to the complexity of tsunamigenic volcano sources and triggers, but they are constrained spatially. MPTHA may benefit from a large meteorological data network allowing for (prototypical) forecasting as well as PTHA applications, but sensitivity to source parameters is still unconstrained.

While modeling and parameterization of individual phenomena are possible, they are often excessively computationally expensive or highly uncertain due to missing constraints on input parameters. The multiple scales involved in PTHA from far-field propagation over oceanic distances to the need to resolve small scale inundation features while capturing physics and resolving uncertainties still represent an open challenge. Yet, this solution is needed to convey PTHA information properly into risk analysis.

Even more challenging is the situation in PTRA, where gaps exist in the transformation of physical hazard to risk and quantifying the uncertainties in the assessment of risk and resilience. Key concepts, such as physical vulnerability and mortality and their related uncertainties, are less developed than the main PTHA elements. There are gaps regarding selection of IM, limited observed damage asset- and location-wise, and limited experimental validation.

Furthermore, tsunami science is immature concerning embedding issues with intrinsically multi-hazard and multi-risk aspects, such as the cascading events that are entangled with tsunami hazards. A weakly developed link between quantitative PTRA and the social sciences is a clear gap. At this point, it is worth noting that terms "vulnerability" and "resilience" are multi-dimensional concepts that are used both in the consequence-based–natural sciences inspired–as well as context-based approaches–motivated by social sciences. Therefore, they may have quite different interpretations depending on the analysis context.

The overarching issue is integrating all the above components and developing an overall consistent sensitivity and uncertainty quantification framework, to understand tsunami risk and identify risk drivers, from the probability of the sources causing hazards to the probability of their physical consequences and societal impact. This understanding must be developed and prioritized in future research.

To guide such efforts, we have performed an expert judgment exercise that we discuss in the following subsection. It may help to identify most pressing research needs as well as prioritize research efforts.

Prioritizing Research Gaps

A scientific sensitivity analysis of the impact of each research gap, as conducted for individual sources in Sepúlveda et al. (2017) or Davies and Griffin (2020), on the overall result of a PTHA or PTRA is certainly out of the scope of a single review paper. However, some guidance on prioritization of efforts is certainly desirable. Since we focused our description on research gaps, we suggest two important metrics for the prioritization: The susceptibility of PTHA and PTRA results on uncertainty due to the research gap (sensitivity) and the difficulty or amount of research effort needed to fill that respective gap (tractability).

In order to assess these two metrics, we conducted a first-pass expert judgment among the more than 50 co-authors of this article–all experts in one or more of the aspects of our review. A questionnaire was designed that asked three questions for each of the 47 research gap subsections that we have described before. The first two questions addressed the two metrics just mentioned. The third question asked if experts were of the opinion if the research gap existed because of a missing theoretical understanding, a lack of data, or both. While this somewhat ad hoc prioritization is not as solid as a rigorous expert elicitation (e.g., Cooke, 1991; Budnitz et al., 1997; Morgan, 2014; for tsunami hazard see an application in Basili et al., 2021, or the discussion in Grezio et al., 2017) and hence could be somehow biased, we believe it still provides a valuable starting point for future efforts. It is a qualitative broad-brush answer to the question, which research gap may be of highest importance. More details on this exercise are given in the **Supplementary Material**.

The result of this exercise is visualized in a priority matrix (**Figure 2**). It may appear natural to respond first to those research gaps that are located in the left upper quadrant of the matrix, since these gaps are considered less difficult to solve, while they are expected to influence the risk considerably. It can be noted that most of the research gaps are judged hard to solve but with a highly sensitive impact on the overall result. This seems natural, since high impact but simple problems would have been solved already.

Based on our qualitative assessment, we can therefore identify some overall trends. First, we see some common challenges related to establishing annualized source probability of occurrence, which tend to cluster in the upper right corner of **Figure 2**. This means that they are considered relatively most important, yet hardest to solve. Of these, obtaining landslide related annual source probabilities (L1) is considered both the largest yet most important obstacle, while a just slightly lower similar prioritization is evident for earthquake and volcano sources (S1 and V2). Another aspect that is considered important (and challenging) is the multi-hazard and cascading

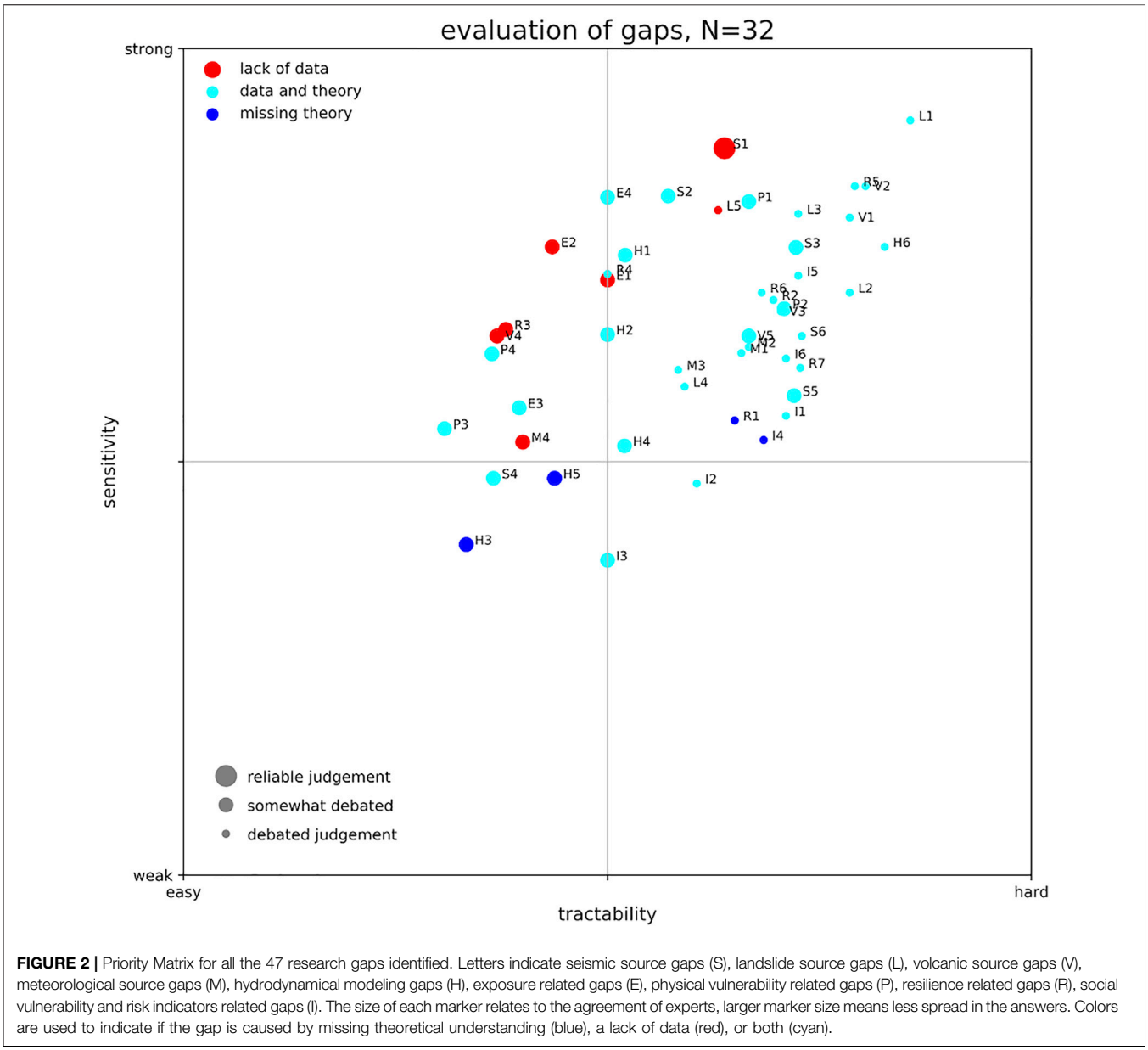

FIGURE 2 | Priority Matrix for all the 47 research gaps identified. Letters indicate seismic source gaps (S), landslide source gaps (L), volcanic source gaps (V), meteorological source gaps (M), hydrodynamical modeling gaps (H), exposure related gaps (E), physical vulnerability related gaps (P), resilience related gaps (R), social vulnerability and risk indicators related gaps (I). The size of each marker relates to the agreement of experts, larger marker size means less spread in the answers. Colors are used to indicate if the gap is caused by missing theoretical understanding (blue), a lack of data (red), or both (cyan).

hazard aspect (R5). On the other hand, the research gaps that appear to be least sensitive and also easy to be filled are related to the numerical modeling of wave propagation (H3), as well as lack of joint intensity measures (I3) and gaps related to earthquake scaling relations (S4). Finally, we also note **Figure 2** allows us to analyze several instances of components with similar sensitivity but with clearly different tractability. For instance, the lack of tsunami exposure data (E2) is considered as important as modeling complicated aspects of inundation (H6), but the former is assumed by the authors of this paper to be more easily achieved. Several other similar examples can be analyzed from **Figure 2**.

It is noteworthy that most of the research gaps that most experts find consensus on are highly sensitive in their impact (all located at the upper margin of the point cloud). It is also worth noting that most research gaps are considered to relate to data and theory gaps and that those that relate to only a missing theoretical understanding are considered of relatively low sensitivity. This may be related to the fact that when we don't understand a phenomenon, we cannot really judge whether it affects our results or not. In other words, this may be an "unknown". Whereas a data related research gap may already have proved to be sensitively influential by a specific example, but due to a lack of data cannot be involved concisely into the workflow.

This priority matrix is just a very first approach. Since tsunami research eventually aims at protecting life from natural hazard, one could also prioritize those research gaps with direct impact on this goal. These would be in particular those topics mentioned in sections "*Gaps in Physical Vulnerability*," "*Gaps in Risk and*

Resilience Metrics," and "*Gaps in Social Vulnerability, Multi-Dimensional Vulnerability and Risk Indicators*" (marked with P, R, and I; respectively).

Final Considerations

We have described and prioritized a comprehensive list of research gaps in PTHA and PTRA. While our approach to prioritization and the metric used to do so are to some extent subjective, it remains for the scientific community and further investigation as well as future incentives to decide, which directions to choose from. Nevertheless, our priority matrix will serve as a first impression on the weight of each of the identified research gaps.

An important part of the future puzzle will be exploring how uncertainties propagate to risk across disciplines. While uncertainties are more extensively explored in earthquake-related hazard analysis, non-seismic hazard, vulnerability, exposure and risk are lagging behind. On the other hand, different levels of maturity of methods and understanding will always exist. Hence, it is imperative to develop PTRA standards and guidelines to appropriately merge all risk analysis components considering their different uncertainty exploration and maturity level.

While validation of individual components has been addressed in several of the sections in our text, validating the PTHA and PTRA workflow as a whole is still ongoing research. Marzocchi and Jordan (2014) propose a methodology for a meaningful test of general probabilistic hazard models and an example of a successful application can be found in Meletti et al. (2021).

Certainly, research gaps exist also outside of the scope of PTHA and PTRA. New computational methods, like fuzzy methods, machine learning techniques and even advances in classical computational methods have to be considered. Rigorous, information theory inspired approaches to validation may also be explored.

Considering the goals of the Sendai Framework for Disaster Risk Reduction and acknowledging the vast number of challenges outlined in the sections before, a concerted interdisciplinary effort to close the most pressing gaps is required. Attempts to gather expertize, facilitate exchange and development, and coordinate community efforts are represented by the Global Tsunami Model (GTM, 2020) and the COST Action AGITHAR. A thorough consolidation of available sources of information in openly accessible databases, documentation of standard workflows, unification of terminology and metrics, as well as information hubs need to be established.

AUTHOR CONTRIBUTIONS

All Authors contributed in early stages of the manuscript by individual contributions from their respective research field. Major contributions are listed as follows: Early compilation of text: MS, FL, SL, JB, IA-Q, TR; Abstract and Conclusions: JB, FL, SL, JS; Introduction: FL, FJ, SL, JB, JS, MS-G; Probabilistic Framework: FJ, MS-G, IA-A; Earthquake Sources: SL, JS, FL, KJ, MV, SM; Landslide Sources: FL, RP, SA, AS; Volcano Sources: JS, FL, SA; Meteotsunami Sources: JB; Hydrodynamic Modeling: JB, FL, JM, IA-Q, AB; Exposure: FJ, TR, MS-G; Physical Vulnerability: TR, FJ, JS, MDZ; Risk/Resilience: IA-A, FJ; Social Vulnerability: FJ, IA-A, IR; substantial revisions: AG, KJ, SL, SM, RDR, MS, JS, RP, AB, RB, SA, MV, MDZ, AS, IA-Q, CC; internal review: all authors.

FUNDING

This article is based upon work from COST Action CA18109 AGITHAR, supported by COST (European Cooperation in Science and Technology). VB and PC obtained support through the VES20 Inter-Cost LTC 20020 project. MS-G obtained support through the Severo Ochoa Centers of Excellence Program (Ref. CEX 2018–000797-S). TU acknowledges funding from the European Union's Horizon 2020 research and innovation program (ChEESE project, Grant Agreement No. 823844).

ACKNOWLEDGMENTS

This work would not have been possible without the help of many researchers, who are too many to be named individually, but we thank all participants of COST Action AGITHAR for their valuable input in official or informal conversations, workshops and interactions. We would like to thank the reviewers and editor for very considerate and challenging suggestions that improved this manuscript substantially.

SUPPLEMENTARY MATERIAL

The Supplementary Material for this article can be found online at: https://www.frontiersin.org/articles/10.3389/feart.2021.628772/full#supplementary-material

REFERENCES

Abadie, S., Paris, A., Ata, R., Le Roy, S., Arnaud, G., Poupardin, A., et al. (2020). La Palma landslide tsunami: calibrated wave source and assessment of impact on French territories. *Nat. Hazards Earth Syst. Sci.* 20, 1–20. doi:10.5194/nhess-20-1-202010.5194/nhess-20-3019-2020

AGITHAR. (2020). Accelerating global science in tsunami hazard and risk analysis. Available at: https://www.agithar.uni-hamburg.de (Accessed November 5, 2020).

Aguirre-Ayerbe, I., Martínez Sánchez, J., Aniel-Quiroga, Í., González-Riancho, P., Merino, M., Al-Yahyai, S., et al. (2018). From tsunami risk assessment to disaster risk reduction—the case of Oman. *Nat. Hazards Earth Syst. Sci.* 18, 2241–2260. doi:10.5194/nhess-18-2241-2018

Akiyama, M., Frangopol, D. M., Arai, M., and Koshimura, S. (2013). Reliability of bridges under tsunami hazards: emphasis on the 2011 Tohoku-oki earthquake. *Earthq. Spectra* 29 (S1), S295–S314. doi:10.1193/1.4000112

Akiyama, M., Frangopol, D. M., and Ishibashi, H. (2020). Toward life-cycle reliability-, risk- and resilience-based design and assessment of bridges and bridge networks under independent and interacting hazards: emphasis on

earthquake, tsunami and corrosion. *Struct. Infrastruct. Eng.* 16 (1), 26–50. doi:10.1080/15732479.2019.1604770

Alam, M. S., Barbosa, A. R., Scott, M. H., Cox, D. T., and van de Lindt, J. W. (2018). Development of physics-based tsunami fragility functions considering structural member failures. *J. Struct. Eng.* 144 (3), 04017221. doi:10.1061/(ASCE)ST.1943-541X.0001953

Albini, P., Musson, R. M. W., Rovida, A., Locati, M., Gomez Capera, A. A., and Viganò, D. (2014). The global earthquake history. *Earthq. Spectra* 30 (2), 607. doi:10.1193/122013EQS297

Allen, T. I., and Hayes, G. P. (2017). Alternative rupture-scaling relationships for subduction interface and other offshore environments. *Bull. Seismol. Soc. Amer.* 107, 1240–1253. doi:10.1785/0120160255

Androsov, A., Behrens, J., and Danilov, S. (2011). "Tsunami modelling with unstructured grids Interaction between tides and tsunami waves," in,*Computational science and high performance computing IV*. Editors E. Krause, Y. Shokin, M. Resch, D. Kröner, and N. Shokina (Heidelberg: Springer Berlin), 115, 191–206. doi:10.1007/978-3-642-17770-5_15

Annaka, T., Satake, K., Sakakiyama, T., Yanagisawa, K., and Shuto, N. (2007). Logic-tree approach for probabilistic tsunami hazard analysis and its applications to the Japanese coasts. *Pure Appl. Geophys.* 164, 577–592. doi:10.1007/s00024-006-0174-3

Antofie, T., Luoni, S., Faiella, A., and Marin Ferrer, M. (2019). *Risk data hub—web platform to facilitate management of disaster risks*. Luxembourg: Publications Office of the European Union. doi:10.2760/68372

Araki, E., Saffer, D. M., Kopf, A. J., Wallace, L. M., Kimura, T., Machida, Y., et al. (2017). Recurring and triggered slow-slip events near the trench at the Nankai Troaugh subduction megathrust. *Science* 356 (6343), 1157–1160. doi:10.1126/science.aan3120

Aranguiz, R., Catalán, P. A., Cecioni, C., Bellotti, G., Henriquez, P., and González, J. (2019). Tsunami resonance and spatial pattern of natural oscillation modes with multiple resonators. *J. Geophys. Res. Oceans* 124 (11), 7797–7816. doi:10.1029/2019JC015206

Arcos, M. E. M., and LeVeque, R. J. (2015). Validating velocities in the GeoClaw tsunami model using observations near Hawaii from the 2011 Tohoku tsunami. *Pure Appl. Geophys.* 172, 849–867. doi:10.1007/s00024-014-0980-y

Argyroudis, S. A., MitoulisA., S., Winter, M. G., and Kaynia, A. M. (2019). Fragility of transport assets exposed to multiple hazards: state-of-the-art review toward infrastructural resilience. *Reliab. Eng. Syst. Saf.* 191. 106567. doi:10.1016/j.ress.2019.106567

Attary, N., Unnikrishnan, V. U., van de Lindt, J. W., Cox, D. T., and Barbosa, A. R. (2017). Performance-based tsunami engineering methodology for risk assessment of structures. *Eng. Struct.* 141, 676–686. doi:10.1016/j.engstruct.2017.03.071

Attary, N., Van De Lindt, J. W., Barbosa, A. R., Cox, D. T., and UnnikrisAhnan, V. U. (2019). Performance-based tsunami engineering for risk assessment of structures subjected to multi-hazards: tsunami following earthquake. *J. Earthq. Eng.* 7, 1–20. doi:10.1080/13632469.2019.1616335

Auker, M. R., Sparks, R. S. J., Siebert, L., Crosweller, H. S., and Ewert, J. (2013). A statistical analysis of the global historical volcanic fatalities record. *J. Appl. Volcanol.* 2, 2. doi:10.1186/2191-5040-2-2

Ayyub, B. M. (2014). Systems resilience for multihazard environments: definition, metrics, and valuation for decision making. *Risk Anal.* 34, 340–355. doi:10.1111/risa.12093

Baiguera, M., Rossetto, T., Robertson, I. N., and Petrone, C. (2019). "Towards a tsunami nonlinear static analysis procedure for the ASCE 7 standard," in 2nd International conference on natural hazards and infrastructure. Available at: https://discovery.ucl.ac.uk/id/eprint/10078809

Barbato, M., Petrini, F., Unnikrishnan, V. U., and Ciampoli, M. (2013). Performance-based hurricane engineering (PBHE) framework. *Struct. Saf.* 45, 24–35. doi:10.1016/j.strusafe.2013.07.002

Basili, R., Brizuela, B., Herrero, A., Iqbal, S., Lorito, S., Maesano, F. E., et al. (2021). , The making of the NEAM tsunami hazard model 2018 (NEAMTHM18). *Front. Earth Sci.* 8, 616594. doi:10.3389/feart.2020.616594

Basili, R., Tiberti, M. M., Kastelic, V., Romano, F., Piatanesi, A., Selva, J., et al. (2013). Integrating geologic fault data into tsunami hazard studies. *Nat. Hazards Earth Syst. Sci.* 13, 1025–1050. doi:10.5194/nhess-13-1025-2013

Beauval, C., Yepes, H., Audin, L., Alvarado, A., Nocquet, J.-M., Monelli, D., et al. (2014). Probabilistic seismic-hazard assessment in quito, estimates and uncertainties. *Seismol. Res. Lett.* 85 (6), 1316–1327. doi:10.1785/0220140036

Bebbington, M. (2010). Trends and clustering in the onsets of volcanic eruptions. *J Geophys. Res.* 115, B01203. doi:10.1029/2009jb006581

Bebbington, M. (2008). Incorporating the eruptive history in a stochastic model for volcanic eruptions. *J. Volcanol. Geothermal Res.* 175, 325–333. doi:10.1016/j.jvolgeores.2008.03.013

Begét, J. E., Cecioni, C., and Yepes, H. (2000). "Volcanic tsunamis," in *Encyclopedia of volcanoes*. Editor Sigurdsson, H. (London, UK: Academic Press), 1005–1013.

Behrens, J., and Dias, F. (2015). New computational methods in tsunami science. *Phil. Trans. R. Soc. A.* 373 (2053), 20140382. doi:10.1098/rsta.2014.0382

Bellotti, G., Cecioni, C., and de Girolamo, P. (2008). Simulation of small-amplitude frequency-dispersive transient waves by means of the mild-slope equation. *Coastal Eng.* 55, 447–458.

Bellotti, G., Di Risio, M., and De Girolamo, P. (2009). Feasibility of tsunami early warning systems for small volcanic islands. *Nat. Hazards Earth Syst. Sci.* 9, 1911–1919. doi:10.5194/nhess-9-1911-2009

Bevilacqua, A., Neri, A., Bisson, M., Esposti Ongaro, T., Flandoli, F., Isaia, R., et al. (2017). The effects of vent location, event scale, and time forecasts on pyroclastic density current hazard maps at Campi Flegrei caldera (Italy). *Front. Earth Sci.* 5, 112. doi:10.3389/feart.2017.00072

Bilek, S. L. (2010). Invited review paper: seismicity along the South American subduction zone: review of large earthquakes, tsunamis, and subduction zone complexity. *Tectonophysics* 495 (1–2), 2–14. doi:10.1016/j.tecto.2009.02.037

Bilek, S. L., and Lay, T. (1999). Rigidity variations with depth along interplate megathrust faults in subduction zones. *Nature* 400, 443–446. doi:10.1038/22739

Bilek, S. L., and Lay, T. (2018). Subduction zone megathrust earthquakes. *Geosphere* 14, 1468–1500. doi:10.1130/GES01608.1

Bird, P., Jackson, D. D., Kagan, Y. Y., Kreemer, C., and Stein, R. S. (2015). GEAR1: a global earthquake activity rate model constructed from geodetic strain rates and smoothed seismicity. *Bull. Seismol. Soc. Amer.* 105, 2538–2554. doi:10.1785/0120150058

Bird, P., and Kagan, Y. Y. (2004). Plate-tectonic analysis of shallow seismicity: apparent boundary width, beta, corner magnitude, coupled lithosphere thickness, and coupling in seven tectonic settings. *Bull. Seismol. Soc. Amer.* 94 (6), 2380–2399. doi:10.1785/0120030107

Bird, P., and Kreemer, C. (2015). Revised tectonic forecast of global shallow seismicity based on version 2.1 of the global strain rate map. *Bull. Seismol. Soc. Amer.* 105, 152–166. doi:10.1785/0120140129

Birkmann, J., Cardona, O. D., Carreño, M. L., Barbat, A. H., Pelling, M., Schneiderbauer, S., et al. (2013). Framing vulnerability, risk and societal responses: the MOVE framework. *Nat. Hazards* 67 (2), 193–211. doi:10.1007/s11069-013-0558-5

Blake, D., Johnston, D., Leonard, G., McLaren, L., and Becker, J. (2018). A citizen science initiative to understand community response to the kaikōura earthquake and tsunami warning in petone and eastbourne, wellington, aotearoa/New Zealand. *Bull. Seismol. Soc. Amer.* 108 (3B), 1807–1817. doi:10.1785/0120170292

Blaser, L., Krüger, F., Ohrnberger, M., and Scherbaum, F. (2010). Scaling relations of earthquake source parameter estimates with special focus on subduction environment. *Bull. Seismol. Soc. Amer.* 100, 2914–2926. doi:10.1785/0120100111

Bletery, Q., Thomas, A. M., Rempel, A. W., Karlstrom, L., Sladen, A., and De Barros, L. (2016). Mega-earthquakes rupture flat megathrusts. *Science* 354 (6315), 1027–1031. doi:10.1126/science.aag0482

Blikra, L. H., Longva, O., Harbitz, C., and Løvholt, F. (2005). Quantification of rock-avalanche and tsunami hazard in Storfjorden, western Norway. *Landslides Avalanches: ICFL Conf. Proc.* 12, 57–64. doi:10.1007/springerreference_5010

Bommer, J. J., and Stafford, P. J. (2016). *Seismic hazard and earthquake actions*, in *Seismic design of buildings to eurocode 8*. Editor A. Elghazouli (Boca Raton: CRC Press), 21–54. doi:10.1201/9781315368221-9

Bougouin, A., Paris, R., and Roche, O. (2020). Impact of fluidized granular flows into water: implications for tsunamis generated by pyroclastic flows. *J. Geophys. Res. Solid Earth* 7, e2019JB018954. doi:10.1002/asl2.471

Bozza, A., Asprone, D., and Manfredi, G. (2015). Developing an integrated framework to quantify resilience of urban systems against disasters. *Nat. Hazards* 78 (3), 1729–1748. doi:10.1007/s11069-015-1798-3

Brown, S. K., Jenkins, S. F., Sparks, R. S. J., Odbert, H., and Auker, M. R. (2017). Volcanic fatalities database: analysis of volcanic threat with distance and victim classification. *J. Appl. Volcanol.* 6, 15. doi:10.1186/s13617-017-0067-4

Bryn, P., Berg, K., Forsberg, C. F., Solheim, A., and Kvalstad, T. J. (2005). Explaining the storegga slide. *Mar. Pet. Geol.* 22 (1–2), 11–19. doi:10.1016/j.marpetgeo.2004.12.003

Budnitz, R. J., Apostolakis, G., and Boore, D. M. (1997). Nuclear regulatory commission, Washington: The Academy Press. Recommendations for probabilistic seismic hazard analysis: guidance on uncertainty and use of experts. Technical Report. doi:10.2172/479072

Bullard, G. K., Mulligan, R. P., Carreira, A., and Take, W. A. (2019). Experimental analysis of tsunamis generated by the impact of landslides with high mobility. *Coastal Eng.* 152, 103538. doi:10.1016/j.coastaleng.2019.103538

Burbidge, D., Cummins, P. R., Mleczko, R., and Thio, H. K. (2008). A probabilistic tsunami hazard assessment for western Australia. *Pure Appl. Geophys.* 165, 2059–2088. doi:10.1007/s00024-008-0421-x

Bürgmann, R., and Chadwell, D. (2014). Seafloor geodesy. *Annu. Rev. Earth Planet. Sci.* 42, 509–534. doi:10.1146/annurev-earth-060313-054953

Cardona, O. D. (2001). Estimación holística del riesgo sísmico utilizando sistemas dinámicos complejos. Ph.D. Thesis. Barcelona, Spain: Polytechnic University of Catalonia.

Cardona, O. D., Ordaz, M., Salgado-Gálvez, M. A., Barbat, A. H., and Carreño, M. L. (2018). Latin American and caribbean earthquakes in the GEM's earthquake consequences database (GEMECD). *Nat. Hazards* 93 (1), S113–S125. doi:10.1007/s11069-017-3087-9

Carlton, B., Vanneste, M., Forsberg, C. F., Knudsen, S., Løvholt, F., Kvalstad, T., et al. (2019). Geohazard assessment related to submarine instabilities in Bjørnafjorden, London. *Spec. Publ. Geol. Soc.* 477, 549–566. doi:10.1007/bf00305006

Carreño, M.-L., Cardona, O. D., and Barbat, A. H. (2007). Urban seismic risk evaluation: a holistic approach. *Nat. Hazards* 40 (1), 137–172. doi:10.1007/s11069-006-0008-8

Cecioni, C., and Bellotti, G. (2010). Inclusion of landslide tsunamis generation into a depth integrated wave model. *Nat. Hazards Earth Syst. Sci.* 10 (11), 2259–2268. doi:10.5194/nhess-10-2259-2010

Chagué-Goff, C., Andrew, A., Szczuciński, W., Goff, J., and Nishimura, Y. (2012). Geochemical signatures up to the maximum inundation of the 2011 Tohoku-oki tsunami—implications for the 869 AD Jogan and other palaeotsunamis. *Sediment. Geol.* 282, 65–77. doi:10.1016/j.sedgeo.2012.05.021

Chakraborty, J., Tobin, G. A., and Montz, B. E. (2005). Population evacuation: assessing spatial variability in geophysical risk and social vulnerability to natural hazards. *Nat. Hazards Rev.* 6 (1), 23–33. doi:10.1061/(asce)1527-6988(2005)6:1(23)

Charvet, I., Macabuag, J., and Rossetto, T. (2017). Estimating tsunami-induced building damage through fragility functions: critical review and research needs. *Front. Built Environ.* 3, 121. doi:10.3389/fbuil.2017.00036

Charvet, I., Suppasri, A., Kimura, H., Sugawara, D., and Imamura, F. (2015). A multivariate generalized linear tsunami fragility model for Kesennuma City based on maximum flow depths, velocities and debris impact, with evaluation of predictive accuracy. *Nat. Hazards* 79 (3), 2073–2099. doi:10.1007/s11069-015-1947-8

Chaytor, J. D., Uri, S., Solow, A. R., and Andrews, B. D. (2009). Size distribution of submarine landslides along the US Atlantic margin. *Mar. Geol.* 264 (1-2), 16–27. doi:10.1016/j.margeo.2008.08.007

Chock, G. (2016). Design for tsunami loads and effects in the ASCE 7-16 standard. *J. Struct. Eng.* 142 (11), 04016093. doi:10.1061/(ASCE)ST.1943-541X.0001565

Chock, G. Y., Robertson, I., and Riggs, H. R. (2011). "Tsunami structural design provisions for a new update of building codes and performance-based engineering," in *Solutions to coastal disasters 2011*, Editors Wallendorf, L.A., Jones, C., and Ewing, L. (London: ASCE) 423–435. doi:10.1061/41185(417)38

Chock, G., Yu, G., Thio, H. K., and Lynett, P. J. (2016). Target structural reliability analysis for tsunami hydrodynamic loads of the ASCE 7 standard. *J. Struct. Eng.* 142, 04016092–4016112. doi:10.1061/(ASCE)ST.10.1061/(asce)st.1943-541x.0001499

Choi, B. H., Pelinovsky, E., Kim, K. O., and Lee, J. S. (2003). Simulation of the trans-oceanic tsunami propagation due to the 1883 Krakatau volcanic eruption. *Nat. Hazards Earth Syst. Sci.* 3, 321–332. doi:10.5194/nhess-3-321-2003

Churchill, D. D., Houston, S. H., and Bond, N. A. (1995). The daytona beach wave of 3-4 july 1992: a shallow-water gravity wave forced by a propagating squall line. *Bull. Amer. Meteorol. Soc.* 76 (1), 21–32. doi:10.1175/1520-0477(1995)076<0021:tdbwoj>2.0.co;2

Clare, M., Chaytor, J., Dabson, O., Gamboa, D., Georgiopoulou, A., Eady, H., et al. (2019). A consistent global approach for the morphometric characterization of subaqueous landslides. *Geol. Soc. Lond. Spec. Publ.* 477 (1), 455–477. doi:10.1144/sp477.15

Cooke, R. M. (1991). *Experts in uncertainty: opinion and subjective probability in science*. Oxford: Oxford University Press.

Cornell, C. A. (1968). Engineering seismic risk analysis. *Bull. Seismol. Soc. Amer.* 58, 1583–1606.

Crosta, G. B., Imposimato, S., and Roddeman, D. (2016). Landslide spreading, impulse water waves and modelling of the Vajont rockslide. *Rock Mech. Rock Eng.* 49 (6), 2413–2436. doi:10.1007/s00603-015-0769-z

Cutter, S. L., Boruff, B. J., and Shirley, W. L. (2003). Social vulnerability to environmental hazards*. *Soc. Sci. Q.* 84 (2), 242–261. doi:10.1111/1540-6237.8402002

Daniell, J. E., Schaefer, A. M., and Wenzel, F. (2017). Losses associated with secondary effects in earthquakes. *Front. Built Environ.* 3, 133. doi:10.3389/fbuil.2017.00030

Dao, M. H., and Tkalich, P. (2007). Tsunami propagation modelling—a sensitivity study. *Nat. Hazards Earth Syst. Sci.* 7, 741–754. doi:10.5194/nhess-7-741-2007

Davies, G., and Griffin, J. (2018). The 2018 Australian probabilistic tsunami hazard assessment *Record 2018/41*. Canberra: Geoscience Australia. doi:10.11636/Record

Davies, G., Griffin, J., Løvholt, F., Glimsdal, S., Harbitz, C., Thio, H. K., et al. (2018). A global probabilistic tsunami hazard assessment from earthquake sources. *Geol. Soc. Lond. Spec. Publ.* 456, 219–244. doi:10.1144/SP456.5

Davies, G., and Griffin, J. (2019). Sensitivity of probabilistic tsunami hazard assessment to far-field earthquake slip complexity and rigidity depth-dependence: case study of Australia. *Pure Appl. Geophys.* 177, 1521–1548. doi:10.1007/s00024-019-02299-w

Davies, G., and Griffin, J. (2020). Sensitivity of probabilistic tsunami hazard assessment to far-field earthquake slip complexity and rigidity depth-dependence: case study of Australia. *Pure Appl. Geophys.* 177, 1521–1548. doi:10.1007/s00024-019-02299-w

Davies, G., Horspool, N., and Miller, V. (2015). Tsunami inundation from heterogeneous earthquake slip distributions: evaluation of synthetic source models. *J. Geophys. Res. Solid Earth* 120, 6431–6451. doi:10.1002/2015JB012272

Davies, G. (2019). Tsunami variability from uncalibrated stochastic earthquake models: tests against deep ocean observations 2006-2016. *Geophys. J. Int.* 218, 1939–1960. doi:10.1093/gji/ggz260

Davoudi, S., Shaw, K., Haider, L. J., Quinlan, A. E., Peterson, G. D., Wilkinson, C., et al. (2012). Resilience: a bridging concept or a dead end? "Reframing" resilience: challenges for planning theory and practice interacting traps: resilience assessment of a pasture management system in northern Afghanistan urban resilience: what does it mean in planning practice? Resilience as a useful concept for climate change adaptation? The politics of resilience for planning: a cautionary note. *Plann. Theor. Pract.* 13 (2), 299–333. doi:10.1080/14649357.2012.677124

Day, S. J., et al. (2015). Volcanic tsunamis, in *Encyclopedia of volcanoes*. Editor Sigurdsson, H. (London, UK:Academic Press), 993–1009.

De Bono, A., and Chatenoux, B. (2015). A global exposure model for GAR 2015. UNEP-GRID, GAR.

De Bono, A., and Mora, M. G. (2014). A global exposure model for disaster risk assessment. *Int. J. Disaster Risk Reduct.* 10, 442–451. doi:10.1016/j.ijdrr.2014.05.008

de la Asunción, M., Castro, M. J., Fernández-Nieto, E. D., Mantas, J. M., Acosta, S. O., and González-Vida, J. M. (2013). Efficient GPU implementation of a two waves TVD-WAF method for the two-dimensional one layer shallow water system on structured meshes. *Comput. Fluids* 80, 441–452. doi:10.1016/j.compfluid.2012.01.012

De Risi, R., and Goda, K. (2016). Probabilistic earthquake–tsunami multi-hazard analysis: application to the Tohoku region. *Jpn. Front. Built Environ.* 2, 25. doi:10.3389/fbuil.2016.00025

De Risi, R., Goda, K., Mori, N., and Yasuda, T. (2017). Bayesian tsunami fragility modeling considering input data uncertainty. *Stoch. Environ. Res. Risk Assess.* 31, 1253–1269. doi:10.1007/s00477-016-1230-x

De Risi, R., and Goda, K. (2017). Simulation-based probabilistic tsunami hazard analysis: empirical and robust hazard predictions. *Pure Appl. Geophys.* 174, 3083–3106. doi:10.1007/s00024-017-1588-9

De Risi, R., Jalayer, F., De Paola, F., Iervolino, I., Giugni, M., Topa, M. E., et al. (2013). Flood risk assessment for informal settlements. *Nat. Hazards* 69 (1), 1003–1032. doi:10.1007/s11069-013-0749-0

De Risi, R., Muhammad, A., and Goda, K. (2018). *A way forward to resilient infrastructures against earthquake-tsunami multi-hazard* in *Routledge handbook of sustainable and resilient infrastructure*. Editor P. Gardoni (Oxon, U.K.: Routledge), 180–196.

Del Zoppo, M., Di Ludovico, M., and Prota, A. (2021). Methodology for assessing the performance of RC structures with breakaway infill walls under tsunami inundation. *J Struct Eng.* 147 (2), 04020330. doi:10.1016/b978-0-12-107180-6.50009-3

Del Zoppo, M., Rossetto, T., Di Ludovico, M., and Prota, A. (2019). "Assessing the effect of tsunami-induced vertical loads on RC frames," in Proceedings of the 1st fib Italy Symposium on Concrete and Concrete Structures. Parma, Italy.

Dueñas-Osorio, L., and Vemuru, S. M. (2009). Cascading failures in complex infrastructure systems. *Struct. Saf.* 31 (2), 157–167. doi:10.1016/j.strusafe.2008.06.007

Dusek, G., DiVeglio, C., Licate, L., Heilman, L., Kirk, K., Paternostro, C., et al. (2019). A meteotsunami climatology along the U.S. East coast. *Bull. Amer. Meteorol. Soc.* 100, 1329–1345. doi:10.1175/BAMS-D-18-0206.1

Global Volcanism Program. (2013). "Volcanoes of the world," Editor Venzke, E. (London: Smithsonian Institution) (Accessed Januray 5, 2021). doi:10.5479/si.GVP.VOTW4-2013

Eguchi, R. T., Eguchi, M. T., Bouabid, J., Koshimura, S., and Graf, W. P. (2014). "Benchmarking, validation and calibration of newly-developed HAZUS tsunami methodology." in 10th U.S. National conference on earthquake engineering: Frontiers of earthquake engineering. NCEE 2014. Anchorage: United States. doi:10.4231/D31834329

EM-DAT. (2020). The international disaster database CRED. Available at: https://www.emdat.be (Accessed November 4, 2020).

Esteva, L. (1967). "Criteria for the construction of spectra for seismic design," in Presented at third Panamerican symposium on structures. Caracas, Venezuela.

Fardis, M. N. (2009). *Seismic design, assessment and retrofitting of concrete buildings: based on EN-Eurocode 8*. Berlin: Springer. doi:10.1007/978-1-4020-9842-0

FEMA (2017b). Federal emergency management agency. Hazus tsunami model technical guidance. FEMA, fed. Emerg. Manag. Agency, Washingt. DC. Available at: https://www.fema.gov/media-library-data/1511284000276-4f18206fb0c7bab3c5ecbbbdf504b9fd/Hazus_40_Tsunami_Tech_Manual.pdf

FEMA (2017a). Federal emergency management agency. Hazus tsunami model user guidance. FEMA, fed. Emerg. Manag. Agency, Washingt. DC. Available at: https://www.fema.gov/media-library-data/1511284000292-4f18206fb0c7bab3c5ecbbbdf504b9fd/Hazus_40_Tsunami_User_Manual.pdf.

Flanagan, B. E., Gregory, E. W., Hallisey, E. J., Heitgerd, J. L., and Lewis, B. (2011). A social vulnerability index for disaster management. *J. Homeland Security Emerg. Manag.* 8 (1), 3. doi:10.2202/1547-7355.1792

Foster, J. H., Ericksen, T. L., and Bingham, B. (2020). Wave glider-enhanced vertical seafloor geodesy. *J. Atmos. Oceanic Technol.* 37, 417–427. doi:10.1175/JTECH-D-19-0095.1

Fraser, S. A., Wood, N. J., Johnston, D. M., Leonard, G. S., Greening, P. D., and Rossetto, T. (2014). Variable population exposure and distributed travel speeds in least-cost tsunami evacuation modelling. *Nat. Hazards Earth Syst. Sci.* 14 (11), 2975–2991. doi:10.5194/nhess-14-2975-2014

Freundt, A. (2003). Entrance of hot pyroclastic flows into the sea: experimental observations. *Bull. Volcanol.* 65 (2-3), 144–164. doi:10.1007/s00445-002-0250-1

Fritz, H. M., Hager, W. H., and Minor, H.-E. (2003). Landslide generated impulse waves. *Experiments in Fluids* 35 (6), 505–519. doi:10.1007/s00348-003-0659-0

Fukutani, Y., Moriguchi, S., Terada, K., Kotani, T., Otake, Y., and Kitano, T. (2019). Tsunami hazard and risk assessment for multiple buildings by considering the spatial correlation of wave height using copulas. *Nat. Hazards Earth Syst. Sci.* 19 (11), 2619–2634. doi:10.5194/nhess-19-2619-2019

Gailler, A., Hébert, H., Schindelé, F., and Reymond, D. (2018). Coastal amplification laws for the French tsunami warning center: numerical modeling and fast estimate of tsunami wave heights along the French riviera. *Pure Appl. Geophys.* 175 (4), 1429–1444. doi:10.1007/s00024-017-1713-9

Gallotti, G., Passaro, S., Armigliato, A., Zaniboni, F., Pagnoni, G., Wang, L., et al. (2020). Potential mass movements on the Palinuro volcanic chain (southern Tyrrhenian Sea, Italy) and consequent tsunami generation. *J. Volcanol. Geothermal Res.* 404, 107025. doi:10.1016/j.jvolgeores.2020.107025

Gallotti, G., and Tinti, S. (2020). A new approach for landslide modeling: application to the Scilla 1783 tsunamigenic landslide, South Italy. *Pure Appl. Geophys.* 177, 3563–3576. doi:10.1007/s00024-020-02546-5

Gayer, G., Leschka, S., Nöhren, I., Larsen, O., and Günther, H. (2010). Tsunami inundation modelling based on detailed roughness maps of densely populated areas. *Nat. Hazards Earth Syst. Sci.* 10 (8), 1679–1687. doi:10.5194/nhess-10-1679-2010

Geist, E. L., and Bilek, S. L. (2001). Effect of depth-dependent shear modulus on tsunami generation along subduction zones. *Geophys. Res. Lett.* 28, 1315–1318. doi:10.1029/2000GL012385

Geist, E. L., Brink, U. S., and Parsons, U. S. (2019). Offshore landslide hazard curves from mapped landslide size distributions. *J. Geophys. Res. Solid Earth* 124 (4), 3320–3334. doi:10.1029/2018jb017236

Geist, E. L., Chaytor, J. D., Parsons, T., and Brink, U. T. (2013). Estimation of submarine mass failure probability from a sequence of deposits with age dates. *Geosphere* 9 (2), 287–298. doi:10.1130/ges00829.1

Geist, E. L., and Oglesby, D. D. (2014). Earthquake mechanism and seafloor deformation for tsunami generation, in *Encyclopedia of earthquake engineering*. Editors M. Beer, I. A. Kougioumtzoglou, E. Patelli, and I. S.-K. Au (Berlin, Heidelberg: Springer), 1–17. doi:10.1007/978-3-642-36197-5_296-1

Geist, E. L., Oglesby, D. D., and Ryan, K. J. (2019). "Tsunamis: stochastic models of occurrence and generation mechanisms," in *Encyclopedia of complexity and systems science*," Editor R. A. Meyers (Berlin, Heidelberg: Springer), 1–30. doi:10.1007/978-3-642-27737-5_595-2

Geist, E. L., and Parsons, T. (2006). Probabilistic analysis of tsunami hazards*. *Nat. Hazards* 37, 277–314. doi:10.1007/s11069-005-4646-z

Geist, E. L., and Parsons, T. (2014). Undersampling power-law size distributions: effect on the assessment of extreme natural hazards. *Nat. Hazards* 72, 565–595. doi:10.1007/s11069-013-1024-0

Geist, E. L., ten Brink, U. S., and Gove, M. (2014). A framework for the probabilistic analysis of meteotsunamis. *Nat. Hazards* 74, 123–142. doi:10.1007/s11069-014-1294-1

Geist, E., and Lynett, P. (2014). Source processes for the probabilistic assessment of tsunami hazards. *Oceanog* 27 (2), 86–93. doi:10.5670/oceanog.2014.43

Genadt, A. (2019). Three lessons from Japan on architectural resilience. *Architectural Histories* 7 (1), 16. doi:10.5334/ah.393

Germanovich, L. N., Kim, S., and Puzrin, A. M. (2016). Dynamic growth of slip surfaces in catastrophic landslides. *Proc. R. Soc. A.* 472 (2185), 20150758. doi:10.1098/rspa.2015.0758

Gibbons, S. J., Lorito, S., Macías, J., Løvholt, F., Selva, J., Volpe, M., et al. (2020). Probabilistic tsunami hazard analysis: high performance computing for massive scale inundation simulations. *Front. Earth Sci.* 8, 623. doi:10.3389/feart.2020.591549

Giles, D., Gopinathan, D., Guillas, S., and Dias, F. (2020). Faster than real time tsunami warning with associated hazard uncertainties. *Front. Earth Sci.* 8, 66. doi:10.3389/feart.2020.597865

Glimsdal, S., Løvholt, F., Harbitz, C. B., Romano, F., Lorito, S., Orefice, S., et al. (2019). A new approximate method for quantifying tsunami maximum inundation height ProbabilityA new approximate method for quantifying tsunami maximum inundation height probability. Pure appl. *Pure Appl. Geophys.* 176, 3227–3246. doi:10.1007/s00024-019-02091-w

Glimsdal, S., Pedersen, G. K., Harbitz, C. B., and Løvholt, F. (2013). Dispersion of Tsunamis: does it really matter?. *Nat. Hazards Earth Syst. Sci.* 13, 1507–1526. doi:10.5194/nhess-13-1507-2013

Goda, K., and De Risi, R. (2018). Multi-hazard loss estimation for shaking and tsunami using stochastic rupture sources. *Int. J. Disaster Risk Reduct.* 28, 539–554. doi:10.1016/j.ijdrr.2018.01.002

Goda, K. (2020). Multi-hazard portfolio loss estimation for time-dependent shaking and tsunami hazards. *Front. Earth Sci.* 8, 512. doi:10.3389/feart.2020.592444

Goda, K., Petrone, C., De Risi, R., and Rossetto, T. (2017). Stochastic coupled simulation of strong motion and tsunami for the 2011 Tohoku, Japan earthquake. *Stoch. Environ. Res. Risk Assess.* 31 (9), 2337–2355. doi:10.1007/s00477-016-1352-1

Goda, K., and Song, J. (2019). Influence of elevation data resolution on tsunami loss estimation and insurance rate-making. *Front. Earth Sci.* 7, 246. doi:10.1016/b978-0-12-107180-6.50007-x

Goda, K. (2019). Time-dependent probabilistic tsunami hazard analysis using stochastic rupture sources. *Stoch. Environ. Res. Risk Assess.* 33, 341–358. doi:10.1007/s00477-018-1634-x

Goda, K., Yasuda, T., Mori, N., and Maruyama, T. (2016). New scaling relationships of earthquake source parameters for stochastic tsunami simulation. *Coastal Eng. J.* 58, 1650010–1650011. doi:10.1142/S0578563416500108

González, F. I., Geist, E. L., Jaffe, B., Kânoğlu, U., Mofjeld, H., Synolakis, C. E., et al. (2009). Probabilistic tsunami hazard assessment at Seaside, Oregon, for near- and far-field seismic sources. *J. Geophys. Res.* 114, 37. doi:10.1029/2008JC005132

González, J. I., Farreras, S. F., and Ochoa, J. (2001). Seismic and meteorological tsunami contributions in the Manzanillo and Cabo San Lucas Seiches of September 14, 1995. *Mar. Geodesy* 24 (4), 219–227. doi:10.1080/014904101753227860

Greenslade, D. J. M., Annunziato, A., Babeyko, A. Y., Burbidge, D. R., Ellguth, E., Horspool, N., et al. (2014). An assessment of the diversity in scenario-based tsunami forecasts for the Indian Ocean. *Continental Shelf Res.* 79, 36–45. doi:10.1016/j.csr.2013.06.001

Gregg, C. E., Houghton, B. F., Paton, D., Lachman, R., Lachman, J., Johnston, D. M., et al. (2006). Natural warning signs of tsunamis: human sensory experience and response to the 2004 great Sumatra earthquake and tsunami in Thailand. *Thai. Earthq. Spectra* 22 (S3), 671–691. doi:10.1193/1.2206791

Grezio, A., Babeyko, A., Baptista, M. A., Behrens, J., Costa, A., Davies, G., et al. (2017). Probabilistic tsunami hazard analysis: multiple sources and global applications. *Rev. Geophys.* 55, 1158–1198. doi:10.1002/2017RG000579

Grezio, A., Cinti, F. R., Costa, A., Faenza, L., Perfetti, P., Pierdominici, S., et al. (2020). Multisource bayesian probabilistic tsunami hazard analysis for the Gulf of Naples (Italy). *J. Geophys. Res. Oceans* 125, 12. doi:10.1029/2019JC015373

Grezio, A., Marzocchi, W., Sandri, L., and Gasparini, P. (2010). A bayesian procedure for probabilistic tsunami hazard assessment. *Nat. Hazards* 53, 159–174. doi:10.1007/s11069-009-9418-8

Griffin, J., Latief, H., Kongko, W., Harig, S., Horspool, N., Hanung, R., et al. (2015). An evaluation of onshore digital elevation models for modeling tsunami inundation zones. *Front. Earth Sci.* 3, 32. doi:10.3389/feart.2015.00032

Grilli, S. T., Taylor, O. D. S., Baxter, C. D., and Maretzki, S. (2009). A probabilistic approach for determining submarine landslide tsunami hazard along the upper east coast of the United States. *Mar. Geol.* 264 (1–2), 74–97. doi:10.1016/j.margeo.2009.02.010

Grilli, S. T., and Watts, P. (2005). Tsunami generation by submarine mass failure. I: modeling, experimental validation, and sensitivity analyses. *J. Waterway, Port, Coastal, Ocean Eng.* 131 (6), 283–297. doi:10.1061/(asce)0733-950x(2005)131:6(283)

GTM (2020). Global Tsunami Model. http://edanya.uma.es/gtm/ (Accessed November 12, 2020).

Gylfadóttir, S. S., Kim, J., Helgason, J. K., Brynjólfsson, S., Höskuldsson, Á., Jóhannesson, T., et al. (2017). The 2014 Lake Askja rockslide-induced tsunami: optimization of numerical tsunami model using observed data. *J. Geophys. Res. Oceans* 122 (5), 4110–4122. doi:10.1002/2016jc012496

Hananto, N. D., Leclerc, F., Li, L., Etchebes, M., Carton, H., Tapponnier, P., et al. (2020). Tsunami earthquakes: vertical pop-up expulsion at the forefront of subduction megathrust. *Earth Planet. Sci. Lett.* 538, 116197. doi:10.1016/j.epsl.2020.116197

Harbitz, C. B. (1992). Model simulations of tsunamis generated by the Storegga slides. *Mar. Geol.* 105 (1-4), 1–21. doi:10.1016/0025-3227(92)90178-k

Harbitz, C. B., Løvholt, F., and Bungum, H. (2014). Submarine landslide tsunamis: how extreme and how likely?. *Nat. Hazards* 72 (3), 1341–1374. doi:10.1007/s11069-013-0681-3

Harig, S., Chaeroni, Pranowo, W. S., and Behrens, J. (2008). Tsunami simulations on several scales. *Ocean Dyn.* 58, 429–440. doi:10.1007/s10236-008-0162-5

Haslett, S. K., Mellor, H. E., and Bryant, E. A. (2009). Meteo-tsunami hazard associated with summer thunderstorms in the United Kingdom. *Phys. Chem. Earth, Parts A/B/C* 34, 1016–1022. doi:10.1016/j.pce.2009.10.005

Hatayama, K. (2014). "Damage to oil storage tanks due to tsunami of the Mw9.0 2011 off the Pacific coast of Tohoku, Japan." in 10th U.S. National conference on earthquake engineering, frontiers of earthquake engineering. Anchorage, USA: Earthquake Engineering Research Institute. doi:10.4231/D3VX0639C

Hayes, G. P., Moore, G. L., Portner, D. E., Hearne, M., Flamme, H., Furtney, M., et al. (2018). Slab2, a comprehensive subduction zone geometry model. *Science* 362 (6410), 58–61. doi:10.1126/science.aat4723

Heller, V., and Hager, W. H. (2010). Impulse product parameter in landslide generated impulse waves. *J. Waterway, Port, Coastal, Ocean Eng.* 136 (3), 145–155. doi:10.1061/(asce)ww.1943-5460.0000037

Heller, V. (2011). Scale effects in physical hydraulic engineering models. *J. Hydraulic Res.* 49 (3), 293–306. doi:10.1080/00221686.2011.578914

Hermanns, R., Oppikofer, T., Anda, E., Blikra, L., Böhme, M., Bunkholt, H., et al. (2013). Hazard and risk classification for large unstable rock slopes in Norway. *It. J. Eng. Geol. Env.* 11, 28. doi:10.4408/IJEGE.2013-06.B-22

Herrero, A., and Bernard, P. (1994). A kinematic self-similar rupture process for earthquakes. *Bull. Seismol. Soc. Amer.* 84, 1216–1228.

Herslund, L. B., Jalayer, F., Jean-Baptiste, N., Jørgensen, G., Kabisch, S., Kombe, W., et al. (2016). A multi-dimensional assessment of urban vulnerability to climate change in Sub-Saharan Africa. *Nat. hazards* 82 (2), 149–172. doi:10.1007/s11069-015-1856-x

Heuret, A., Conrad, C. P., Funiciello, F., Lallemand, S., and Sandri, L. (2012). Relation between subduction megathrust earthquakes, trench sediment thickness and upper plate strain. *Geophys. Res. Lett.* 39, a. doi:10.1029/2011GL050712

Hoechner, A., Babeyko, A. Y., and Zamora, N. (2016). Probabilistic tsunami hazard assessment for the Makran region with focus on maximum magnitude assumption. *Nat. Hazards Earth Syst. Sci.* 16, 1339–1350. doi:10.5194/nhess-16-1339-2016

Horspool, N., Pranantyo, I., Griffin, J., Latief, H., Natawidjaja, D. H., Kongko, W., et al. (2014). A probabilistic tsunami hazard assessment for Indonesia. *Nat. Hazards Earth Syst. Sci.* 14, 3105–3122. doi:10.5194/nhess-14-3105-2014

Huang, X., and García, M. H. (1998). A Herschel-Bulkley model for mud flow down a slope. *J. Fluid Mech.* 374, 305–333. doi:10.1017/s0022112098002845

Hufschmidt, G., Crozier, M., and Glade, T. (2005). Evolution of natural risk: research framework and perspectives. *Nat. Hazards Earth Syst. Sci.* 5 (3), 375–387. doi:10.5194/nhess-5-375-2005

Huhn, K., Arroyo, M., Cattaneo, A., Clare, M. A., Gràcia, E., Harbitz, C. B., et al. (2019). "Modern submarine landslide complexes: a short review," in *Submarine. Landslides: Subaqueous mass transport deposits from outcrops to seismic profiles*. Editor Ogata, K. (Hoboken, NJ, USA:Wiley), 181–200.

Huthnance, J. M. (1975). On trapped waves over a continental shelf. *J. Fluid Mech.* 69 (4), 689–704. doi:10.1017/S0022112075001632

Huyck, C., Hu, Z., Amyx, P., Esquivias, M. H., Eguchi, M., Contributors, K., et al. (2019). METEOR: exposure data classification. *Metadata Popul. Confidence Assess. Rep. Number* 3, 2. doi:10.3403/30126912u

Huyck, C. K., and Eguchi, M. T. (2017). GFDRR africa disaster risk financing-result area 5 exposure development. Replace. Cost Refinements Expo. Data. Prepared for World Bank/GFDRR.

Huyck, C. K., Esquivias, G., Gamba, P., Hussain, M., Odhiambo, O., Jaiswal, K., et al. (2011). D2.2 survey of available input databases for GED, report produced in the context of the global exposure databases for the global earthquake model (IDCT). *Constraints Databases* 4, 139–161. doi:10.1007/978-1-4615-5515-5_7

ITIC (2020). International tsunami information center. Available at: http://itic.ioc-unesco.org/ (Accessed November 11, 2020).

Jaimes, M. A., Reinoso, E., Ordaz, M., Huerta, B., Silva, R., Mendoza, E., et al. (2016). A new approach to probabilistic earthquake-induced tsunami risk assessment. *Ocean Coastal Manage.* 119, 68–75. doi:10.1016/j.ocecoaman.2015.10.007

Jalayer, F., Carozza, S., De Risi, R., Manfredi, G., and Mbuya, E. (2016). Performance-based flood safety-checking for non-engineered masonry structures. *Eng. Struct.* 106, 109–123. doi:10.1016/j.engstruct.2015.10.007

Jalayer, F., and Ebrahimian, H. (2020). Seismic reliability assessment and the nonergodicity in the modelling parameter uncertainties. *Earthq. Eng. Struct. Dyn.* 49 (5), 434–457. doi:10.1002/eqe.3247

Jasanoff, S. (1993). Bridging the two cultures of risk Analysis1,2. *Risk Anal.* 13 (2), 123–129. doi:10.1111/j.1539-6924.1993.tb01057.x

Jelínek, R., and Krausmann, E. (2008). Approaches to tsunami risk assessment. *JRC Sci. Tech. Rep.* 48713, 112. doi:10.4324/9781351140843-3

Johnston, D., Tarrant, R., Tipler, K., Lambie, E., Crawford, M., Becker, J., et al. (2016). Towards tsunami-safer schools in the Wellington Region, New Zealand:

evaluating drills and awareness programmes. *Aust. J. Emerg. Manage.* 31, 59–66. doi:10.7717/peerj-cs.386/table-1

Jop, P., Forterre, Y., and Pouliquen, O. (2006). A constitutive law for dense granular flows. *Nature* 441 (7094), 727–730. doi:10.1038/nature04801

JRC Risk Data Hub (2020). Available at: https://ec.europa.eu/jrc/en (Accessed November 11, 2020).

Kagan, Y. Y., and Jackson, D. D. (1991). Long-term earthquake clustering. *Geophys. J. Int.* 104, 117–134. doi:10.1111/j.1365-246X.1991.tb02498.x

Kagan, Y. Y., and Jackson, D. D. (2014). Statistical earthquake focal mechanism forecasts. *Geophys. J. Int.* 197, 620–629. doi:10.1093/gji/ggu015

Kagan, Y. Y. (2002). Seismic moment distribution revisited: I. Statistical results. *Geophys. J. Int.* 148, 520–541. doi:10.1046/j.1365–246x.2002.01594.x

Kaiser, G., Scheele, L., Kortenhaus, A., Løvholt, F., Römer, H., and Leschka, S. (2011). The influence of land cover roughness on the results of high resolution tsunami inundation modeling. *Nat. Hazards Earth Syst. Sci.* 11 (9), 2521–2540. doi:10.5194/nhess-11-2521-2011

Kajiura, K. (1963). The leading wave of a tsunami. *B. Earthq. Res. Inst.* 41, 535–571.

Karafagka, S., Fotopoulou, S., and Pitilakis, K. (2018). Analytical tsunami fragility curves for seaport RC buildings and steel light frame warehouses. *Soil Dyn. Earthq. Eng.* 112, 118–137. doi:10.1016/j.soildyn.2018.04.037

Kelfoun, K., and Druitt, T. H. (2005). Numerical modeling of the emplacement of socompa rock avalanche, Chile. *J. Geophys Res: solid Earth.* 110 (B12), 113. doi:10.3133/ofr01383

Kienle, J., Kowalik, Z., and Murty, T. S. (1987). Tsunamis generated by eruptions from mount st. Augustine volcano, Alaska. *Science* 236, 1442–1447. doi:10.1126/science.236.4807.1442

Kim, D. H., Lynett, P. J., and Socolofsky, S. A. (2009). A depth-integrated model for weakly dispersive, turbulent, and rotational fluid flows. *Ocean Model.* 27 (3–4), 198–214. doi:10.1016/j.ocemod.2009.01.005

Kim, J., Løvholt, F., Issler, D., and Forsberg, C. F. (2019). Landslide material control on tsunami genesis-the storegga slide and tsunami (8,100 Years BP). *J. Geophys. Res. Oceans* 124 (6), 3607–3627. doi:10.1029/2018jc014893

King, G. C. P., Stein, R. S., and Lin, J. (1994). Static stress changes and the triggering of earthquakes. *Bull. Seismol. Soc. Am.* 84, 935–953.

Kiureghian, A. D., and Ditlevsen, O. (2009). Aleatory or epistemic? Does it matter? *Struct. Saf.* 31 (2), 105–112. doi:10.1016/j.strusafe.2008.06.020

Kiureghian, A. D. (2005). Non-ergodicity and PEER's framework formula. *Earthq. Eng. Struct. Dyn.* 34 (13), 1643–1652. doi:10.1002/eqe.504

Kopp, H. (2013). Invited review paper: the control of subduction zone structural complexity and geometry on margin segmentation and seismicity. *Tectonophysics* 589, 1–16.

Koshimura, S., Oie, T., Yanagisawa, H., and Imamura, F. (2009). Developing fragility functions for tsunami damage estimation using numerical model and post-tsunami data from Banda Aceh, Indonesia. *Coastal Eng. J.* 51 (3), 243–273. doi:10.1142/s0578563409002004

Kozdon, J. E., and Dunham, E. M. (2013). Rupture to the trench: dynamic rupture simulations of the 11 march 2011 Tohoku earthquake. *Bull. Seismol. Soc. Amer.* 103, 1275–1289. doi:10.1785/0120120136

Kriebel, D. L., Lynett, P. J., Cox, D. T., Petroff, C. M., Robertson, I. N., and Chock, G. Y. (2017). Energy method for approximating overland tsunami flows. *J. Waterway Port Coastal Ocean Eng.* 143 (5),04017014. doi:10.1061/(ASCE)WW.1943-5460.0000393

Lam, N. S., Reams, M., Li, K., Li, C., and Mata, L. P. (2016). Measuring community resilience to coastal hazards along the northern Gulf of Mexico. *Nat. Hazards Rev.* 17 (1), 113. doi:10.1061/(ASCE)NH.1527-6996.0000193

Lane, E. M., Mountjoy, J. J., Power, W. L., and Mueller, C. (2016). "Probabilistic hazard of tsunamis generated by submarine landslides in the cook strait canyon (New Zealand), in *Global tsunami science Past and Future*. Editor Geist, H. (Basel, Switzerland: birkhäuser), Vol. I, 3757–3774.

Latter, J. H. (1981). Tsunamis of volcanic origin: summary of causes, with particular reference to Krakatoa, 1883. *Bull. Volcanol* 44, 467–490. doi:10.1007/bf02600578

Lee, H. J. (2009). Timing of occurrence of large submarine landslides on the Atlantic Ocean margin. *Mar. Geol.* 264 (1-2), 53–64. doi:10.1016/j.margeo.2008.09.009

LeMéhauté, B. L., and Wang, S. (1996). *Water waves generated by underwater explosion. Advanced series on ocean engineering*. New Jersey: World Scientific.

Li, S., Moreno, M., Rosenau, M., Melnick, D., and Oncken, O. (2014). Splay fault triggering by great subduction earthquakes inferred from finite element models. *Geophys. Res. Lett.* 41, 385–391. doi:10.1002/2013GL058598

Lin, I.-C., and Tung, C. C. (1982). A preliminary investigation of tsunami hazard. *Bull. Seismol. Soc. Amer.* 72, 2323–2337.

Logan, D. C. (2009). Known knowns, known unknowns, unknown unknowns and the propagation of scientific enquiry. *J. Exp. Bot.* 60 (3), 712–714. doi:10.1093/jxb/erp043

Lorito, S., Romano, F., and Lay, T. (2016). "Tsunamigenic major and great earthquakes (2004–2013): source processes inverted from seismic, geodetic, and sea-level data," in *Encyclopedia of complexity and systems science*. Editor R. A. Meyers (Berlin, Heidelberg: Springer), 1–52. doi:10.1007/978-3-642-27737-5_641-1

Lorito, S., Selva, J., Basili, R., Romano, F., Tiberti, M. M., and Piatanesi, A. (2015). Probabilistic hazard for seismically induced tsunamis: accuracy and feasibility of inundation maps. *Geophys. J. Int.* 200 (1), 574–588. doi:10.1093/gji/ggu408

Lotto, G. C., Dunham, E. M., Jeppson, T. N., and Tobin, H. J. (2017). The effect of compliant prisms on subduction zone earthquakes and tsunamis. *Earth Planet. Sci. Lett.* 458, 213–222. doi:10.1016/j.epsl.2016.10.050

Lotto, G. C., Jeppson, T. N., and Dunham, E. M. (2019). Fully coupled simulations of megathrust earthquakes and tsunamis in the Japan trench, nankai trough, and cascadia subduction zone. *Pure Appl. Geophys.* 176, 4009–4041. doi:10.1007/s00024-018-1990-y

Loveless, J. P., and Meade, B. J. (2011). Spatial correlation of interseismic coupling and coseismic rupture extent of the 2011 MW= 9.0 Tohoku-oki earthquake. *Geophys. Res. Lett.* 38 (17), 39. doi:10.1029/2011GL048561

Løvholt, F., Bondevik, S., Laberg, J. S., Kim, J., and Boylan, N. (2017). Some giant submarine landslides do not produce large tsunamis. *Geophys. Res. Lett.* 44 (16), 8463–8472. doi:10.1002/2017GL074062

Løvholt, F., Fraser, S., Salgado-Galvez, M., Lorito, S., Selva, J., Romano, F., et al. (2019). Global trends in advancing tsunami science for improved hazard and risk understanding. Contributing Paper to GAR19, June. doi:10.1109/urgenthpc49580.2019.00011

Løvholt, F., Glimsdal, S., and Harbitz, C. B. (2020). On the landslide tsunami uncertainty and hazard. *Landslides* 17, 2301–2315. doi:10.1007/s10346-020-01429-z

Løvholt, F., Glimsdal, S., Harbitz, C. B., Zamora, N., Nadim, F., Peduzzi, P., et al. (2012). Tsunami hazard and exposure on the global scale. *Earth-Sci. Rev.* 110 (1–4), 58–73. doi:10.1007/978-3-642-27737-5_642-1

Løvholt, F., Griffin, J., and Salgado-Gálvez, M. (2015a). Tsunami hazard and risk assessment on the global scale, in *Encyclopedia of complexity and systems science*. Editor R. A. Meyers (Berlin, Heidelberg: Springer), 1–34. doi:10.1007/978-3-642-27737-5642-1

Løvholt, F., Harbitz, C. B., and Haugen, K. B. (2005). A parametric study of tsunamis generated by submarine slides in the Ormen Lange/Storegga area off western Norway. *Mar. Pet. Geol.* 22 (1–2), 219–231. doi:10.1016/b978-0-08-044694-3.50023-8

Løvholt, F., Pedersen, G., and Gisler, G. (2008). Oceanic propagation of a potential tsunami from the La palma island. *J Geophs Res: Oceans.* 113 (C9), 38. doi:10.1029/2007JC004603

Løvholt, F., Pedersen, G., Harbitz, C. B., Glimsdal, S., and Kim, J. (2015b). On the characteristics of landslide tsunamis. *Phil. Trans. R. Soc. A.* 373 (2053), 20140376. doi:10.1098/rsta.2014.0376

Løvholt, F., Setiadi, N. J., Birkmann, J., Harbitz, C. B., Bach, C., Fernando, N., et al. (2014). Tsunami risk reduction–are we better prepared today than in 2004? *Int. J. Disaster Risk reduction* 10, 127–142.

Lynett, P. J., Gately, K., Wilson, R., Montoya, L., Arcas, D., Aytore, B., et al. (2017). Inter-model analysis of tsunami-induced coastal currents. *Ocean Model.* 114, 14–32. doi:10.1016/j.ocemod.2017.04.003

Ma, S. (2012). A self-consistent mechanism for slow dynamic deformation and tsunami generation for earthquakes in the shallow subduction zone. *Geophys. Res. Lett.* 39 (11), 12. doi:10.1029/2012GL051854

Macabuag, J., Rossetto, T., Ioannou, I., Suppasri, A., Sugawara, D., Adriano, B., et al. (2016). A proposed methodology for deriving tsunami fragility functions for buildings using optimum intensity measures. *Nat. Hazards* 84 (2), 1257–1285. doi:10.1007/s11069-016-2485-8

Macías, J., Castro, M. J., and Escalante, C. (2020). Performance assessment of the Tsunami-HySEA model for NTHMP tsunami currents benchmarking.

Laboratory data. *Coastal Eng.* 158, 103667. doi:10.1016/j.coastaleng.2020.103667

Macías, J., Castro, M. J., Ortega, S., Escalante, C., and González-Vida, J. M. (2017). Performance benchmarking of tsunami-HySEA model for NTHMP's inundation mapping activities. *Pure Appl. Geophys.* 174, 3147–3183. doi:10.1007/s00024-017-1583-1

Maeno, F., and Imamura, F. (2011). Tsunami generation by a rapid entrance of pyroclastic flow into the sea during the 1883 Krakatau eruption, Indonesia. *J Geophys Res.* 116 (B09), 205. doi:10.1029/2011JB008253

Mai, P. M., and Beroza, G. C. (2002). A spatial random field model to characterize complexity in earthquake slip. *J. Geophys. Res.* 107, 10–11. doi:10.1029/2001JB000588

Mansinha, L., and Smylie, D. E. (1971). The displacement of the earthquake fault model. *Bull. Seismol. Soc. Amer.* 61, 1433–1440.

Marras, S., and Mandli, K. T. (2021). Modeling and simulation of tsunami impact: a short review of recent advances and future challenges. *Geosciences* 11 (1), 5. doi:10.3390/geosciences11010005

Marzocchi, W., and Jordan, T. H. (2014). Testing for ontological errors in probabilistic forecasting models of natural systems. *Proc. Natl. Acad. Sci.* 111 (33), 11973–11978. doi:10.1073/pnas.1410183111

Mas, E., Koshimura, S., Suppasri, A., Matsuoka, M., Matsuyama, M., Yoshii, T., et al. (2012). Developing Tsunami fragility curves using remote sensing and survey data of the 2010 Chilean Tsunami in Dichato. *Nat. Hazards Earth Syst. Sci.* 12, 2689–2697. doi:10.5194/nhess-12-2689-2012

Masterlark, T. (2003). Finite element model predictions of static deformation from dislocation sources in a subduction zone: sensitivities to homogeneous, isotropic, Poisson-solid, and half-space assumptions. *J. Geophys. Res.* 108, 12. doi:10.1029/2002JB002296

McGuire, R. K. (2008). Probabilistic seismic hazard analysis: early history. *Earthq. Eng. Struct. Dyn.* 37, 329–338. doi:10.1002/eqe.765

McLaughlin, S., and Cooper, J. A. G. (2010). A multi-scale coastal vulnerability index: a tool for coastal managers?. *Environ. Hazards* 9 (3), 233–248. doi:10.3763/ehaz.2010.0052

Meade, B. J. (2007). Algorithms for the calculation of exact displacements, strains, and stresses for triangular dislocation elements in a uniform elastic half space. *Comput. Geosci.* 33, 1064–1075. doi:10.1016/j.cageo.2006.12.003

Mebarki, A., Jerez, S., Prodhomme, G., and Reimeringer, M. (2016). Natural hazards, vulnerability and structural resilience: tsunamis and industrial tanks. *Geomat. Nat. Hazards Risk* 7 (Suppl. 1), 5–17. doi:10.1080/19475705.2016.1181458

Meletti, C., Marzocchi, W., D'Amico, V., Lanzano, G., Luzi, L., and Martinelli, F., et al.; MPS19 Working Group (2021). The new Italian seismic hazard model (MPS19). *Ann. Geophys.* 64 (1), SE112. doi:10.4401/ag-8579

Melgar, D., LeVeque, R. J., Dreger, D. S., and Allen, R. M. (2016). Kinematic rupture scenarios and synthetic displacement data: an example application to the Cascadia subduction zone. *J. Geophys. Res. Solid Earth* 121, 6658–6674. doi:10.1002/2016JB013314

Melnick, D., Moreno, M., Quinteros, J., Baez, J. C., Deng, Z., Li, S., et al. (2017). The super-interseismic phase of the megathrust earthquake cycle in Chile. *Geophys. Res. Lett.* 44, 784–791. doi:10.1002/2016GL071845

Métois, M., Socquet, A., and Vigny, C. (2012). Interseismic coupling, segmentation and mechanical behavior of the central Chile subduction zone. *J. Geophys. Res.* 117, 18. doi:10.1029/2011JB008736

Miyashita, T., Mori, N., and Goda, K. (2020). Uncertainty of probabilistic tsunami hazard assessment of Zihuatanejo (Mexico) due to the representation of tsunami variability. *Coastal Eng. J.* 62, 413–428. doi:10.1080/21664250.2020.1780676

Molinari, I., Tonini, R., Lorito, S., Piatanesi, A., Romano, F., Melini, D., et al. (2016). Fast evaluation of tsunami scenarios: uncertainty assessment for a Mediterranean Sea database. *Nat. Hazards Earth Syst. Sci.* 16 (12), 2593–2602. doi:10.5194/nhess-16-2593-2016

Monserrat, S., Vilibić, I., and Rabinovich, A. B. (2006). Meteotsunamis: atmospherically induced destructive ocean waves in the tsunami frequency band. *Nat. Hazards Earth Syst. Sci.* 6, 1035–1051. doi:10.5194/nhess-6-1035-2006

Moreno, M., Haberland, C., Oncken, O., Rietbrock, A., Angiboust, S., and Heidbach, O. (2014). Locking of the Chile subduction zone controlled by fluid pressure before the 2010 earthquake. *Nat. Geosci.* 7, 292–296. doi:10.1038/ngeo2102

Morgan, M. G. (2014). Use (and abuse) of expert elicitation in support of decision making for public policy. *Proc. Natl. Acad. Sci.* 111 (20), 7176–7184. doi:10.1073/pnas.1319946111

Muldashev, I. A., and Sobolev, S. V. (2020). What controls maximum magnitudes of giant subduction earthquakes?. *Geochem. Geophys. Geosyst.* 21, e2020GC009145. doi:10.1029/2020GC009145

Murotani, S., Miyake, H., and Koketsu, K. (2008). Scaling of characterized slip models for plate-boundary earthquakes. *Earth Planet. Sp* 60, 987–991. doi:10.1186/BF03352855

Murotani, S., Satake, K., and Fujii, Y. (2013). Scaling relations of seismic moment, rupture area, average slip, and asperity size for M ~9 subduction-zone earthquakes. *Geophys. Res. Lett.* 40, 5070–5074. doi:10.1002/grl.50976

Murphy, S., Di Toro, G., Romano, F., Scala, A., Lorito, S., Spagnuolo, E., et al. (2018). Tsunamigenic earthquake simulations using experimentally derived friction laws. *Earth Planet. Sci. Lett.* 486, 155–165. doi:10.1016/j.epsl.2018.01.011

Murphy, S., Scala, A., Herrero, A., Lorito, S., Festa, G., Trasatti, E., et al. (2016). Shallow slip amplification and enhanced tsunami hazard unravelled by dynamic simulations of mega-thrust earthquakes. *Sci. Rep.* 6, 35007. doi:10.1038/srep35007

Musa, A., Watanabe, O., Matsuoka, H., Hokari, H., Inoue, T., Murashima, Y., et al. (2018). Real-time tsunami inundation forecast system for tsunami disaster prevention and mitigation. *J. Supercomput.* 74, 3093–3113. doi:10.1007/s11227-018-2363-0

Nadim, F., and Glade, T. (2006). "On tsunami risk assessment for the west coast of Thailand," in *Geohazards*. Available at: https://dc.engconfintl.org/geohazards/28/

Nes, N. (2018). Past slope collapse and current unstable slopes along a cliff at Hyllestad Kommune. MSc thesis, Norway: Techical University Science.

Nikkhoo, M., and Walter, T. R. (2015). Triangular dislocation: an analytical, artefact-free solution. *Geophys. J. Int.* 201, 1119–1141. doi:10.1093/gji/ggv035

Nistor, I., Goseberg, N., and Stolle, J. (2017b). Tsunami-driven debris motion and loads: a critical review. Front. *Built Environ.* 3, 2. doi:10.3389/fbuil.2017.00002

Nistor, I., Goseberg, N., Stolle, J., Mikami, T., Shibayama, T., Nakamura, R., et al. (2017a). Experimental investigations of debris dynamics over a horizontal plane. *J. Waterway Port Coastal Ocean Eng.* 143, 04016022. doi:10.2139/ssrn.2277688

Nomanbhoy, N., and Satake, K. (1995). Generation mechanism of tsunamis from the 1883 Krakatau eruption. *Geophys. Res. Lett.* 22, 509–512. doi:10.1029/94gl03219

Nosov, M. A., and Kolesov, S. V. (2007). Elastic oscillations of water column in the 2003 Tokachi-oki tsunami source: *in-situ* measurements and 3-D numerical modelling. *Nat. Hazards Earth Syst. Sci.* 7, 243–249. doi:10.5194/nhess-7-243-2007

NTHMP. (2018). National tsunami hazard mitigation program Landslide tsunami modelling benchmark workshop—Benchmark problems. http://www1.udel.edu/kirby/landslide/problems.html

O'Brien, K., Eriksen, S., Nygaard, L. P., and Schjolden, A. (2007). Why different interpretations of vulnerability matter in climate change discourses. *Clim. Pol.* 7 (1), 73–88. doi:10.1080/14693062.2007.9685639

Oishi, Y., Imamura, F., and Sugawara, D. (2015). Near-field tsunami inundation forecast using the parallel TUNAMI-N2 model: application to the 2011 Tohoku-Oki earthquake combined with source inversions. *Geophys. Res. Lett.* 42, 1083–1091. doi:10.1002/2014GL062577

Okada, Y. (1992). Internal deformation due to shear and tensile faults in a half-space. *Bull. Seismol. Soc. Am.* 82, 1018–1040.

Okal, E. A. (2015). The quest for wisdom: lessons from 17 tsunamis, 2004-2014. *Phil. Trans. R. Soc. A.* 373 (2053), 20140370. doi:10.1098/rsta.2014.0370

Okumura, N., Jonkman, S. N., Esteban, M., Hofland, B., and Shibayama, T. (2017). A method for tsunami risk assessment: a case study for Kamakura, Japan. *Nat. Hazards* 88 (3), 1451–1472. doi:10.1007/s11069-017-2928-x

OpenStreetMap. (2020). Available at: https://www.openstreetmap.org/ (Accessed November 1, 2020).

Ordaz, M. (2000). Metodología para la evaluación del riesgo sísmico enfocada a la gerencia de seguros por terremoto. Universidad Nacional Autónoma de México. México DF.

Ordaz, M. (2015). A simple probabilistic model to combine losses arising from the simultaneous occurrence of several hazards. *Nat. Hazards* 76, 389–396. doi:10.1007/s11069-014-1495-7

Ordaz, M., Salgado-Gálvez, M. A., Huerta, B., Rodríguez, J. C., and Avelar, C. (2019). Considering the impacts of simultaneous perils. *Dpm* 28 (6), 823–837. doi:10.1108/DPM-09-2019-0295

Ota, Y., and Yamaguchi, M. (2004). Holocene coastal uplift in the western Pacific Rim in the context of late Quaternary uplift. *Quat. Int.* 120 (1), 105–117. doi:10.1016/j.quaint.2004.01.010

Páez-Ramírez, J., Lizarazo-Marriaga, J., Medina, S., Estrada, M., Mas, E., and Koshimura, S. (2020). A comparative study of empirical and analytical fragility functions for the assessment of tsunami building damage in Tumaco, Colombia. *Coastal Eng. J.* 62 (3), 362–372. doi:10.1080/21664250.2020.1726558

Pagnoni, G., Armigliato, A., and Tinti, S. (2019). *Estimation of human damage and economic loss of buildings related to tsunami inundation in the city of Augusta, Italy. Special publications, 501*. London: Geological Society.

Pampell-Manis, A., Horrillo, J., Shigihara, Y., and Parambath, L. (2016). Probabilistic assessment of landslide tsunami hazard for the northern Gulf of Mexico. *J. Geophys. Res. Oceans* 121 (1), 1009–1027. doi:10.1007/978-3-642-13296-4_8

Paris, R., Falvard, S., Chagué, C., Goff, J., Etienne, S., and Doumalin, P. (2020). Sedimentary fabric characterized by X-ray tomography: a case-study from tsunami deposits on the Marquesas Islands, French Polynesia. *Sedimentology* 67, 1207–1229. doi:10.1111/sed.12582

Paris, R. (2015). Source mechanisms of volcanic tsunamis. *Phil. Trans. R. Soc. A.* 373, 20140380. doi:10.1098/rsta.2014.0380

Paris, R., Switzer, A. D., Belousova, M., Belousov, A., Ontowirjo, B., Whelley, P. L., et al. (2014). Volcanic tsunami: a review of source mechanisms, past events and hazards in Southeast Asia (Indonesia, Philippines, Papua New Guinea). *Nat. Hazards* 70, 447–470. doi:10.1007/s11069-013-0822-8

Paris, R., Ulvrova, M., Selva, J., Brizuela, B., Costa, A., Grezio, A., et al. (2019). Probabilistic hazard analysis for tsunamis generated by subaqueous volcanic explosions in the Campi Flegrei caldera, Italy. *J. Volcanol. Geothermal Res.* 379, 106–116. doi:10.1016/j.jvolgeores.2019.05.010

Park, H., Alam, M. S., Cox, D. T., Barbosa, A. R., and van de Lindt, J. W. (2019). Probabilistic seismic and tsunami damage analysis (PSTDA) of the Cascadia Subduction Zone applied to Seaside, Oregon. *Int. J. Disaster Risk Reduct.* 35, 101076. doi:10.1016/j.ijdrr.2019.101076

Park, H., Cox, D. T., Lynett, P. J., Wiebe, D. M., and Shin, S. (2013). Tsunami inundation modeling in constructed environments: a physical and numerical comparison of free-surface elevation, velocity, and momentum flux. *Coastal Eng.* 79, 9–21. doi:10.1016/j.coastaleng.2013.04.002

Park, S., van de Lindt, J. W., Cox, D., Gupta, R., and Aguiniga, F. (2012). Successive earthquake-tsunami analysis to develop collapse fragilities. *J. Earthq. Eng.* 16 (6), 851–863. doi:10.1080/13632469.2012.685209

Pasquet, S., Vilibić, I., and Šepić, J. (2013). A survey of strong high-frequency sea level oscillations along the US East Coast between 2006 and 2011. *Nat. Hazards Earth Syst. Sci.* 13, 473–482. doi:10.5194/nhess-13-473-2013

Pattiaratchi, C. B., and Wijeratne, E. M. S. (2015). Are meteotsunamis an underrated hazard? *Phil. Trans. R. Soc. A.* 373, 20140377. doi:10.1098/rsta.2014.0377

Pedersen, G. (2008). *Advanced numerical models for simulating tsunami waves and runup. Modeling runup with depth integrated equation models*. Singapore: World Scientific, 3–41.

Pedersen, G. K., Lindstrøm, E., Bertelsen, A. F., Jensen, A., Laskovski, D., and Sælevik, G. (2013). Runup and boundary layers on sloping beaches. *Phys. Fluids.* 25 (1), 012102. doi:10.1063/1.4773327

Pellikka, H., Laurila, T. K., Boman, H., Karjalainen, A., Björkqvist, J.-V., and Kahma, K. K. (2020). Meteotsunami occurrence in the Gulf of Finland over the past century. *Nat. Hazards Earth Syst. Sci.* 20, 2535–2546. doi:10.5194/nhess-20-2535-2020

Petrone, C., Rossetto, T., Baiguera, M., la Barra Bustamante, C. D., and Ioannou, I. (2020). Fragility functions for a reinforced concrete structure subjected to earthquake and tsunami in sequence. *Eng. Struct.* 205, 110120. doi:10.1016/j.engstruct.2019.110120

Petrone, C., Rossetto, T., and Goda, K. (2017). Fragility assessment of a RC structure under tsunami actions via nonlinear static and dynamic analyses. *Eng. Struct.* 136, 36–53. doi:10.1016/j.engstruct.2017.01.013

Philibosian, B., and Meltzner, A. J. (2020). Segmentation and supercycles: a catalog of earthquake rupture patterns from the Sumatran Sunda Megathrust and other well-studied faults worldwide. *Quat. Sci. Rev.* 241, 106390. doi:10.1016/j.quascirev.2020.106390

Pitilakis, K., Argyroudis, S., Fotopoulou, S., Karafagka, S., Kakderi, K., and Selva, J. (2019). Application of stress test concepts for port infrastructures against natural hazards. The case of Thessaloniki port in Greece. *Reliab. Eng. Syst. Saf.* 184, 240–257. doi:10.1016/j.ress.2018.07.005

Pittore, M., Wieland, M., and Fleming, K. (2017). Perspectives on global dynamic exposure modelling for geo-risk assessment. *Nat. Hazards* 86 (1), 7–30. doi:10.1007/s11069-016-2437-3

Polese, M., Di Ludovico, M., Gaetani d'Aragona, M., Prota, A., and Manfredi, G. (2020). Regional vulnerability and risk assessment accounting for local building typologies. *Int. J. Disaster Risk Reduct.* 43, 101400. doi:10.1016/j.ijdrr.2019.101400

Polet, J., and Kanamori, H. (2016). "Tsunami earthquakes," in *Encyclopedia of complexity and systems science*. Editor R. A. Meyers (Berlin, Heidelberg: Springer), 1–22. doi:10.1007/978-3-642-27737-5567-2

Power, W., Downes, G., and Stirling, M. (2007). Estimation of tsunami hazard in New Zealand due to south American earthquakes. *Pure Appl. Geophys.* 164, 547–564. doi:10.1007/s00024-006-0166-3

Priest, G. R., Witter, R. C., Zhang, Y. J., Goldfinger, C., Wang, K., and Allan, J. C. (2017). New constraints on coseismic slip during southern Cascadia subduction zone earthquakes over the past 4600 years implied by tsunami deposits and marine turbidites. *Nat. Hazards* 88, 285–313. doi:10.1007/s11069-017-2864-9

Proudman, J. (1929). The effects on the sea of changes in atmospheric pressure. *International* 2, 197–209. doi:10.1111/j.1365-246x.1929.tb05408.x

Puzrin, A. M., Germanovich, L. N., and Friedli, B. (2016). Shear band propagation analysis of submarine slope stability. *Géotechnique* 66 (3), 188–201. doi:10.1680/jgeot.15.lm.002

Ramírez-Herrera, M. T., Kostoglodov, V., and Urrutia-Fucugauchi, J. (2011). Overview of recent coastal tectonic deformation in the Mexican subduction zone. *Pure Appl. Geophys.* 168, 1415–1433. doi:10.1007/s00024-010-0205-y

Reese, S., Cousins, W. J., Power, W. L., Palmer, N. G., Tejakusuma, I. G., and Nugrahadi, S. (2007). Tsunami vulnerability of buildings and people in South Java—field observations after the July 2006 Java tsunami. *Nat. Hazards Earth Syst. Sci.* 7, 573–589. doi:10.5194/nhess-7-573-2007

Rijsingen, E.V, Funiciello, F., Corbi, F., and Lallemand, S. (2019). Rough subducting seafloor reduces interseismic coupling and mega-earthquake occurrence: insights from analogue models. *Geophys. Res. Lett.* 46 (6), 3124–3132. doi:10.1029/2018GL081272

Rikitake, T., and Aida, I. (1988). Tsunami hazard probability in Japan. *Bull. Seismol. Soc. Amer.* 78, 1268–1278.

Rivera, F., Rossetto, T., and Twigg, J.(2020). An interdisciplinary study of the seismic exposure dynamics of Santiago de Chile. *Int. J. Disaster Risk Reduct.* 48, 101581. doi:10.1016/j.ijdrr.2020.101581

Rondon, L., Pouliquen, O., and Aussillous, P. (2011). Granular collapse in a fluid: role of the initial volume fraction. *Phys. Fluids* 23 (7), 073301. doi:10.1063/1.3594200

Rong, Y., Jackson, D. D., Magistrale, H., and Goldfinger, C. (2014). Magnitude limits of subduction zone earthquakes. *Bull. Seismol. Soc. Amer.* 104, 2359–2377. doi:10.1785/0120130287

Rosi, M., Di Traglia, F., Pistolesi, M., Esposti Ongaro, T., de' Michieli Vitturi, M., and Bonadonna, C. (2018). Dynamics of shallow hydrothermal eruptions: new insights from Vulcano's Breccia di Commenda eruption. *Bull. Volcanol.* 80, 83. doi:10.1007/s00445-018-1252-y

Rossetto, T., De la Barra, C., Petrone, C., De la Llera, J. C., Vásquez, J., and Baiguera, M. (2019). Comparative assessment of nonlinear static and dynamic methods for analysing building response under sequential earthquake and tsunami. *Earthq. Eng. Struct. Dyn.* 48, 867–887. doi:10.1002/eqe.3167

Rossetto, T., Petrone, C., Eames, I., De La Barra, C., Foster, A., and Macabuag, J. (2018). *Advances in the assessment of buildings subjected to earthquakes and tsunami. In European Conference on Earthquake Engineering Thessaloniki Greece* (Cham, Switzerland: Springer), 545–562.

Ryan, K. J., Geist, E. L., Barall, M., and Oglesby, D. D. (2015). Dynamic models of an earthquake and tsunami offshore Ventura, California. *Geophys. Res. Lett.* 42, 6599–6606. doi:10.1002/2015GL064507

Šepić, J., Vilibić, I., and Strelec Mahović, N. (2012). Northern Adriatic meteorological tsunamis: observations, link to the atmosphere, and predictability. *J. Geophys. Res.* 117, C02002. doi:10.1029/2011JC007608

Saja, A. M. A., Goonetilleke, A., Teo, M., and Ziyath, A. M. (2019). A critical review of social resilience assessment frameworks in disaster management. *Int. J. Disaster Risk Reduct.* 35, 101096. doi:10.1016/j.ijdrr.2019.101096

Salamon, A., and Di Manna, P. (2019). Empirical constraints on magnitude-distance relationships for seismically-induced submarine tsunamigenic landslides. *Earth-Sci. Rev.* 191, 66–92. doi:10.1016/j.earscirev.2019.02.001

Salgado-Gálvez, M. A., Zuloaga, D., Henao, S., Bernal, G. A., and Cardona, O. D. (2018). Probabilistic assessment of annual repair rates in pipelines and of direct economic losses in water and sewage networks. Application to Manizales, Colombia. *Nat. Hazards* 93 (1), S5–S24. doi:10.1007/s11069-017-2987-z

Salgado-Gálvez, M. A., Zuloaga Romero, D., Velásquez, C. A., Carreño, M. L., Cardona, O.-D., and Barbat, A. H. (2016). Urban seismic risk index for Medellín, Colombia, based on probabilistic loss and casualties estimations. *Nat. Hazards* 80 (3), 1995–2021. doi:10.1007/s11069-015-2056-4

Salgado-Gálvez, M. A., Zuloaga-Romero, D., Bernal, G. A., Mora, M. G., and Cardona, O.-D. (2014). Fully probabilistic seismic risk assessment considering local site effects for the portfolio of buildings in Medellín, Colombia. *Bull. Earthq. Eng.* 12 (2), 671–695. doi:10.1007/s10518-013-9550-4

Sallarès, V., and Ranero, C. R. (2019). Upper-plate rigidity determines depth-varying rupture behaviour of megathrust earthquakes. *Nature* 576, 96–101. doi:10.1038/s41586-019-1784-0

Salmanidou, D. M., Guillas, S., Georgiopoulou, A., and Dias, F. (2017). Statistical emulation of landslide-induced tsunamis at the rockall bank, NE atlantic. *Proc. R. Soc. A.* 473 (2200), 20170026. doi:10.1098/rspa.2017.0026

Sandri, L., Tierz, P., Costa, A., and Marzocchi, W. (2018). Probabilistic hazard from pyroclastic density currents in the Neapolitan area (Southern Italy). *J. Geophys. Res. Solid Earth* 123, 3474–3500. doi:10.1002/2017JB014890

Santos, A., and Koshimura, S. (2015). The historical review of the 1755 lisbon tsunami. *J. Geodesy Geomat. Eng.* 1, 38–52. doi:10.17265/2332-8223/2015.04.004

Sarri, A., Guillas, S., and Dias, F. (2012). Statistical emulation of a tsunami model for sensitivity analysis and uncertainty quantification. *Nat. Hazards Earth Syst. Sci.* 12 (6), 2003. doi:10.5194/nhess-12-2003-2012

Savage, S. B., Babaei, M. H., and Dabros, T. (2014). Modeling gravitational collapse of rectangular granular piles in air and water. *Mech. Res. Commun.* 56, 1–10. doi:10.1016/j.mechrescom.2013.11.001

Scala, A., Festa, G., Vilotte, J. P., Lorito, S., and Romano, F. (2019). Wave interaction of reverse-fault rupture with free surface: numerical analysis of the dynamic effects and fault opening induced by symmetry breaking. *J. Geophys. Res. Solid Earth* 124, 1743–1758. doi:10.1029/2018JB016512

Scala, A., Lorito, S., Romano, F., Murphy, S., Selva, J., Basili, R., et al. (2020). Effect of shallow slip amplification uncertainty on probabilistic tsunami hazard analysis in subduction zones: use of long-term balanced stochastic slip models. *Pure Appl. Geophys.* 177, 1497–1520. doi:10.1007/s00024-019-02260-x

Schmidtlein, M. C., Deutsch, R. C., Piegorsch, W. W., and Cutter, S. L. (2008). A sensitivity analysis of the social vulnerability index. *Int. J.* 28 (4), 1099–1114. doi:10.1111/j.1539-6924.2008.01072.x

Selva, J., Acocella, V., Bisson, M., Caliro, S., Costa, A., Della Seta, M., et al. (2019). Multiple natural hazards at volcanic islands: a review for the Ischia volcano (Italy). *J. Appl. Volcanol.* 8 (1), 5. doi:10.1186/s13617-019-0086-4

Selva, J., Bonadonna, C., Branca, S., De Astis, G., Gambino, S., Paonita, A., et al. (2020). Multiple hazards and paths to eruptions: a review of the volcanic system of Vulcano (Aeolian Islands, Italy). *Earth-Sci. Rev.* 207, 103186. doi:10.1016/j.earscirev.2020.103186

Selva, J., Tonini, R., Molinari, I., Tiberti, M. M., Romano, F., Grezio, A., et al. (2016). Quantification of source uncertainties in seismic probabilistic tsunami hazard analysis (SPTHA). *Geophys. J. Int.* 205, 1780–1803. doi:10.1093/gji/ggw107

Sepúlveda, I., Liu, P. L.-F., Grigoriu, M., and Pritchard, M. (2017). Tsunami hazard assessments with consideration of uncertain earthquake slip distribution and location. *J. Geophys. Res. Solid Earth* 122, 7252–7271. doi:10.1002/2017JB014430

Shi, F., Kirby, J. T., Harris, J. C., Geiman, J. D., and Grilli, S. T. (2012). A high-order adaptive time-stepping TVD solver for Boussinesq modeling of breaking waves and coastal inundation. *Ocean Model.* 43, 36–51. doi:10.1016/j.ocemod.2011.12.004

Si, P., Shi, H., and Yu, X. (2018b). A general numerical model for surface waves generated by granular material intruding into a water body. *Coastal Eng.* 142, 42–51. doi:10.1016/j.coastaleng.2018.09.001

Si, P., Shi, H., and Yu, X. (2018a). Development of a mathematical model for submarine granular flows. *Phys. Fluids* 30, 083302. doi:10.1063/1.5030349

Sibley, A. M., Cox, D., and Tappin, D. R. (2020). Convective rear-flank downdraft as driver for meteotsunami along English Channel and North Sea coasts 28-29 May 2017. *Nat. Hazards* 14, 114. doi:10.1007/s11069-020-04328-7

Silva, V., Amo-Oduro, D., Calderon, A., Dabbeek, J., Despotaki, V., Martins, L., et al. (2018a). *Global Earthquake Model (GEM) Seismic Risk Map (version 2018.1)*, Available at: https://maps.openquake.org/map/global-seismic-risk-map (Accessed November 10, 2020).

Silva, V., Yepes-Estrada, C., Dabbeek, J., Martins, L., and Brzev, S. (2018b). GED4ALL-Global exposure database for multi-hazard risk analysis–multi-hazard exposure taxonomy. GEM Technical Report 2018-01. Pavia: GEM Foundation.

Skarlatoudis, A. A., Somerville, P. G., and Thio, H. K. (2016). Source-scaling relations of interface subduction earthquakes for strong ground motion and tsunami simulation. *Bull. Seismol. Soc. Amer.* 106, 1652–1662. doi:10.1785/0120150320

Smit, A., Kijko, A., and Stein, A. (2017). Probabilistic tsunami hazard assessment from incomplete and uncertain historical catalogues with application to tsunamigenic regions in the pacific ocean. *Pure Appl. Geophys.* 174, 3065–3081. doi:10.1007/s00024-017-1564-4

Snelling, B., Neethling, S., Horsburgh, K., Collins, G., and Piggott, M. (2020). Uncertainty quantification of landslide generated waves using Gaussian process emulation and variance-based sensitivity analysis. *Water* 12 (2), 416. doi:10.3390/w12020416

So, E. K. M., Pomonis, A., Below, R., Cardona, O., King, A., Zulfikar, C., et al. (2012). "An introduction to the global earthquake consequences database (GEMECD)," in Proceedings of the 15th world conference on earthquake engineering. Lisbon: Springer.

Song, J., De Risi, R., and Goda, K. (2017). Influence of flow velocity on tsunami loss estimation. *Geosciences* 7 (4), 114. doi:10.3390/geosciences7040114

Sørensen, M. B., Spada, M., Babeyko, A., Wiemer, S., and Grünthal, G. (2012). Probabilistic tsunami hazard in the mediterranean sea. *J. Geophys. Res.* 117 (B1), 13. doi:10.1029/2010JB008169

Spielman, S. E., Tuccillo, J., Folch, D. C., Schweikert, A., Davies, R., Wood, N., et al. (2020). Evaluating social vulnerability indicators: criteria and their application to the Social Vulnerability Index. *Nat. Hazards* 100 (1), 417–436. doi:10.1007/s11069-019-03820-z

Stolle, J., Takabatake, T., Hamano, G., Ishii, H., Iimura, K., Shibayama, T., et al. (2019). Debris transport over a sloped surface in tsunami-like flow conditions. *Coastal Eng. J.* 61 (2), 241–255. doi:10.1080/21664250.2019.1586288

Strasser, F. O., Arango, M. C., and Bommer, J. J. (2010). Scaling of the source dimensions of interface and intraslab subduction-zone earthquakes with moment magnitude. *Seismol. Res. Lett.* 81, 941–950. doi:10.1785/gssrl.81.6.9410.1785/gssrl.81.6.941

Strunz, G., Post, J., Zosseder, K., Wegscheider, S., Mück, M., Riedlinger, T., et al. (2011). Tsunami risk assessment in Indonesia. *Nat. Hazards Earth Syst. Sci.* 11 (1), 67–82. doi:10.5194/nhess-11-67-2011

Stucchi, M., Albini, P., Mirto, M., and Rebez, A. (2004). Assessing the completeness of Italian historical earthquake data. *Ann. Geophys.* 47, 35. doi:10.4401/ag-3330

Sugawara, D., Goto, K., and Jaffe, B. E. (2014). Numerical models of tsunami sediment transport—current understanding and future directions. *Mar. Geol.* 352, 295–320. doi:10.1016/j.margeo.2014.02.007

Suppasri, A., Charvet, I., Imai, K., and Imamura, F. (2015). Fragility curves based on data from the 2011 tohoku-oki tsunami in ishinomaki city, with discussion of parameters influencing building damage. *Earthq. Spectra* 31, 841–868. doi:10.1193/053013EQS138M

Suppasri, A., Hasegawa, N., Makinoshima, F., Imamura, F., Latcharote, P., and Day, S. (2016). An analysis of fatality ratios and the factors that affected human fatalities in the 2011 Great East Japan tsunami. *Front. Built Environ.* 2, 32. doi:10.3389/fbuil.2016.00032

Synolakis, C. E., Bernard, E. N., Titov, V. V., Kânoğlu, U., and González, F. I. (2008). Validation and verification of tsunami numerical models. *Pure Appl. Geophys.* 165, 2197–2228. doi:10.1007/s00024-004-0427-y

Šepić, J., Vilibić, I., and Monserrat, S. (2016). Quantifying the probability of meteotsunami occurrence from synoptic atmospheric patterns. *Geophys. Res. Lett.* 43, 10377–10384. doi:10.1002/2016GL070754

Tappin, D. R., Watts, P., and Grilli, S. T. (2008). The Papua New Guinea tsunami of 17 July 1998: anatomy of a catastrophic event. *Nat. Hazards Earth Syst. Sci.* 8 (2), 243–266. doi:10.5194/nhess-8-243-2008

ten Brink, U., Geist, E. L., and Andrews, B. D. (2006). Size distribution of submarine landslides and its implication to tsunami hazard in Puerto Rico. *Geophys. Res. Lett.*. 33 (11), 23. doi:10.1142/9789812774613_0004

Thingbaijam, K. K. S., Martin Mai, P., and Goda, K. (2017). New empirical earthquake source-scaling laws. *Bull. Seismol. Soc. Am.* 107, 2225–2246. doi:10.1785/0120170017

Thio, H. K., Somerville, P., and Ichinose, G. (2007). Probabilistic analysis of strong ground motion and tsunami hazards in southeast asia. *J. Earthq. Tsunami* 01, 119–137. doi:10.1142/S1793431107000080

Tiberti, M. M., Basili, R., and Vannoli, P. (2014). Ups and downs in western Crete (Hellenic subduction zone). *Sci. Rep.* 4, 5677. doi:10.1038/srep05677

Tinti, S. (1991). Assessment of tsunami hazard in the Italian seas. *Nat. Hazards* 4, 267–283. doi:10.1007/bf00162792

Tinti, S., Bortolucci, E., and Armigliato, A. (1999). Numerical simulation of the landslide-induced tsunami of 1988 on Vulcano Island, Italy. *Bull. Volcanol.* 61 (1), 121–137. doi:10.1007/s004450050267

Tinti, S., Bortolucci, E., and Vannini, C. (1997). A block-based theoretical model suited to gravitational sliding. *Nat. Hazards* 16, 1–28. doi:10.1023/A10.1023/a:1007934804464

Tinti, S., Pagnoni, G., and Zaniboni, F. (2006). The landslides and tsunamis of the 30th of December 2002 in Stromboli analysed through numerical simulations. *Bull. Volcanol.* 68, 462–479. doi:10.1007/s00445-005-0022-9

Tonini, R., Basili, R., Maesano, F. E., Tiberti, M. M., Lorito, S., Romano, F., et al. (2020). Importance of earthquake rupture geometry on tsunami modelling: the Calabrian Arc subduction interface (Italy) case study. *Geophys. J. Int.* 223, 1805–1819. doi:10.1093/gji/ggaa409

Trapper, P. A., Puzrin, A. M., and Germanovich, L. N. (2015). Effects of shear band propagation on early waves generated by initial breakoff of tsunamigenic landslides. *Mar. Geol.* 370, 99–112. doi:10.1016/j.margeo.2015.10.014

Triantafyllou, I., Novikova, T., Charalampakis, M., Fokaefs, A., and Papadopoulos, G. A. (2019). Quantitative tsunami risk assessment in terms of building replacement cost based on tsunami modelling and GIS methods: the case of crete isl., hellenic arc. *Pure Appl. Geophys.* 176 (7), 3207–3225. doi:10.1007/s00024-018-1984-9

Tufekci, D., Suzen, M. L., Yalciner, A. C., and Zaytsev, A. (2018). Revised MeTHuVA method for assessment of tsunami human vulnerability of Bakirkoy district, Istanbul. *Nat. Hazards* 90 (2), 943–974. doi:10.1007/s11069-017-3082-1

Ulrich, T., Gabriel, A.-A., Ampuero, J.-P., and Xu, W. (2019a). Dynamic viability of the 2016 Mw 7.8 Kaikōura earthquake cascade on weak crustal faults. *Nat. Commun.* 10 (1), 1213. doi:10.1038/s41467-019-09125-w

Ulrich, T., Vater, S., Madden, E. H., Behrens, J., van Dinther, Y., van Zelst, I., et al. (2019b). Coupled, physics-based modeling reveals earthquake displacements are critical to the 2018 palu, sulawesi tsunami. *Pure Appl. Geophys.* 176, 4069–4109. doi:10.1007/s00024-019-02290-5

Ulvrova, M., Paris, R., Nomikou, P., Kelfoun, K., Leibrandt, S., Tappin, D. R., et al. (2016). Source of the tsunami generated by the 1650 AD eruption of Kolumbo submarine volcano (Aegean Sea, Greece). *J. Volcanol. Geothermal Res.* 321, 125–139. doi:10.1016/j.jvolgeores.2016.04.034

UNISDR. (2013). *United Nations international Office for disaster risk reduction. Global assessment report on disaster risk reduction 2013*. Geneva: Springer.

UNISDR. (2015). *United Nations international Office for disaster risk reduction. Global assessment report on disaster risk reduction 2015*. Geneva: Switzerland..

UNISDR. (2007). United Nations international Office for disaster risk reduction. Hyogo framework for action 2005–2015: building the resilience of Nations and communities to disasters. Geneva. Switzerland. Available at: https://www.unisdr.org/files/1037_hyogoframeworkforactionenglish.pdf (Accessed October 22, 2020).

Urgeles, R., and Camerlenghi, A. (2013). Submarine landslides of the Mediterranean Sea: trigger mechanisms, dynamics, and frequency-magnitude distribution. *J. Geophys. Res. Earth Surf.* 118 (4), 2600–2618. doi:10.1002/2013jf002720

Urlaub, M., Talling, P. J., and Masson, D. G. (2013). Timing and frequency of large submarine landslides: implications for understanding triggers and future geohazard. *Quat. Sci. Rev.* 72, 63–82. doi:10.1016/j.quascirev.2013.04.020

van de Lindt, J. W., and Dao, T. N. (2009). Performance-based wind engineering for wood-frame buildings. *J. Struct. Eng.* 135 (2), 169–177. doi:10.1061/(asce)0733-9445(2009)135:2(169)

Vela, J., Pérez, B., González, M., Otero, L., Olabarrieta, M., Canals, M., et al. (2014). Tsunami resonance in palma bay and harbor, majorca island, as induced by the 2003 western mediterranean earthquake. *J. Geol.* 122 (2), 165–182. doi:10.1086/675256

Vilibić, I. (2008). Numerical simulations of the Proudman resonance. *Continental Shelf Res.* 28 (4), 574–581. doi:10.1016/j.csr.2007.11.005

Vilibić, I., Horvath, K., Strelec Mahović, N., Monserrat, S., Marcos, M., Amores, A., et al. (2014). Atmospheric processes responsible for generation of the 2008 Boothbay meteotsunami. *Nat. Hazards* 74, 25–53. doi:10.1007/s11069-013-0811-y

Vilibić, I., and Šepić, J. (2009). Destructive meteotsunamis along the eastern adriatic coast: overview. Physics and chemistry of the Earth. *Parts A/B/C* 34 (17–18), 904–917. doi:10.1016/j.pce.2009.08.004

Volpe, M., Lorito, S., Selva, J., Tonini, R., Romano, F., and Brizuela, B. (2019). From regional to local SPTHA: efficient computation of probabilistic tsunami inundation maps addressing near-field sources. *Nat. Hazards Earth Syst. Sci.* 19, 455–469. doi:10.5194/nhess-19-455-2019

Walter, T. R., Haghshenas Haghighi, M., Schneider, F. M., Coppola, D., Motagh, M., Saul, J., et al. (2019). Complex hazard cascade culminating in the Anak Krakatau sector collapse. *Nat. Commun.* 10, 4339. doi:10.1038/s41467-019-12284-5

Wang, K., Hu, Y., and He, J. (2012). Deformation cycles of subduction earthquakes in a viscoelastic Earth. *Nature* 484, 327–332. doi:10.1038/nature11032

Wang, L., Zhang, X., and Tinti, S. (2019). Shallow landslides modeling using a particle finite element model with emphasis on landslide evolution. 11, 21. doi:10.5194/esurf-2019-17

Ward, S. N. (2001). Landslide tsunami. *J. Geophys. Res.* 106 (B6), 11201–11215. doi:10.1029/2000jb900450

Watts, P., Grilli, S. T., Kirby, J. T., Fryer, G. J., and Tappin, D. R. (2003). Landslide tsunami case studies using a Boussinesq model and a fully nonlinear tsunami generation model. *Nat. Hazards Earth Syst. Sci.* 3, 391–402. doi:10.5194/nhess-3-391-2003

Watts, P. (2000). Tsunami features of solid block underwater landslides. *J. Waterway Port Coastal Ocean Eng.* 126 (3), 144–152. doi:10.1061/(asce)0733-950x(2000)126:3(144)

Watts, P., and Waythomas, C. F. (2003). Theoretical analysis of tsunami generation by pyroclastic flows. *J. Geophys. Res.* 108 (B12), 2563. doi:10.1029/2002JB002265

Wei, Y., Bernard, E. N., Tang, L., Weiss, R., Titov, V. V., Moore, C., et al. (2008). Real-time experimental forecast of the Peruvian tsunami of August 2007 for U.S. coastlines. *Geophys. Res. Lett.* 35 (4), 67. doi:10.1029/2007GL032250

Wells, D. L., and Coppersmith, K. J. (1994). New empirical relationships among magnitude, rupture length, rupture width, rupture area, and surface displacement. *Bull. Seismol. Soc. Am.* 84, 974–1002.

Wendt, J., Oglesby, D. D., and Geist, E. L. (2009). Tsunamis and splay fault dynamics. *Geophys. Res. Lett.* 36 (15), 34. doi:10.1029/2009GL038295

Whitmore, P., and Knight, B. (2014). "Meteotsunami forecasting: sensitivities demonstrated by the 2008 Boothbay, Maine, event," in *Meteorological Tsunamis, U. S. The East Coast, and Other Coastal Regions*. Editors Vilibić, I., Monserrat, S., and Rabinovich, A. B. (Cham, Switzerland: Springer). doi:10.1007/978-3-319-12712-5_2

Williamson, A. L., Rim, D., Adams, L. M., LeVeque, R. J., Melgar, D., and González, F. I. (2020). A source clustering approach for efficient inundation modeling and regional scale probabilistic tsunami hazard assessment. *Front. Earth Sci.* 8, 442. doi:10.3389/feart.2020.591663

Woodruff, I., Kirby, J., Shi, F., and Grilli, S. (2018). Estimating meteo-tsunami occurrences for the US East coast. *Int. Conf. Coastal. Eng.* 1 (36) 66. doi:10.9753/icce.v36.currents.66

Yamao, S., Esteban, M., Yun, N. Y., Mikami, T., and Shibayama, T. (2015). "Estimation of the current risk to human damage life posed by future tsunamis in Japan," in *Handbook of coastal disaster mitigation for engineers and planners*. Editor Esteban, M. (Boston: Butterworth-Heinemann), 257–275.

Yamashita, K., Suppasri, A., Oishi, Y., and Imamura, F. (2018). Development of a tsunami inundation analysis model for urban areas using a porous body model. *Geosciences* 8 (1), 12. doi:10.3390/geosciences8010012

Yavari-Ramshe, S., and Ataie-Ashtiani, B. (2016). Numerical modeling of subaerial and submarine landslide-generated tsunami waves-recent advances and future challenges. *Landslides* 13 (6), 1325–1368. doi:10.1007/s10346-016-0734-2

Yokoyama, I. (1987). A scenario of the 1883 Krakatau tsunami. *J. Volcanol. Geothermal Res.* 34, 123–132. doi:10.1016/0377-0273(87)90097-7

Zechar, J. D., and Frankel, K. L. (2009). Incorporating and reporting uncertainties in fault slip rates. *J. Geophys. Res.* 114, 121. doi:10.1029/2009JB006325

Zengaffinen, T., Løvholt, F., Pedersen, G. K., and Harbitz, C. B. (2020). *Effects of rotational submarine slump dynamics on tsunami genesis: new insight from idealized models and the 1929 Grand Banks event Special publications*. London: Geological Society.

Conflict of Interest: HT was employed by AECOM.

The remaining authors declare that the research was conducted in the absence of any commercial or financial relationships that could be construed as a potential conflict of interest.

CONCLUDING REMARKS

The earthquake source in PTHA is generally modeled as a uniform slip distribution on a rectangular fault. However, PTHA has a remarkable dependency on the slip distribution. Therefore, different slip generation techniques have been proposed in the scientific literature. Nonetheless, there is still the need to understand how much these techniques may accurately represent the slip distribution of a real tsunamigenic earthquake. One way to test them is to compare tsunami models generated with synthetic slip distributions to tsunami observations, to quantify the uncertainty related to the tsunami source model.

In this study, we have used different slip generation techniques to generate synthetic tsunamis and tested them with observations of 15 events from open ocean DART sensors in the Pacific Ocean over the last two decades.

We have compared the tsunamis generated with slip models, obtained from the telesesimic finite fault inversion (Ye et al., 2016) with observed tsunamis for 10 of the same 15 earthquakes. It has been observed that the tsunamis generated by kinematic slip models, are in a quite poor agreement with the tsunami observations, possibly due to the simplified model and the fact that teleseismic data resolve better different features of the seismic source, rather than the slip position and amplitude which control the tsunami on the first order.

Starting from the magnitude and the location of this set of tsunamigenic earthquakes, we have then produced an ensemble of tsunami simulations from stochastic slip models using

different physical assumptions using an extended version of the Scala et al. (2020) model. Rupture areas are obtained with different aspect ratio and scaling laws and using these areas heterogeneous slip models are generated for both depth-dependent and depth-independent rigidity profiles. The positions and magnitudes of the events are free to vary around those of the real events. If the tsunami generation technique is accurate, the observed tsunamis should appear as one member of a statistically homogeneous population of synthetic tsunamis (Davies, 2019). The comparison of each model class, RECT-Murotani, RECT-Strasser, CIRL-Murotani and CIRL-Strasser, with observations reveals that the model scenarios have comparably good fit to the observed data. The model ensemble is also compared with each of the classes explored by Davies (2019). We observed that depth-independent Strasser models generate scenarios with better agreement to the observation than the models of Davies (2019). It is important to note that the number of scenarios used in this study is more than one order of magnitude smaller than that used by Davies (2019). Therefore, it can be argued that if Strasser model is used while creating an ensemble for PTHA, proper results can be obtained even with much smaller number of scenarios.

The bias of each model from ensemble is also tested. While the whole ensemble seems unbiased by passing null-hypothesis significance test, the separate examination of each model class reveals that our models show some biases. While Strasser models over-estimate the observations by generating larger tsunamis, Murotani models generally under-estimate the observations, at least for a depth-independent rigidity profile. However, Murotani models show the same tendency as Strasser models in the case of dept-dependent rigidity. Although models are biased, they feature reasonable kinematic properties in slip and size. The bias adjustment of each model can be done by using non-uniform weights to scenarios. One of the

first possible future developments of the study is adjusting model biases and repeat the coverage statistics analysis.

It has been observed that shallow slip amplification often occurs during tsunamigenic earthquakes and it should be incorporated into tsunami hazard analysis. However, the comparison of scenario fit shows that depth-dependent and depth-independent models provide similar results, so there is not a significant improvement with a depth-dependent model. It must be considered though that we are using data mostly in the far-field of the tsunami source, and that the presence of shallow slip may be highly variable depending on the specific event. Moreover, scenarios with depth-dependent rigidity show a tendency to generate larger tsunamis which cause an over-estimation of the observations. Calibrating rigidity and coupling profiles that are used to enhance shallow slip may adjust this bias and this calibration can be another step to expand this study. Moreover, keeping the rigidity constant and considering a variation of stress drop, or a combination of rigidity and stress drop variation with depth (e.g. Bilek and Lay, 1999) can be applied for the generation of depth-dependent models.

The method, which is implemented for the generation of stochastic slip models in this study, is already used in the computation of a probabilistic tsunami hazard map for the North-East Atlantic, Mediterranean and connected seas (NEAM) region (Basili et al., 2021). This study is the first attempt to test this technique against the real observations since there is a lack of tsunami records in the NEAM region. It has been observed that depth-dependent slip models generally produce larger tsunamis relative to observations. This behavior may also cause over estimation of hazard. Therefore, after the correction of all biases on stochastic slip models

depending on the observations in Pacific, hazard estimations in NEAM region may also be calibrated accordingly.

REFERENCES

Aki, K. (1967). Scaling law of seismic spectrum. *Journal of Geophysical Research*, *72*(4), 1217–1231.

Anderson, J. G. (1997). Seismic energy and stress-drop parameters for a composite source model. *Bulletin of the Seismological Society of America*, *87*(1), 85–96.

Andrews, D. J. (1980). A stochastic fault model: 1. Static case. *Journal of Geophysical Research: Solid Earth*, *85*(B7), 3867–3877.

Andrews, D. J. (1981). A stochastic fault model: 2. Time-dependent case. *Journal of Geophysical Research: Solid Earth*, *86*(B11), 10821–10834.

Aniko Wirp, S., Gabriel, A. A., Schmeller, M., H. Madden, E., van Zelst, I., Krenz, L., van Dinther, Y., & Rannabauer, L. (2021). 3D Linked Subduction, Dynamic Rupture, Tsunami, and Inundation Modeling: Dynamic Effects of Supershear and Tsunami Earthquakes, Hypocenter Location, and Shallow Fault Slip. *Frontiers in Earth Science*, *9*(June). https://doi.org/10.3389/feart.2021.626844

Argyroudis, S. A., Fotopoulou, S., Karafagka, S., Pitilakis, K., Selva, J., Salzano, E., Basco, A., Crowley, H., Rodrigues, D., & Matos, J. P. (2020). A risk-based multi-level stress test methodology: application to six critical non-nuclear infrastructures in Europe. *Natural Hazards*, *100*(2), 595–633.

Basili, R., Brizuela, B., Herrero, A., Iqbal, S., Lorito, S., Maesano, F. E., Murphy, S., Perfetti, P., Romano, F., Scala, A., Selva, J., Taroni, M., Tiberti, M. M., Thio, H. K., Tonini, R., Volpe, M., Glimsdal, S., Harbitz, C. B., Løvholt, F., … Zaytsev, A. (2021). The Making of the NEAM Tsunami Hazard Model 2018 (NEAMTHM18). *Frontiers in Earth Science*, *8*(March), 1–29. https://doi.org/10.3389/feart.2020.616594

Behrens, J., & Dias, F. (2015). New computational methods in tsunami science. *Philosophical Transactions of the Royal Society A: Mathematical, Physical and Engineering Sciences*, *373*(2053). https://doi.org/10.1098/rsta.2014.0382

Behrens, Jörn. (2006). Data Structures for Computational Efficiency. In *Adaptive Atmospheric Modeling* (pp. 49–69). Springer.

Behrens, Jörn, Løvholt, F., Jalayer, F., Lorito, S., Salgado-Gálvez, M. A., Sørensen, M., Abadie, S., Aguirre-Ayerbe, I., Aniel-Quiroga, I., & Babeyko, A. (2021). Probabilistic Tsunami Hazard and Risk Analysis: A Review of Research Gaps. *Frontiers in Earth Science*, *9*, 114.

Begét, J. E. (2000). Volcanic Tsunamis. In H. Sigurdsson, et al. (Eds.), Encyplopedia of volcanoes (pp. 1005–1013). London, UK: Academic Press.

Beresenev, I., & Atkinson, G. M. (1997). Modeling finite fault radiation from wn spectrum. *Bull. Seismol. Soc. Am*, *87*, 67–84.

Berger, M. J., George, D. L., LeVeque, R. J., & Mandli, K. T. (2011). The GeoClaw software for depth-averaged flows with adaptive refinement. *Advances in Water Resources*, *34*(9), 1195–1206.

Bilek, S. L., Lay, T., & Ruff, L. J. (2004). Radiated seismic energy and earthquake source duration variations from teleseismic source time functions for shallow subduction zone thrust earthquakes. *Journal of Geophysical Research: Solid Earth*, *109*(9), 1–14. https://doi.org/10.1029/2004JB003039

Bilek, Susan L, & Lay, T. (2002). Tsunami earthquakes possibly widespread manifestations of frictional conditional stability. *Geophysical Research Letters*, *29*(14), 11–18.

Bilek, Susan L., & Lay, T. (1999). Rigidity variations with depth along interplate megathrust

faults in subduction zones. *Nature*, *400*(6743), 443–446. https://doi.org/10.1038/22739
Boatwright, J. (1982). A dynamic model for far-field acceleration. *Bulletin of the Seismological Society of America*, *72*(4), 1049–1068.
Boatwright, J. (1988). The seismic radiation from composite models of faulting. *Bulletin of the Seismological Society of America*, *78*(2), 489–508.
Bonev, B., Hesthaven, J. S., Giraldo, F. X., & Kopera, M. A. (2018). Discontinuous Galerkin scheme for the spherical shallow water equations with applications to tsunami modeling and prediction. *Journal of Computational Physics*, *362*, 425–448.
Brace, W. F., & Byerlee, J. D. (1966). Stick-slip as a mechanism for earthquakes. *Science*, *153*(3739), 990–992.
Briggs, M. J., Synolakis, C. E., Harkins, G. S., & Green, D. R. (1995). Laboratory experiments of tsunami runup on a circular island. *Pure and Applied Geophysics*, *144*(3), 569–593.
Brune, J. N. (1970). Tectonic stress and the spectra of seismic shear waves from earthquakes. *Journal of Geophysical Research*, *75*(26), 4997–5009.
Burgmann, R., Ayhan, M. E., Fielding, E. J., Wright, T. J., McClusky, S., Aktug, B., Demir, C., Lenk, O., & Turkezer, A. (2002). Deformation during the 12 November 1999 Duzce, Turkey, earthquake, from GPS and InSAR data. *Bulletin of the Seismological Society of America*, *92*(1), 161–171.
Butler, R., Walsh, D., & Richards, K. (2017). Extreme tsunami inundation in Hawai‘i from Aleutian–Alaska subduction zone earthquakes. *Natural Hazards*, *85*(3), 1591–1619. https://doi.org/10.1007/s11069-016-2650-0
Comninou, M., 1973. Angular dislocation in a half space. Ph.D. Dissertation, Northwestern University, Evanston, Ill, 45pp.
Carrier, G. F. (1966). Gravity waves on water of variable depth. *Journal of Fluid Mechanics*, *24*(4), 641–659.
Castro, M. J., Ortega, S., De la Asuncion, M., Mantas, J. M., & Gallardo, J. M. (2011). GPU computing for shallow water flow simulation based on finite volume schemes. *Comptes Rendus Mécanique*, *339*(2–3), 165–184.
Chock, G. (2015). The ASCE 7 tsunami loads and effects design standard for the United States. In *Handbook of coastal disaster mitigation for engineers and planners* (pp. 437–460). Elsevier.
Choi, B. H., Pelinovsky, E., Kim, K. O., & Lee, J. S. (2003). Simulation of the trans-oceanic tsunami propagation due to the 1883 Krakatau volcanic eruption. *Natural Hazards and Earth System Sciences*, *3*(5), 321–332.
Cross III, R. H. (1967). Tsunami surge forces. *Journal of the Waterways and Harbors Division*, *93*(4), 201–231.
Davies, G. (2019). Tsunami variability from uncalibrated stochastic earthquake models: Tests against deep ocean observations 2006-2016. *Geophysical Journal International*, *218*(3), 1939–1960. https://doi.org/10.1093/gji/ggz260
Davies, G., Horspool, N., & Miller, V. (2015). Tsunami inundation from heterogeneous earthquake slip distributions: Evaluation of synthetic source models. *Journal of Geophysical Research: Solid Earth*, *120*(9), 6431–6451. https://doi.org/10.1002/2015JB012272
Dawson, C., & Mirabito, C. M. (2008). The shallow water equations. *University of Texas, Austin*, *29*.
Day, S. J. (2015). Volcanic Tsunamis. In H. Sigurdsson, et al. (Eds.), Encyplopedia of volcanoes (2nd ed., pp. 993–1009). London, UK: Academic Press.

de la Asunción, M., Castro, M. J., Fernández-Nieto, E. D., Mantas, J. M., Acosta, S. O., & González-Vida, J. M. (2013). Efficient GPU implementation of a two waves TVD-WAF method for the two-dimensional one layer shallow water system on structured meshes. *Computers & Fluids*, *80*, 441–452.

De La Asunción, M., Mantas, J. M., & Castro, M. J. (2011). Simulation of one-layer shallow water systems on multicore and CUDA architectures. *The Journal of Supercomputing*, *58*(2), 206–214.

Ekström, G., Nettles, M., & Dziewoński, A. M. (2012). The global CMT project 2004–2010: Centroid-moment tensors for 13,017 earthquakes. *Physics of the Earth and Planetary Interiors*, *200*, 1–9.

Eshelby, J. D. (1957). The determination of the elastic field of an ellipsoidal inclusion, and related problems. *Proceedings of the Royal Society of London. Series A. Mathematical and Physical Sciences*, *241*(1226), 376–396.

Festa, G., & Zollo, A. (2012). From data to source parameters: kinematic modeling. *The Mechanics of Faulting: From Laboratory to Real Earthquakes*, *37*, 66.

Frankel, A. (1991). High-frequency spectral falloff of earthquakes, fractal dimension of complex rupture, b value, and the scaling of strength on faults. *Journal of Geophysical Research: Solid Earth*, *96*(B4), 6291–6302.

Frankel, A. (1995). Simulating strong motions of large earthquakes using recordings of small earthquakes: the Loma Prieta mainshock as a test case. *Bulletin of the Seismological Society of America*, *85*(4), 1144–1160.

Fritz, H. M., Hager, W. H., & Minor, H.-E. (2001). Lituya Bay case: rockslide impact and wave run-up. *Science of Tsunami Hazards*, *19*(1), 3–22.

Fritz, H. M., Hager, W. H., & Minor, H.-E. (2004). Near field characteristics of landslide generated impulse waves. *Journal of Waterway, Port, Coastal, and Ocean Engineering*, *130*(6), 287–302.

Galvez, P., Ampuero, J.-P., Dalguer, L. A., Somala, S. N., & Nissen-Meyer, T. (2014). Dynamic earthquake rupture modelled with an unstructured 3-D spectral element method applied to the 2011 M 9 Tohoku earthquake. *Geophysical Journal International*, *198*(2), 1222–1240.

Geist, E. L. (2002). Complex earthquake rupture and local tsunamis. *Journal of Geophysical Research*, *107*(B5). https://doi.org/10.1029/2000jb000139

Geist, E. L., & Bilek, S. L. (2001). Effect of depth-dependent shear modulus on tsunami generation along subduction zones. *Geophysical Research Letters*, *28*(7), 1315–1318. https://doi.org/10.1029/2000GL012385

Geist, E. L., & Dmowska, R. (1999). Local tsunamis and distributed slip at the source. In *Seismogenic and tsunamigenic processes in shallow subduction zones* (pp. 485–512). Springer.

Geist, E. L., & Lynett, P. J. (2014). Source processes for the probabilistic assessment of tsunami hazards. *Oceanography*, *27*(2), 86–93.

Geist, E. L., & Parsons, T. (2006). Probabilistic analysis of tsunami hazards. *Natural Hazards*, *37*(3), 277–314. https://doi.org/10.1007/s11069-005-4646-z

Gibbons, S. J., Lorito, S., Macías, J., Løvholt, F., Selva, J., Volpe, M., Sánchez-Linares, C., Babeyko, A., Brizuela, B., Cirella, A., Castro, M. J., de la Asunción, M., Lanucara, P., Glimsdal, S., Lorenzino, M. C., Nazaria, M., Pizzimenti, L., Romano, F., Scala, A., … Vöge, M. (2020). Probabilistic Tsunami Hazard Analysis: High Performance Computing for Massive Scale Inundation Simulations. *Frontiers in Earth Science*, *8*(December), 1–20.

https://doi.org/10.3389/feart.2020.591549
Gica, E., Teng, M. H., Liu, P. L.-F., Titov, V., & Zhou, H. (2007). Sensitivity analysis of source parameters for earthquake-generated distant tsunamis. *Journal of Waterway, Port, Coastal, and Ocean Engineering*, *133*(6), 429–441.
Giles, D., Gopinathan, D., Guillas, S., & Dias, F. (2021). Faster Than Real Time Tsunami Warning with Associated Hazard Uncertainties. *Frontiers in Earth Science*, *8*(January), 1–16. https://doi.org/10.3389/feart.2020.597865
Goda, K., Mai, P. M., Yasuda, T., & Mori, N. (2014). Sensitivity of tsunami wave profiles and inundation simulations to earthquake slip and fault geometry for the 2011 Tohoku earthquake. *Earth, Planets and Space*, *66*(1), 1–20. https://doi.org/10.1186/1880-5981-66-105
González, F I, Geist, E. L., Jaffe, B., Kânoğlu, U., Mofjeld, H., Synolakis, C. E., Titov, V. V, Arcas, D., Bellomo, D., & Carlton, D. (2009). Probabilistic tsunami hazard assessment at seaside, Oregon, for near-and far-field seismic sources. *Journal of Geophysical Research: Oceans*, *114*(C11).
González, Frank I, Satake, K., Boss, E. F., & Mofjeld, H. O. (1995). Edge wave and non-trapped modes of the 25 April 1992 Cape Mendocino tsunami. In *Tsunamis: 1992–1994* (pp. 409–426). Springer.
Grezio, A., Babeyko, A., Baptista, M. A., Behrens, J., Costa, A., Davies, G., Geist, E. L., Glimsdal, S., González, F. I., Griffin, J., Harbitz, C. B., LeVeque, R. J., Lorito, S., Løvholt, F., Omira, R., Mueller, C., Paris, R., Parsons, T., Polet, J., … Thio, H. K. (2017). Probabilistic Tsunami Hazard Analysis: Multiple Sources and Global Applications. *Reviews of Geophysics*, *55*(4), 1158–1198. https://doi.org/10.1002/2017RG000579
Hammack, J. L. (1973). A note on tsunamis: their generation and propagation in an ocean of uniform depth. *Journal of Fluid Mechanics*, *60*(4), 769–799.
Harbitz, C. B., Glimsdal, S., Bazin, S., Zamora, N., Løvholt, F., Bungum, H., Smebye, H., Gauer, P., & Kjekstad, O. (2012). Tsunami hazard in the Caribbean: Regional exposure derived from credible worst case scenarios. *Continental Shelf Research*, *38*, 1–23.
Harbitz, C. B., Glimsdal, S., Løvholt, F., Kveldsvik, V., Pedersen, G. K., & Jensen, A. (2014). Rockslide tsunamis in complex fjords: from an unstable rock slope at Åkerneset to tsunami risk in western Norway. *Coastal Engineering*, *88*, 101–122.
Hartzell, S. H. (1978). Earthquake aftershocks as Green's functions. *Geophysical Research Letters*, *5*(1), 1–4.
Hayashi, Y. (2010). Empirical relationship of tsunami height between offshore and coastal stations. *Earth, Planets and Space*, *62*(3), 269–275.
Hayes, G. P. (2011). Rapid source characterization of the 2011 Mw 9.0 off the pacific coast of tohoku earthquake. *Earth, Planets and Space*, *63*(7), 529–534. https://doi.org/10.5047/eps.2011.05.012
Hayes, G. P., Moore, G. L., Portner, D. E., Hearne, M., Flamme, H., Furtney, M., & Smoczyk, G. M. (2018). Zone Geometry Model. *Science*, *362*(6410), 58–61.
Hu, Y., & Wang, K. (2008). Coseismic strengthening of the shallow portion of the subduction fault and its effects on wedge taper. *Journal of Geophysical Research: Solid Earth*, *113*(B12).
Hyndman, R. D., Yamano, M., & Oleskevich, D. A. (1997). The seismogenic zone of subduction thrust faults. *Island Arc*, *6*(3), 244–260.
Imamura, F. Tsunami Numerical Simulation with the Staggered Leap-frog Scheme (Numerical Code of TUNAMI-N1 and N2); Disaster Control Res. Center Tohoku Univ.: Miyagi, Japan,

1989.
Imamura, F. (1996). Review of tsunami simulation with a finite difference method. *Long-Wave Runup Models*, 25–42.
Imamura, Fumihiko, Yalçiner, A. C., & Ozyurt, G. (2006). Tsunami modelling manual. *Tsunami Modelling Manual*, *April*, 58.
Irikura, K., & Kamae, K. (1994). *Estimation of strong ground motion in broad-frequency band based on a seismic source scaling model and an empirical Green's function technique*.
Jeyakumaran, M., Rudnicki, J. W., & Keer, L. M. (1992). Modeling slip zones with triangular dislocation elements. *Bulletin of the Seismological Society of America*, *82*(5), 2153–2169.
Kajiura, K. (1963). The leading wave of a tsunami. *Bulletin of the Earthquake Research Institute, University of Tokyo*, *41*(3), 535–571.
Kalligeris, N., Skanavis, V., Charalampakis, M., Melis, N. S., Voukouvalas, E., Annunziato, A., & Synolakis, C. E. (2021). Field survey of the 30 October 2020 Samos (Aegean Sea) tsunami in the Greek islands. *Bulletin of Earthquake Engineering*, 1–33.
Kanamori, H. (1977). The energy release in great earthquakes. *Journal of Geophysical Research*, *82*(20), 2981–2987.
Kanamori, H., & Anderson, D. L. (1975). Theoretical basis of some empirical relations in seismology. *Bulletin of the Seismological Society of America*, *65*(5), 1073–1095.
Kanamori, H., & Kikuchi, M. (1993). The 1992 Nicaragua earthquake: a slow tsunami earthquake associated with subducted sediments. *Nature*, *361*(6414), 714–716.
Kienle, J., Kowalik, Z., & Murty, T. S. (1987). Tsunamis generated by eruptions from Mount St. Augustine volcano, Alaska. *Science*, *236*(4807), 1442–1447.
Larsen, B. E., & Fuhrman, D. R. (2019). Full-scale CFD simulation of tsunamis. Part 1: Model validation and run-up. *Coastal Engineering*, *151*, 22–41.
Latter, J. H. (1981). Tsunamis of volcanic origin: summary of causes, with particular reference to Krakatoa, 1883. *Bulletin Volcanologique*, *44*(3), 467–490.
Lauterjung, J., Münch, U., & Rudloff, A. (2010). The challenge of installing a tsunami early warning system in the vicinity of the Sunda Arc, Indonesia. *Natural Hazards and Earth System Sciences*, *10*(4), 641–646.
Lay, T. (2018). A review of the rupture characteristics of the 2011 Tohoku-oki Mw 9.1 earthquake. *Tectonophysics*, *733*(July 2017), 4–36. https://doi.org/10.1016/j.tecto.2017.09.022
Lay, T., & Bilek, S. (2007). 15. Anomalous Earthquake Ruptures at Shallow Depths on Subduction Zone Megathrusts. In *The seismogenic zone of subduction thrust faults* (pp. 476–511). Columbia University Press.
Lay, T., Kanamori, H., Ammon, C. J., Koper, K. D., Hutko, A. R., Ye, L., Yue, H., & Rushing, T. M. (2012). Depth-varying rupture properties of subduction zone megathrust faults. *Journal of Geophysical Research: Solid Earth*, *117*(4). https://doi.org/10.1029/2011JB009133
Lay, T., & Wallace, T. C. (1995). *Modern global seismology*. Elsevier.
Le Gal, M., Violeau, D., & Benoit, M. (2017). Influence of timescales on the generation of seismic tsunamis. *European Journal of Mechanics-B/Fluids*, *65*, 257–273.
Le Méhauté, B., & Wang, S. (1996). *Water waves generated by underwater explosion* (Vol. 10). World Scientific.
Lee, S. J., Huang, B. S., Ando, M., Chiu, H. C., & Wang, J. H. (2011). Evidence of large scale repeating slip during the 2011 Tohoku-Oki earthquake. *Geophysical Research Letters*, *38*(19), 1–6. https://doi.org/10.1029/2011GL049580

LeVeque, R. J. (2002). *Finite volume methods for hyperbolic problems* (Vol. 31). Cambridge university press.

LeVeque, R. J., Waagan, K., González, F. I., Rim, D., & Lin, G. (2016). Generating random earthquake events for probabilistic tsunami hazard assessment. In *Global Tsunami Science: Past and Future, Volume I* (pp. 3671–3692). Springer.

Levin, B. W., & Nosov, M. (2009). *Physics of tsunamis* (Vol. 2016). Springer.

Li, L., Switzer, A. D., Chan, C., Wang, Y., Weiss, R., & Qiu, Q. (2016). How heterogeneous coseismic slip affects regional probabilistic tsunami hazard assessment: A case study in the South China Sea. *Journal of Geophysical Research: Solid Earth*, *121*(8), 6250–6272.

Liu, P. L.-F., Cho, Y.-S., Briggs, M. J., Kanoglu, U., & Synolakis, C. E. (1995). Runup of solitary waves on a circular island. *Journal of Fluid Mechanics*, *302*, 259–285.

Lorito, S., Piatanesi, A., Cannelli, V., Romano, F., & Melini, D. (2010). Kinematics and source zone properties of the 2004 Sumatra-Andaman earthquake and tsunami: Nonlinear joint inversion of tide gauge, satellite altimetry, and GPS data. *Journal of Geophysical Research*, *115*(B2), 1–20. https://doi.org/10.1029/2008jb005974

Lorito, S, Selva, J., Basili, R., Romano, F., Tiberti, M. M., & Piatanesi, A. (2015). Probabilistic hazard for seismically induced tsunamis: accuracy and feasibility of inundation maps. *Geophysical Journal International*, *200*(1), 574–588.

Lorito, Stefano, Piatanesi, A., & Lomax, A. (2008). Rupture process of the 18 April 1906 California earthquake from near-field tsunami waveform inversion. *Bulletin of the Seismological Society of America*, *98*(2), 832–845. https://doi.org/10.1785/0120060412

Lotto, G. C., Dunham, E. M., Jeppson, T. N., & Tobin, H. J. (2017). The effect of compliant prisms on subduction zone earthquakes and tsunamis. *Earth and Planetary Science Letters*, *458*, 213–222. https://doi.org/10.1016/j.epsl.2016.10.050

Løvholt, F., Bungum, H., Harbitz, C. B., Glimsdal, S., Lindholm, C. D., & Pedersen, G. (2006). Earthquake related tsunami hazard along the western coast of Thailand. *Natural Hazards and Earth System Science*, *6*(6), 979–997. https://doi.org/10.5194/nhess-6-979-2006

Løvholt, Finn, Glimsdal, S., Harbitz, C. B., Zamora, N., Nadim, F., Peduzzi, P., Dao, H., & Smebye, H. (2012). Tsunami hazard and exposure on the global scale. *Earth-Science Reviews*, *110*(1–4), 58–73.

Løvholt, Finn, Lorito, S., Macĺas, J., Volpe, M., Selva, J., & Gibbons, S. (2019). Urgent tsunami computing. *Proceedings of UrgentHPC 2019: 1st International Workshop on HPC for Urgent Decision Making - Held in Conjunction with SC 2019: The International Conference for High Performance Computing, Networking, Storage and Analysis*, 45–50. https://doi.org/10.1109/UrgentHPC49580.2019.00011

Løvholt, FJMR, Griffin, J., & Salgado-Gálvez, M. A. (2022). Tsunami hazard and risk assessment on the global scale. *Complexity in Tsunamis, Volcanoes, and Their Hazards*, 213–246.

Lynett, P. J. (2006). Nearshore wave modeling with high-order Boussinesq-type equations. *Journal of Waterway, Port, Coastal, and Ocean Engineering*, *132*(5), 348–357.

Lynett, P. J. (2011). Tsunami Inundation, Modeling of. *Extreme Environmental Events*, 1008–1021. https://doi.org/10.1007/978-1-4419-7695-6_53

Lynett, P. J., Gately, K., Wilson, R., Montoya, L., Arcas, D., Aytore, B., Bai, Y., Bricker, J. D., Castro, M. J., & Cheung, K. F. (2017). Inter-model analysis of tsunami-induced coastal currents. *Ocean Modelling*, *114*, 14–32.

Ma, S., & Beroza, G. C. (2008). Rupture dynamics on a bimaterial interface for dipping faults.

Bulletin of the Seismological Society of America, *98*(4), 1642–1658.
Ma, S., & Nie, S. (2019). Dynamic wedge failure and along-arc variations of tsunamigenesis in the Japan trench margin. *Geophysical Research Letters*, *46*(15), 8782–8790.
Macías, J., Castro, M. J., & Escalante, C. (2020). Performance assessment of the Tsunami-HySEA model for NTHMP tsunami currents benchmarking. Laboratory data. *Coastal Engineering*, *158*(July 2018), 103667. https://doi.org/10.1016/j.coastaleng.2020.103667
Macías, J., Castro, M. J., Ortega, S., Escalante, C., & González-Vida, J. M. (2017). Performance Benchmarking of Tsunami-HySEA Model for NTHMP's Inundation Mapping Activities. *Pure and Applied Geophysics*, *174*(8), 3147–3183. https://doi.org/10.1007/s00024-017-1583-1
Macías, J., Castro, M. J., Ortega, S., Sánchez, C. E., & González-Vida, J. M. (2016). *NTHMP benchmarking of Tsunami-HySEA model for propagation and inundation. The 2011 NTHMP model benchmarking workshop*. *November*, 46. https://doi.org/10.13140/RG.2.2.35077.76001
Madsen, P. A., & Sørensen, O. R. (1992). A new form of the Boussinesq equations with improved linear dispersion characteristics. Part 2. A slowly-varying bathymetry. *Coastal Engineering*, *18*(3–4), 183–204.
Maeno, F., & Imamura, F. (2011). Tsunami generation by a rapid entrance of pyroclastic flow into the sea during the 1883 Krakatau eruption, Indonesia. *Journal of Geophysical Research: Solid Earth*, *116*(B9).
Mai, P. M. (2004). SRCMOD - Database of finite-source rupture models. Annual Meeting of the Southern California Earthquake Center (SCEC), 19–23 September, 2004, Palm Springs, California (abstract).
Mai, P. M. (2007). SRCMOD - Database of finite-source rupture models. Available online at: http://www.seismo.ethz.ch/srcmod/
Marras, S, Kopera, M. A., & Giraldo, F. X. (2015). Simulation of shallow-water jets with a unified element-based continuous/discontinuous Galerkin model with grid flexibility on the sphere. *Quarterly Journal of the Royal Meteorological Society*, *141*(690), 1727–1739.
Marras, Simone, Kopera, M. A., Constantinescu, E. M., Suckale, J., & Giraldo, F. X. (2018). A residual-based shock capturing scheme for the continuous/discontinuous spectral element solution of the 2d shallow water equations. *Advances in Water Resources*, *114*, 45–63.
Marras, Simone, & Mandli, K. T. (2021). Modeling and simulation of tsunami impact: A short review of recent advances and future challenges. *Geosciences (Switzerland)*, *11*(1), 1–19. https://doi.org/10.3390/geosciences11010005
Masson, D. G., Harbitz, C. B., Wynn, R. B., Pedersen, G., & Løvholt, F. (2006). Submarine landslides: processes, triggers and hazard prediction. *Philosophical Transactions of the Royal Society A: Mathematical, Physical and Engineering Sciences*, *364*(1845), 2009–2039.
McCloskey, J., Antonioli, A., Piatanesi, A., Sieh, K., Steacy, S., Nalbant, S., Cocco, M., Giunchi, C., Huang, J., & Dunlop, P. (2008). Tsunami threat in the Indian Ocean from a future megathrust earthquake west of Sumatra. *Earth and Planetary Science Letters*, *265*(1–2), 61–81.
McCloskey, J., Antonioli, A., Piatanesi, A., Sieh, K., Steacy, S., Nalbant, S. S., Cocco, M., Giunchi, C., Huang, J. D., & Dunlop, P. (2007). Near-field propagation of tsunamis from megathrust earthquakes. *Geophysical Research Letters*, *34*(14).

McGuire, J. J., & Segall, P. (2003). Imaging of aseismic fault slip transients recorded by dense geodetic networks. *Geophysical Journal International*, *155*(3), 778–788.

Meade, B. J. (2007). Algorithms for the calculation of exact displacements, strains, and stresses for triangular dislocation elements in a uniform elastic half space. *Computers and Geosciences*, *33*(8), 1064–1075. https://doi.org/10.1016/j.cageo.2006.12.003

Mohammed, F., & Fritz, H. M. (2012). Physical modeling of tsunamis generated by three-dimensional deformable granular landslides. *Journal of Geophysical Research: Oceans*, *117*(C11).

Moore, J. C., & Saffer, D. (2001). Updip limit of the seismogenic zone beneath the accretionary prism of southwest Japan: An effect of diagenetic to low-grade metamorphic processes and increasing effective stress. *Geology*, *29*(2), 183–186.

Mori, N., Mai, P. M., Goda, K., & Yasuda, T. (2017). Tsunami inundation variability from stochastic rupture scenarios: Application to multiple inversions of the 2011 Tohoku, Japan earthquake. *Coastal Engineering*, *127*, 88–105.

Mori, N., Takahashi, T., Yasuda, T., & Yanagisawa, H. (2011). Survey of 2011 Tohoku earthquake tsunami inundation and run-up. *Geophysical Research Letters*, *38*(7).

Mueller, C., Power, W., Fraser, S., & Wang, X. (2015). Effects of rupture complexity on local tsunami inundation: Implications for probabilistic tsunami hazard assessment by example. *Journal of Geophysical Research: Solid Earth*, *120*(1), 488–502.

Murotani, S., Satake, K., & Fujii, Y. (2013). Scaling relations of seismic moment, rupture area, average slip, and asperity size for M~9 subduction-zone earthquakes. *Geophysical Research Letters*, *40*(19), 5070–5074. https://doi.org/10.1002/grl.50976

Murphy, S., Di Toro, G., Romano, F., Scala, A., Lorito, S., Spagnuolo, E., Aretusini, S., Festa, G., Piatanesi, A., & Nielsen, S. (2018). Tsunamigenic earthquake simulations using experimentally derived friction laws. *Earth and Planetary Science Letters*, *486*, 155–165. https://doi.org/10.1016/j.epsl.2018.01.011

Murphy, S., Scala, A., Herrero, A., Lorito, S., Festa, G., Trasatti, E., Tonini, R., Romano, F., Molinari, I., & Nielsen, S. (2016). Shallow slip amplification and enhanced tsunami hazard unravelled by dynamic simulations of mega-thrust earthquakes. *Scientific Reports*, *6*(September), 1–12. https://doi.org/10.1038/srep35007

Nielsen, S. B. (1998). Free surface effects on the propagation of dynamic rupture. *Geophysical Research Letters*, *25*(1), 125–128.

Nomanbhoy, N., & Satake, K. (1995). Generation mechanism of tsunamis from the 1883 Krakatau eruption. *Geophysical Research Letters*, *22*(4), 509–512.

Nosov, M. A., & Kolesov, S. V. (2011). Optimal initial conditions for simulation of seismotectonic Tsunamis. *Pure and Applied Geophysics*, *168*(6–7), 1223–1237. https://doi.org/10.1007/s00024-010-0226-6

Oden, J. T. (2008). *A short-course on nonlinear continuum mechanics*. CAM.

Okada, Y. (1992). Internal deformation due to shear and tensile faults in a half-space. *Bulletin - Seismological Society of America*, *82*(2), 1018–1040. https://doi.org/10.1785/bssa0820021018

Okada, Yoshimitsu. (1985). Surface deformation due to shear and tensile faults in a half-space. *Bulletin of the Seismological Society of America*, *75*(4), 1135–1154.

Okal, E. A., & Synolakis, C. E. (2008). Far-field tsunami hazard from mega-thrust earthquakes in the Indian Ocean. *Geophysical Journal International*, *172*(3), 995–1015.

Omira, R., Baptista, M. A., Leone, F., Matias, L., Mellas, S., Zourarah, B., Miranda, J. M., Carrilho, F., & Cherel, J.-P. (2013). Performance of coastal sea-defense infrastructure at

El Jadida (Morocco) against tsunami threat: lessons learned from the Japanese 11 March 2011 tsunami. *Natural Hazards and Earth System Sciences*, *13*(7), 1779–1794.

Panton, R. L. (2013). *Incompressible flow*. John Wiley & Sons.

Papageorgiou, A. S., & Aki, K. (1983). A specific barrier model for the quantitative description of inhomogeneous faulting and the prediction of strong ground motion. I. Description of the model. *Bulletin of the Seismological Society of America*, *73*(3), 693–722.

Paris, R. (2015). Source mechanisms of volcanic tsunamis. *Philosophical Transactions of the Royal Society A: Mathematical, Physical and Engineering Sciences*, *373*(2053), 20140380.

Pattiaratchi, C. B., & Wijeratne, E. M. S. (2015). Are meteotsunamis an underrated hazard? *Philosophical Transactions of the Royal Society A: Mathematical, Physical and Engineering Sciences*, *373*(2053), 20140377.

Plesch, A., Shaw, J. H., & Group, S. C. W. (2003). SCEC CFM-a WWW accessible community fault model for Southern California. *AGU Fall Meeting Abstracts*, *2003*, S12B-0395.

Polet, J., & Kanamori, H. (2022). Tsunami earthquakes. *Complexity in Tsunamis, Volcanoes, and Their Hazards*, 3–23.

Romano, F., Piatanesi, A., Lorito, S., D'Agostino, N., Hirata, K., Atzori, S., Yamazaki, Y., & Cocco, M. (2012). Clues from joint inversion of tsunami and geodetic data of the 2011 Tohoku-oki earthquake. *Scientific Reports*, *2*, 1–8. https://doi.org/10.1038/srep00385

Romano, F., Trasatti, E., Lorito, S., Piromallo, C., Piatanesi, A., Ito, Y., Zhao, D., Hirata, K., Lanucara, P., & Cocco, M. (2014). Structural control on the Tohoku earthquake rupture process investigated by 3D FEM, tsunami and geodetic data. *Scientific Reports*, *4*, 1–11. https://doi.org/10.1038/srep05631

Rubin, A. M., & Ampuero, J. (2007). Aftershock asymmetry on a bimaterial interface. *Journal of Geophysical Research: Solid Earth*, *112*(B5).

Ruiz, J. A., Baumont, D., Bernard, P., & Berge-Thierry, C. (2011). Modelling directivity of strong ground motion with a fractal, k-2, kinematic source model. *Geophysical Journal International*, *186*(1), 226–244. https://doi.org/10.1111/j.1365-246X.2011.05000.x

Saito, T. (2019). *Tsunami generation and propagation*. Springer.

Saito, T., Baba, T., Inazu, D., Takemura, S., & Fukuyama, E. (2019). Synthesizing sea surface height change including seismic waves and tsunami using a dynamic rupture scenario of anticipated Nankai trough earthquakes. *Tectonophysics*, *769*, 228166.

Saito, T., Ito, Y., Inazu, D., & Hino, R. (2011). Tsunami source of the 2011 Tohoku-Oki earthquake, Japan: Inversion analysis based on dispersive tsunami simulations. *Geophysical Research Letters*, *38*(7).

Satake, K., Fujii, Y., Harada, T., & Namegaya, Y. (2013). Time and space distribution of coseismic slip of the 2011 Tohoku earthquake as inferred from tsunami waveform data. *Bulletin of the Seismological Society of America*, *103*(2B), 1473–1492.

Savage, J. C., & Burford, R. O. (1973). Geodetic determination of relative plate motion in central California. *Journal of Geophysical Research*, *78*(5), 832–845.

Scala, A., Lorito, S., Romano, F., Murphy, S., Selva, J., Basili, R., Babeyko, A., Herrero, A., Hoechner, A., Løvholt, F., Maesano, F. E., Perfetti, P., Tiberti, M. M., Tonini, R., Volpe, M., Davies, G., Festa, G., Power, W., Piatanesi, A., & Cirella, A. (2020). Effect of Shallow Slip Amplification Uncertainty on Probabilistic Tsunami Hazard Analysis in Subduction Zones: Use of Long-Term Balanced Stochastic Slip Models. *Pure and Applied Geophysics*, *177*(3), 1497–1520. https://doi.org/10.1007/s00024-019-02260-x

Scala, Antonio, Festa, G., & Vilotte, J. P. (2017). Rupture dynamics along biomaterial

interfaces: A parametric study of the shear-normal traction coupling. *Geophysical Journal International*, *209*(1), 48–67. https://doi.org/10.1093/gji/ggw489

Scholz, C. H. (1998). Earthquakes and friction laws. *Nature*, *391*(6662), 37–42. https://doi.org/10.1038/34097

Segur, H., & Yamamoto, H. (2009). *The Shallow-Water Equations*.

Selva, J., Tonini, R., Molinari, I., Tiberti, M. M., Romano, F., Grezio, A., Melini, D., Piatanesi, A., Basili, R., & Lorito, S. (2016). Quantification of source uncertainties in Seismic Probabilistic Tsunami Hazard Analysis (SPTHA). *Geophysical Journal International*, *205*(3), 1780–1803. https://doi.org/10.1093/gji/ggw107

Selva, Jacopo, Lorito, S., Perfetti, P., Tonini, R., Romano, F., Bernardi, F., Piatanesi, A., Babeyko, A., Volpe, M., Pintore, S., Mariano Mele, F., & Amato, A. (2019). Probabilistic Tsunami Forecasting (PTF) for Tsunami Early Warning operations. *EGU General Assembly Conference Abstracts*, *21*, 17775. https://ui.adsabs.harvard.edu/abs/2019EGUGA..2117775S

Selva, Jacopo, Tonini, R., Molinari, I., Tiberti, M. M., Romano, F., Grezio, A., Melini, D., Piatanesi, A., Basili, R., Lorito, S., Scala, A., Lorito, S., Romano, F., Murphy, S., Selva, J., Basili, R., Babeyko, A., Herrero, A., Hoechner, A., … Console, R. (2016). Journal of Geophysical Research : Solid Earth. *Geophysical Journal International*, *177*(3), 3782–3803. https://doi.org/10.1002/2015JB012608.Received

Sepúlveda, I., Liu, P. L. F., Grigoriu, M., & Pritchard, M. (2017). Tsunami hazard assessments with consideration of uncertain earthquake slip distribution and location. *Journal of Geophysical Research: Solid Earth*, *122*(9), 7252–7271. https://doi.org/10.1002/2017JB014430

Solheim, A., Berg, K., Forsberg, C. F., & Bryn, P. (2005). The Storegga Slide complex: repetitive large scale sliding with similar cause and development. *Marine and Petroleum Geology*, *22*(1–2), 97–107.

Song, Y. T., Mohtat, A., & Yim, S. C. (2017). New insights on tsunami genesis and energy source. *Journal of Geophysical Research: Oceans*, *122*(5), 4238–4256.

Strasser, F. O., Arango, M. C., & Bommer, J. J. (2010). Scaling of the source dimensions of interface and intraslab subduction-zone earthquakes with moment magnitude. *Seismological Research Letters*, *81*(6), 941–950.

Suppasri, A., Hasegawa, N., Makinoshima, F., Imamura, F., Latcharote, P., & Day, S. (2016). An analysis of fatality ratios and the factors that affected human fatalities in the 2011 Great East Japan tsunami. *Frontiers in Built Environment*, *2*, 32.

Suzuki, W., Aoi, S., Sekiguchi, H., & Kunugi, T. (2011). Rupture process of the 2011 Tohoku-Oki mega-thrust earthquake (M9. 0) inverted from strong-motion data. *Geophysical Research Letters*, *38*(7).

Synolakis, C., & Kânoğlu, U. (2015). The Fukushima accident was preventable. *Philosophical Transactions of the Royal Society A: Mathematical, Physical and Engineering Sciences*, *373*(2053), 20140379.

Synolakis, Costas E, & Bernard, E. N. (2006). Tsunami science before and beyond Boxing Day 2004. *Philosophical Transactions of the Royal Society A: Mathematical, Physical and Engineering Sciences*, *364*(1845), 2231–2265.

Synolakis, Costas Emmanuel. (1987). The runup of solitary waves. *Journal of Fluid Mechanics*, *185*, 523–545.

Tadepalli, S., & Synolakis, C. E. (1994). The run-up of N-waves on sloping beaches. *Proceedings of the Royal Society of London. Series A: Mathematical and Physical*

Sciences, *445*(1923), 99–112.
Tanioka, Y., & Satake, K. (1996). Tsunami generation by horizontal displacement of ocean bottom. *Geophysical Research Letters*, *23*(8), 861–864.
Thio, H. K., Wei, Y., Chock, G., & Li, W. (2017). Development of offshore probabilistic tsunami exceedance amplitudes for ASCE 7-16. *Proceedings of the Sixteenth World Conference on Earthquake Engineering*.
Tinti, S., & Armigliato, A. (2003). The use of scenarios to evaluate the tsunami impact in southern Italy. *Marine Geology*, *199*(3–4), 221–243.
Tinti, S., Armigliato, A., Pagnoni, G., & Zaniboni, F. (2005). Scenarios of giant tsunamis of tectonic origin in the Mediterranean. *ISET Journal of Earthquake Technology*, *42*(4), 171–188.
Titov, V. V, & Gonzalez, F. I. (1997). *Implementation and testing of the method of splitting tsunami (MOST) model*.
Tolkova, E. (2014). Land–water boundary treatment for a tsunami model with dimensional splitting. *Pure and Applied Geophysics*, *171*(9), 2289–2314.
Tomita, T., & Honda, K. (2009). Tsunami estimation including effect of coastal structures and buildings by 3D model. In *Coastal Structures 2007: (In 2 Volumes)* (pp. 681–692). World Scientific.
Tselentis, G.-A., Gkika, F., & Sokos, E. (2006). Tsunami hazards associated with the Perachora fault at eastern Corinth Gulf, Greece. *Bulletin of the Seismological Society of America*, *96*(5), 1649–1661.
Udías, A., Vallina, A. U., Madariaga, R., & Buforn, E. (2014). *Source mechanisms of earthquakes: theory and practice*. Cambridge University Press.
Ulrich, T., Gabriel, A.-A., & Madden, E. (2020). *Stress, rigidity and sediment strength control megathrust earthquake and tsunami dynamics*.
Ulvrova, M., Selva, J., Paris, R., Brizuela, B., Costa, A., Grezio, A., Lorito, S., & Tonini, R. (2016). Probabilistic tsunami hazard assessment related to underwater explosions in the Campi Flegrei caldera: Gulfs of Napoli and Pozzuoli (Tyrrhenian Sea, Italy). *EGU General Assembly Conference Abstracts*, EPSC2016-16366.
Uphoff, C., Rettenberger, S., Bader, M., Madden, E. H., Ulrich, T., Wollherr, S., & Gabriel, A.-A. (2017). Extreme scale multi-physics simulations of the tsunamigenic 2004 sumatra megathrust earthquake. *Proceedings of the International Conference for High Performance Computing, Networking, Storage and Analysis*, 1–16.
Van Zelst, I., Wollherr, S., Gabriel, A., Madden, E. H., & van Dinther, Y. (2019). Modeling megathrust earthquakes across scales: One-way coupling from geodynamics and seismic cycles to dynamic rupture. *Journal of Geophysical Research: Solid Earth*, *124*(11), 11414–11446.
Vater, S., Beisiegel, N., & Behrens, J. (2015). A limiter-based well-balanced discontinuous Galerkin method for shallow-water flows with wetting and drying: One-dimensional case. *Advances in Water Resources*, *85*, 1–13.
Volpe, M., Lorito, S., Selva, J., Tonini, R., Romano, F., & Brizuela, B. (2018). From regional to local SPTHA: efficient computation of probabilistic inundation maps addressing near-field sources. *Natural Hazards and Earth System Sciences Discussions*, 1–19. https://doi.org/10.5194/nhess-2018-202
Vreugdenhil, C. B. (1994). *Numerical methods for shallow-water flow* (Vol. 13). Springer Science & Business Media.
Wang, D., & Mori, J. (2011). Rupture process of the 2011 off the Pacific coast of Tohoku

Earthquake (Mw, 9.0) as imaged with back-projection of teleseismic P-waves. *Earth, Planets and Space*, *63*(7), 603–607. https://doi.org/10.5047/eps.2011.05.029

Wang, X. (2009). USER MANUAL FOR COMCOT VERSION 1 . 7 (FIRST DRAFT) by. *Control*, *7*.

Watts, Ph, & Waythomas, C. F. (2003). Theoretical analysis of tsunami generation by pyroclastic flows. *Journal of Geophysical Research: Solid Earth*, *108*(B12).

Watts, Philip. (2000). Tsunami features of solid block underwater landslides. *Journal of Waterway, Port, Coastal, and Ocean Engineering*, *126*(3), 144–152.

Wei, Y., Thio, H. K., Titov, V., Chock, G., Zhou, H., Tang, L., & Moore, C. (2017). Inundation modeling to Create 2,500-year return period tsunami design zone maps for the ASCE 7-16 standard. *Proceedings of the Sixteenth World Conference on Earthquake Engineering*.

Wells, D. L., & Coppersmith, K. J. (1994). New empirical relationships among magnitude, rupture length, rupture width, rupture area, and surface displacement. *Bulletin of the Seismological Society of America*, *84*(4), 974–1002.

Wijayaratna, N., Suzuki, T., & Jayaratne, R. (2005). *The 2004 Sumatra earthquake tsunami , tsunami field survey in southern part of Sri Lanka*. *January 2019*.

Wood, N. J., Jones, J., Spielman, S., & Schmidtlein, M. C. (2015). Community clusters of tsunami vulnerability in the US Pacific Northwest. *Proceedings of the National Academy of Sciences*, *112*(17), 5354–5359.

Wünnemann, K., & Weiss, R. (2015). The meteorite impact-induced tsunami hazard. *Philosophical Transactions of the Royal Society A: Mathematical, Physical and Engineering Sciences*, *373*(2053), 20140381.

Yalciner, A.; Pelinovsky, E.; Zaytsev, A.; Kurkin, A.; Ozer, C.; Karakus, H. NAMI DANCE Manual; Technical Report; METU, Civil Engineering Department, Ocean Engineering Research Center: Ankara, Turkey, 2006.

Yao, H., Shearer, P. M., & Gerstoft, P. (2013). Compressive sensing of frequency-dependent seismic radiation from subduction zone megathrust ruptures. *Proceedings of the National Academy of Sciences of the United States of America*, *110*(12), 4512–4517. https://doi.org/10.1073/pnas.1212790110

Ye, L., Lay, T., Kanamori, H., & Rivera, L. (2016). Rupture characteristics of major and great (Mw≥ 7.0) megathrust earthquakes from 1990 to 2015: 1. Source parameter scaling relationships. *Journal of Geophysical Research: Solid Earth*, *121*(2), 826–844.

Yeh, H. (2010). Gender and age factors in tsunami casualties. *Natural Hazards Review*, *11*(1), 29–34.

Yeh, H., Liu, P., Briggs, M., & Synolakis, C. (1994). Propagation and amplification of tsunamis at coastal boundaries. *Nature*, *372*(6504), 353–355.

Yokota, Y., Koketsu, K., Fujii, Y., Satake, K., Sakai, S., Shinohara, M., & Kanazawa, T. (2011). Joint inversion of strong motion, teleseismic, geodetic, and tsunami datasets for the rupture process of the 2011 Tohoku earthquake. *Geophysical Research Letters*, *38*(7).

Yokoyama, I. (1987). A scenario of the 1883 Krakatau tsunami. *Journal of Volcanology and Geothermal Research*, *34*(1–2), 123–132.

Yue, H, & Lay, T. (2011). Inversion of high-rate (1 sps) GPS data for rupture process of the 11 March 2011 Tohoku earthquake (Mw 9.1). *Geophysical Research Letters*, *38*(7).

Yue, Han, & Lay, T. (2013). Source rupture models for the M w 9.0 2011 Tohoku earthquake from joint inversions of high-rate geodetic and seismic data. *Bulletin of the Seismological Society of America*, *103*(2B), 1242–1255.

Zeng, Y., Anderson, J. G., & Yu, G. (1994). A composite source model for computing realistic synthetic strong ground motions. *Geophysical Research Letters*, *21*(8), 725–728.

https://doi.org/10.1029/94GL00367

APPENDIX

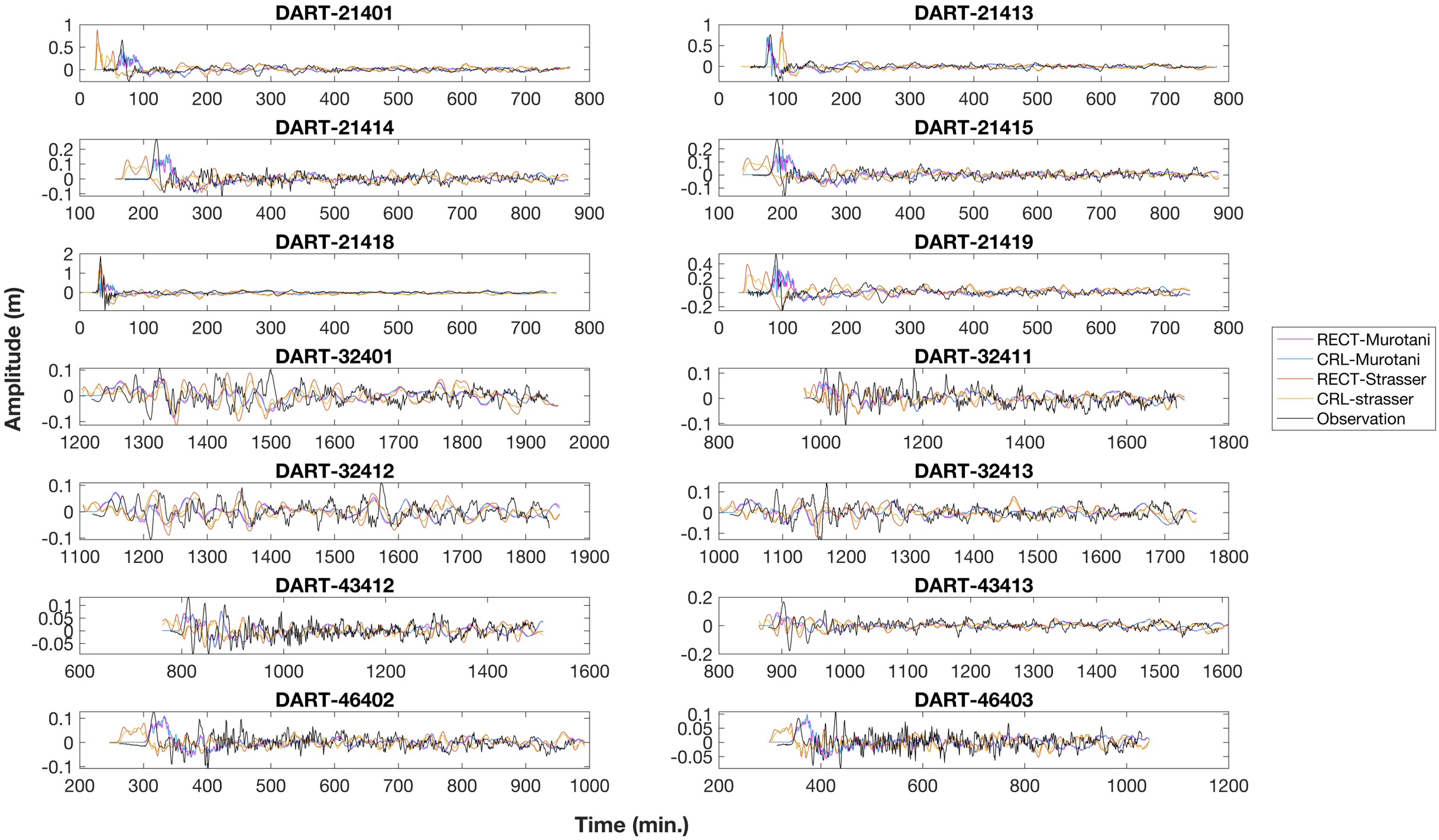

Figure 3.5.2a: *Synthetic tsunami waveforms of a random scenario from 2011 Tohoku event for different model types*

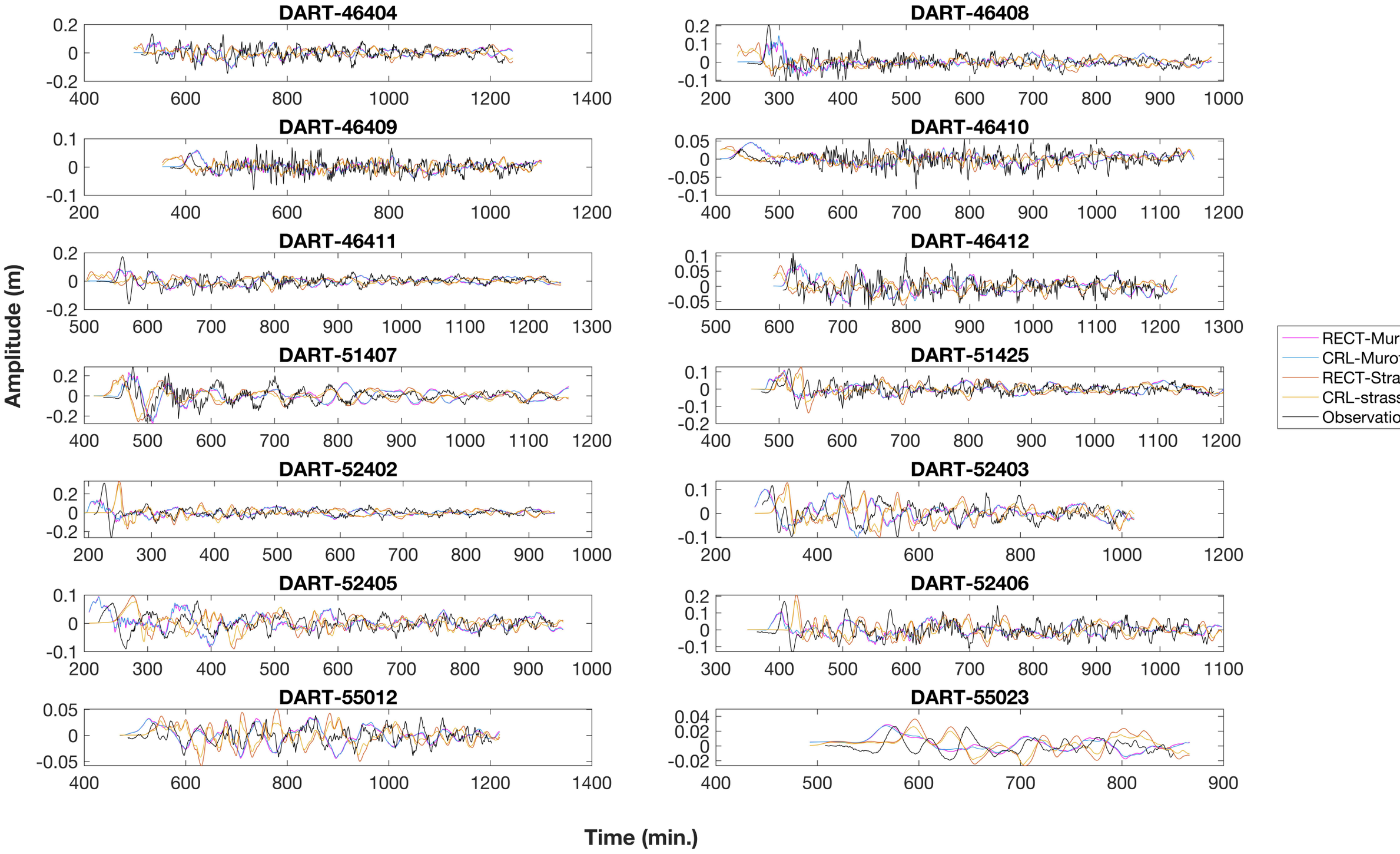

Figure 3.5. 2b: *Synthetic tsunami waveforms of a random scenario from 2011 Tohoku event for different model types*

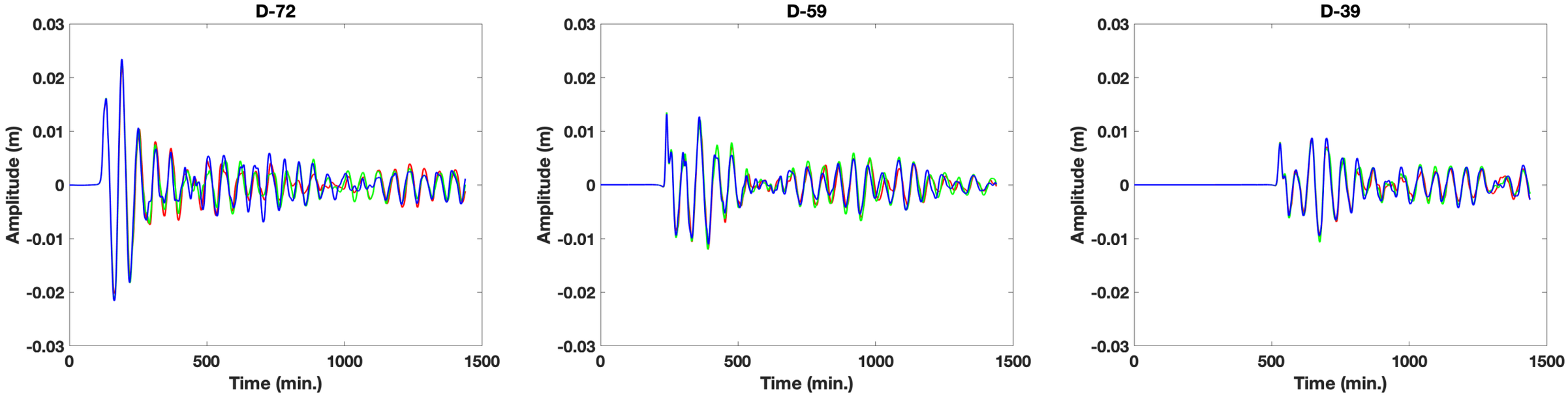

Figure 3.4.3: *Tsunami time-series at different synthetic gauge points for the Tocopilla, Chile 2007 event.*

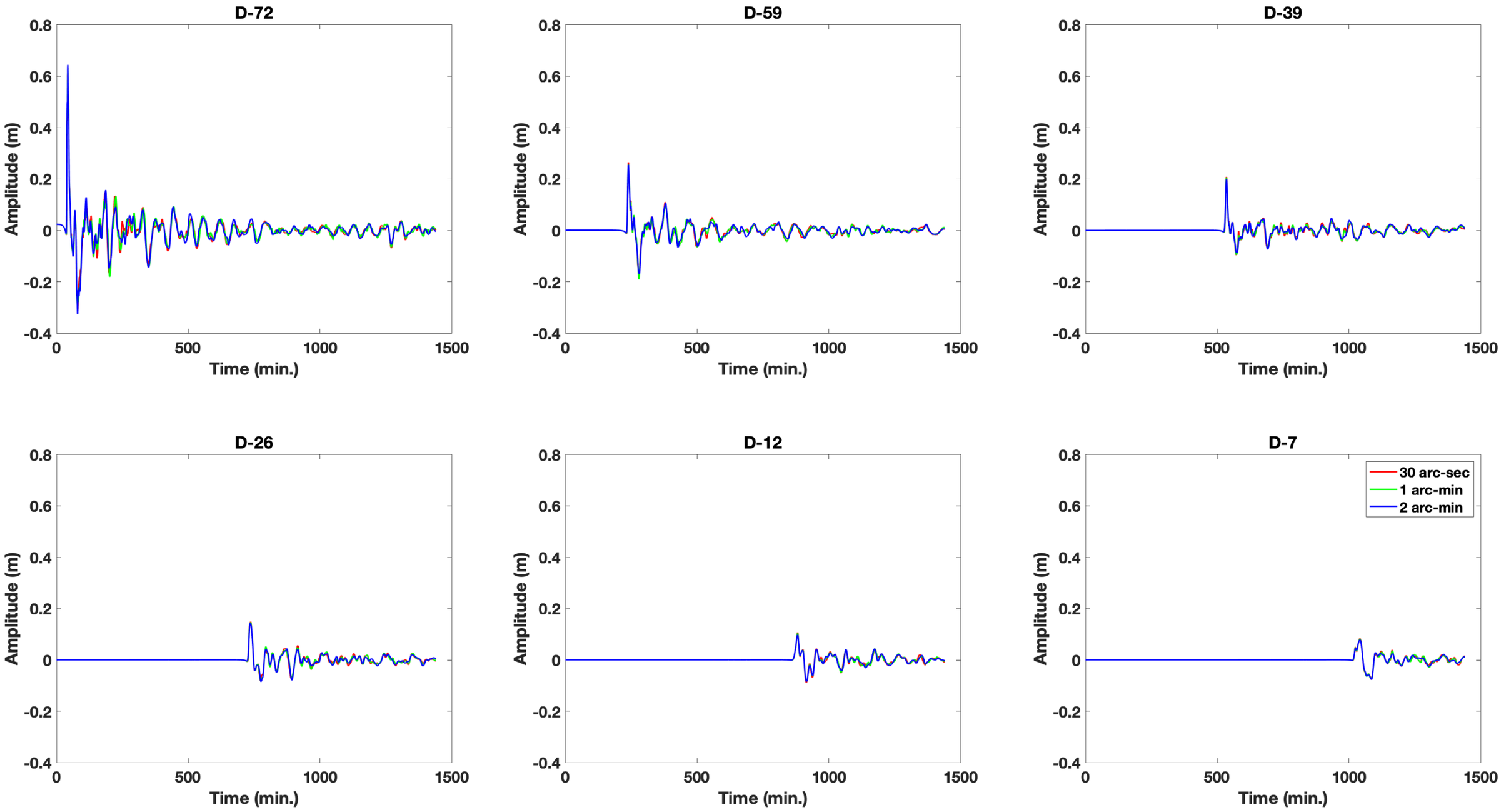

Figure 3.4.4: *Tsunami time-series at different synthetic gauge points for Maule, Chile, 2010 event.*

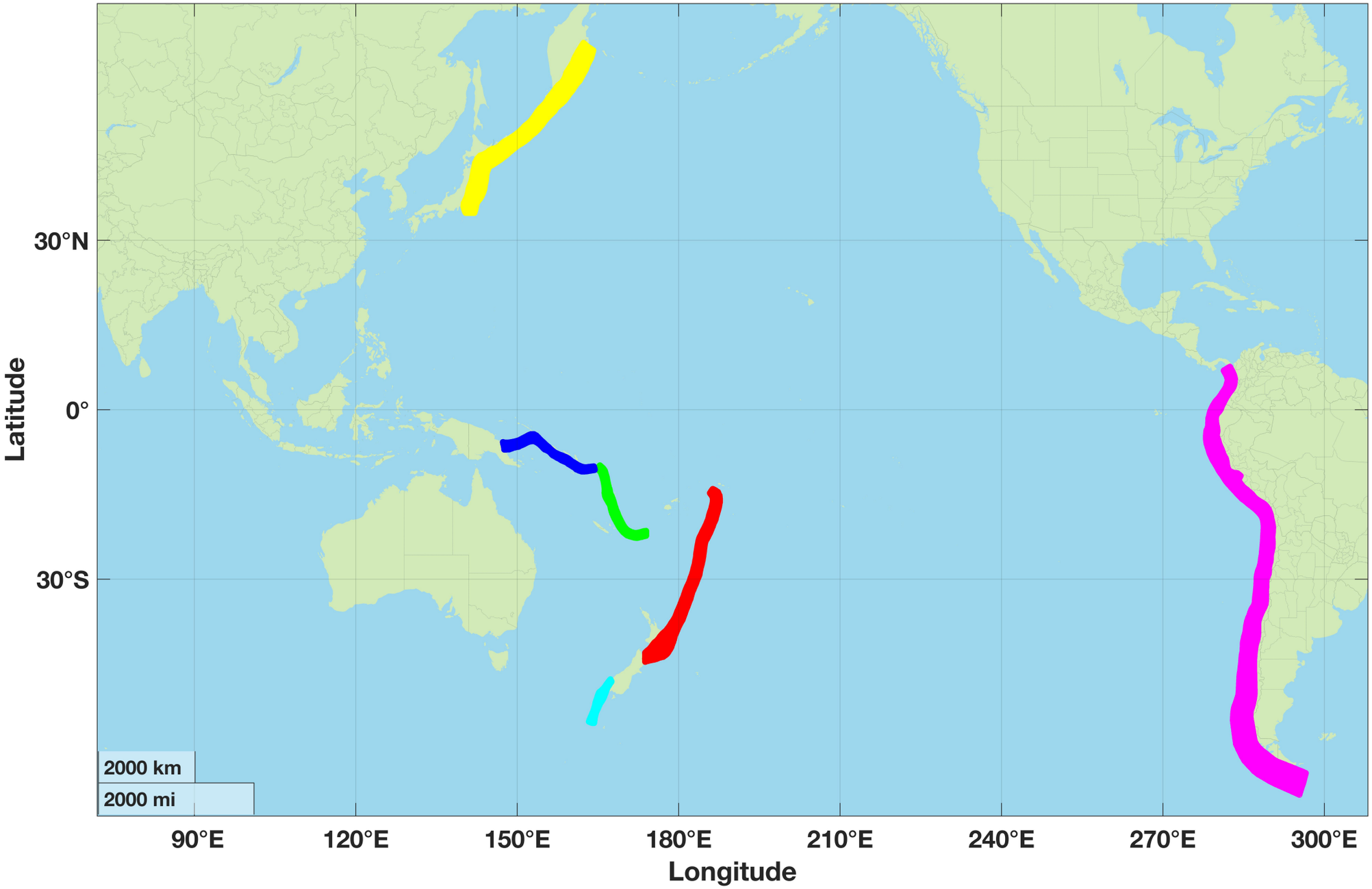

Figure A1: *Location of each subduction zone used in the generation of stochastic slip modelling. The colors yellow, blue, green, red, cyan and pink represent the location of the Kurils-Japan, Solomons, New-Hebrides, Kermadec-Tonga, Puysegur and South America slabs, respectively.*

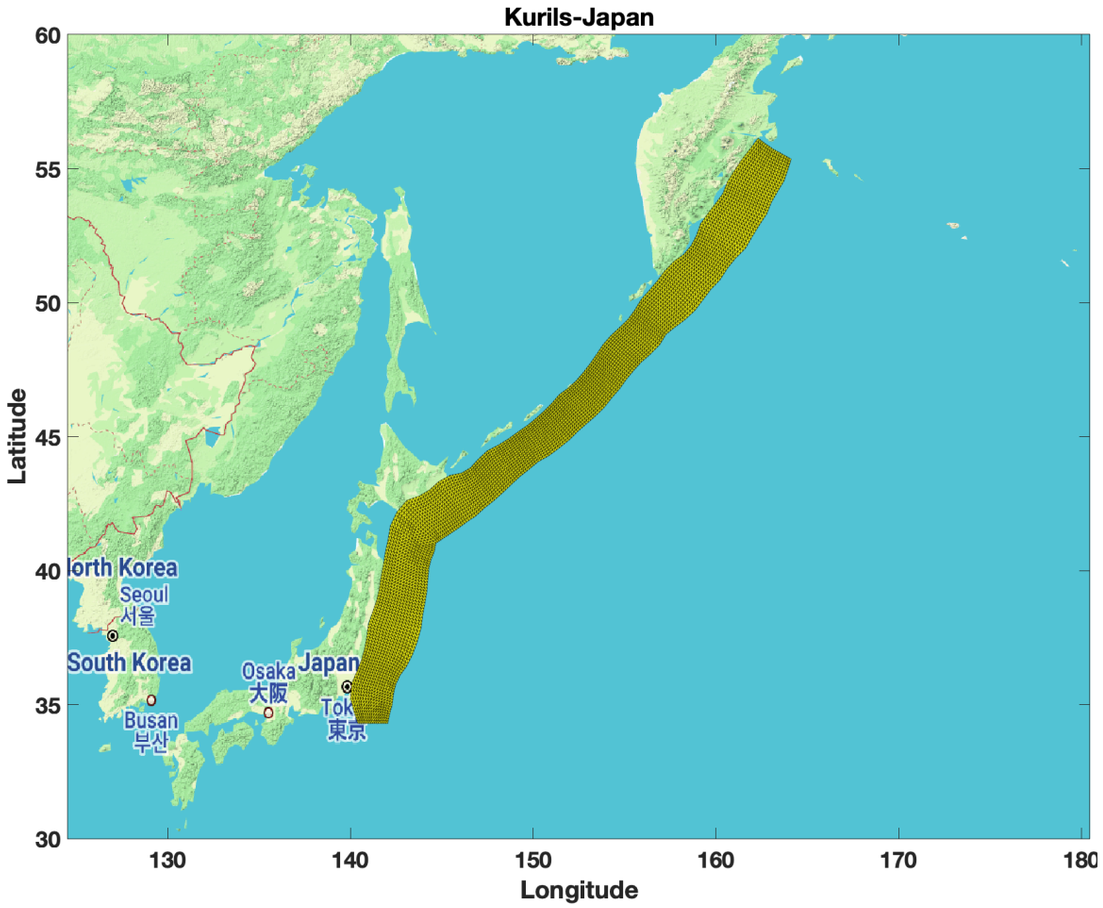
Kurils-Japan
Latitude
Longitude
North Korea
Seoul
서울
South Korea
Busan
부산
Osaka
大阪
Japan
Tok
東京

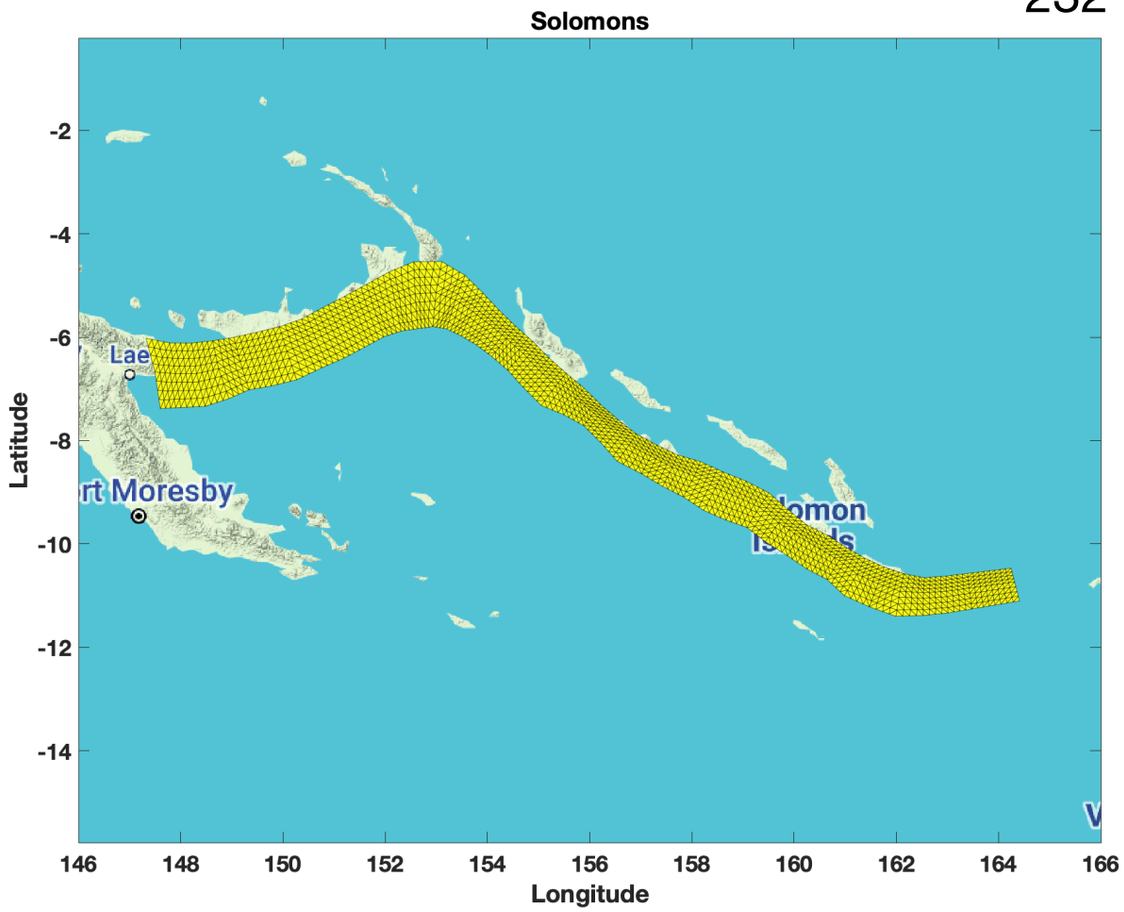
Solomons
Latitude
Longitude
Lae
rt Moresby

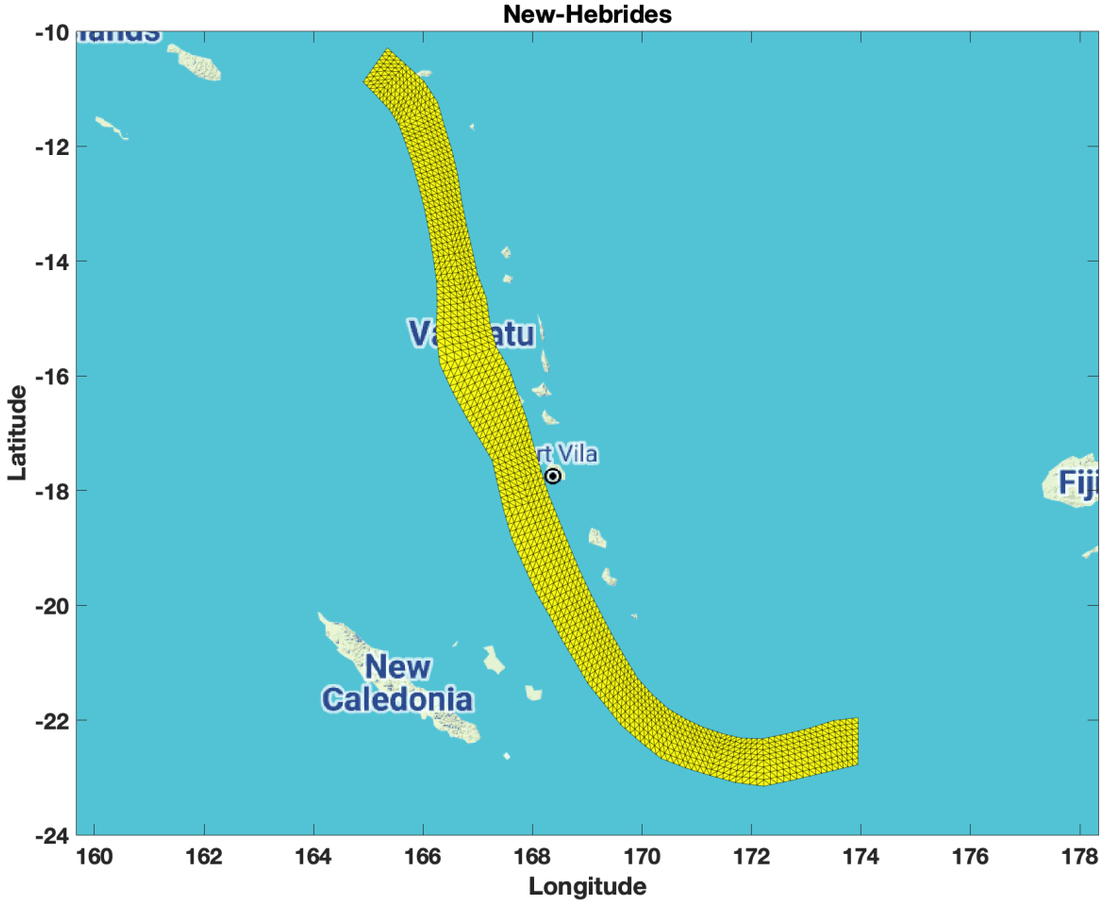
New-Hebrides
Latitude
Longitude
rt Vila
Fiji
New
Caledonia

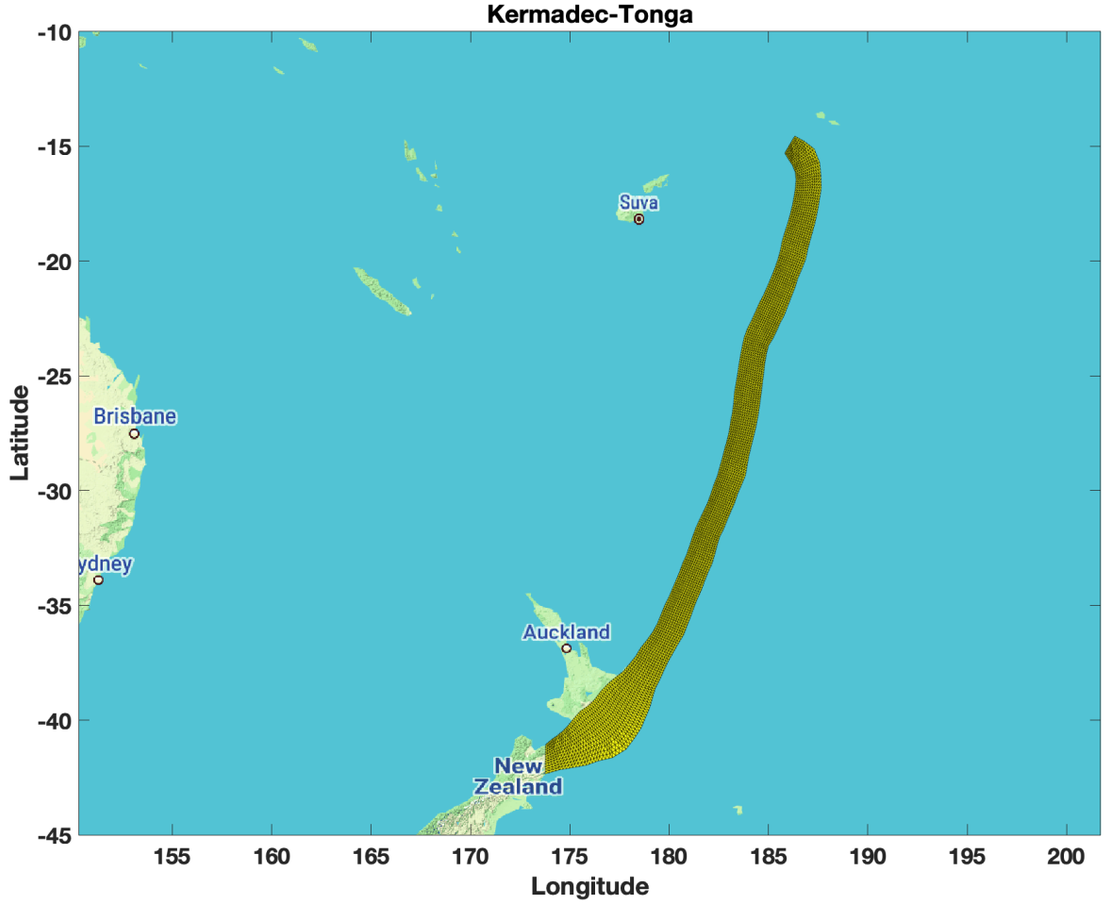
Kermadec-Tonga
Latitude
Longitude
Suva
Brisbane
ydney
Auckland
New
Zealand

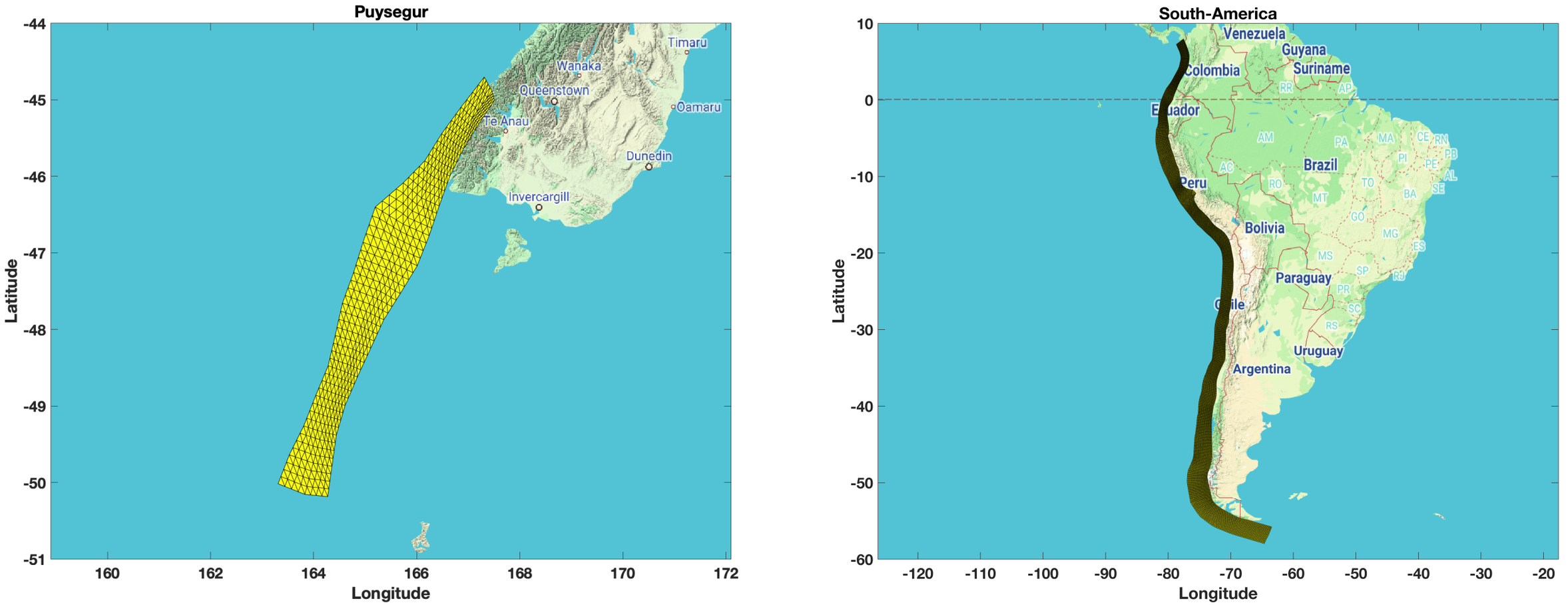

Figure A2: *Triangular discretization of each slab used in the generation of stochastic slip modelling.*